STRUCTURAL, MAGNETIC AND TRANSPORT PROPERTIES OF BISMUTH AND RARE EARTH MANGANITES

A thesis submitted for the degree of

DOCTOR OF PHILOSOPHY

in

PHYSICS

by

RAMESH ADE

SCHOOL OF PHYSICS
UNIVERSITY OF HYDERABAD
HYDERABAD-500046
TELANGANA
INDIA

NOVEMBER 2015

To

My Parents

DECLARATION

I, Ramesh Ade, hereby declare that the thesis entitled "**STRUCTURAL, MAGNETIC AND TRANSPORT PROPERTIES OF BISMUTH AND RARE EARTH MANGANITES"** submitted by me under the guidance and supervision of Prof. Rajender Singh is a bonafide research work which is also free from plagiarism. I also declare that it has not been submitted previously in part or in full to this University or any other University or Institution for the award of any degree or diploma. I hereby agree that my thesis can be deposited in Shodganga/INFLIBNET.

A report on plagiarism statistics from the University Librarian is enclosed.

Date: Ramesh Ade

(Reg. No. 10PHPH07)

Signature of the Supervisor

CERTIFICATE

This is to certify that the research work presented in the thesis entitled "**STRUCTURAL, MAGNETIC AND TRANSPORT PROPERTIES OF BISMUTH AND RARE EARTH MANGANITES"** is an original work carried out by **RAMESH ADE.** This work has been carried out under my supervision. The thesis is submitted by **RAMESH ADE** for the degree of **DOCTORATE IN PHILOSOPHY** in the School of Physics. This thesis work has not been submitted to any other university partially or fully for the award of any degree.

Prof. Rajender Singh
(Supervisor)

Dean
School of Physics
Date:

Acknowledgments

I would like to express my deep gratitude to my supervisor, **Prof. R. Singh.** Without his valuable guidance this thesis would have been impossible. Dear Sir, thank you for keeping me in a proper direction. Working with you has been an enjoyable and informative experience.

I would like to thank, the present Dean Prof. R. Singh and the former Deans, Prof. C. Bansal, Prof. S. P. Tewari and Prof. S. Chaturvedi, School of Physics, for providing all the facilities to carry out my research. I would also like to thank the faculty, School of Physics. Special thanks to my doctoral committee members, Prof. C. S. Sunandana, Prof. P. K. Suresh, Prof. M. Ghanashyam Krishna and Dr. S. V. S. Nageswara Rao, for their valuable suggestions. I also thank Dr. G. Venkataiah, for his valuable suggestions.

I thank Mr. T. Abraham for the help he has extended in the administrative matters. I thank Mr. Laxminarayana, Mr. Tirumal, Mr. Ravi Shankar, Ms. Arundhathi, Ms. Deepthi, Ms. Sunitha and other non-teaching staff of School of Physics, who helped in measurements.

I would also like to thank the staff of central instruments laboratory (CIL) for their unlimited help. I thank Dr. S. M. Ahmed, Mr. Suresh, Dr. S. Manjunath, Mr. Pavan Kumar, Mr. Sudhakar, Mr. Ellayya, and Mr. Nagaraju, for the technical support and for the hands on experience on the instruments. I also thank Mr. Sambasiva Rao, Mr. Mantoo Kumar, Mr. Giri Bahadur and Mr. Sai for providing liquid Nitrogen and Helium for low-temperature experiments.

I thank coordinators of center for nanotechnology, Prof. S. N. Kaul, Prof. V. Seshubai and Prof. M. Ghanashyam Krishna, for providing PPMS-VSM facility.

I thank SEST Dean for providing XRD facility. I also thank XRD operator Mr. Ramana.

I would like to thank UGC-CSIR, India for the financial assistance.

I thank my senior Dr. Joji Kurian for his continuous support and valuable suggestions throughout my Ph. D work.

I thank my labmates Dr. P. Sandhyarani, Dr. D. Vijayan, Dr. M. Venkaiah, Dr. S. Saipriya, G. Thirupathi, M. Padmavathi, Kiran, Jasmeeth, Ravibabu, Atiya and Nisha.

I thank Dr. B. Yugandhar and Dr. A. Sendil, for their help in magnetization and structural analysis part.

I am very much thankful to Nageswara Rao Sir, UV institute, for giving fruitful suggestions while preparing for UGC-CSIR (NET) exam.

I thank B. Ravikumar, M. Uma Sankar (Late), Pavan Venu Prakash and Binoy for their help in magnetization measurements.

I thank B. Ravikumar and Raju Botta for their continuous support and the help.

Here it is a special group, again Raju and Ravi, Pasha, Ashok, Yadaiah, Pavan Sugali, Pundarikam, Satyanarayana, Dr. Suman Kalyan and Dr. Ananthaiah, thanks one and all. I also thank Dr. Ramudu, Dr. Swaroop, Dr. P. D. Shankar, Dr. N. Shankariah, Dr. Suresh, Dr. Balu, Dr. Satyanaryana, Aalu, Sanjeev, I. V. Shankar, Narasihma Raju, Uma Lavanya, Ramya, Monisha, Luhluh, Dr. Siva N. Chari, Dr. Deepthi, Madhu, Dr. Ravikanth, Sanjeeb, Manikanta, Anil, Ramakanth, Nagireddy, Bashaiah, Sandeep, Mohan, Srinu, Dr. Kiran, Dr. Ahmad, Dr. Ramesh, Laxminarayana, Santanu, Lakshun, Narasihmappa, Shiva RK, Varma, Kiran, Sravan, Durga Prasad, Shankarnath, Alkathi and Andrews.

I also thank all my friends from ACRHEM, SEST and Chemistry.

I thank my B. Sc fiends Srinivas, Ramesh, Satish, Kanakaiah, Thirupathi, Ramreddy and all other B. Sc batchmates and senior friends. I thank all M. Sc batch friends.

I don't know whether God is there or not, but I saw the God in my parents, **Shankaraiah Ade and Lakshmi Ade**. My father hard working in his agriculture is the grate inspiration for me in the education. Amma thanks for your love. Though we have financial problems, you never disappointed me for anything. Thanks Amma and Nanna.

I thank my brothers Rayamallu and Srinivas for their continuous support. My brother Srinivas stopped his education after 10th class due to financial problems and encouraged me for higher studies. Anna thanks once again. I also thank my sister in-laws, Vijaya and Rama Devi, for your support. Dear sweet Haritha, cute Anjali, Akshay and Manoj, thank you for your love on me.

I thank my babai, Venkanna, for his valuable guidance from my childhood stage onwards.

I never forget support from my elder sister, Latha Aare and brother in-law, Satyanarayana Aare. They helped me a lot and solved many problems in various stages of my life. Along with my nephew Srivenu and niece Sandhyarani, it is also like my family.

I thank my brother in-laws, Srinivas, Gangadhar, Laxman and Suresh for their support. I also thank Pochanna, Srinivas. I would like to thank Shobhan and Srinivas Shere.

I am very fortune to have Jamuna as my life partner. Her love and care gave me boost in the final stage of Ph. D work. Thanks Ra.

I thank Prof. Khaja Althaf Hussain, Kakatiya University, who encouraged me towards research field. I thank J. V. R Sir for his valuable guidance from under graduate level. I also thank all my teachers who kept me in right direction and supported. Thanks teachers.

Still, so many people helped me in different stages or situations. Though, I have not listed their names here, those all are in my heart, Thank you one and all.

Finally, I thank ALL OF THEM who made my life fruitful and showed a right path to achieve my goals.

Abstract

Manganites crystallize in a 'perovskite' structure with the general formula represented as ABO_3. Here the A-site constitutes a trivalent (La^{3+}, Pr^{3+}, Bi^{3+}, etc.) and/or divalent (Ca^{2+}, Sr^{2+}, Ba^{2+}, etc.) ion, the B-site is Mn ion and 'O' is oxygen ion. Manganites exhibit unusual magnetic and transport properties which are important for technological applications. These unusual properties are due to the strong coupling between the charge, the concomitant spin and orbital degrees of freedom. The interesting thing about the manganites is that the strength of coupling can be altered by disorder introduced by different types of substitutions/doping at A/B-sites and change in grain size of the system. The disorder is created due to the change in the chemical pressure, which in turn affects the Mn^{3+}/Mn^{4+} ratio, the Mn-O bond length and the Mn-O-Mn bond angle and in turn affects the crystal structure, magnetic and transport properties of the system

The present study is undertaken to get deeper understanding of the effect of doping (at A/B-site) in Bi and rare earth manganites on their structural, magnetic and transport properties. The effect of grain size on these properties is also studied for $Bi_{0.5}Ca_{0.5}MnO_3$ composition.

The present study shows that the doping (at A/B-site) and changes in grain size induces changes in structural, magnetic and transport properties of the samples. The changes in magnetic and transport properties of the samples are correlated with the change in structural parameters. ESR and magnetization studies reveal that the phase separation is an intrinsic phenomenon in these manganite systems.

Contents

Chapter 1

Introduction

Manganites, which belong to the branch of strongly correlated systems, exhibit unusual magnetic and transport properties [1, 2] and have been used in technological applications like microelectronic, magnetic and spintronic devices, etc. [3-5]. Manganites have a general formula represented as ABO_3 where the A-site represents trivalent (La^{3+}, Pr^{3+}, Bi^{3+}, etc.) and/or divalent (Ca^{2+}, Sr^{2+}, etc.) ions and the B-site represents Mn ions. The three main reasons which have triggered the wide interest in manganites are: i) vaguely explained transport properties in these low-bandwidth materials. They are insulators at room temperature, changing into bad metals at low-temperatures. Upon application of small magnetic fields, these compounds exhibit metallic properties along with the appearance of colossal magnetoresistance (CMR), ii) rich phase diagrams and iii) intrinsic inhomogeneities in most of the temperature (T) versus hole density (x) plots even in single crystals [6].

The interplay between magnetic, structure and electronic transport in these materials gives rise to several novel phenomena such as double-exchange (DE) and superexchange (SE) interaction which occur due to hopping of charge carriers between Mn ions (Mn^{3+}/Mn^{4+}) via oxygen anions [6]. The properties of manganese oxides are mainly influenced by Mn^{3+}/Mn^{4+} ratio, the Mn-O-Mn bond length and the Mn-O-Mn bond angle, which give the emergence of various physical properties [7-22].

In this chapter the important aspects of manganites, i.e., structure, effect of various parameters on the physical properties of manganites and various phenomena exhibited by manganites, are discussed.

Important aspects of manganites

1.1. Structure of manganites

Perovskite is a calcium titanium oxide mineral species composed of calcium titanate, with the chemical formula of $CaTiO_3$. The mineral was discovered by

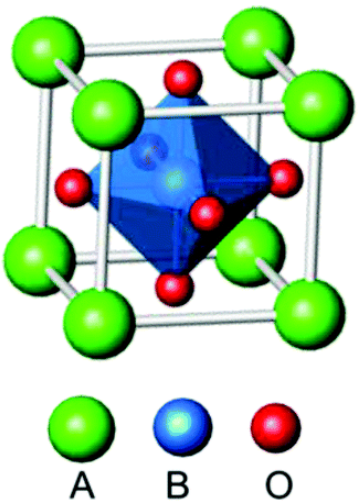

Fig. 1.1. The ABO_3 perovskite structure.

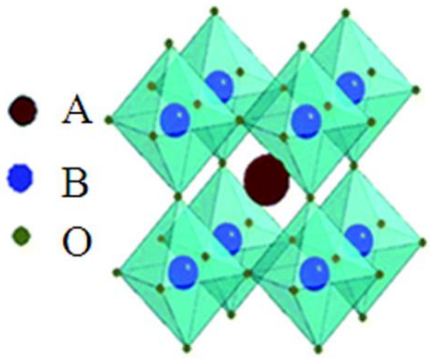

Fig. 1.2. The extended network of an ideal perovskite structure connected by the corner-shared octahedral.

Gustav Rose in 1839 and is named as perovskite after the Russian mineralogist, L. A. Perovskii (1791-1856). Later his name has been used for compounds which possess crystal structure similar to $CaTiO_3$ [23].

Manganites crystallize in the perovskite structure, as shown in Fig. 1.1. The details of A and B are mentioned in the above section. The mixed-valence manganites have been intensely studied after Jonker and van Santen [24] prepared them for the first time. Mixed-valence manganites have the general formula represented as $RE_{1-x}AE_xMnO_3$ (RE = rare earth ions, AE= alkaline earth ions). In these compounds, Mn ion exists in 3+ and 4+ states, whose values change depending on the value of *x*. The A-site ions will be located at the corners of the unit cell, the B-site ions occupying the center of the cube while the oxygen ions will be located at the center of the faces. Fig. 1.2 shows the extended network of perovskite structure consisting of a three-dimensional vertex sharing network of BO_6 octahedron with interstitial A-site cations. An ideal perovskite structured materials, possess cubic structure and have strong ionic bonds. In this structure, these bonds keep the electrons from hopping, as a result these materials exhibit insulating properties.

1.2. Tolerance factor

Tolerance factor (*t*) plays a significant role on the properties of the manganites. Tolerance factor gives the information about the stability and distortion of crystal structures. In the early stage, it is used to calculate the stability of the perovskite structure. The *t* can be expressed as

$$t = \left(r_A + r_o\right) \Big/ \sqrt{2}\left(r_B + r_o\right) \tag{1.1}$$

where r_A, r_B and r_o denote the radii of ions A, B and O, respectively.

The perovskite structure is stable only if *t* value equals to unity [25]. For example, *t* for $SrTiO_3$ is 1. Substitution of cations or changes in oxygen

stoichiometry modifies the ideal cubic perovskite structure to lower symmetry structures by changing its t value. If t slightly deviates from unity, then the structure of the perovskite distorts and/or cooperatively rotates the MO_6 octahedra. In case of $t = 1$ the Mn-O-Mn bond angle is 180^o and for $t < 1$ or $t > 1$ the Mn-O-Mn bond angle changes from 180^o, which leads to structures of lower symmetry. Due to this the octahedra tilt/rotate to reduce the excess space around the A-site cation [26]. Depending on the magnitude of the distortion one can tune the relation among structure, magnetic and electrical properties [27].

1.3. The average ionic size of A-site cation and the variance of A-site cation size distribution

In manganites, as it is mentioned, the disorder originates both from A-site as well as B-site doping. Doping at A-site modifies the average ionic size of A-site cations ($<r_A>$) and the variance of the A-site cation size distribution (σ^2) resulting in structural disorder. This in turn affects the Mn-O-Mn bond length, the Mn-O-Mn bond angle and band gap and hence the properties of manganites.

Although the value of tolerance factor is used to correlate the magnetic, transport and lattice structure of manganites, it can not provide information related to the disorder of A-site ions. In order to calculate A-site cation disorder, the σ^2 term was introduced which affects the magnetic and transport properties of manganites. The expression for σ^2 is as follows

$$\sigma^2 = \sum_i x_i r_i^2 - \langle r_A \rangle^2 \tag{1.2}$$

Here x_i and r_i are the atomic fraction and ionic radii of i-type ions at A-site, respectively [28]. The change in the value of σ^2 changes the oxygen position which results in the changes of magnetic and transport properties of the

manganites. It can also modify the transition temperatures of transitions like ferromagnetic metallic (FMM) to paramagnetic insulating (PMI), cluster glass (CG) and spin glass (SG) state. The detailed discussion on the effect of average size of the A-site cations and the variance of A-site cation size is given in chapters 3, 4 and 5.

1.4. Crystal field and Jahn-Teller effect

1.4.1. d-orbital configuration

Transition metal complexes form when a central ion which is called coordination center is surrounded by ligands or complexing agents. Ligands are the ions or molecules which are bound to the central ion to form a coordination complex. These transition metal complexes or oxides have five d-orbitals and it is known that the shape of the each orbital is differs from the other. As a result, these orbitals interact differently with the electric field created by the ligands which are coordinated through the central ion.

The configuration of five d-orbitals is shown in Fig. 1.3. The circles with green in color with negative sign represent the coordinating electron-pairs of the

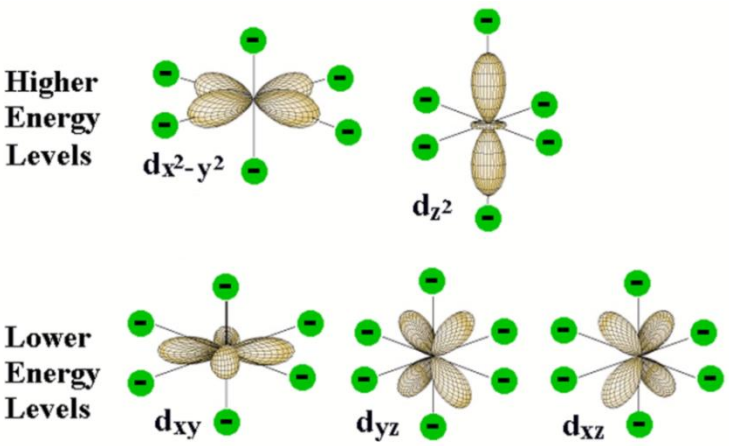

Fig. 1.3. Representation of the d-orbital configuration.

ligands which are located at the six corners of the octahedron around the central ion. In d_{z^2} and $d_{x^2} - d_{y^2}$ orbitals the electron cloud point directly towards ligand atoms. The electrons occupying these orbitals will experience more repulsion by the electron pairs which bind the ligands that are situated at corresponding corners of the octahedron. As a result, the energies of these two orbitals increase compared to the other three orbitals whose lobes are not directed toward the octahedral position.

1.4.2. Crystal field theory

The crystal field theory (CFT) is used to explain the breaking of 'd' or 'f' orbital degeneracy. A static electric field produced by a surrounding ion charge distribution helps in degeneracy breaking. This theory is used to describe various properties such as spectroscopic and magnetic properties of transition metal elements, which are having active d-shell with five degenerate orbitals. If a transition metal element is in empty space, degeneracy exists due to rotational invariance within the angular momentum l = 2 subspace. When the ions of this element are part of the crystal structure, the crystal axis orients in specific directions. As a result, system loses its rotational invariance which results in the splitting of the l = 2 levels. This is called crystal-field splitting [29].

When the ligand approaches metal ions, which are part of the compound, the ions of transition metal element and the non-bonding electrons of ligand repel. This results in lifting of degeneracy of the energy levels. The electrons of the orbitals of the d-shell which are close to the electrons of the ligand repel more; as a result these electrons get more energy and vice-versa. This causes the difference in the energy levels. The nature of metal ions and their oxidation states and the nature of ligands surrounding the ion decide the energy difference (Δ) of splitting levels. This energy difference can be represented as

$$\Delta \approx \langle r \rangle^4 / R \tag{1.3}$$

where r is the radius of the d-orbital and R is metal-ligand internuclear distance. A large crystal field splitting can be provided with the ligands of high negative charge and smaller ionic radii and with the metal cations of a large oxidation number.

Various types of crystal field splitting occur, namely cubic crystal field splitting, octahedral crystal field splitting, tetrahedral crystal field splitting, etc. Octahedral (O_h) crystal field splitting, in which the ligands surrounding the metal ions form an octahedron structure, is important in the present work and it is shown in the Fig. 1.4. In this structure, the d-shell orbitals split into two groups. The first group orbitals d_{xy}, d_{yz} and d_{xz} form π-bonding and possess lower energy.

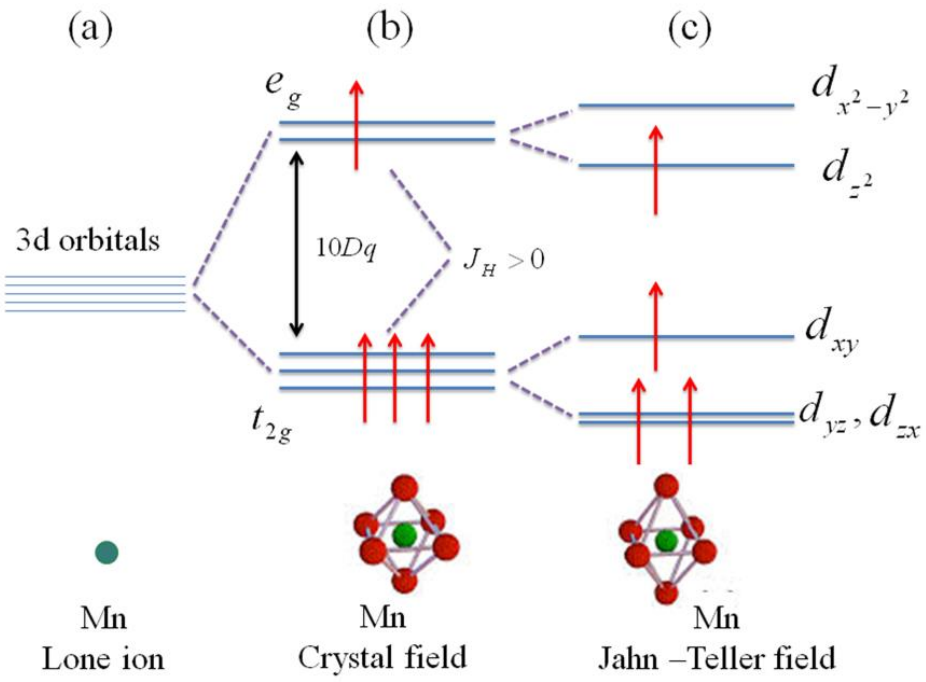

Fig. 1.4. Crystal field and Jahn-Teller effect of Mn 3d-orbitals.

The second group orbitals d_{z^2} and $d_{x^2}-d_{y^2}$ form σ-bonding and possess high energy. The first and the second group orbitals belong to the t_{2g} and e_g symmetry category, respectively. It is known that in case of π-bonding d_{xy}, d_{yz} and d_{xz} orbitals are farther from the ligands compared to the case of σ-bonding in which d_{z^2} and $d_{x^2}-d_{y^2}$ orbitals are close to the ligands. As a result, the interaction between the electrons of d_{xy}, d_{yz} and d_{xz} orbitals and the electrons of ligands become weak and these orbitals get lower energy, whereas the interaction between the electrons of d_{z^2} and $d_{x^2}-d_{y^2}$ orbitals and the electrons of ligands become strong and get higher energy.

1.4.3. Jahn-Teller effect

The Jahn-Teller (J-T) effect is also known as Jahn-Teller distortion, describes the geometrical distortion of molecules and ions that is associated with certain electron configuration and this electronic effect is named after H. A. Jahn and E. Teller [30]. The J-T theorem states that "in an electronically degenerate system, a non-linear molecule undergoes distortion to remove the degeneracy by lowering the symmetry and thus by lowering the energy".

The effect of crystal field on the degenerate 3d-orbitals is shown in the section 1.4.2. In this section, it is also shown that e_g has doublet and t_{2g} have triplet states. An electron ($3d^1$) may occupy any one of the degenerate orbitals and these orbitals are said to be asymmetrically occupied. As we know that asymmetrically occupied orbitals acquire more energy. In this state, the system tries to reduce its energy by lowering overall symmetry of the molecule via lattice motion. As a result, the system undergoes distortion. This in turn removes the degeneracy of doublet and triplet. The effect of removing the degeneracy through an orbital-lattice interaction is called J-T effect [30]. The symmetry of the molecule can be

lowered either by elongation or by compression of the bonds along the z-axis.

Isolated manganese has five degenerated 3d-orbitals. When crystal field effect comes into play, these degenerated orbitals split into two categories namely e_g (doublet) and t_{2g} (triplet). If we consider Mn^{3+}, it has $3d^4$ configuration, high energy state, e_g, can be filled by one electron and the lower energy state, t_{2g}, can be filled by three electrons (Fig. 1.4). The energy difference between the e_g and t_{2g} levels is of the order of ~1.0 eV (10 Dq) [29] and the Hund's coupling (J_H) or exchange energy among Mn 3d electrons is of the order of ~2.5 eV. This keeps the electron spins of Mn^{3+} and Mn^{4+} ions in the parallel arrangement. According to Hund's rule and exchange interaction, a high energy state ($t_{2g}^{3\uparrow} e_g^{1\uparrow}$) is favored in case of $3d^4$ configuration. Due to lattice motion or distortion, octahedron elongates in the z-direction. As a result, d_{z^2}, d_{yz} and d_{xz} orbitals move further away from the oxygen p-orbitals, which results in the splitting of doublet and triplet. If there are odd numbers of electrons only, then the energy of e_g orbitals will be lowered. Since there is no electron for lowering the energy of e_g orbitals, d^3 (Mn^{4+}) configuration does not exhibit J-T distortion.

1.5. Exchange interactions

As it is mentioned in the previous section, the properties of manganites such as structure, magnetic and transport depend on the interplay of the spin, charge, orbital and lattice degrees of freedom. Depending on the interaction, magnetism can be divided into two categories. In the first category, each moment acts as the individual; no interaction exists between the individual moments. Both Dia and Para magnetism come under this category. In the second category magnetism arises because of coupling between magnetic moments, results in the formation of magnetically ordered states. This coupling is quantum mechanical in nature, is known as the exchange interaction. In manganites, the oxygen ion separates the

two Mn ions and the extent of overlap between the d-orbitals of the Mn ion and the p-orbitals of the oxygen ion influence these interactions, which occur when an electron jumps between the Mn^{3+}-O-Mn^{3+}, Mn^{4+}-O-Mn^{4+} and Mn^{3+}-O-Mn^{4+}.

Exchange interactions between the neighboring ions force the individual moments to form either parallel or anti-parallel orientation with their neighbors. Three types of exchange interactions known as direct, indirect and superexchange (SE) exist and the details are given below.

Fig. 1.5. Antiparallel alignment for smaller interatomic distances.

Fig. 1.6 Parallel alignment for larger interatomic distances.

The direct exchange occurs between the moments, which are close enough to have sufficient overlap of their wave functions. It is strong, but a short-range phenomenon and the strength of the short-range coupling decrease rapidly, whenever separation between the ions takes place. In order to understand direct exchange phenomena in details, the case of two atoms is considered. In this, two cases can arise the first one is with smaller interatomic distance and the second one is with larger interatomic distance as shown in Fig. 1.5 and Fig. 1.6, respectively. In the first case, in which the two atoms are closely placed, Coulomb interaction between the electrons can be minimized when the electrons spend most of their time in between nuclei. According to Pauli's exclusion principle, the electrons which are placed at the same place in space possess opposite spins. The oppositely oriented spins give rise to an antiparallel alignment and hence negative exchange. The second case is that, whenever the two atoms are far from each

other, electrons spend their time away from each other to minimize the electron-electron repulsion which gives rise to parallel alignment and hence positive exchange.

For many-electron systems, the exchange energy is given by the expectation value of the Heisenberg Hamiltonian,

$$H_{ex} = -2\sum_{i<j} J_{ij}\,\hat{S}_i.\hat{S}_j \qquad (1.4)$$

where J_{ij} is the exchange integral which describes the coupling between two spins or magnetic moments represented by the spin operators $\hat{S}_i$ and $\hat{S}_j$.

Indirect exchange is also known as the RKKY interaction named after Ruderman, Kittel, Kasuya and Yoshida, plays an important role when there is no direct overlap of the wave functions with unpaired electrons. In this case, the

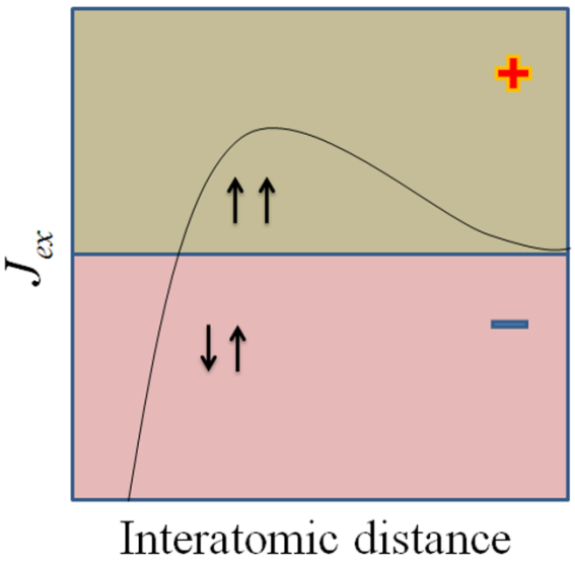

Fig. 1.7. Direct exchange energy as a function of interatomic distance.

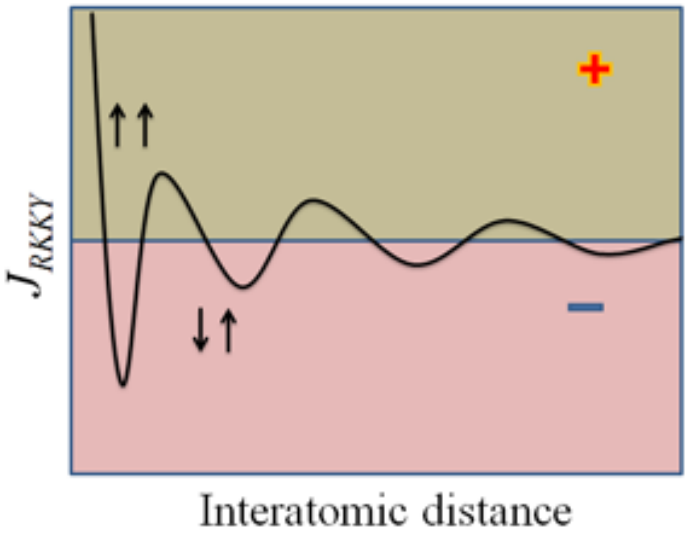

Fig. 1.8. RKKY exchange energy as a function of interatomic distance.

interaction between two magnetic moments at sites *i* and *j* is mediated by the polarization of the conduction electrons.

Direct exchange energy as a function of interatomic distance is shown in Fig. 1.7. The negative and positive value of the exchange energy results in the AFM and FM ground state coupling, respectively. The RKKY exchange coefficient J_{RKKY} has oscillatory nature and it oscillates from positive to negative as the separation of the ion changes; shown in Fig. 1.8 [31]. Depending on the separation between the ions their magnetic coupling can be either FM or AFM. Spin polarization which is induced by the magnetic ion in the conduction electrons (itinerant electrons) is felt by the moments of other magnetic ions within the range, leading to an indirect coupling. In contrary to the direct exchange, the indirect exchange is a long-range type.

The various types of interactions are shown in Fig. 1.9 [32]. Among all these, a few of the interactions favor the electron localization mechanism while the others support the electron delocalization mechanism. It is well known that kinetic energy prefers the electron delocalization process. The electron-spin interaction,

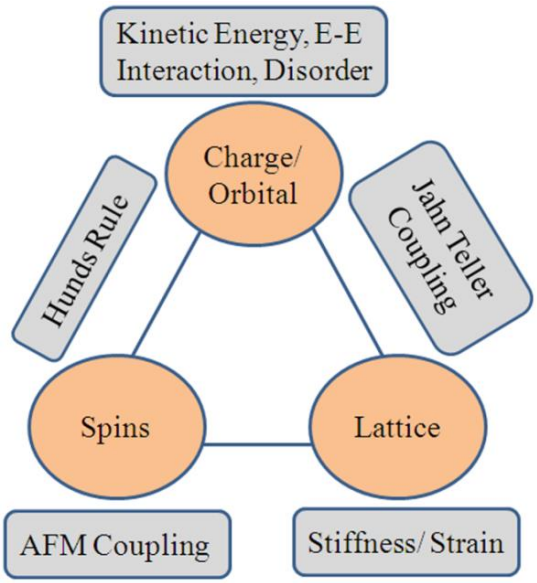

Fig. 1.9. Various types of interactions in the manganite systems.

which arises from Hund's coupling between the electrons of Mn d-shells, favors the ferromagnetism due to delocalization of electrons. AFM interactions among core spins lead to delocalization of electrons, suppressing the FM order. The other interesting phenomena, electron-lattice interaction, favor the electron localization by forming lattice polarons. The electron-electron interaction also favors the localization process.

1.6. Double-exchange

The double-exchange (DE) is also a type of magnetic exchange interaction which occurs between the ions of different valence states. This mechanism was first proposed by a scientist, Clarence Zener for explaining ferromagnetism [33-35]. Anderson and Hasegawa [35] reformulated this mechanism by using a second-order process involving an intermediate sate, Mn^{3+}-O^{-}-Mn^{3+}. They stated that the effective hopping amplitude (t_h), reflecting the electron mobility, depends on the angle between the classic spin of localized core electrons of the

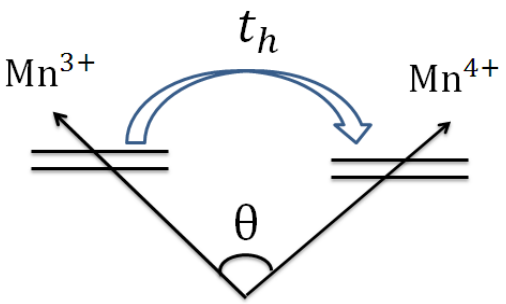

Fig. 1.10. Schematic diagram of hopping amplitude (t_h).

neighboring Mn ions. Fig. 1.10 shows the schematic diagram of t_h, given by the expression

$$t_h = t_0 \cos\left(\theta/2\right) \tag{1.5}$$

where θ is the angle between the localized spins.

Clarence Zener proposed that the transfer of the electron from Mn^{3+} to Mn^{4+} via O^{2-} occurs simultaneously. However, it contradicts Anderson and Hasegawa model in which the transfer of electron between the ions occurs one by one. Later DE mechanism was further refined by de Gennes by introducing the double-exchange lattice model by adding an AFM superexchange interaction in the Mn^{3+}-O^{2-}-Mn^{3+} or Mn^{4+}-O^{2-}-Mn^{4+} in manganites [37]. He predicted that a small amount of doping in the parent manganite compound led to the canting of spins. These results in the relative orientation of the Mn ions with respect to the bridging oxygen ion, as a result, different phases occur in manganites [38-40].

The schematic diagram of the DE mechanism is shown in the Fig. 1.11. DE mechanism occurs, when two electrons are transferred simultaneously, one from a bridging O^{2-} ion to the Mn^{4+} centre and one from a Mn^{3+} ion to the O^{2-} ion. According to Pauli's exclusion principle, when an electron is transferred from O^{2-} ion to the Mn^{4+} centre, then at the same time the electron which is originated from

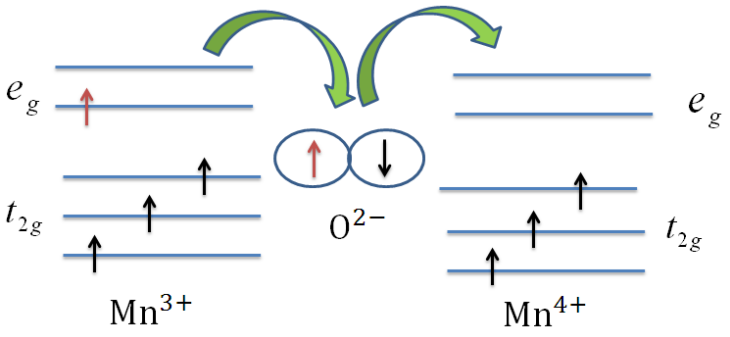

Fig. 1.11. Schematic daigram of DE mechanism in manganites.

the Mn^{3+} ion replaces the gap created by the earlier electron on the O^{2-} ion, such that their spins are identical. This leads to a FM arrangement.

1.7. Superexchange

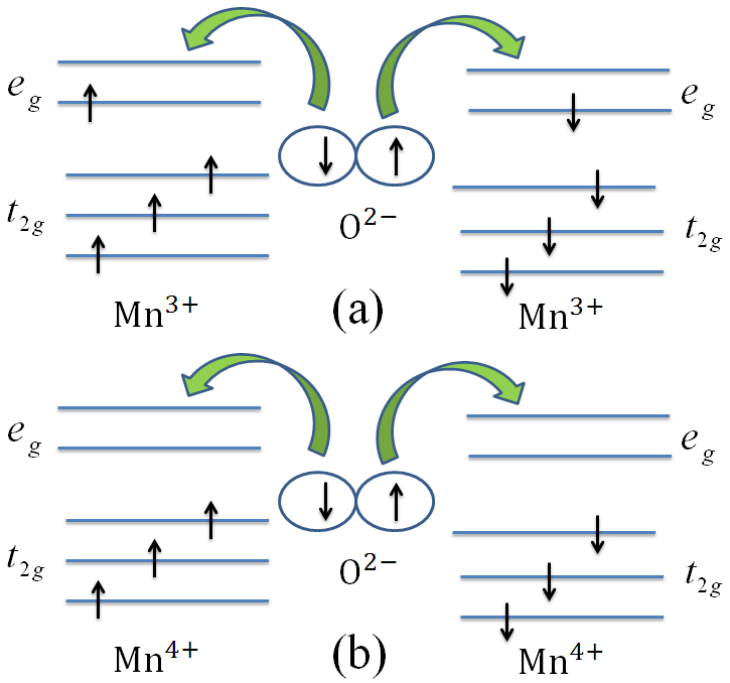

Fig. 1.12. Superexchange mechanism in manganites.

Superexchange phenomenon is also known as Kramers-Anderson superexchange [41, 42] that arises due to the interaction between the ions which are far apart to be connected with direct exchange, but coupled with a non-magnetic ion. A DE phenomenon arises due to the hopping of electrons between the Mn ions of different valences, whereas SE arises due to the hopping of electrons between the Mn ions of the same valency via the intermediate O^{2-} ion [Fig. 1.12].

The properties of manganites depend on various types of ordering mechanisms; like charge ordering, orbital ordering and spin ordering, and the detailed discussions on the various ordering phenomena are given below.

1.8. Charge ordering

Charge ordering (CO) is defined as the ordering of metal ions in different valence states at specific lattice sites of mixed-valent materials. When charge

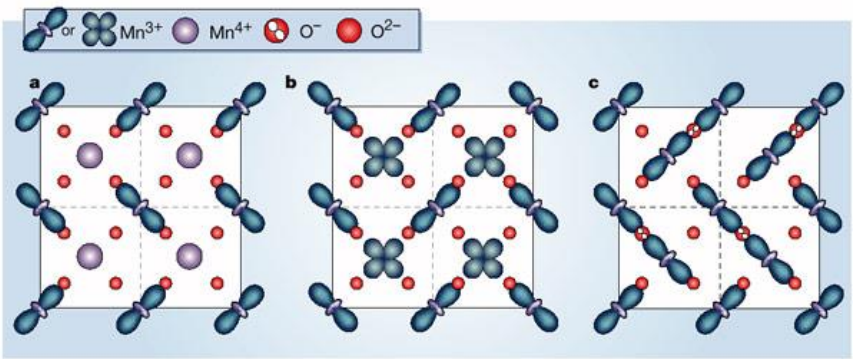

Fig. 1.13 (a) Chequerboard pattern charge ordered arrangement of Mn^{3+} and Mn^{4+} ions. (b) Orbital ordering pattern for Mn^{3+} ions, implying an incomplete occupancy of the oxygen 2p shell. (c) An ordered alignment of O^{-} ions between the Mn^{3+} ions in the Zener polaron model. Out of six, four oxygen ions forming an octahedral cage around each Mn ion, the other two would be located below and above the plane. Ref. [38, 45-47].

ordering occurs, localization of charges takes place in the material; as a result the hopping of electrons will become difficult which leads to the semiconducting properties of the materials. The phenomenon of charge ordering in solids was first predicted by E. Wigner in 1930. The charge ordering phenomena is a long-range type, and it was first discovered in magnetite by Verwey [43]. He observed an increment in the resistivity by two orders of magnitude at a temperature 120 K and it was solved recently by a group that was led by J. P. Attfield [44]. Fig. 1.13 shows charge and orbital ordering of manganese ion, taken from Ref. [38, 45-47].

As it was mentioned that charge ordering is resulting due to the localization of charges [48], therefore it is associated with insulating and AFM phases, whereas the DE is associated metalicity along with ferromagnetism. As a result, a competition arises between FM metallic and cooperative J-T effect with charge ordering. Charge ordering phenomena usually associated with a peak in the magnetization, a sharp change in the resistivity and change in the lattice parameters [49].

It has been reported that CO state can be destroyed or melted by the application of magnetic fields [50], pressure [51], etc. In recent, suppression of CO state is reported when the size of grains/particles is reduced to a critical size [52]. At the same time, a few reports [53, 54] have also suggested that CO state is robust in nature and it exists in short-range form, even if the size of the grains is reduced to nanoscale range.

1.9. Orbital ordering

Transition metal oxides exhibit various physical properties, which depend on whether the electrons in d-shell localized on individual transition metal sites or delocalized throughout the solid. Systems with cations in the orbitally degenerate state, where the preferential occupation of specific d-orbitals can lead to the

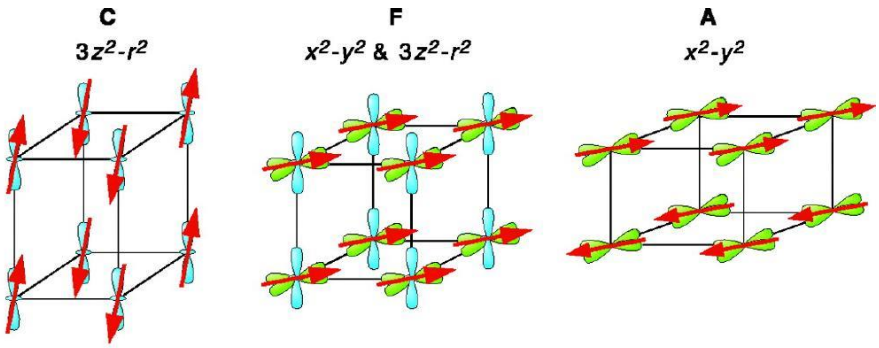

Fig. 1.14 Schematic representation of various types (C, F and A) of orbital ordering patterns of manganese oxides Ref. [57].

development of long-range ordered pattern. This phenomenon is called as orbital ordering.

Fig. 1.13 shows the typical charge, spin and orbital ordering as per Goodenough predictions. Fig.1.14 depicts various types of orbital ordering occurring in manganese oxides. The most important orbital ordering which occurs in manganites is CE-type in which both the charge and orbital order occur simultaneously. The phenomenon of orbital ordering is coupled with J-T distortion [55, 56]. As it was mentioned earlier, when J-T effect occurs, e_g state splits into two states, as a result the single electron of Mn^{3+} ion occupies one of the two e_g orbitals which are aligned in the specific orientation. Nature of ground state (either FM or AFM) of the system depends on the direction or orientation of the orbitals on neighboring sites.

1.10. Spin ordering

The interaction of atoms with their neighbors aligns the spins of electrons in a particular direction. The alignment can lead to ordering of spins, called as spin ordering. Depending on the alignment of spins whether parallel or antiparallel,

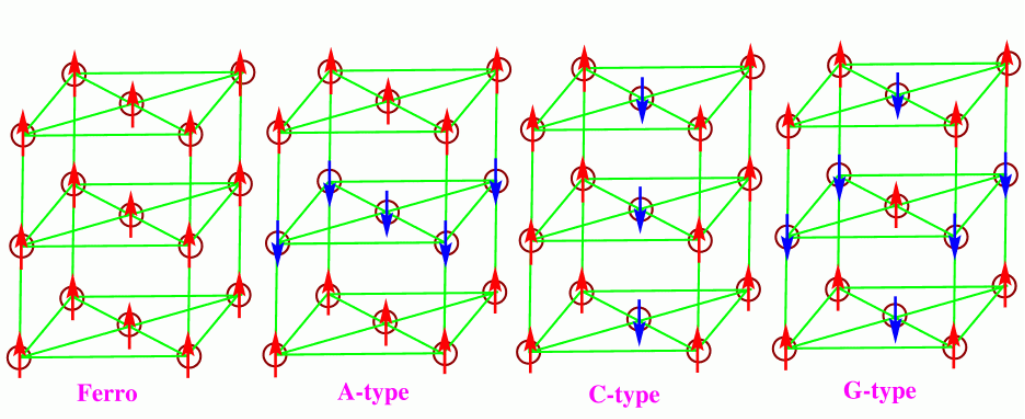

Fig. 1.15. Schematic representation of Ferro and various types of antiferromagnetic spin ordering. Ref. [57].

materials exhibit ferromagnetism or antiferromagnetism respectively. The interplay between the Coulomb's and Pauli's exclusion principle affect the spin-spin interactions which will give a platform for forming long-range ordered states in mangnites. The strength of the spin-spin interactions depends on the doping content and the temperature.

In manganites, mainly three types of AFM spin ordering exist, namely A-type, C-type and G-type. FM as well as various AFM spin alignments is shown in Fig. 1.15 [57]. In A-type perovskites, the intra-plane coupling is FM while inter-plane coupling is AFM type. In contrast to A-type perovskites, in C-type, the intra-plane coupling is AFM while inter-plane coupling is FM type. Whereas in G-type perovskites both intra and inter plane couplings are AFM type.

1.11. Phase separation

Manganites are known to exhibit both compositional and electronic inhomogeneities arising from the existence of more than one phase which is responsible for displaying fascinating properties like CMR. This phenomenon is called as phase separation (PS). PS phenomena occur when a system transforms

from one phase to the other when the temperature is raised or lowered or by changing its chemical composition. The PS can be electronic or structural accompanied with percolation. Electronic PS (EPS) occurs when cluster formation takes place at nano-metric level [58] while structural PS is due to disorder [59, 60]. The micrometer-size clusters formed due to disorder assist in percolation leading to first-order transitions [60].

A simple example for EPS is the existence of FM clusters in the PM matrix. The concept of EPS was first introduced by Nagaev [61-63] in semiconductors. The very first report on the EPS in perovskite manganites was by Wollan and Koehler [64]. They reported the co-existence of FM and AFM phases by neutron scattering studies of $La_{1-x}Ca_xMnO_3$. However, popularity came for this concept after the discovery of CMR. Jonker and van Santen [65] explained the occurrence of FM exchange interaction between Mn^{3+} and Mn^{4+} when La replaced by Ca, Sr and Ba in $LaMnO_3$. Transmission electron microscopy technique gave the coexistence of FM metallic and charge ordered insulating phase in $La_{5/8-y}Pr_yCa_{3/8}MnO_3$ [10]. Mori and his group have reported nanoscale electronic inhomogeneities in the thin films of (La, Ca) MnO_3 using high-resolution transmission electron microscopy (HRTEM) [66]. Renner and his group have found charge ordered and metallic domains in $Bi_{0.25}Ca_{0.75}MnO_3$ [67]. Later EPS [68, 69] phenomenon has been observed in various manganites by several measurements such as thermal expansion and neutron scattering [70], transport and magnetic [71, 72], Mossbauer spectroscopy [73] and zero-field magnetic resonance [74] in a wide temperature range.

When an EPS takes place in a material, phases with different carrier densities as well as magnetic and transport properties coexist as carrier-rich FM clusters or domains along with a carrier-poor AFM phases. This results in microscopic or mesoscopic inhomogeneous distribution of electrons (Fig. 1.16), which in turn leads to rich phase diagrams of manganites [58, 75]. This is due to the presence of

Coulomb interaction which breaks the large phase separated domains into small pieces with different charge densities. Typical phase diagram of LCMO, PCMO [76] and SCMO [77] manganites is shown in Fig. 1.17. Depending on the distribution of FM clusters in an AFM host, manganites exhibit spin glass, cluster glass, etc., properties. However, understanding phase separation in manganites is difficult because the transition from one phase to the other is not sharp. The nature of phase separation in manganites depends on the various factors such as $<r_A>$ which is associated with disorder, carrier concentration, temperature, magnetic and electric fields [75]. One of the origins for the occurrence of phase separation is due to strain effects that try to minimize the lattice energy. Orbital degeneracy in association with charges and the strong electron phonon coupling which arise due to the J-T distortion of Mn^{3+} octahedron are the principal factors for explaining the phase separation phenomenon [78]. It is reported that due to the presence of intrinsic inhomogeneous martensitic accommodation strain, charge

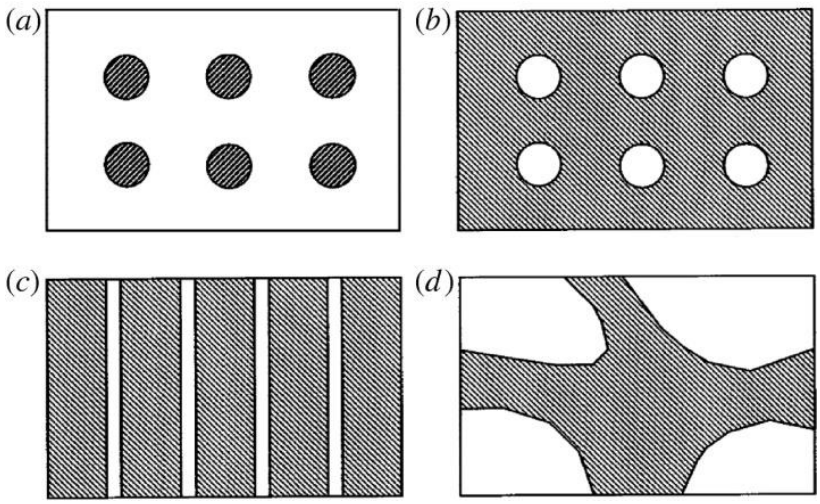

Fig. 1.16. Representation of electronic phase separation. FM metallic region is shown with shaded regions and the AFM insulating region is shown with the unshaded regions. (a) FM metallic (shaded circles) regions with an insulating background, (b) insulating AFM regions with metallic background, (c) charge strips and (d) PS on mesoscopic scale. Ref. [76].

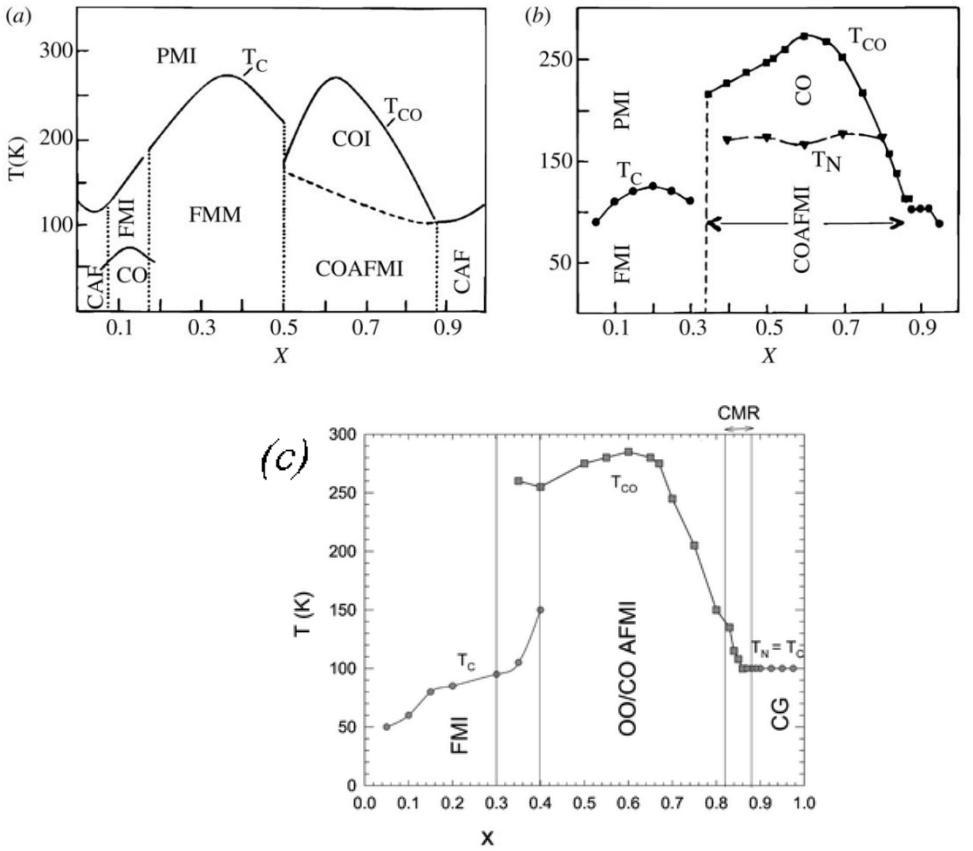

Fig. 1.17. Phase diagram of (a) $La_{1-x}Ca_xMnO_3$, (b) $Pr_{1-x}Ca_xMnO_3$ and (c) $Sm_{1-x}Ca_xMnO_3$. CAF: canted antiferromagnetic, CO: charge ordered, FMI: ferromagnetic metal insulator, PMI: paramagnetic insulator, COAFI: charge ordered antiferromagnetic insulator, COI: charge ordered insulator. Ref. [76] and [77].

ordered and charge disordered phases coexist, which stabilizes the large-scale phase separation in manganites [79]. The co-existence of the variety of phases in the manganites is because of band gap changes due to strain effects [80]. Griffiths [81] explained the concept of the coexistence FM and AFM phases. In recent years, an EPS phenomenon has extensively been reported in manganite nanoparticles [82-85].

1.12. Literature review

1.12.1. Review on $Bi_{1-x}Ca_xMnO_3$ system

The end members of $Bi_{1-x}Ca_xMnO_3$, i.e., $BiMnO_3$ and $CaMnO_3$, crystallize in the monoclinic and cubic structure, respectively [64, 86]. X-ray diffraction studies of $Bi_{1-x}Ca_xMnO_3$ revealed that for $x < 0.40$, two monoclinic and one orthorhombic phase evolve as a function of temperature [86]. The structure of $BiMnO_3$ changes from cubic to monoclinic at low temperatures. For $0.40 \leq x \leq 0.83$, the cubic phase present at high-temperature transforms to a monoclinic one at low-temperatures. For $x > 0.83$, the more distorted monoclinic phase transforms to a high-symmetry orthorhombic phase. For $x < 0.90$, magnetization results have revealed the existence of ferromagnetic (FM)-like behavior at high-temperatures. The observed properties are ascribed to Bi $6s^2$ lone pair electrons and the off-centered MnO_6 octahedra in $BiMnO_3$ [86]. It is reported [87] that $Bi_{1-x}Ca_xMnO_3$ manganite is insulating over a broad composition range. For $x \geq 0.15$ the system behaves as FM-spin glass (SG) and exhibits as SG-charge ordered (CO) AFM behavior for $0.25 < x < 0.32$ [87]. High-resolution synchrotron x-ray and neutron powder diffraction studies of $Bi_{1-x}Ca_xMnO_3$ ($x \geq 0.75$) have shown that these systems present phase segregation coinciding with the electronic localization of the e_g electrons [88]. The system with the compositions, $x \geq 0.875$, exhibits FM behavior with reduced resistivity [89]. Although the BCMO system exhibits different behavior from that of $La_{1-x}Ca_xMnO_3$ (LCMO) system, in spite of Bi and La possessing similar ionic radii, the x-ray absorption spectroscopy (XAS) results indicate that increasing Bi in $CaMnO_3$ stabilizes the increasing Mn^{3+} character, similar to that in the LCMO system [8]. In this authors have performed magnetization, temperature dependent resistivity and x-ray diffraction measurements on the $Bi_{1-x}Ca_xMnO_3$ system for correlating structural, magnetic and transport properties. Their measurements have shown that the system is

insulating and exhibits AFM behavior for $x \geq 0.40$, except near $x \sim 0.90$, where they found a canted spin arrangement. They have also shown the importance of Mn-O distortions in stabilizing the CO state in manganites by correlating the structural and magnetization data. For BCMO system, above the charge ordered-structural transition temperature, there exist FM-spin fluctuations, which are indicative of double-exchange (DE) interactions induced by the e_g electron hopping. Below this temperature FM interactions are replaced by AFM interactions [9]. The temperature and magnetic field dependent small-angle neutron scattering (SANS) measurements on $Bi_{0.125}Ca_{0.875}MnO_3$ [90] revealed the formation of FM clusters in an AFM background when the temperature is reduced to 108 K. With further reduction in temperature or the application of external magnetic field, the clusters begin to form in large numbers, resulting in overall enhancement of magnetization below Curie temperature (T_C). Semiconducting and AFM behavior is observed in $CaMnO_3$ manganite [91]. S. Yoon et al. [92] have reported Raman scattering study of anomalous spin, charge and lattice dynamics in the CO phase of $Bi_{1-x}Ca_xMnO_3$ ($x > 0.5$). M. Rubhausen et al. [93] presented spectroscopic ellipsometry study of $Bi_{1-x}Ca_xMnO_3$ crystals in which they observed a sudden increase of low-frequency dielectric function below charge ordering temperature (T_{CO}), which reflects the CO state. Magnetometry, diffraction and muon spin relaxation measurements by J. L. Garcia-Munoz group [94] confirm the spin disorder and frustrated interactions of $Bi_{0.75}Ca_{0.25}MnO_3$. Nuclear magnetic resonance (NMR) studies on $Bi_{0.125}Ca_{0.875}MnO_3$ and $CaMnO_3$ also suggest that the AFM regions in these materials are in canted spin states [95]. W. J. Lu et al. [79] presented the effect of intrinsic strain on the coexistence of charge ordered and charge disordered phases in $Bi_{0.4}Ca_{0.6}MnO_3$. They observed the softening of the shear modulus in the vicinity of T_{CO}. They have also observed two internal friction peaks at temperatures 320 and 260 K. According to them the peak at 320 K originates from the CO transition with typical signatures of a

martensitic transformation and the peak at 260 K related to relaxation mechanism and is ascribed to the motion of CO and charge disordered domains. Their shear modulus measurements confirm the strong electron-lattice coupling effect, due to which lattice distortion takes place before and after CO state. As a result, inhomogeneous strain arises in the sample. $Bi_{0.67}Ca_{0.33}MnO_3$ shows a complex behavior at low-temperature. It shows SG behavior below 39 K. This behavior arises due to the existence of magnetic frustration caused by the competition between FM and AFM interactions. It exhibits high-temperature Curie-Weiss behavior with FM-spin fluctuations characterized by the Curie-Weiss temperature (θ_C) at 20 K [96]. The formation of charge stripes associated with the low-temperature structural phase transition in the single crystal of ($Bi_{0.24}Ca_{0.76}$) MnO_3 has been observed using x- ray techniques [97]. In this study, weak satellite peaks with a modulation vector were observed below the transition temperature. These are associated with the charge ordering of Mn^{3+} and Mn^{4+} ions into charge (and spin) stripes within the perovskite structure. The temperature dependence of the intensity and width of the charge ordering satellites demonstrates the first-order nature of the structural phase transition that accompanies the formation of charge and spin ordering. The correlation length of the charge order is long-range and in all directions, below the structural phase transition. I. Smolyaninov et al. [98] reported the high-resolution study of permanent photoinduced reflectivity changes and CO domain switching in $Bi_{0.3}Ca_{0.7}MnO_3$. In this study, the high spatial resolution images of photoinduced effects in CO $Bi_{0.3}Ca_{0.7}MnO_3$ reveal fine optical contrast on a submicrometer scale. Their observation opens the possibility of creating photonic band gap structures using manganite materials. S. B. Wilkins et al. [99] presented x-ray scattering results of charge and orbital ordering in $Bi_{0.24}Ca_{0.76}MnO_3$. Their results confirm that super lattice reflections occurring at a modulation wave vector of (0.5, 0, 0) are due to CO in the Mn^{3+}/Mn^{4+} ordering pattern. They also measured the superlattice reflections corresponding to the

orbital order at a modulation vector of (0.25, 0, 0). The temperature dependence of the orbital and charge order revealed that CO shows a distinct second-order like behavior, while the structural modulation due to the J-T distortion shows a first-order like behavior; it also appeared like the orbital order was driven by charge order. The stability of charge ordered phases of Bi-based manganites was investigated by magnetization measurements in magnetic fields up to 130 T [100], where an unconventional behavior of Bi charge ordered compounds compared to other rare earth manganites, was reported. The reports on $Bi_{0.75}Ca_{0.25}MnO_3$ and $Bi_{0.75}Sr_{0.25}MnO_3$ by J. L. Garcia-Munoz and C. Frontera [101] state the difference between the physical properties of these compounds. The different ground state property in $Bi_{0.75}Ca_{0.25}MnO_3$ is due to its distinct charge/orbital configuration. Y. Murakami et al. [102] have reported long periodic structures with 32-fold and 36-fold periodicity to the original unit lattice distance in $Bi_{0.2}Ca_{0.8}MnO_3$ manganite at ~130 K, in addition to the one with four-fold periodicity. According to them, the occurrence of charge ordering of Mn^{3+} and Mn^{4+} ions is responsible for the creation of the long-period structure in $Bi_{0.2}Ca_{0.8}MnO_3$ manganite. H. L. Liu et al. [103] have used optical reflectivity study and explained the different coexisting phases in $Bi_{1-x}Ca_xMnO_3$ (x = 0.74 and 0.82) single crystals. Their results conclude that in the high-temperature phase, i.e., $T > T_{CO}$ (charge ordering temperature), the low-energy contribution to the optical conductivity is dominated by small polaron dynamics. In the temperature range, $T_{CO} > T > T_N$ (Neel temperature), both small polaron and charge-gap-like features are present. Below T_N the polaron responses are completely suppressed and a complete charge-gap develops. This is consistent with the onset of long-range AFM ordering. Kurian and Singh [7, 104] have reported electron spin resonance (ESR) and resistivity studies of some of the compositions of $Bi_{1-x}Ca_xMnO_3$ system synthesized by solid state reaction method.

1.12.2. Review on Bi and Sm doped La-manganites

The studies on $La_{1-x}Ca_xMnO_3$ (LCMO) have shown that the end members of LCMO, i.e., $LaMnO_3$ and $CaMnO_3$ are antiferromagnetic (AFM) insulators. The small amount of hole or electron doping into this induces ferromagnetic (FM) saturation. Walsh et al. [105] investigated magnetic and electronic properties of $La_{0.67-x}Bi_xCa_{0.33}MnO_3$. They assigned the peak observed in magnetoresistivity ratio as a function of temperature for the Curie temperature (T_C). The ferromagnetic resonance (FMR) spectra of these samples show a single resonance above T_C, whereas below T_C, samples with low Bi content show two resonances. However, these resonances cannot be clearly resolved due to the line broadening and the identification of the resolution become difficult with the increase in Bi content. The results are interpreted in terms of the effects of Bi on the structure of grain boundaries. Sun et al. [106] studied the doping effects on the phase separation in perovskite $La_{0.67-x}Bi_xCa_{0.33}MnO_3$. Their electron spin resonance, magnetization and neutron diffraction studies confirm that the partial replacement of La by Bi develops the charge ordered (CO) AFM phase, whereas the undoped system is FM-type. In fact, these two phases occur simultaneously. As a result, they were able to observe two subsequent magnetic transitions. It is reported that the $La_{0.62}Bi_{0.05}Ca_{0.33}MnO_3$ compound exhibits large magnetic entropy change [107]. Atalay et al. [108] have also reported the magnetic entropy change in $La_{0.67-x}Bi_xCa_{0.33}MnO_3$. They found that the maximum value of the magnetic entropy change was 6.08J/kg K at 30 kOe for the sample with $x = 0.05$. This value is approximately similar to the value obtained for the undoped sample. Xia et. al [109] reported the effect of $6s^2$ loan pair of the Bi^{3+} ion on the electrical transport process and magnetic domain rotation and growth behavior simultaneously in the compound $(La_{1-x}Bi_x)_{0.67}Ca_{0.33}MnO_3$. In the recent, the magnetotransport properties of polycrystalline $(La_{0.9}Bi_{0.1})_{2/3}Ca_{1/3}MnO_3$ have been investigated in pulsed

magnetic field up to 400 kOe over a wide temperature range [110]. The large value of the average spin moment indicates the presence of magnetic clusters in the sample, which was induced by the short-range FM ordering.

Neutron diffraction [111] studies reveal changes in the magnetic structure from ferromagnetic $La_{0.65}Bi_{0.05}Ca_{0.3}MnO_3$ to antiferromagnetic $Bi_{0.7}Ca_{0.3}MnO_3$. The covalent character of Bi-O bond explains the increasing localization of the 3d electrons of Mn atoms and the insulating character of $Bi_{0.70}Ca_{0.3}MnO_3$. Anomalous hysteresis and metamagnetic behavior are observed in $La_{0.5}Bi_{0.2}Ca_{0.3}MnO_3$ [112]. Jiang et al. [113] investigated the magnetic and electrical transport properties of $(La_{0.9}Bi_{0.1})_{2/3}Ca_{1/3}MnO_3$. In this study, the thermal hysteresis in resistance and magnetization was observed. The thermal hysteresis in resistance was suppressed by the application of 50 kOe magnetic fields. D. Vijayan et al. [114] investigated the effect of Bi-doping on ESR of $La_{0.7-x}Bi_xCa_{0.3}MnO_3$. Their ESR studies reveal the existence of phase separation in the system. L Righi et al. [115] reported the structural, magnetic and transport properties in perovskite $La_{0.7-x}Bi_xCa_{0.3}MnO_3$ ($0.05 \leq x \leq 0.70$). The FM behavior is observed for the samples with $x \leq 0.15$. The AFM interactions were observed with increasing Bi concentration. For the sample with $x = 0.20$ an antiferro-ferromagnetic transition was induced with the application of magnetic field. Their results confirm that the sample with $x = 0.70$ is an antiferromagnet. However, FM correlations still existed in all the samples. They interpreted their results in terms of charge localization probably due to the covalent nature of the Bi.

Renwen Li et al. [116] studied the magnetic properties of $La_{0.5-x}Bi_xCa_{0.5}MnO_3$. The systematic substitution of La by Bi enhances the charge ordering temperature. Their ESR and magnetization studies reveal the coexistence of FM, AFM domains in PM matrix below charge ordering temperature (T_{CO}) in the composition range $0 \leq x \leq 3/8$. The counterclockwise thermal hysteresis in the temperature dependent magnetization curves is ascribed to the compressive strain

effects, which arises from the coexistence of PM, FM and AFM domains. The effect of high pressure on Jahn-Teller (J-T) distortion in perovskite $La_{0.5-x}Bi_xCa_{0.5}MnO_3$ has been reported by X. Wang and his group [12]. Upon application of pressure, an impressible decrease of the J-T distortion in MnO_6 was observed. The substitution of Bi^{3+} for La^{3+} introduces distortion into the system, which was attributed to the unique lone pair characteristics of Bi. The results of measurements of x-ray photoelectron and infrared absorption spectra in $La_{0.5-x}Bi_xCa_{0.5}MnO_3$ ($0 \leq x \leq 0.25$) compounds confirm that the changes in Mn-O bond length and Mn-O-Mn angle of MnO_6 octahedra with doping are due to $6s^2$ loan pair of Bi^{3+} ions [117].

State switching is observed in $La_{0.477}Bi_{0.193}Ca_{0.3}MnO_3$ [118]. The electric and magnetic field induced switching behavior between a high resistive and a low resistive state were observed in $(La_{0.73}Bi_{0.27})_{0.67}Ca_{0.33}MnO_3$ [119].The application of external field partially annihilates the localized FM and CO states, leading to the FM state growth, which is responsible for a switch between a high resistive state and low resistive one. This fascinating result makes that the doped manganites are the suitable systems for both electric and magnetic field sensor materials.

Anwar et al. [120] studied the disorder effects on structure, magnetic and magnetocaloric properties of $La_{0.7-x}Sm_xCa_{0.3}MnO_3$ manganites. The studies on these compounds confirm the transformation of first order PM-FM transition observed in the undoped sample to the second order PM-FM transition for the doped sample. T_C decreased with Sm-doping. The systematic study on $La_{0.7-x}Sm_xCa_{0.3}MnO_3$ suggests that these compounds can be used as the potential magnetic refrigerating material in a wide range of temperature.

1.12.3. Review on Mn-site doped manganites

In order to understand the effect doping at Mn-site, detailed information is extracted from the literature. A lot of work has been reported on the effect of Mn-site substitution by magnetic and nonmagnetic ions [121-139]. The doping of magnetic ion enhances the magnetic properties, whereas nonmagnetic ion doping suppresses the magnetic properties. However there are few theoretical [140, 141] and experimental [130, 138, 142] reports suggesting that a small amount of nonmagnetic ion doping can also enhance the magnetic properties due to the development of disorder in the samples at low-temperatures. Disorder modifies the effective Mn^{3+}/Mn^{4+} ratio which results in either increase or decrease in magnetic properties. In nonmagnetic ion doped systems, changes in magnetic properties are mainly due to the variations of local lattice structure [129]. Nonmagnetic doping leads to coexisting FM and AFM phases [136]. Crystal structure is modified with magnetic ion doping, whereas nonmagnetic ion doping does not affect the crystal structure. Magnetic dopants in charge ordered manganite promote percolative FM metallic behavior [143]. In contrast to the general behavior of nonmagnetic doping, A-type AFM state is destabilized in $LaMnO_3$. Charge ordered $Pr_{0.5}Ca_{0.5}MnO_3$ manganite transforms towards FM ground state by 2.5% to 10 % Al substitution at Mn-site [137, 138]. Al substitution introduces random impurities in the Mn-O-Mn lattice and reduces the range of CO interaction, resulting in the formation of weak charge ordered clusters. With decreasing temperature AFM state is stabilized within these clusters and below T_G they thermally blocked with respect to the time scales of their experimental probes [124].The charge ordered CE- type antiferromagnetic state in $La_{0.5}Ca_{0.5}Mn_{1-x}B_xO_3$(B= Al) is not affected in the composition range, $0.01 \leq x \leq 0.03$. However, this phase coexists with ferromagnetic metallic phase. For $x > 0.03$ both CE-AFM and FM state phases suppress and A-type AFM phase stabilizes in the composition range $0.05 \leq x \leq 0.07$. With further increase in the Al

content A-type AFM phase is also suppressed [121]. Magnetic Compton scattering study reveal the disappearance of orbital moment due to doping of Al in $La_{0.7}Ca_{0.3}Mn_{1-x}Al_xO_3$ (x = 0, 0.02 and 0.06) [133]. Due to similar ionic radii of Al^{3+} and Mn^{3+}, Al^{3+} may replace the Mn^{3+}, which results in the decrease of J-T distortion [134]. Disorder-induced localization of charge carriers control the conduction process due to the doping of Al in $La_{0.7}Ca_{0.3}Mn_{1-x}Al_xO_3$ ($0 \leq x \leq 0.1$) [144]. It is known that the ionic radii of Mg^{2+} is identical to the ionic radii of Mn, due to which substitution would not introduce lattice effects in the system. The decrease in magnetization, the widening of paramagnetic to ferromagnetic transition and the cluster-glass state is observed in the Mg doped $La_{0.67}Sr_{0.33}Mn_{1-x}Mg_xO_3$ ($0 \leq x \leq 0.20$) [127]. Mg^{2+} substitution leads to an decrease of Mn^{3+} /Mn^{4+} ratio and enhances the role of interaction between Mn^{4+}-Mn^{3+} [135].

In the $Bi_{0.3}Ca_{0.7}Mn_{1-x}V_xO_3$ compound, the replacement of Mn^{4+} ion by V^{5+} ion has been reported [122]. This results in an increment of Jahn-Teller distortion of the MnO_6 octahedron due to the increased Mn^{3+} ions, which favors the charge ordering. D. Vijayan et al. [131, 132] have reported ESR and magnetization studies of transition element doped $Bi_{0.5}Ca_{0.5}Mn_{0.95}TE_{0.05}O_3$ (Cr, Fe, Co, Ni, V, Cu and Zn).

Motivation and objective of the present work

The unusual properties of manganites are due to the strong coupling between the charge, the concomitant spin and orbital degrees of freedom [7-9]. The strength of coupling between the charge, spin and orbital depends on several perturbations caused by disorder effects [10], hydrostatic pressure [11, 12], magnetic and electric fields [13, 14] and size of the particles [15, 16]. The other interesting thing is that the coupling can also be altered by different types of substitutions/doping at A-site [17-19] and B-site [20-22], which introduces

disorder into the system. The other fascinating feature of manganites is that when the size of the grain is reduced to nanoscale, they exhibit unusual properties such as suppression of charge ordered state, increase in magnetization, exchange bias effects, CMR effects, etc., as compared to their bulk counterparts. This is due to the increased surface to volume ratio of nano-grains which modifies the disorder. The disorder is due to change in the chemical pressure [10] which in turn affects Mn^{3+}/Mn^{4+} ratio, Mn-O-Mn bond length and Mn-O-Mn bond angle and hence, altering the properties of the manganites.

The present study is undertaken to get deeper insight in understanding the effect of doping (at A and B- site) induced changes in the structural, magnetic and transport properties of Bi and rare earth manganites. The effect of grain size on the structural, magnetic and transport properties of Bi-manganite was also studied. In this study, the following series of samples were synthesized by sol-gel method.

I. A- site doping

1. $Bi_{1-x}Ca_xMnO_3$ (x = 0.40, 0.50, 0.60, 0.65, 0.70, 0.75, 0.80, 0.85 and 0.90)
2. $Bi_{0.5-x}Pr_xCa_{0.5}MnO_3$($x$ = 0.0, 0.05, 0.10, 0.15, 0.20, 0.30, 0.40 and 0.50)
3. $La_{0.37}D_{0.30}Ca_{0.33}MnO_3$ (D = Bi, Sm) and $La_{0.37}Bi_{0.15}Sm_{0.15}Ca_{0.33}MnO_3$

II. B-site doping

4. $Bi_{0.7}Ca_{0.3}MnO_3$ and $Bi_{0.7}Ca_{0.3}Mn_{0.95}Y_{0.05}O_3$ (Y = Mg, Al and Sn)

III. Grain size effects

5. Nanoparticles of $Bi_{0.5}Ca_{0.5}MnO_3$

Chapter 2

Experimental techniques

2.1. Material synthesis

The physical properties of the sample depend on conditions used for processing the materials. The material synthesis or sample preparation is thus, the most important part of the research activity. There are various methods; such as solid state reaction, sol-gel; co-precipitation, etc., used for the synthesis of bulk and nanoparticles of manganites. Among these methods, the sol-gel method is a versatile technique, used for the synthesis of nanoparticles [52], nanorods/nanowires [145, 146], nanoflowers [147], etc. This method gives homogeneous materials at processing temperatures lower than that of other methods like solid state reaction method [29]. The process involves the conversion of monomers into a colloidal solution, called 'sol' which acts as the precursor for an integrated network, called 'gel' of either discrete particles or network polymers [148].

2.1.1. Mechanism of the gel formation

Vazquez-Vazquez et al. [149] have reported the detailed mechanism of the gel formation using urea as the gelification agent. In sol-gel process, urea (CH_4N_2) plays a significant role in the formation of the gel. As the temperature rises to a temperature greater than 75 ^oC, the aqueous solution of urea decomposes into CO_3^{2-} and NH_3^+ by releasing hydroxide ions. In the absence of acids the following reaction takes place:

$$CH_4N_2 \rightarrow NH_4^+ + CNO^-$$

In acidic media cyanate ion converts into an ammonium ion [150], given by the following reaction

$$CNO^- + 2H^+ + 2H_2O \rightarrow NH_4^+ + H_2CO_3$$

The rate of decomposition of urea depends on the temperature and its concentration. A few ligands appear in solution which can substitute water molecules in their coordination around the metal ions. The degree of substitution of water by other ligands depends on the nature and concentration of metallic ions and ligands. The evaporation of water promotes the substitution of water ligands represented by the following equation

$$[M(H_2O)_m]^{n+} + xL^{q-} \rightarrow [M(H_2O)_{m-x}.L_x]^{p+} + xH_2O$$

In the above equation M can be Bi, Ca or Mn and L can be NH_3, OH^-, CO_3^{2-}or urea. Mn^{II} coordination takes place through the oxygen of urea [151]. The coordination between urea ligands and metallic ions takes place through the carbonyl or the amino group [152]. The initial aqueous solution is slightly acidic (pH ~ 5.2) but as water evaporates slowly, the solution reaches neutral pH (~7) value. The increase in pH indicates the urea decomposition which releases hydroxide ions there by favoring the hydrolysis of cations. This leads to the formation of small amounts of a precipitate.

The hydrolysis reaction can be represented by the following equation

$$[Mn(H_2O)_x]^{n+} \leftrightarrow [Mn(H_2O)_{x-1}(OH)]^{(n-1)+} + H_{aq}^+$$

On further increase in temperature, the volume of solution decreases and the value of pH rise to ~7, indicating the formation of the basic solution. Then the

precipitation resolves and the gel forms as the precipitate cools down. The gel formation is due to the condensation of the monomers through the hydroxide ligands which forms long chains.

When the temperature reaches to melting point (137 ^{o}C) of urea [153], a large amount of urea decomposes and can be easily identified by the smell of ammonia and the bubbles in the mixture. When this hot mixture is cooled, viscosity of the mixture increases, leading to the formation of the gel.

In the present study, we have used urea and citric acid for the preparation of various series of samples by sol-gel method.

For the synthesis of $Bi_{1-x}Ca_xMnO_3$ ($0.40 \leq x \leq 0.90$) samples, urea is used as gelification agent and citric acid [154] is used for remaining series of samples. The details of sample preparation for each series of samples are given in the corresponding chapters.

2.2. Characterization techniques

2.2.1. X-ray diffraction

X-rays were discovered in 1895 by Rontgen [155]. These are the form of electromagnetic radiation, having the wavelength in the range of 1-100 Å with energies ranging from 100 eV-1000 keV. The x-rays with photon energy in the range of 1-120 keV, are called hard x-rays, used for diffraction studies. In order to study the samples for their structure, chemical composition and physical properties, x- ray diffractometer is used extensively in many of the fields [156]. It works based on the principle of Bragg's law of diffraction.

When the incident beam of x-rays of wavelength, λ, hit the any material, a part of it gets transmitted, some part of it scattered and also a part of it gives rise to fluorescence. If the material is crystalline, the x-rays scatter from different sets of planes as shown in Fig. 2.1. The scattered wave undergoes either constructive or

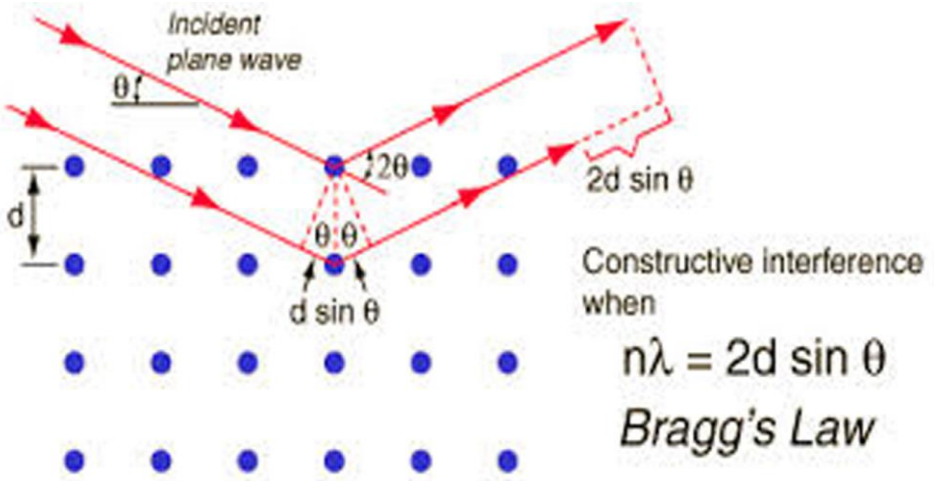

Fig. 2.1. Diffraction of x-rays by a crystal.

destructive interference depending upon the path difference of the interfering waves. Constructive interference occurs when the path difference between the interfering waves is $n\lambda$, where n is the order of diffraction and can takes the values 1, 2, 3 …, etc. Destructive interference takes plays when the two waves are half a cycle out of phase (n = 1/2, 3/2, etc.). If θ is angle of incidence of the x-rays with respect to the plane of the crystal and d is inter-planar spacing, constructive interference occurs when path difference

$$n\lambda = 2d\sin\theta \tag{2.1}$$

This relation was first formulated by W. L. Bragg and is known as Bragg's law. There are two geometrical facts which are useful in experiments. The first one is that the incident beam, the normal to the diffraction plane and the diffracted beam are always co-planar. The second one is the angle between diffracted beam and the transmitted beam is always 2θ. This is known as diffraction angle which is measured experimentally, rather than θ.

Since sinθ cannot exceed 1, then the above equation can be written as

$$\frac{n\lambda}{2d} = \sin\theta < 1 \tag{2.2}$$

The above equation clearly states that $n\lambda$ must be less than 2d. Here the smallest value of n for the occurrence of diffraction is 1, then equation becomes

$$\lambda < 2\mathrm{d} \tag{2.3}$$

For most sets of crystal planes, d is of the order of 3 Å. This clearly indicates that λ cannot exceed of the order of 6 Å.

The x- ray diffractometer is shown in Fig. 2.2 consists of the x-ray source. The x- rays emitted from the x-ray source are directed to the sample mounted on the sample stage or holder. The x-rays which are scattered from the different planes of the sample are detected with the x-ray detector. An electronic system

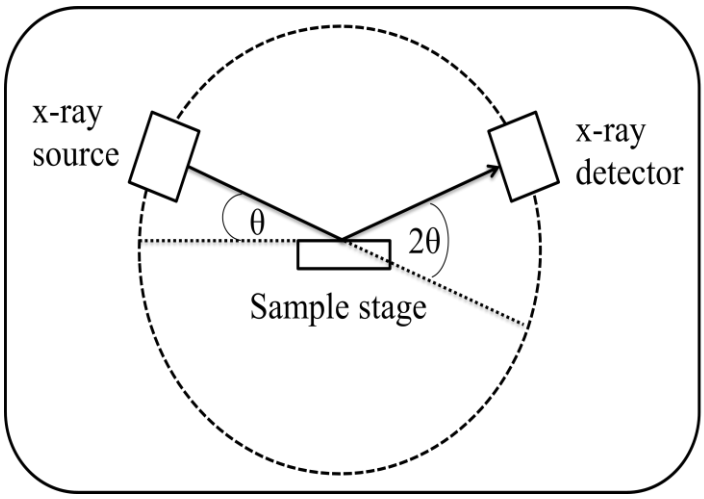

Fig. 2.2. The x-ray diffractometer.

which converts charge into voltage pulse is attached to the detector. A voltage pulse is directly proportional to the intensity of the diffracted beam. Each peak in the XRD pattern corresponds to one set of parallel planes. In general each set of parallel planes will be indicated above the peak with their corresponding Miller indices.

The shape of the XRD peak is neither a perfect Gaussian nor Lorentzian, so that Pseudo-Voigt function is used to fit the peaks and to estimate its full width at half-maximum (FWHM= β). Gaussian function accounts for size and Lorentzian accounts for stress, but Pseudo-Voigt function accounts both for size and stress. The Pseudo-Voigt is given by the expression [157]

$$I_p(x) = I_p[\eta L(x) + (1-\eta)G(x)] \tag{2.4}$$

where $L(x)$ and $G(x)$ represents Lorentzian and Gaussian contribution respectively. The η is a measure of the Gaussian component in the peak. It takes the values between 0 and 1.

The average crystallite size and strain of the samples is calculated using Williamson and Hall (W-H) plot, given by the expression [155].

$$\beta_{hkl}\cos\theta = \frac{c\lambda}{D} + 2\varepsilon\sin\theta, \tag{2.5}$$

where β_{hkl} is the fullwidth half maximum, D is the average crystallite size, λ is the x-ray wavelength; θ is the diffraction angle, c is the shape factor (~ 0.90 for spherical particles) and ε is strain induced in the samples.

2.2.2. Rietveld refinement

Rietveld refinement is carried out using FullProf Suite to gain the structural information which includes atomic positions, unit-cell parameters, bond length, average bond angle, etc. For the best fit, the difference between the calculated patterns to the observed pattern will be the minimum. The refinement can be continued until the best fit is achieved. Various *R*-factors decide the quality of the agreement between the observed and calculated intensity of various peaks [158, 159]. In the present work, the goodness of fit (*S*) given by the following equation

$$S = \frac{R_{wp}}{R_e} \tag{2.6}$$

where R_{wp} is the *R*-weighted pattern and R_e is the R- expected, will be given for all the samples.

2.2.3. Scanning electron microscopy

When a beam of electrons strike the sample (Fig. 2.3), the electrons interacts

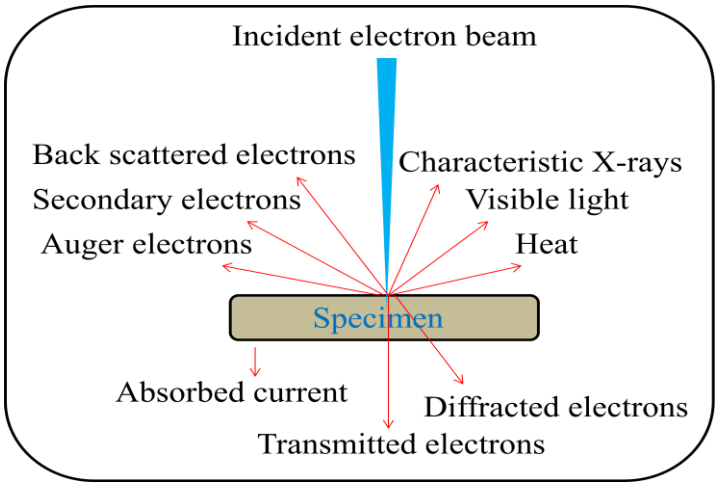

Fig. 2.3. Interaction of a beam of electrons with matter.

with the atoms of the sample, which results in the emission of secondary electrons (SE), back scattered electrons (BSE), x-rays, diffracted electrons, light, current, transmitted electrons, etc. The most common detected signals are secondary electrons. The BSE electrons are used to get the information about the distribution of different elements in the sample. The characteristic x-rays provide information about the composition and also measure the abundance of the elements in the sample [160]. The scanning electron microscopy (SEM) is used to study the surface morphology of the samples. Though, it is difficult to construct equipment that would have all possible signals; secondary electron detectors are standard equipment in all SEMs.

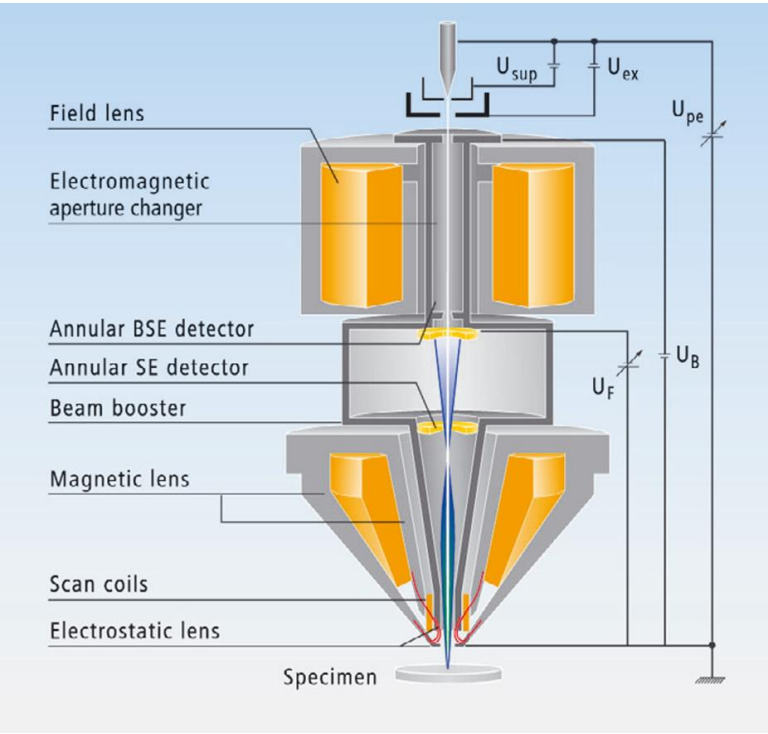

Fig. 2.4 Cross section of Gemini electron optical column utilized in the Ultra FESEM. U_{ex}, U_{pe}, U_B and U_F represents extractor voltage of first anode, primary beam voltage, booster voltage and EsB filtering voltage respectively[161].

The field emission scanning electron microscopy (FESEM) (Fig. 2.4) was introduced to improve the resolution of the image with tungsten source. It consists of an electron source, electromagnetic lenses, inlens detector. In order to reduce the work function and to enhance the emission, tungsten is covered by a layer of ZrO_2. When a beam of electrons is accelerated to a high potential, it emits electrons and these electrons pass through the electromagnetic lenses. The beam scans in a raster scan pattern. Secondary detector and back scatter detector detects secondary and back-scattered electrons emitted from the sample converts to a voltage signal. When the amplified voltage is applied to the cathode ray tube it appears as variations in the brightness which results in an image which is a distribution map of the intensity of the signal that is being emitted from the scanned area of the sample.

2.2.4. Energy dispersive x-ray spectroscopy

Energy dispersive x-ray spectroscopy (EDX) coupled along with SEM, is a technique used for the elemental analysis or chemical characterization of the sample. It works on the principle of the x-ray spectrum emitted by a solid sample. When a beam of electrons or photons strikes the sample (Fig. 2.5) which is being

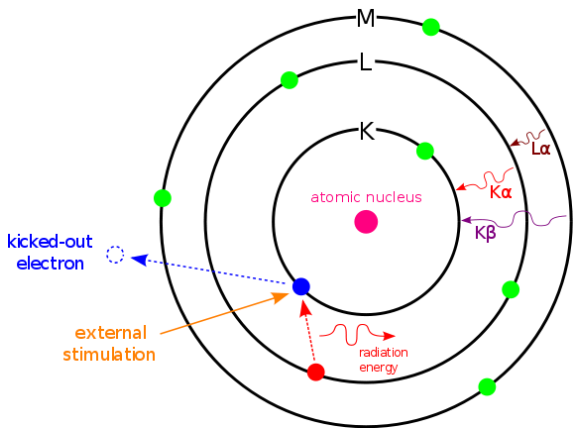

Fig. 2.5. Emission of x-rays from the sample.

studied, the incident beam may excite an electron in an inner shell. Whenever an electron ejects from the shell, it creates an electron-hole in the place of ejected electron. At the same time, an electron from an outer shell jumps into the inner shell and fills it. The difference in energy of an outer and an inner shell releases in the form of x-rays. These x-rays are called as characteristic x-rays. When an electron falls from the L-shell to the K-shell, then the emitted x-rays are called as K_α x-rays, and if an electron falls from the M-shell to the K-shell, then the emitted x-rays are called as K_β x-rays and it is applicable for other shells also. Energy dispersive spectrometer detects the number and the energy of the x-rays emitted from the sample. The energy of the emitted x-rays is the characteristic of the difference in energy of the two shells and of the atomic structure of the element from which the electrons are emitted. This grants the elemental composition of the sample to be measured [162].

2.2.5. Electron spin resonance

Electron spin resonance (ESR) or electron paramagnetic resonance (EPR) is one of the spectroscopic techniques and it was discovered by Zavoiskii in 1944 in $MnSO_4$ using 47.60 G dc magnetic field and 133 MHz rf-magnetic field [163]. This technique is an extension of famous Stern-Gerlach experiment. It is used for studying the materials having unpaired electrons. The concepts of ESR are similar to those of nuclear magnetic resonance (NMR) except that in ESR electron spins are excited whereas in NMR the spins of atomic nuclei are excited. ESR spectrometers are made commercially in several frequency ranges as shown in table 2.1. The most common choice ESR spectrometer is the X-band microwaves which have frequency of 9-10 GHz, the corresponding wavelength is in the range of 3.0-3.3 cm and in the middle of X-band the free electron resonance is found at 3390 G.

Table 2.1. List of the frequency, wavelength and magnetic field ranges of various ESR spectrometers.

Designation	Frequency (GHz)	Wavelength(cm)	Magnetic field (G)
S	3.0	10.0	1070
X	9.5	3.15	3390
K	23.0	1.30	8200
Q	35.0	0.86	12500

Origin of an ESR signal

When an electron placed in a magnetic field, the degeneracy of the electron spin energy levels takes place, which can be represented by spin Hamiltonian [164]

$$\hat{H}_s = g\mu_B B\hat{S}_z \tag{2.7}$$

where g is called the g-factor (g = 2.002), and μ_B is the Bohr magneton, B is the magnetic field strength and $\hat{S}_z$ is the z-component of the spin angular momentum

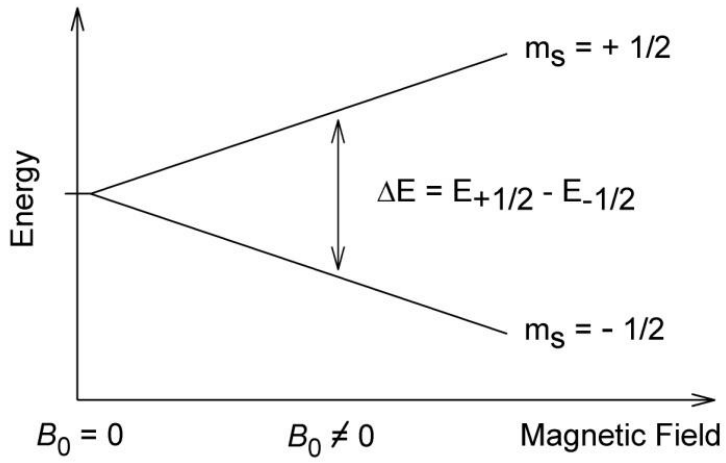

Fig. 2.6. Splitting of spectral line in the presence of magnetic field.

operator. The energy eigenvalues of the electron spin energy levels can be calculated by applying $\hat{H}_s$ to the electron spin eigenfunctions corresponding to magnetic component $m_s = \pm 1/2$

$$\hat{H}_s \left| \pm \frac{1}{2} \right\rangle = \pm \frac{1}{2} g\mu_B B = E_{\pm} \left| \pm \frac{1}{2} \right\rangle \tag{2.8}$$

From this, energy eigenvalues can be written as

$$E_{\pm} = \pm \frac{1}{2} g\mu_B B \tag{2.9}$$

Thus, the difference in energy between two levels can be given as

$$\Delta E = E_{+} - E_{-} = g\mu_B B \tag{2.10}$$

The movement of an electron takes place between the two energy levels by either absorbing or emitting of a photon of energy $h\nu$, where h is Plank constant and ν is the frequency of the photon.

Hence, the above equation takes the form

$$\Delta E = g\mu_B B = h\nu \tag{2.11}$$

This is the fundamental equation in ESR spectroscopy. The splitting of energy levels in the presence of magnetic field is shown in Fig. 2.6.

As ESR sample is consisting of collection of many paramagnetic species, so that its statistical distribution according to Maxwell-Boltzmann distribution can

be written by the following equation

$$\frac{N_+}{N_-} = \exp\left(-\frac{E_+ - E_-}{kT}\right) = \exp\left(-\frac{g\mu_B B}{kT}\right) = \exp\left(-\frac{h\nu}{kT}\right) \qquad (2.12)$$

In the above equation N_+ and N- denote the number of paramagnetic centers occupying upper energy state and lower energy state, respectively, k is the Boltzmann constant and T is the temperature.

For an X-band ESR spectrometer microwave frequency ν = 9.70 GHz. Substitution of ν value in the above equation gives $\frac{N_+}{N_-} = 0.99$. This indicate that the upper state has the lower population than the lower state which mean transition from the lower level to the higher level is more probable and this occurs via absorption (Fig. 2.7) of energy.

As we know that $N_+ = N- = N/2$, the population difference can be written as

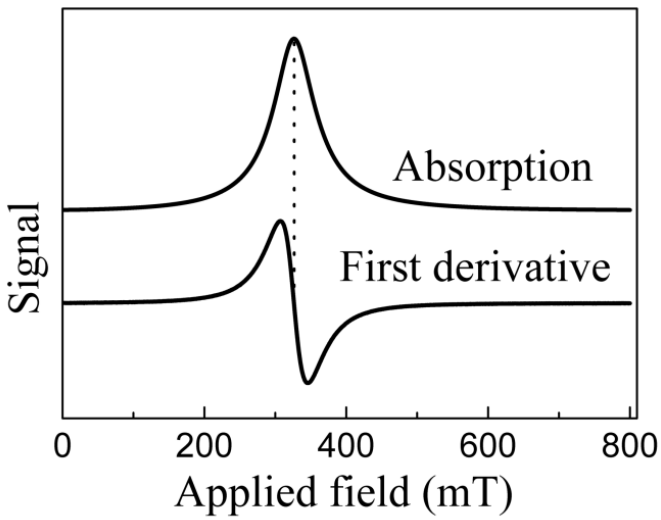

Fig. 2.7. Conversion of absorption signal to the first derivative of ESR signal.

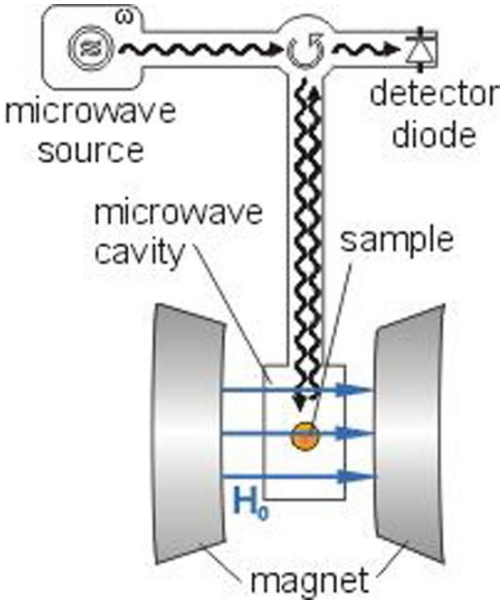

Fig. 2.8. Block diagram of an ESR spectrometer.

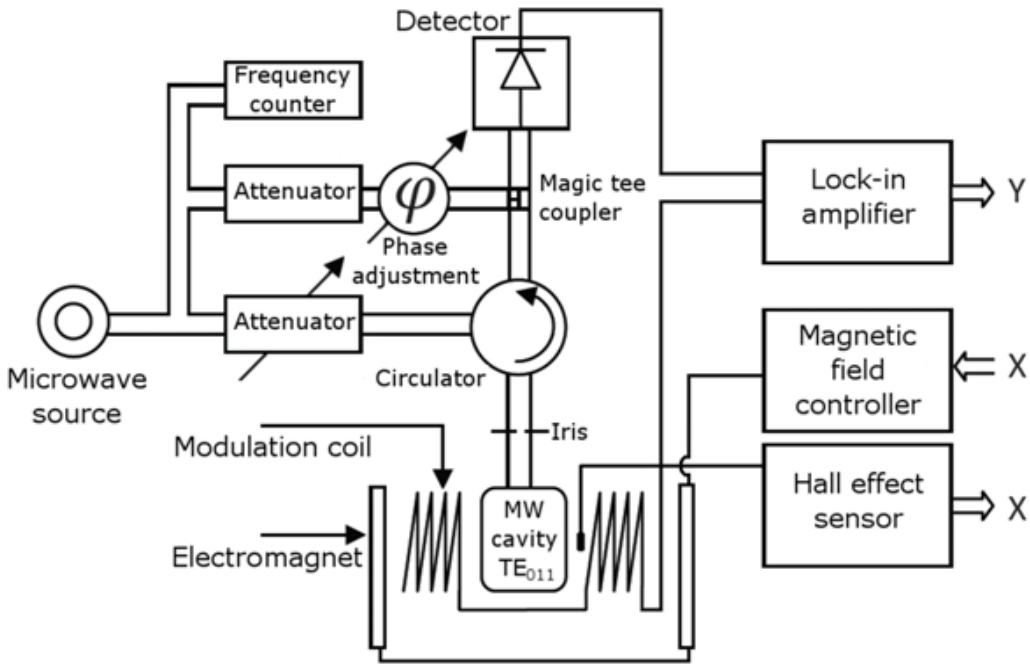

Fig. 2.9. Schematic of an ESR spectrometer.

$$N_{-} - N_{+} = \frac{Ng\mu_B B}{2kT} \tag{2.13}$$

This equation gives the information that the ESR sensitivity increases with the total number of spins, *N*, with increasing magnetic field strength and decreasing temperature. An absorption field is proportional to microwave frequency which means that the higher frequency band spectrometers have more sensitivity.

Block diagram of an ESR is shown in Fig 2.8. It consists of microwave source, cavity, magnet, sample holder and detector diode. Schematic of an ESR spectrometer is shown in Fig. 2.9 [165]. Microwaves are generated by a Klystron oscillator pass through a rectangular waveguide to the Attenuator. The power level is adjusted with the Attenuator. The Attenuator transfers its output to the resonator in which the sample is placed. When the microwave radiation from the cavity is reflected to the detector containing a diode, that coverts the microwave power into electric current. It is then amplified and fed to a suitable recorder. The circulator acts as traffic circle through which microwaves are passed. The magnetic field is swept across the resonance condition by varying the current using the modulation coils mounted on the cavity walls. The amplified ESR signal appeared as absorption or first derivative curves as shown in Fig. 2.7.

2.2.6. Vibrating sample magnetometer

Vibrating sample magnetometer (VSM) was invented by S. Foner in 1955 [166]. It works based on the principle of Faraday's law which tells that an electromagnetic force is generated in a coil when there is a change in flux linking the coil.

According to Faraday's law, the voltage induced across the coil is given by the expression

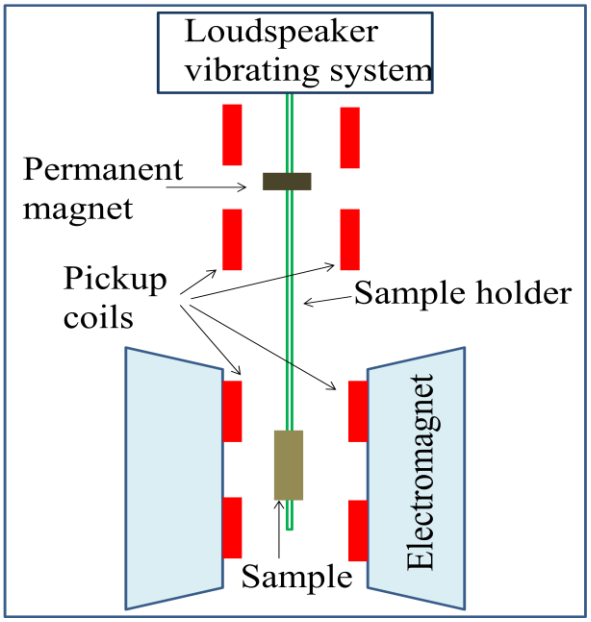

Fig. 2.10. Block diagram of vibrating sample magnetometer.

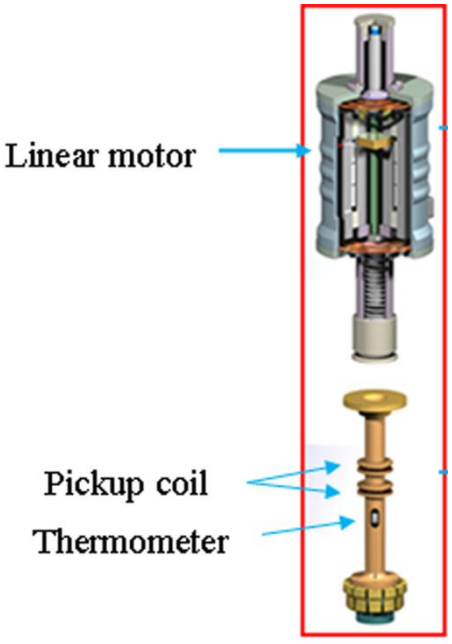

Fig. 2.11 Linear motor, pickup coils and thermometer of PPMS-VSM.

$$V(t) = C\frac{d\Phi}{dt} = C\frac{d\Phi}{dz}\frac{dz}{dt} \tag{2.14}$$

where C is the coupling constant, Φ denotes the flux enclosed by the pickup coil, z is the vertical position of the sample with respect to the coil and t is time. In this sample oscillates sinusoidally, therefore, $V(t)$ can be written as

$$V(t) = 2\pi fCmA\sin(2\pi ft) \tag{2.15}$$

In this equation m, A and f represents magnetic moment, amplitude of oscillation and frequency of oscillation, respectively. By measuring the value of $V(t)$ one can find the magnetic moment of sample to be measured.

The Quantum design vibrating sample magnetometer option for the physical property measurement system (PPMS) is a fast and sensitive dc magnetometer, used in the study of the magnetic properties of the materials. The magnetic properties of the present series of samples were studied using PPMS-VSM. The advantage of PPMS-VSM is that by using a compact gradiometer pickup coil configuration, relatively large oscillation amplitude of a few millimeters and a frequency of 40 Hz, the system is able to resolve the magnetization changes of less than 10^{-6} emu at a data rate of 1 Hz.

The block diagram of VSM is shown in Fig. 2.10. The sample, whose magnetic properties are to be studied, is attached to the end of the nonmagnetic rod, placed in a homogeneous magnetic field. The other end of the rod is attached to the mechanical vibrator. In PPM-VSM, it is attached to a linear motor (Fig. 2.11). When a magnetic sample is placed in a homogeneous magnetic field, the domains or the individual spins align in a particular direction with the field, as a result sample gets magnetize. The linear motor enforces the sample to move in a sinusoidal fashion in the magnetic field. The oscillating magnetic field of the

vibrating sample induces an alternating voltage in the detection coils. The magnitude of this voltage is proportional to the magnetic moment of the sample. The induced voltage is then amplified by lock-in amplifier provided with a reference signal at the frequency of vibration, which can come from an optical, magnetic, or capacitive sensor coupled to the driving system. The linear motor keeps the amplitude and frequency of vibration at a constant value throughout the experiment. In other cases in which the driving system works based on the loudspeaker (Fig. 2.10) can have amplitude and frequency of vibration of 0.10 mm and 100 Hz, respectively. The induced voltage is proportional to the magnetic moment of sample, thus controlling and monitoring the various components of VSM interfaced with the computer, the magnetic moment of the sample can be measured. In this case, the amplitude varies depending on the mass of the sample and its interaction with magnetic field. Controlling the amplitude as well as the frequency of such systems is difficult and a method which controls the amplitude and frequency is given as follows. A small permanent magnet is attached to the sample rod with another set of coils, outside the varying field region. The signals from these coils can be used in feedback loop to maintain constant amplitude of vibration.

2.2.7. Closed cycle refrigerator

The temperature dependent resistivity measurements were conducted using a closed cycle refrigerator (CCR) with four-probe setup. The operation of the measurement controlled with Labview programmer. The schematic diagram of the CCR is shown in Fig. 2.12. The closed cycle refrigerator works on the Gifford-McMahon principle. In this helium gas is used as the refrigerant. The compressor head is separated with cold head using with flexible or rigid pressure tubing so that the lighter weight cold head can be placed in any mounting position as we want. The connections are made via self-sealing screw couplings.

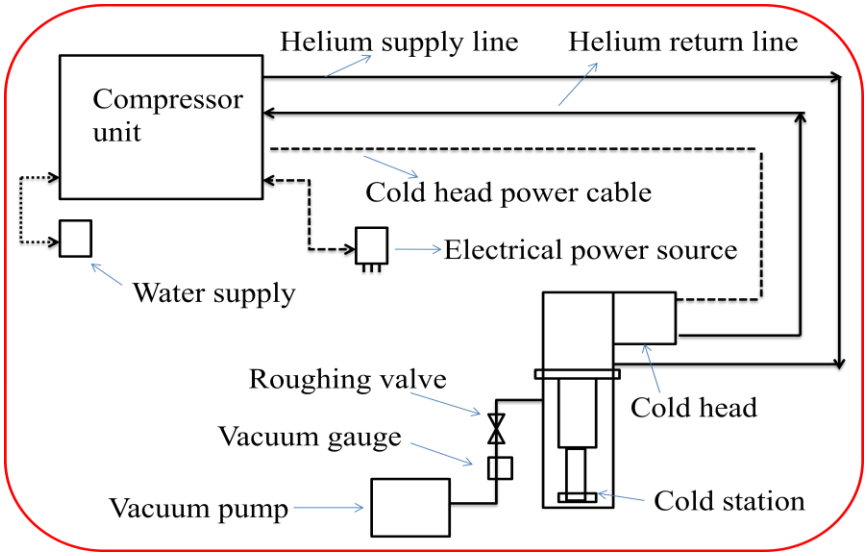

Fig. 2.12. Schematic diagram of a closed cycle refrigerator.

This controls the loss of helium when screwed on/off repeatedly. On the other hand, the other features of CCR are PID parameters, temperature controller and temperature sensors. In addition to these components, the typical laboratory systems will have water supply for cooling the compressor and vacuum pump for the sample space.

Helium gas is first compressed then from one of the gas lines; the high-pressure helium is supplied to the cold head which acts as the refrigerator. In this unit the compressed helium is cooled by expansion, and provides cooling to the heat station on the refrigerator. When the refrigerator is cooled, the gas is returned to the compressor via the other gas line to complete the cycle. By repeating this process one can obtain low temperatures in the refrigerator and temperature can be controlled with the temperature controller attached to the system.

2.2.8. Four probe method

The resistivity can be measured in two ways either by two probe or four probe

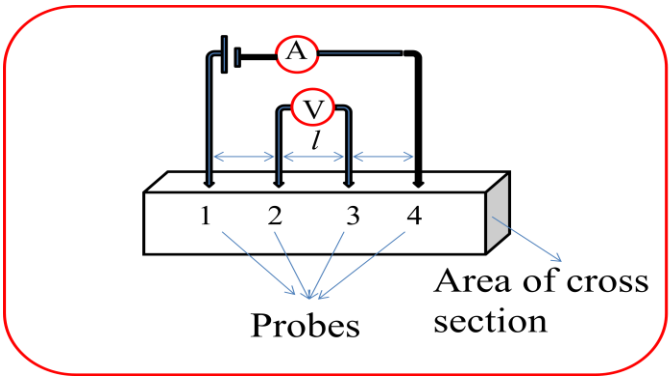

Fig. 2.13. Schematic four probe setup for temperature dependences resistivity measurements.

method. Two probe methods involve measuring the current and voltage in the same connector wires, used for measuring the high resistivity in which contact resistance can be neglected. Four probe methods are used for low resistivity measurements. In the present work four probe method (Fig. 2.13) is employed for measuring the resistivity of samples. In this process, first the samples are cut in rectangular shape. Then the electrical contacts are made by fixing the copper wires on the sample with silver paste. This whole set up is fixed on the cold station. The chamber is evacuated to the pressure of the order of 10^{-5} Torr. Current is the order of 100 nm to 100μA is used in the present work.

The electrical resistivity can be calculated using the expression,

$$\rho = \frac{V.A}{I.l} \tag{2.16}$$

where V is the voltage measured across 2 and 3 probes, I is current applied to the sample, l is the distance between the voltage terminals and A is the area of cross-section of the sample. In this way, the electrical resistivity of the sample can be measured.

Chapter 3

Effect of Ca doping on the properties of $Bi_{1-x}Ca_xMnO_3$ ($0.40 \leq x \leq 0.90$) manganites

3.1. Introduction

$Bi_{1-x}Ca_xMnO_3$ (BCMO) is an interesting system which exhibits phenomena like charge ordering (CO), orbital ordering (OO) and long-range antiferromagnetic (AFM) ordering [7-9]. The properties of rare earth manganites depend on the average ionic size of the A-site cations ($<r_A>$), the variance of the A-site cation size distribution (σ^2), Jahn-Teller (J-T) distortion and tolerance factor (t), etc. Whereas, in the case of Bi-manganites, the physical properties not only depend on the above-mentioned parameters but also on the highly polarizable $6s^2$ lone pair electrons of Bi^{3+}ions. In this system, the Bi cations and oxygen anions stabilize in different magnetic and structural phases in comparison to rare earth manganites [7-9]. Although, there are few reports on BCMO system, there remains a lot of physics which can be understood by systematic Ca-doping in place of Bi. Kurian and Singh [7, 104] have reported electron spin resonance (ESR) and resistivity (ρ) studies of some of the compositions of $Bi_{1-x}Ca_xMnO_3$ system synthesized by solid state reaction method. The present study covers a wide range of compositions of $Bi_{1-x}Ca_xMnO_3$ (x = 0.40, 0.50, 0.60, 0.65, 0.70, 0.75, 0.80, 0.85 and 0.90) system synthesized by sol-gel method.

3.2. Sample preparation

The stoichiometric amounts of pure $Bi(NO_3)_3.5H_2O$, $Ca(NO_3)_2.4H_2O$ and $MnCl_2.4H_2O$ were dissolved in water. Urea concentration was fixed at Ω = 10, with Ω = Urea/{$[Bi^{3+}]+[Ca^{2+}]+[Mn^{2+}]$}. The solvent was evaporated at

temperatures ranging from 80 ^{o}C to 137 ^{o}C. While cooling, a pink gel was formed, which was decomposed in an oven at 250 ^{o}C for 3 hours (hrs), yielding a fairly porous precursor. The samples were annealed in air using the furnace at 900 ^{o}C for a few hrs with intermediate grinding in an agate mortar. Then, the sample was pressed into a pellet and sintered in air at 900 ^{o}C for 4 hrs.

3.3. Results and discussion

3.3.1. Structure and morphology studies

Fig. 3.1 depicts the Rietveld refinement of x-ray diffraction (XRD) pattern of the samples. With the Rietveld refinement, XRD data is reproduced with *Pnma* space group orthorhombic structure for all the samples. However, refinement did not give a satisfactory reproducibility for the samples with $x \geq 0.85$. A few reports have suggested that in the Ca-rich samples, Ca deficiency results in forming non-stoichiometric compounds [78, 88]. This non-stoichiometry might probably lead to comparatively inferior refinement in Ca-rich samples. From the refinement, the estimated values of various structural parameters such as atomic positions (x, y, and z), the average Mn-O bond length ($<d_{Mn-O}>$), the average Mn-O-Mn bond angle (<Mn-O-Mn>) and the goodness of fit (*S*) are listed in table 3.1. The calculated $<r_A>$, σ^2 [using equation (1.2)] and *t* [using equation (1.1)] of various samples are also listed in table 3.1. Deviation of the Mn-O-Mn bond angle from 180^{o} (which is expected for non-distorted cubic perovskites) is clearly visible from the crystal structure of $Bi_{0.35}Ca_{0.65}MnO_3$, generated using the refined parameters, shown in Fig. 3.2. Fig. 3.3 depicts the variation in lattice parameters (*a*, *b* and *c*) and the unit cell volume (*V*) (inset of Fig. 3.3) as a function of Ca content, obtained from the refinement of the XRD data. With the increase in Ca content decrease in $<r_A>$, *t*, and unit cell volume is observed. This is ascribed to lower ionic radii of Ca^{2+} (1.12 Å) than that of Bi^{3+} (1.24 Å) ion. The value of σ^2

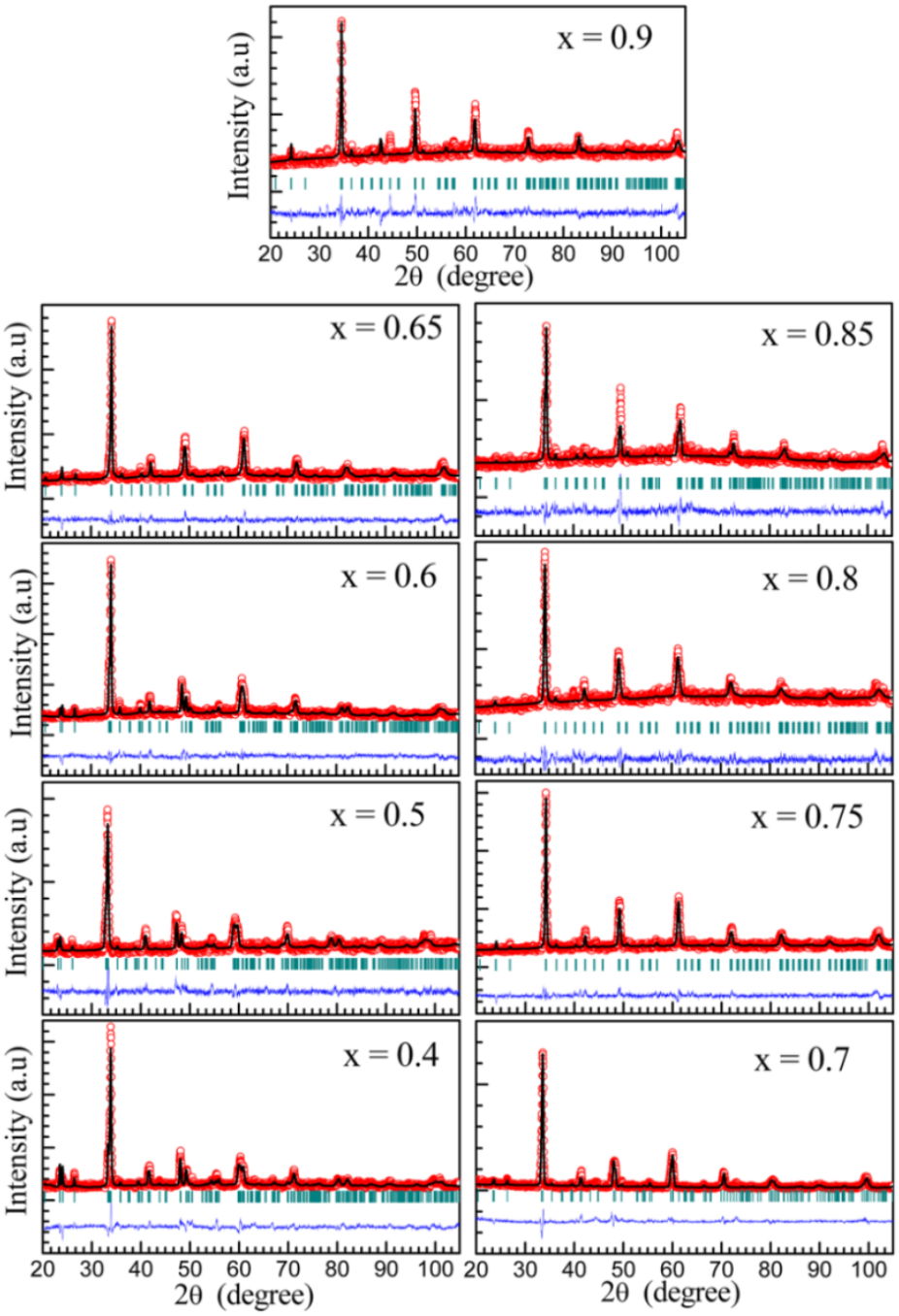

Fig. 3.1. Rietveld refinement (solid black lines) of the XRD data (open red circles) along with diffraction planes (green lines) and the difference between the experimental and fitting data (blue lines) of $Bi_{1-x}Ca_xMnO3$ samples.

Table 3.1. List of the structural parameters [atomic positions(x, y and z), *S*, $<d_{Mn-O}>$ and <Mn-O-Mn>] estimated from the refinement of the XRD data of $Bi_{1-x}Ca_xMnO_3$ samples. The calculated values $<r_A>$, σ^2 and *t* are also listed in the table. The average GS values, estimated from FESEM images, are also listed in the table.

Sample (*x*)	**0.40**	**0.50**	**0.60**	**0.65**	**0.70**	**0.75**	**0.80**	**0.85**	**0.90**
Bi/Ca									
x	0.041	0.040	0.038	0.033	0.032	0.028	0.021	0.023	0.028
y	0.250	0.250	0.250	0.250	0.250	0.250	0.250	0.250	0.250
z	0.984	0.991	0.983	0.975	0.984	0.989	0.987	0.989	0.989
Mn									
x	0.500	0.500	0.500	0.500	0.500	0.500	0.500	0.500	0.500
y	0.500	0.500	0.500	0.500	0.500	0.500	0.500	0.500	0.500
z	0	0	0	0	0.000	0.000	0.000	0.000	0.000
O(1)									
x	0.490	0.483	0.501	0.474	0.4883	0.477	0.552	0.559	0.499
y	0.250	0.250	0.250	0.250	0.250	0.250	0.250	0.250	0.250
z	0.069	0.091	0.068	0.059	0.002	0.055	0.055	0.052	0.072
O(2)									
x	0.188	0.274	0.318	0.324	0.207	0.191	0.276	0.206	0.275
y	0.524	0.526	0.534	0.506	0.525	0.537	0.456	0.487	0.573
z	0.274	0.234	0.259	0.261	0.204	0.246	0.279	0.204	0.188
S	2.10	1.88	1.86	1.58	2.10	1.71	2.11	2.20	2.60
$<d_{Mn-O}>$ (Å)	1.892	1.936	1.905	1.887	1.915	1.887	1.892	1.878	1.882
<Mn-O-Mn>(º)	156.81	150.41	156.97	158.51	160.00	161.33	155.19	155.76	154.74
$<r_A>$ (Å)	1.216	1.210	1.204	1.201	1.198	1.195	1.192	1.189	1.186
σ^2 (10^{-4}) (Å^2)	8.64	9.00	8.64	8.19	7.56	6.75	5.76	4.59	3.24
t	0.929	0.927	0.925	0.924	0.923	0.922	0.921	0.920	0.919
GS (nm)	628	515	580	423	386	303	275	215	270

increases from x = 0.40 to 0.50, then it decreases with increase in Ca content. Lattice parameter and the unit cell volume values of the samples are found to be slightly lower compared to that reported in the literature [78, 122, 167]. However, reports are limited to a few of them alone. This variation might be due to different synthesis techniques and conditions that are followed. A large splitting of the lattice parameters, i.e., difference among the values of a, $b/\sqrt{2}$ and c is observed for the samples with x = 0.40, 0.50 and 0.60, which is a typical feature of CO

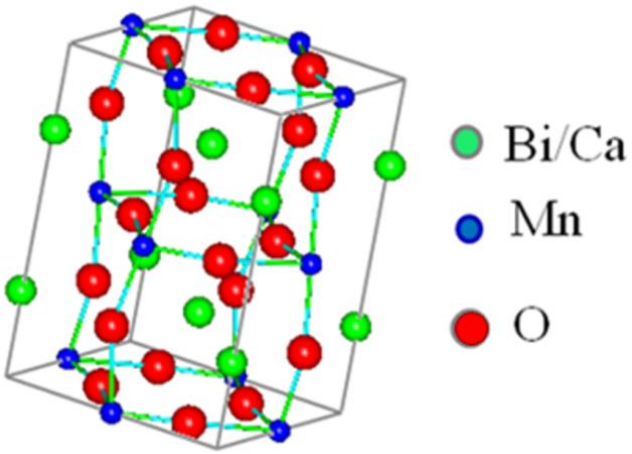

Fig. 3.2. Crystal structure of $Bi_{0.35}Ca_{0.65}MnO_3$.

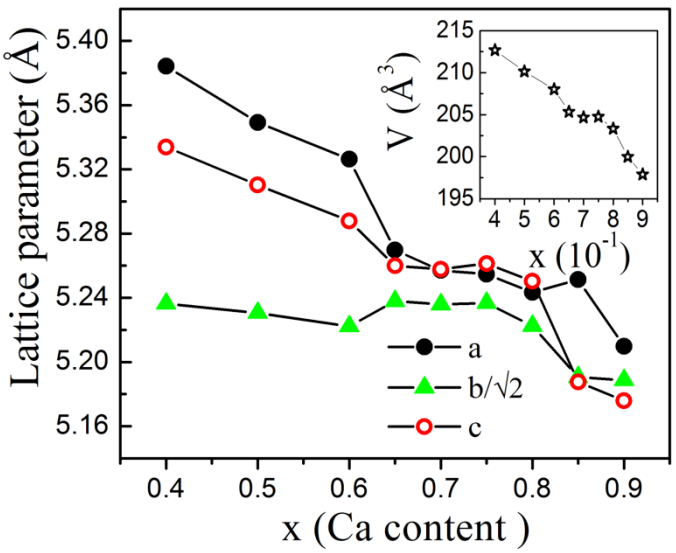

Fig. 3.3. Lattice parameter (*a*, *b* and *c*) vs *x* (Ca content) of $Bi_{1-x}Ca_xMnO_3$ samples. Inset shows the unit cell volume as a function of *x*.

phase with strong J-T distortion [17]. The lattice parameters of the samples with $0.40 \leq x \leq 0.70$ follow a $b/\sqrt{2} \leq c \leq a$ behavior and the lattice parameters of the samples with $x = 0.75$ and 0.80 follow a $b/\sqrt{2} \leq a \leq c$ behavior. The first and the second lattice parameter behaviors are typical signatures of O´-type and O´´-type

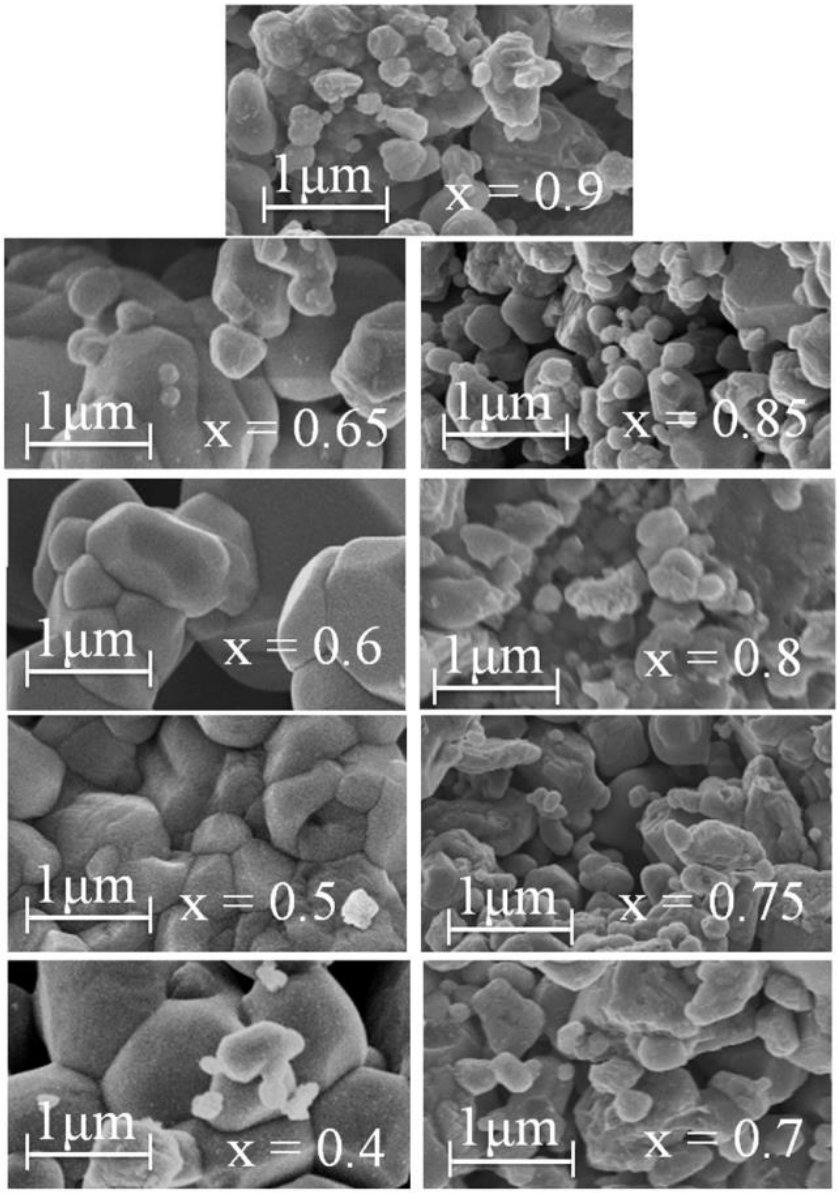

Fig. 3.4. Microstructure of $Bi_{1-x}Ca_xMnO_3$ samples

distorted perovskite structure of manganites, respectively [79, 168]. Whereas, for the sample with x = 0.85 and 0.90 the lattice parameters follow a trend, $c \leq b/\sqrt{2} \leq a$, which is the signature of O-type distorted perovskite structure of manganites [168, 169]. The J-T distortion and MnO_6 tilting together produce O´-type structure

[170]. The O´-type and O´´-type distorted perovskite structures are related to orbital ordered and orbital disordered manganites, respectively. With the increase in Ca content the difference among the lattice parameters decreases, associated with the decrease in the lattice distortion which is due to the decrease in the contents of the J-T Mn^{3+} ion contribution [122]. The average crystallite size and strain of the samples are calculated using equation (2.5). The values of average crystallite size are found to be in the range 80-110 nm and the value of the strain parameter is of the order of $\sim 10^{-5}$ for all the samples. Fig. 3.4 shows the field emission scanning electron microscopy (FESEM) microstructure of the samples. It is observed that for samples with $x = 0.40$, 0.50, 0.60 and 0.65 the concentration of larger grains is high and for samples with $x \geq 0.70$ the concentration of smaller grains is large. The estimated values of the average grain size (GS) of all the samples are listed in table 3.1. The energy dispersive x-ray spectroscopy (EDX) results confirm the purity of the samples.

3.3.2. Electron spin resonance studies

Why electron spin resonance technique?

As DE mechanism is an intrinsic dynamical process, it is important to investigate the dynamics of the spins and their static properties for studying the magnetic properties of the manganites. There are two experimental techniques, namely, magnetic resonance and inelastic neutron scattering, which can be used to describe the spin dynamics. Neutron scattering can provide detailed information about the magnetically ordered phases in the manganites. However, it has limited use in probing the dynamics of the paramagnetic (PM) phases [7, 15, 19, 171-173]. Whereas, electron spin/paramagnetic resonance (ESR/EPR) is a sensitive technique which can help in understanding the spin structure and its dynamics in complex magnetically ordered systems like manganites. This technique has been used by several groups for studying the spin dynamics of manganites [172-179].

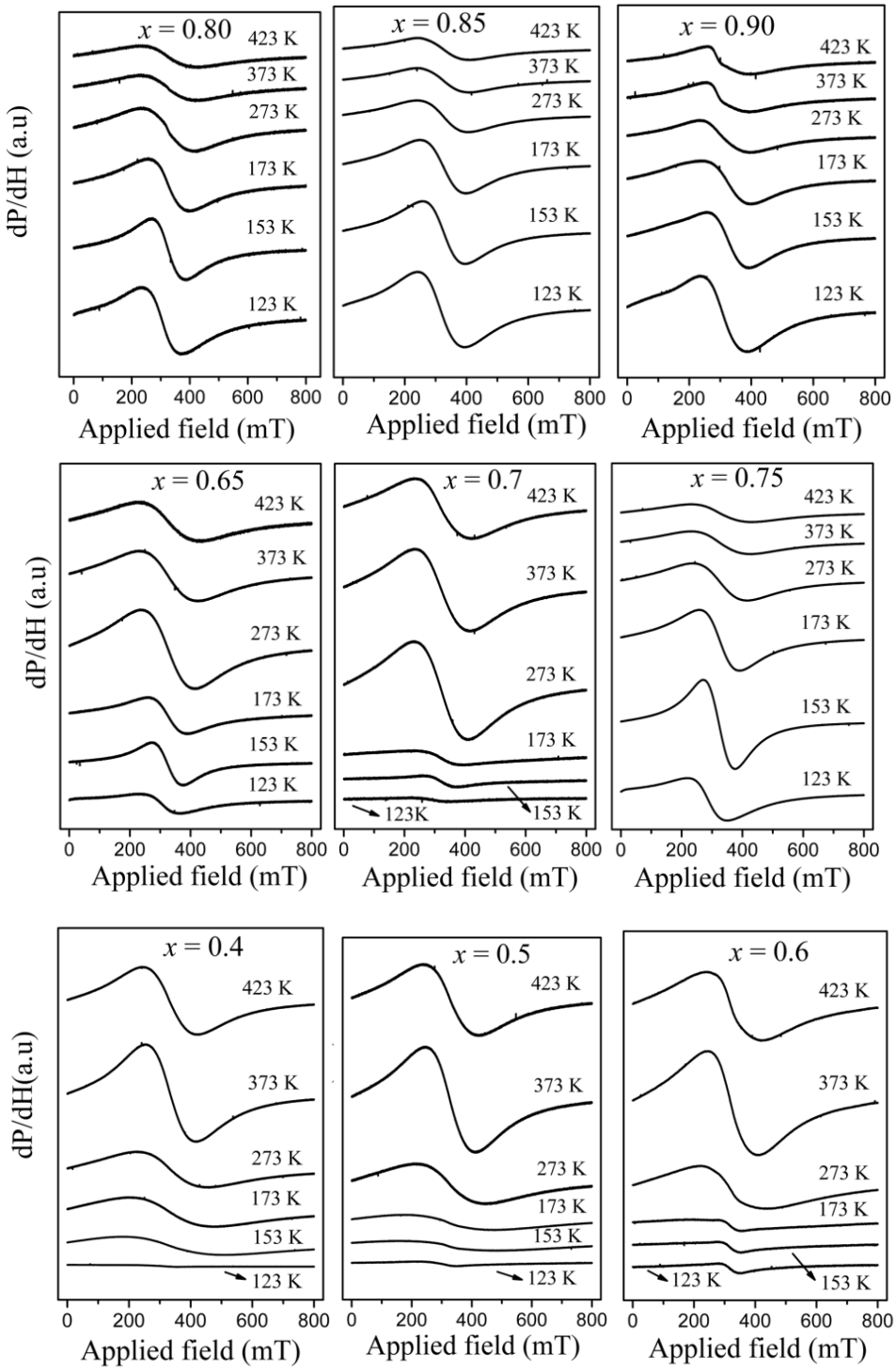

Fig. 3.5. ESR spectra of $Bi_{1-x}Ca_xMnO_3$ samples measured at various temperatures.

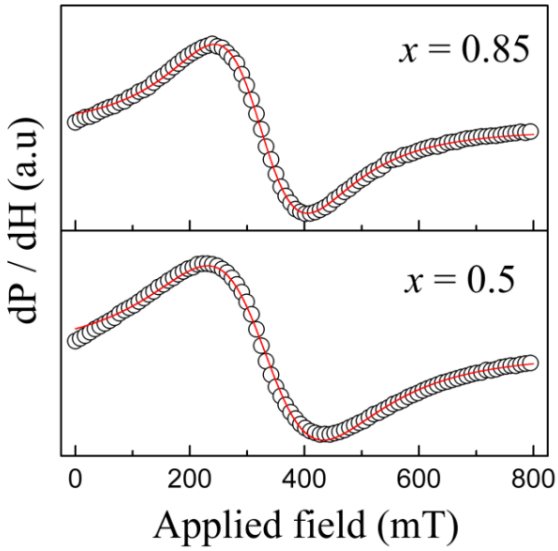

Fig. 3.6. Lorentzian fit (solid red line) to the ESR spectra (open circles) of $Bi_{1-x}Ca_xMnO_3$ measured at 273 K.

In the present work the ESR technique is used to investigate various dynamical processes over a wide range of temperatures.

Fig. 3.5 shows the ESR spectra of the samples at some selected temperatures. Although variations in the intensity and peak to peak linewidth of the ESR signal are observed with the change in composition and temperature, all the spectra are symmetric in the entire measured temperature range (453-123 K). Since the ESR spectra are symmetric, we have used the Lorentzian expression for fitting the experimental data, as shown in Fig. 3.6 for x = 0.50 and 0.85 samples at a temperature 273 K. The expression for Lorentzian can be written as

$$\frac{dP}{dH} = \frac{d}{dH} A\left(\frac{\Delta H}{4(H - H_r)^2 + \Delta H^2} + \frac{\Delta H}{4(H + H_r)^2 + \Delta H^2} \right) \tag{3.1}$$

where H_r is the resonance field, ΔH is the peak to peak linewidth, and A is a quantity proportional to the area under the curve which is related to the intensity

of the signal [174, 178]. The two terms in the equation (3.1) describe the contribution from the clockwise and anti-clockwise circularly polarized components of microwave radiation.

It has been suggested [172] that when the ESR signals are intense near the critical point (Curie temperature, T_C), even for relatively small amount of samples, the ΔH depends strongly on the number of spins in the sample. Whenever the large quantity of sample is used, the sample size effects arise from overloading the cavity through magnetic losses [180]. The ESR signals remain Lorentzian as long as the magnetic losses are not large enough to drive the diode detector out of linearity. When the sample is loaded in the cavity, at a fixed microwave frequency (ω), ΔH can be given by the following expression

$$\Delta H^{obs} = \Delta H(1+b)^{1/2} \tag{3.2}$$

With

$$b = \frac{\left(4\pi/3\right)\eta Q_L \chi_{ESR}\omega}{\gamma \Delta H} \tag{3.3}$$

where χ_{ESR} is the static susceptibility corresponding to the resonant species, η is the fitting factor and Q_L is the loaded Q of the microwave cavity. Similarly the changes in line intensity (I) also occur by the size effects due to magnetic losses, and the expression for this can be given as

$$I = \eta \chi_{ESR} \omega Q_L (1+b)^{-1/2} \tag{3.4}$$

These two equations, (3.2) and (3.4), have certain limitations such as the value of b being much lower than one.

In addition to the sample-dependent effects, frequency or applied field dependences of ΔH have also been reported [181]. Apart from the above-mentioned parameters, skin depth (δ_s) also affects the parameters I and ΔH of the ESR signal, and it is given by the expression

$$\delta_s = \left(\frac{\rho}{\mu_o \omega} \right)^{0.5} \tag{3.5}$$

where ρ is the resistivity of the sample measured at room temperature (RT), μ_o (4π x 10^{-7} Vs/Am) is the permeability of free space and $\omega = 2\pi$ x 9 GHz [29]. The estimated values of δ_s of the various samples are found to be in the range of 0.20-1.50 mm and it is larger than that of the size of the samples. In the present work, we have also taken care of cavity over loading problems. This ensures that the observed ESR signal intensity, ΔH and H_r as a function of temperature are intrinsic in nature.

The ESR spectra for all the samples consist of a resonance line with g value (Lande g-factor) of 1.99 ± 0.02 in the PM state [7]. This value is typical for Mn^{4+} ion in the octahedron coordination. The ESR signals observed in manganites are due to some combination or cluster of Mn^{3+}-Mn^{4+} ions coupled by strong short-range FM-DE interactions [7, 8, 182]. All Mn ions contribute to the ESR signal, and the normalized double integrated intensity (DI) of the ESR signal is proportional to the number of ESR centers which is a measure of ESR susceptibility (χ_{ESR}).

Fig. 3.7 shows DI as a function of temperature for all the samples. For samples with $0.40 \leq x \leq 0.80$, as the temperature decreases from high-temperature (453 K), DI increases and reaches its maximum value at a temperature, which is assigned as the T_{CO}. The increasing behavior of DI, on approaching the ordering

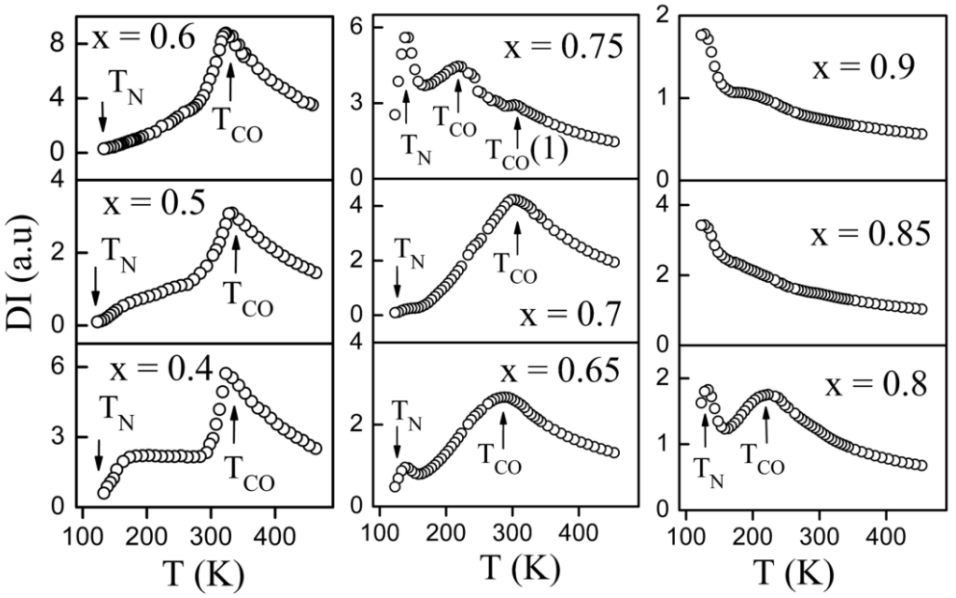

Fig. 3.7. *DI* vs *T* plots of $Bi_{1-x}Ca_xMnO_3$ samples.

temperature (T_{CO} or T_C), is ascribed to the formation of spin clusters in these samples [183]. Various experiments suggest that these clusters result from dynamic phase separation [70, 184, 185,]. Below $T_{CO,}$ *DI* decreases, evidencing the existence of AFM correlations and reaches a minimum and then it increases with further decrease in temperature for $0.65 \leq x \leq 0.80$ samples. For the sample with $x = 0.40$, *DI* shows a temperature independent behavior in the temperature range 280-180 K with decreasing temperature. This behavior is ascribed to orbital ordering. For $x = 0.85$ and 0.90 samples no T_{CO} is observed. For $x = 0.85$ and 0.90 samples, on cooling from high-temperature, *DI* increases gradually. For $0.40 \leq x \leq 0.80$ samples sharp decrease in *DI* below 126-150 K is assigned as the onset of long-range AFM ordering temperature, i.e., Neel temperature (T_N). Below T_N the intensity of the ESR signals become weak as shown in Fig. 3.5 for samples with $0.40 \leq x \leq 0.70$, with $T_N \sim 150$ K.

The 1/*DI* versus (vs) *T* plots for various samples are shown in Fig. 3.8. The linear fit in the high-temperature range is as per Curie-Weiss law. For

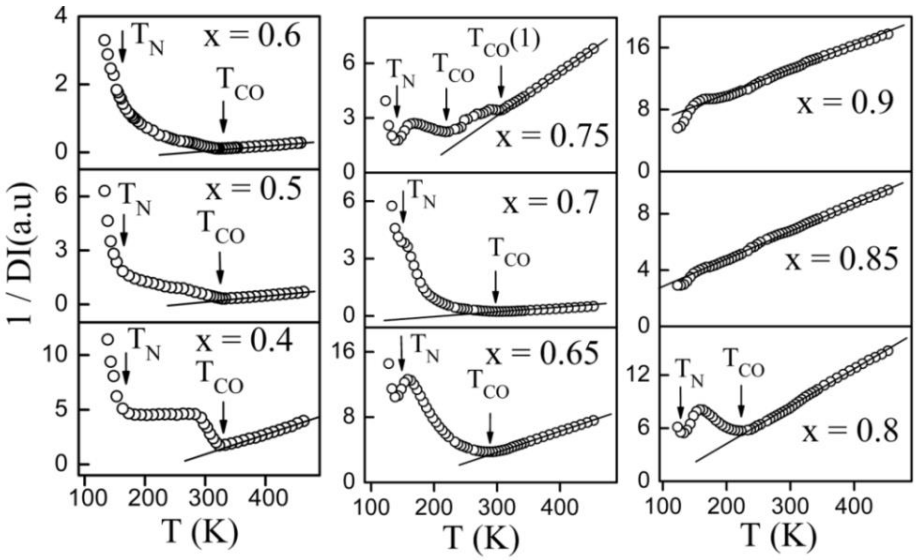

Fig. 3.8. 1/*DI* vs *T* plots of $Bi_{1-x}Ca_xMnO_3$ samples.

$0.40 \leq x \leq 0.80$, the positive intercept on the x-axis in the temperature range $T > T_{CO}$ indicates that the magnetic phase is dominated by local FM fluctuations that are mediated by Mn^{3+}/Mn^{4+} hopping induced DE interactions [8, 9]. The T_{CO} of $0.65 \leq x \leq 0.80$ samples is not as prominent as it was observed for the samples with $x \leq 0.60$. For $x = 0.75$ sample, a weak CO transition at 303 K is also observed along with prominent CO transition at 219 K. This may be due to the existence of Bi-rich CO phase. The upward and downward trend in 1/*DI* vs *T* plots below T_{CO} is an indication of whether AFM or FM interactions dominate in the respective temperature range. The minima in these plots indicate onset of CO or AFM ordering. For the samples with $x = 0.65$, 0.75 and 0.80, 1/*DI* vs *T* plots show a broad peak at ~160 K which is attributed to canted (C)-type AFM correlations [186]. For the samples with $x = 0.85$ and 0.90 the down turn behavior of 1/*DI* below ~148 K can be explained in view of contributions from evolution of short-range ordered FM clusters in the PM matrix, as per Griffiths theory [81, 186]. For $x = 0.85$ and 0.90 the negative intercept on the x-axis indicates

dominant AFM-superexchange (SE) interactions above 150 K, below this localized FM correlations dominate [186].

In order to analyze the high-temperature ESR data, we have used the cluster model proposed by Oseroff et al. [187], given by the relation

$$DI = I_0 \exp(E_a / k_B T) \tag{3.6}$$

where I_0 is a fitting parameter and E_a is the activation energy needed for the dissociation of the FM spin clusters. The higher values of E_a of the samples indicate the existence of strong FM clusters whereas the decrease in its value indicates a decrease in the contribution of FM clusters with the coexistence of AFM phases. This model also suggests that the observed signals are not due to an individual Mn ion of any valence state such as Mn^{2+}, Mn^{3+} or Mn^{4+}. Since ΔH is found to be proportional to the hopping conductivity [188], and static susceptibility, the equation (3.6) is in good agreement with the assumption that the DI is proportional to the χ_{ESR}.

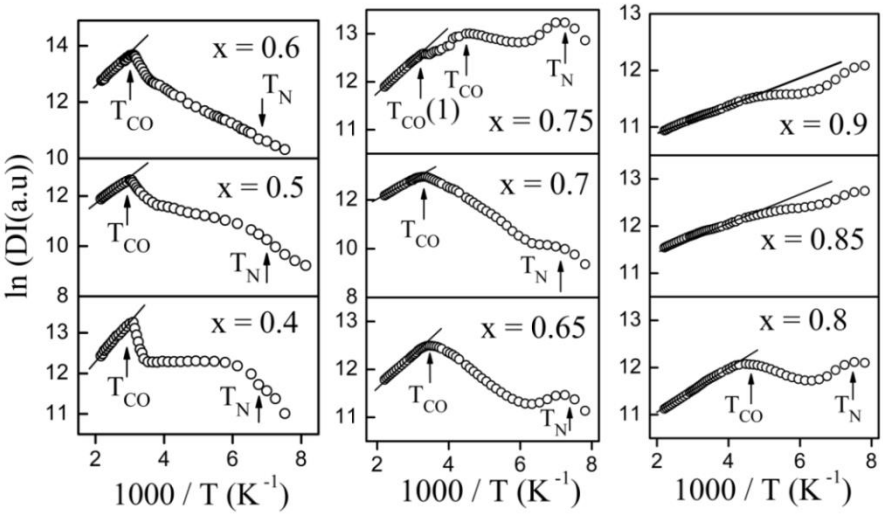

Fig. 3.9. lnDI vs 1000/T plots of $Bi_{1-x}Ca_xMnO_3$ samples.

According to equation (3.6), ln*DI* vs 1000/*T* plots are obtained for all the samples, as shown in Fig. 3.9. For all the samples, on cooling from 453 K, a linear behavior is observed in the high-temperature range, indicating the existence of short-range FM correlations. For samples with $0.40 \leq x \leq 0.80$, the ln*DI* data deviates from linearity below T_{CO}, and then it decreases up to a certain temperature range, ~150-170 K. For samples with $0.65 \leq x \leq 0.80$, again it increases to its maximum. Below T_N, a sharp decrease in ln*DI* is observed for all the samples [179]. The value of E_a is not calculated from the ESR measurements, as it requires various parameters. However, the slope of the ln*DI* vs 1000/*T* plots, which determines the value of E_a, gives the strength of the magnetic interaction. As the Ca content increases, the decrease in slope of the ln*DI* indicates the weakening of the strength of short-range FM interactions or intracluster DE interactions [177] in the high-temperature range and the existence of AFM fluctuations in the CO state.

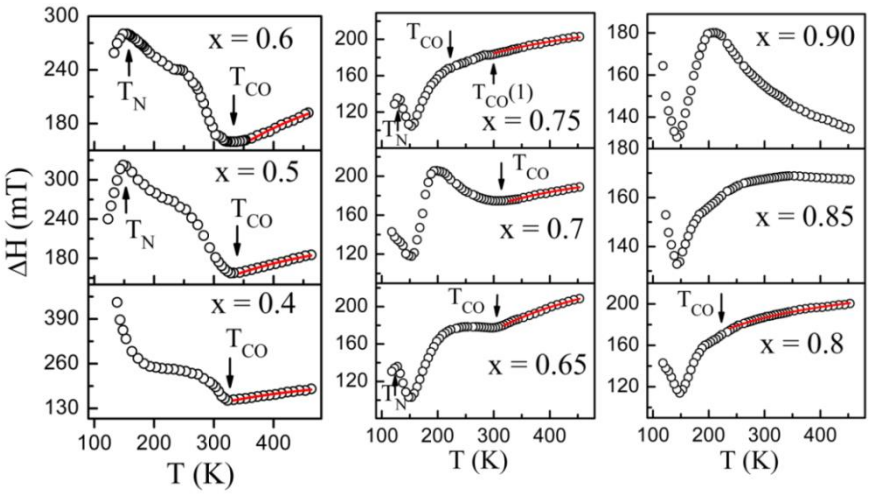

Fig. 3.10. Δ*H* vs *T* plots of $Bi_{1-x}Ca_xMnO_3$ samples. Solid red lines are according to theoretical model given by the equation (3.7) [173, 176].

Fig. 3.10 shows the ΔH as a function of temperature for all the samples. For the samples with x = 0.50, 0.60, 0.65 and 0.75, below T_N, ΔH decreases with decrease in temperature. For the samples with $x \geq 0.65$, ΔH shows a prominent minimum at ~150 K. ΔH increases linearly with the increase in temperature in the temperature range $T > T_{CO}$. As T_{CO} decreases with increase in x, ΔH shows saturation effect with the increase in temperature. This effect is clearly seen for the samples with x = 0.80 and 0.85. For the sample with x = 0.90, the increasing trend of ΔH with decreasing temperature indicates the strengthening of AFM interactions. This behavior is similar to what has been reported for $Y_{1-x}Ca_xMnO_3$ (x = 0.90 and 0.95) and predicted for $CaMnO_3$ [189]. Fig. 3.11 shows the temperature dependence of H_r for all the samples. For the samples with $0.40 \leq x \leq 0.80$, as temperature decreases from high-temperature, H_r is almost constant up to ~150 K. For the samples with x = 0.85 and 0.90, it is observed that there is a decreasing and an increasing trend in H_r with decrease in temperature. This is due to the interplay between FM and AFM correlations as a function of temperature. The sharp decrease in H_r from its PM value at ~150 K is due to spin-spin interactions and net magnetization which arises due to short-range FM

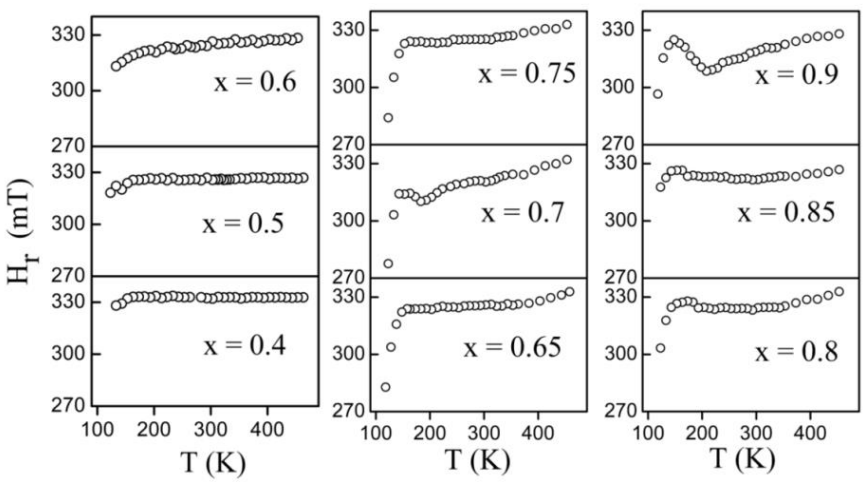

Fig. 3.11. H_r vs T plots of $Bi_{1-x}Ca_xMnO_3$ samples.

correlations as the temperature decreases [175]. The decrease in H_r below ~150 K for all the samples indicates the existence of FM magnetic clusters or inhomogeneities embedded in the PM matrix [172, 175, 190, 191].

In order to extract more information, the spin dynamics of the compounds is studied using Huber et al. [173] and Auslender et al. [176, 192] approach given by the expression

$$\Delta H(T) = (T - \theta_C)\left(\Delta H(\infty)/T + B\right) \tag{3.7}$$

where $\Delta H(T)$ represents linewidth at temperature T, θ_C is the Curie-Weiss temperature, $\Delta H(\infty)$ is the high-temperature asymptote and B is a parameter, describes the strength of interactions between the e_g electrons and impurities with spin reversal [192]. The first and second terms are due to ion-ion spin relaxation [173] and itinerant e_g electrons [192], respectively. $\Delta H(\infty)$ is independent of temperature, but the concentration of divalent ions and the structural phase of the

Table 3.2. List of the various parameters (θ_C, $\Delta H(\infty)$, B, $\mu_{eff}^{exp}(\mu_B)$ and $\mu_{eff}^{th}(\mu_B)$) of $Bi_{1-x}Ca_xMnO_3$ samples estimated from ESR and magnetization data.

x	ESR			Magnetization		
	θ_C (K)	$\Delta H(\infty)$ (G)	B (GK^{-1})	θ_C (K)	$\mu_{eff}^{exp}(\mu_B)$	$\mu_{eff}^{th}(\mu_B)$
0.40	140	2647	0	138	5.92	4.48
0.50	134	2515	0	127	5.59	4.38
0.60	141	2972	0	121	5.10	4.29
0.65	109	2714	0.06	90	5.06	4.23
0.70	75	2261	0	69	5.17	4.18
0.75	61	2274	0.13	76	4.92	4.13
0.80	57	2172	0.16	48	4.90	4.07
0.85	-	-	-	-44	4.76	4.02
0.90	-	-	-	-159	5.41	3.97

material affects its value. The fits based on the equation (3.7) for the ΔH vs T plots, in the temperature range $T \geq T_{CO}$ are shown with solid red lines in Fig. 3.10. From these fits the calculated values of θ_C, $\Delta H(\infty)$ and B are listed in table 3.2. It is observed that the estimated values of $\Delta H(\infty)$ are high for the samples with $0.40 \leq x \leq 0.65$ compared to that of the samples with x = 0.70, 0.75 and 0.80. This indicates the weakening of the strength of ion-ion spin relaxation in Ca-rich samples. Unlike the magnetic ordering temperatures (θ_C and T_C), $\Delta H(\infty)$ does not depend on DE mechanism. For all the samples (except for x = 0.65, 0.75 and 0.80) the fitting parameter B is zero which mean that the electron spin-lattice interactions are not significant in these compounds. The positive values of θ_C and the zero values of B indicate the existence of short-range FM correlation and pure ion-ion spin relaxation in the PM state, respectively [193].

Above T_{CO}, the linear increase in ΔH as a function of temperature has been widely reported in La, Pr and Nd manganites [16, 52, 53, 194]. According to M. S. Seehra and Gupta [195] the temperature dependence of ΔH is primarily due to a spin-lattice relaxation mechanism. Spin-lattice relaxation in manganites is due to the relaxation of spin of e_g J-T polarons to the lattice [196]. D. L. Huber and M. S. Seehra [197] later argued this and derived an expression for ΔH taking into an account of phonon contributions too. According to theoretical model by C. D. Hu [198], the spin correlation caused by DE interaction, SE interaction between Mn ion and anisotropic energy of spins caused by crystal field give rise to linear increase in ΔH in the temperature range $T > T_{CO}$ and a sharp upturn behavior takes place below T_{CO}. Although there were some of the similar reports on this kind of behavior of ΔH below T_{CO}, the phenomenon still remains unexplained clearly. C. D. Hu showed with his theoretical calculation that it is intrinsic and can be due to phase segregation in view of Griffiths phase (GP) formation [81]. Above $T_{CO,}$ the existence of FM interactions in the PM matrix has been reported in many of the CO materials [199]. It has been reported that in manganites three factors, i.e.,

dipolar interaction, crystal field and anti-symmetric exchange arising from Dzyloshinsky-Moriya exchange interaction, contribute to the ΔH of the ESR signal [191, 200]. P. J. Janhavi et al. [191] have explained the temperature dependences of ΔH behavior in the temperature range $T_N < T < T_{CO}$ by using the semi-empirical model of motional narrowing. In most of the reported works, dipolar interactions were neglected because it contributes only a few Gauss to the ΔH of the ESR signal [173]. So that the other two factors only contribute to the ΔH which are led by J-T distortion.

The strength of the CO state depends on the average size of the A-site cations. The manganites for which $<r_A>$ is relatively small exhibit insulating properties with a stable CO ground state. The smaller $<r_A>$ results in the decrease of Mn-O-Mn bond angle, as a result, cooperative J-T distortion increases, which favors the CO phenomenon [49, 201, 202]. The $6s^2$ lone pair electrons of Bi^{3+} ions not only couple with O:$2p_\sigma$ orbitals but also compete directly for the O:$2p_\pi$ electrons with the Mn:t_{2g} orbitals. Due to the hybridization between the 6s lone pair of Bi^{3+} ions and O:$2p_\pi$ electrons, the movement of e_g electrons decrease between the Mn ions and favors the charge ordering phenomena [203, 204].

3.3.3. Magnetization studies

3.3.3.1. Temperature dependent magnetization

Fig. 3.12 shows magnetization (M) as a function of the temperature of the samples. For the samples with $0.40 \leq x \leq 0.80$, M vs T plots show similar trends, i.e., as the temperature decreases from 350 K, both zero-field cooled (ZFC) and field cooled (FC) curves show a peak at T_{CO}. With the further decrease in temperature, M decreases slightly. A broad maximum at ~150 K, representing the long-range AFM order, is observed for samples with $x \leq 0.60$. A sharp rise in M for the samples with $x \leq 0.60$ at ~50 K and with $x \geq 0.65$ at ~115 K is observed. This is related to the cluster glass (CG) behavior. Below this temperature, for all

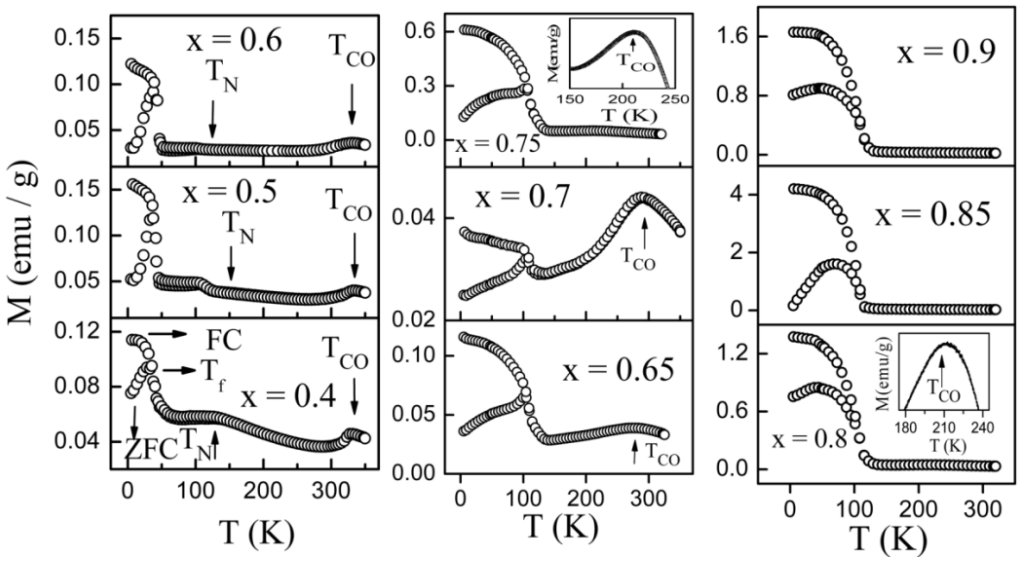

Fig. 3.12. *M* vs *T* plots of $Bi_{1-x}Ca_xMnO_3$samples measured in a static field of 500 Oe.

the samples, *M* in ZFC (M_{ZFC}) mode shows a peak at a temperature called the spin freezing temperature (T_f) [52], whereas *M* in FC (M_{FC}) mode increases continuously with decreasing temperature. For $Bi_{0.125}Ca_{0.875}MnO_3$ sample, a sharp increase in *M* as a function of temperature has been reported, which is due to the formation of FM clusters in the AFM background when the temperature decreases below T_C (~108 K) [90]. This is characteristic of SG behavior, which arises as a result of competition between FM interaction in $BiMnO_3$-type clusters and AFM coupling in clusters in which Mn^{3+} orbits which are frozen in random orientations [87]. However, nonlinear susceptibility and neutron scattering results alone can give the exact nature of the system. Neutron scattering studies on $Bi_{0.67}Ca_{0.33}MnO_3$ support the concept of appearance of SG behavior [96]. Freezing is a cooperative phenomenon where spin or clusters are frustrated due to the evolution of random competing FM and AFM interactions [124]. A small peak in *M* at ~120 K is also observed for sample with $x = 0.50$ which is ascribed to the field-induced spin canting in the AFM phase aided by the spontaneous

canting moment [8, 205, 206]. A bifurcation between M_{ZFC} and M_{FC} curves is observed with lowering of the temperature, similar to other FM manganites [1]. The PM-FM transition may coexist with the PM-FM like canted antiferromagnetic (C-AFM) transition for samples with $0.50 \leq x \leq 0.80$. It has been pointed out that C-AFM state arises due to self-doping effects resulting in strong competition between FM and AFM states [207, 208].

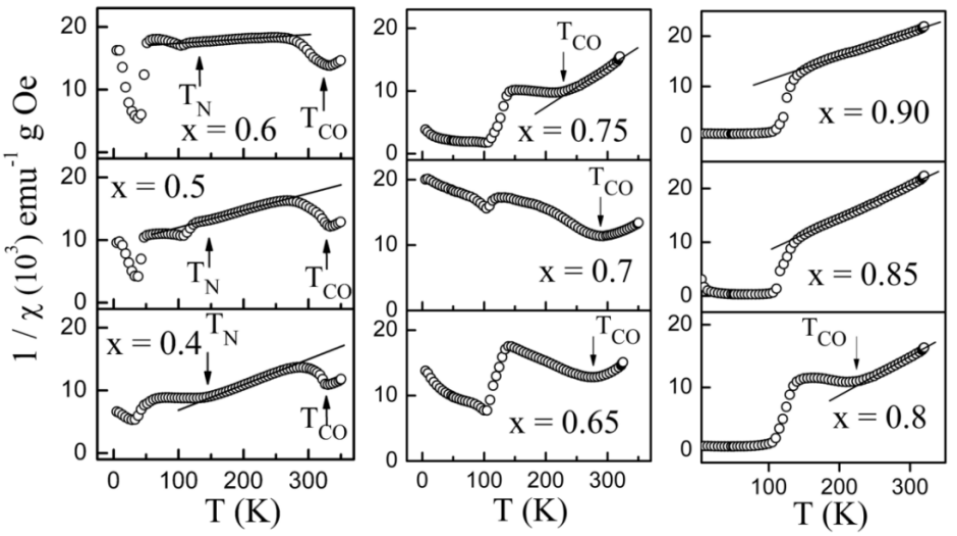

Fig. 3.13. $1/\chi$ vs T plots for M_{ZFC} curves (measured in a static magnetic field of 500 Oe) of $Bi_{1-x}Ca_xMnO_3$ samples.

Using Curie-Weiss law, given by the equation

$$\chi = C/T - \theta_C \tag{3.8}$$

straight line fits are drawn for the inverse susceptibility ($1/\chi$) vs T plots (for M_{ZFC}) of the samples in the temperature range $T > T_{CO}$ and $T_N < T < T_{CO}$, shown in Fig. 3.13.

In equation (3.8) the Curie constant, C, is given by the expression

$$C = N\mu_{eff}^2 / 3k_B \tag{3.9}$$

where N (6.023×10^{23} molecule/mole) is the Avogadro number and k_B (1.381×10^{-23} J/K) is the Boltzmann constant. Here the total effective magnetic moment, μ_{eff}, neglecting spin-orbit coupling can be written as

$$\mu_{eff} = g\mu_B[xS_1(S_1+1)+(1-x)S_2(S_2+1)]^{1/2} \tag{3.10}$$

where g is the Lande g- factor, μ_B (9.274×10^{-24} J/T) is the Bohr magneton and S_1= 3/2 and S_2 = 2 for Mn^{4+} and Mn^{3+}, respectively [209].

From the linear fit, the estimated values of θ_C (for a few samples θ_C is estimated by drawing tangents (not shown) in Fig. 3.13) for $T > T_{CO}$ are listed in table 3.2. The value of θ_C is positive for samples with $0.40 \leq x \leq 0.80$ and decreases with increasing Ca content, indicating the decrease in FM interactions. Below T_{CO} a large negative value of θ_C for x = 0.40, 0.50 and 0.60 samples is observed. For samples with $0.65 \leq x \leq 0.80$, the upward trend in $1/\chi$ vs T plots indicating AFM ordering. For samples with x = 0.85 and 0.90 straight line fits are obtained above 150 K with the negative sign of θ_C indicating the domination of AFM interactions. For the sample with x = 0.50 an upward deviation is replaced by a downward trend at ~120 K indicating a PM to C-AFM transition. This transition becomes stronger for sample with $x \geq 0.65$. For the sample with x = 0.85 and 0.90 only a PM to C- AFM transition is observed. Similar results are reported for x = 0.85 [88] and $CaMnO_3$ [205]. Nuclear magnetic resonance studies on $Bi_{0.125}Ca_{0.875}MnO_3$ and $CaMnO_3$ also suggest canted spin states in these materials [95]. It has also been reported that the samples with $x \geq 0.75$ present a phase segregation coinciding with the electronic localization of the e_g electrons [88]. The presence of phase segregation might be due to different thermal

evolutions of the heterogeneous material [78]. The estimated experimental values for the effective magnetic moment are higher than the theoretical values (table 3.2). This has been observed in other manganites as well and is attributed to the formation of magnetic polarons [207, 210].

3.3.3.2. Magnetic field dependent magnetization

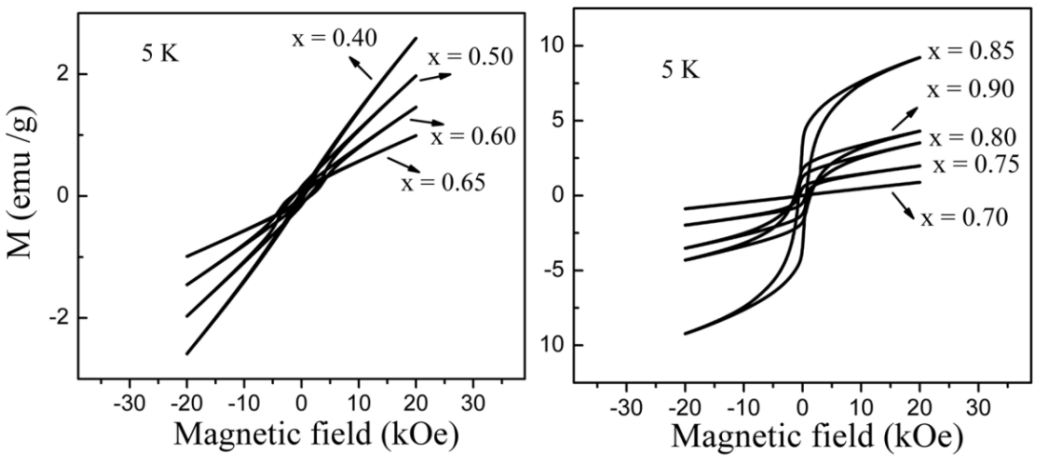

Fig. 3.14. *M* vs Magnetic field (*H*) plots of $Bi_{1-x}Ca_xMnO_3$ samples measured at 5 K.

In order to correlate the bifurcation between M_{ZFC} and M_{FC} curves of *M* vs *T* plots, magnetic field (*H*) dependent magnetization measurements were performed. Fig. 3.14 shows the hysteresis (*M-H*) loops of all the samples measured under the applied maximum magnetic field of 20 kOe at a constant temperature 5 K. Ferromagnetism persists in all samples as it is evidenced from the hysteresis loops. As the calcium content increases this behavior becomes prominent. The absence of saturation in the applied field of 20 kOe indicates the coexistence of FM and AFM phases in the system.

3.3.4. Phase diagram of $Bi_{1-x}Ca_xMnO_3$ system

Fig. 3.15 shows T_{CO} and T_N values of $Bi_{1-x}Ca_xMnO_3$ ($0.30 \leq x \leq 0.90$) (T_{CO} and T_N values of $x = 0.30$ sample are taken from chapter 6) system obtained from the present ESR and magnetization data. For $0.30 \leq x \leq 0.60$ the estimated T_{CO} values

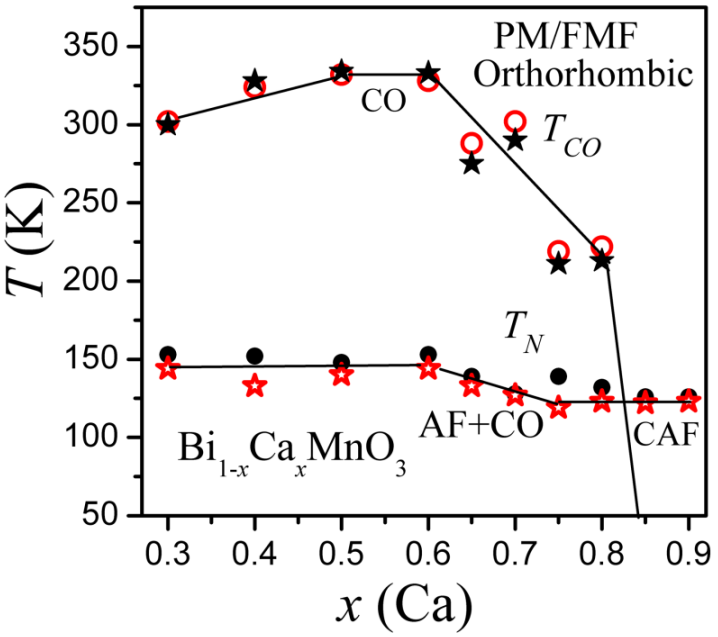

Fig. 3.15. Phase diagram of $Bi_{1-x}Ca_xMnO_3$ system based on the present data. Open circles (T_{CO}) and closed circles (T_N) are from ESR data and closed stars (T_{CO}) and open stars (T_N) from magnetization data. The PM, FMF, CO, AF and CAF indicate paramagnetic state, ferromagnetic fluctuations, charge ordered state, antiferromagnetic state and canted-antiferromagnetic state, respectively.

are similar to the earlier reports for bulk samples. Whereas, for samples with $0.65 \leq x \leq 0.80$ the values are lower than that obtained for bulk samples. Since the present series of samples are synthesized by sol-gel method, T_{CO} might be affected by the reduction in the grain size. In this phase diagram the co-existence of various phases, which have already discussed, are also shown.

3.3.5. Transport studies

Fig. 3.16 depicts ρ vs T plots for various samples. As the temperature decreases the exponential increase of ρ indicates the activated electronic transport nature of the samples. At room temperature the value of ρ of the samples is in the range 0.50-20 Ω cm and it reaches to ~10^6 Ω cm at ~70 K. This is the typical signature of a semiconducting material, which is also observed in other manganites. Charge localization is responsible for the observed semiconducting nature in the manganites [7, 19].

Three models have been proposed to understand the observed resistivity behavior in manganites. The first one is the charge localization due to small-polaron formation as a result of strong electron-lattice interaction which arises from the J-T distortion, the second one is the variable range hopping (VRH) model and the third one is Efros and Shklovskii-VRH (ES-VRH) model.

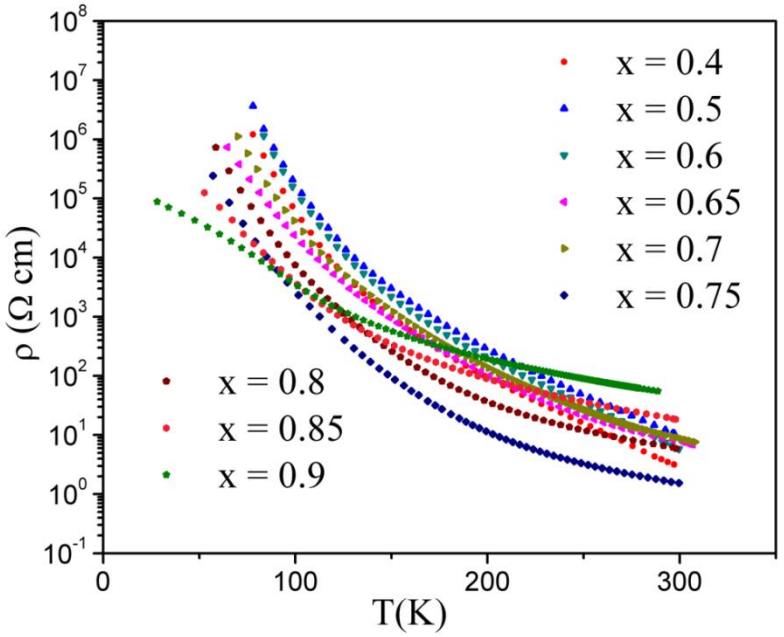

Fig. 3.16. ρ vs T plots of $Bi_{1-x}Ca_xMnO_3$ samples.

According to the small-polaron hopping (SPH) model the expression for ρ is given by the relation

$$\rho = \rho_0 T^n \exp(E_p / k_B T) \tag{3.11}$$

where n = 1 for adiabatic and n = 1.5 for non-adiabatic conduction mechanism. E_p (or E_a) is the activation energy of carriers and k_B is the Boltzmann constant. The expression for E_p is given by the relation

$$E_p = W_H + W_D / 2 \qquad T > \theta_D/2 \tag{3.12}$$

where W_H is the polaron hopping energy, W_D is the disorder energy and θ_D is the Debye temperature [7, 19, 29].

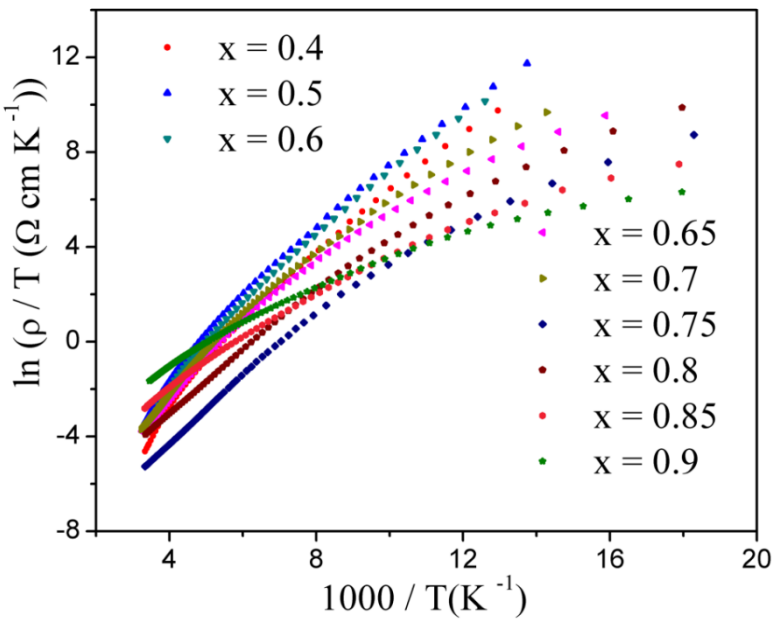

Fig. 3.17. ln(ρ/T) vs 1000/T plots of $Bi_{1-x}Ca_xMnO_3$ samples.

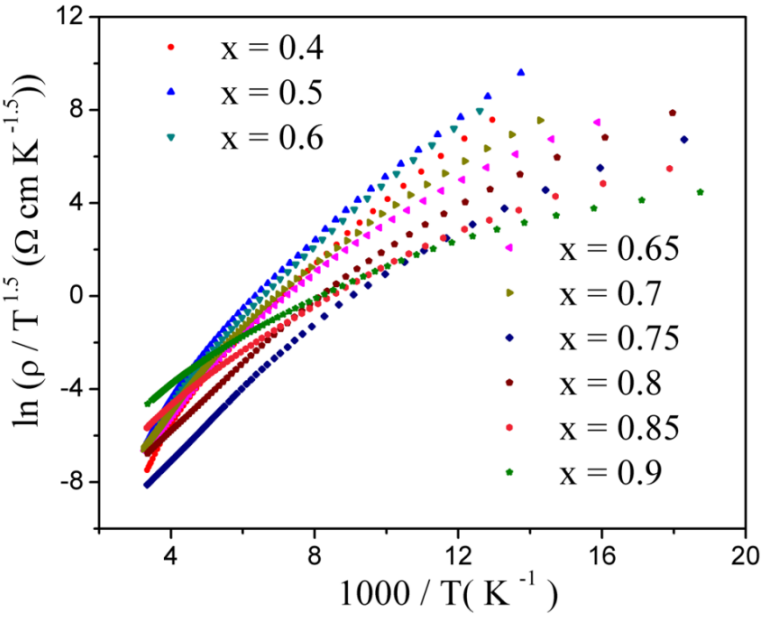

Fig. 3.18. $\ln(\rho/T^{1.5})$ vs $1000/T$ plots of $Bi_{1-x}Ca_xMnO_3$ samples.

According to equation (3.11), $\ln(\rho/T)$ vs $1000/T$ and $\ln(\rho/T^{1.5})$ vs $1000/T$ plots should follow a linear trend. However, these plots (Fig. 3.17 and Fig. 3.18) show a continuous curvature for all samples, which indicates that the SPH model is not useful for analyzing the data of the present series of samples.

Mott's [211] VRH model has been extensively used to analyze the temperature dependence of resistivity data, given by the equation

$$\rho = \rho_0 \exp\{2.06[\alpha^3 / N(E_F)k_B T]^{1/4}\} \qquad (3.13)$$

with

$$k_B T_0 = 18\alpha^3 / N(E_F) \qquad (3.14)$$

where $N(E_F)$ is the density of states at the Fermi level, T_0 is the characteristic temperature and α is the inverse of correlation length (ξ). In the VRH model, $N(E_F)$ near the Fermi level is assumed to be a constant.

At room temperature, the average hopping distance (R) and energy (W) are given by

$$R^4 = 9/8\pi\alpha k_B T N(E_F) \tag{3.15}$$

and

$$W = 3/4\pi R^3 N(E_F) \tag{3.16}$$

respectively.

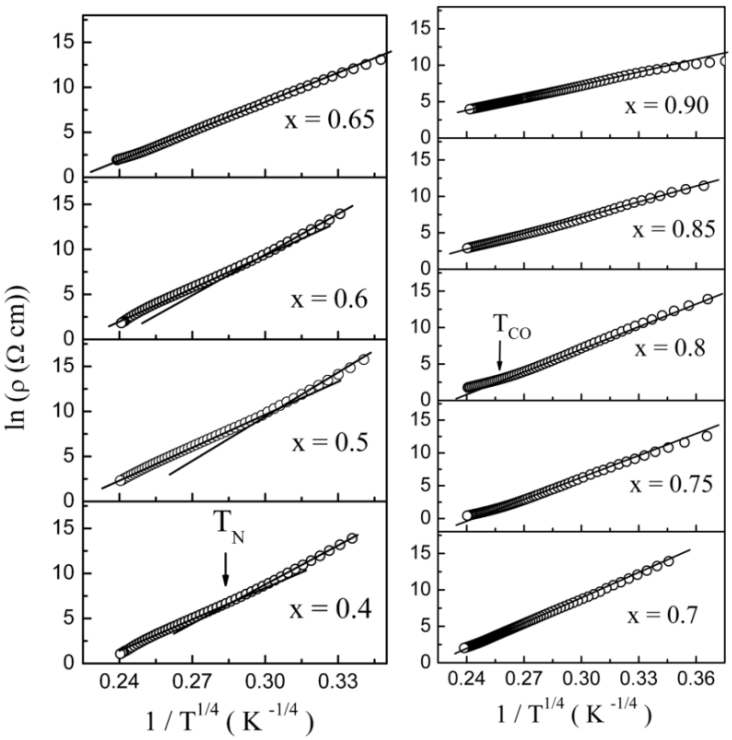

Fig. 3.19. lnρ vs $1/T^{1/4}$ plots of $Bi_{1-x}Ca_xMnO_3$ samples.

Table 3.3. List of the various parameters (T_0 and ρ_0) estimated from VRH model of $Bi_{1-x}Ca_xMnO_3$ samples.

Sample (x)	T_0 (10^8 K)		ρ_0 (10^{-13} Ω cm)	
	$T_{CO} > T > T_N$	$T < T_N$	$T_{CO} > T > T_N$	$T < T_N$
0.40	0.836	1.42	2.622	0.0112
0.50	0.839	1.76	0.947	0.0004
0.60	0.814	1.42	7.091	0.0263

Table 3.4. List of the various parameters (ξ, R and W) estimated from VRH model of $Bi_{1-x}Ca_xMnO_3$ samples.

Sample (x)	ξ (Å)		R (nm)		W (ev)	
	$T_{CO} > T > T_N$	$T < T_N$	$T_{CO} > T > T_N$	$T < T_N$	$T_{CO} > T > T_N$	$T < T_N$
0.40	6.52	5.46	5.62	5.38	0.149	0.170
0.50	6.51	5.08	5.62	5.28	0.149	0.179
0.60	6.57	5.47	5.64	5.38	0.148	0.170

Table 3.5. List of the various parameters (T_0, ρ_0, ξ, R and W) estimated from VRH model ($T < T_{CO}$) of $Bi_{1-x}Ca_xMnO_3$ samples.

Sample (x)	T_0 (10^8 K)	ρ_0 (10^{-13} Ω cm)	ξ (Å)	R (nm)	W (ev)
0.65	0.433	509	8.11	5.94	0.126
0.70	0.527	155	7.60	5.84	0.133
0.75	0.492	20	7.78	5.88	0.130
0.80	0.467	80	7.91	5.90	0.139
0.85	0.062	2.7E7	15.69	7.00	0.077
0.90	0.033	6.3E8	19.08	7.36	0.066

Fig. 3.19 depicts $\ln(\rho)$ vs $1/T^{1/4}$ plots for all the samples in the temperature range 70-300 K. For the samples with $0.40 \leq x \leq 0.60$ two linear trends are observed: one in the temperature range $T_{CO} > T > T_N$ and the other below T_N. For $x \geq 0.65$ data follows a linear trend with a single value of slope below T_{CO}. Various parameters estimated by taking $N(E_F)$ ~3 x10^{18} $cm^{-3}eV^{-1}$, are listed in tables 3.3, 3.4 and 3.5. The correlation length of the present series of samples is greater than the Mn-Mn distance (~5 Å) and the hopping distance (R) which is several times

than the Mn-Mn distance. Hence, the present results are in good agreement with the predicted values, indicating the validity of VRH model [7, 19, 211].

According to ES-VRH [212] model, in which electron-electron Coulomb interaction is considered, the T dependence of ρ can be written as

$$\rho = \rho_0 \exp(T_0 / T)^{1/2} \tag{3.17}$$

with

$$k_B T_0 = e^2 / K\xi \tag{3.18}$$

where K is the dielectric constant. Fig. 3.20 depicts ln(ρ) vs $1/T^{1/2}$ plots for all the samples in the temperature range 70-300 K. All the samples show linear behavior for temperatures below T_{CO}. Various physical parameters have been estimated

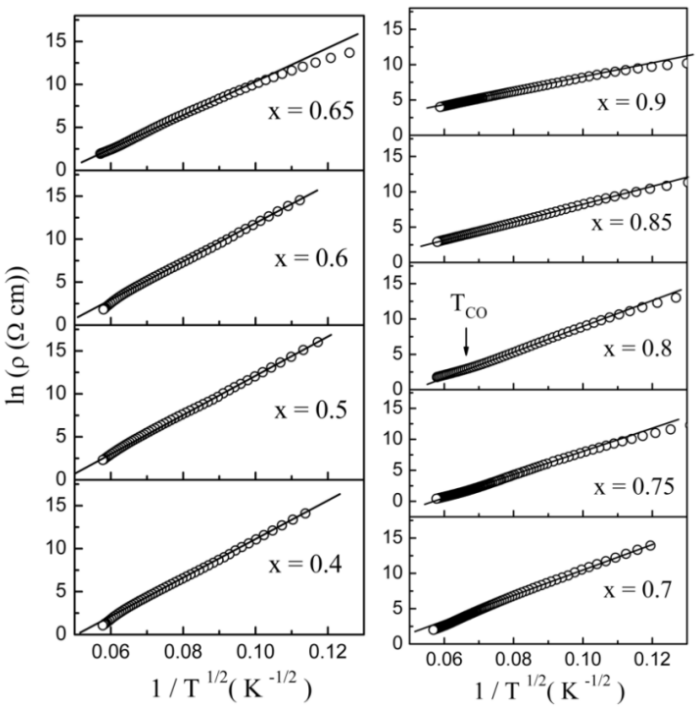

Fig. 3.20. ln(ρ) vs $1/T^{1/2}$ plots of $Bi_{1-x}Ca_xMnO_3$ samples.

Table 3.6. List of the various parameters (T_0, ρ_0 and ξ) of $Bi_{1-x}Ca_xMnO_3$ samples estimated from ES-VRH model.

Sample (x)	T_0 (10^4 K)	ρ_0 (10^{-5} Ω cm)	ξ (Å)
0.40	4.96	1.29	5.79
0.50	5.39	0.24	5.38
0.60	4.27	7.48	6.73
0.65	3.03	62.04	9.41
0.70	3.45	31.91	8.32
0.75	3.25	3.98	8.84
0.80	3.21	12.21	8.95
0.85	1.62	1046.20	17.70
0.90	0.98	17622.38	29.30

(table 3.6), taking K~500. The ρ_0 values of the present system are much lower than the theoretical values predicted by Mott [211], indicating that the present series of samples do not follow the ES-VRH model.

Resistivity increases with increasing Ca content from x = 0.40 to 0.50, then it decreases in the composition range $0.50 < x \leq 0.75$ and again increases up to x = 0.90. Chiba et al. [89] have reported the increase in the resistivity for the samples with $x \geq 0.875$. However, for few samples a cross over in ρ is observed below ~150 K. The samples with $x \leq 0.60$ have higher values of ρ compared to that of the other samples. This, presumably, is due to the distortion arising from the A-site disorder as well as due to the $6s^2$ lone pair electrons of Bi^{3+} ions. The ρ data can be nicely interpreted taking into consideration of the structural parameters estimated from the refinement of the XRD data. Due to the local distortion the Mn-O-Mn bond angle decreases as a result of which the Mn-O bond length increases and hence bandwidth becomes narrow. Probably, this would block the movement of e_g electrons between the Mn ions, favoring the localization of charge carriers. The large splitting among the lattice parameters of these samples also supports these findings. The higher value of ρ (at room temperature) for the sample with x = 0.50 could be due to the increased local distortion, which is

confirmed from its measured higher value of σ^2, which describes the A-site disorder and lower value of the Mn-O-Mn bond angle. For the samples with $0.50 < x \leq 0.75$, the Mn-O-Mn bond angle is increased with increasing Ca content and the sample with $x = 0.75$ shows lowest ρ (in the 100 K< T < 300 K range) for which Mn-O-Mn bond angle has the highest value. This could be due to the weakening of the strength of the $6s^2$ lone pair electrons of Bi^{3+} ions with increasing Ca content. In M vs T plots, the shift in FM-CG state towards higher temperature from ~45 K for the samples with $x \leq 0.60$ to 115 K for the samples with $x \geq 0.65$ is also associated to the decrease in disorder. The rise in ρ, when the system is approaching $CaMnO_3$ in which doped carriers disappear, could be related to the crossover to an insulating behavior [8], which is confirmed from the decreased Mn-O-Mn bond angles. For all the samples, the sharp increase in ρ in the temperature range ~120-150 K is characteristic of the AFM nature. In the AFM state the neighboring spins align antiparallel, whereas in the PM state the alignment of spins is random, as a result of which the hopping of carriers in the AFM state becomes difficult compared to that in the PM state, due to this, the values of T_0 and W increase below T_N.

3.4. Conclusions

In conclusion, we have studied the effect of Ca-doping on the properties of $Bi_{1-x}Ca_xMnO_3$ ($0.40 \leq x \leq 0.90$) samples synthesized by sol-gel method. The structural studies on these samples confirm the single phase orthorhombic nature with *Pnma* space group. The estimated values of charge ordering temperature (T_{CO}) and long range antiferromagnetic (AFM) ordering temperature, i.e., Néel temperature (T_N) are used to construct the magnetic phase diagram of the system. The growth of ferromagnetic (FM) like canted-antiferromagnetic (C-AFM) state at ~ 120 K starts at $x = 0.50$. The paramagnetic (PM) to AFM transition at

~150 K co-exists with PM to C-AFM transition at ~120 K for samples with 0.50 $\leq x \leq$ 0.80. Whereas for samples with x = 0.85 and 0.90 only PM to C-AFM transition is observed. Resistivity data analyses reveal the semiconducting behavior of all the samples.

This page is intentionally left blank

Chapter 4

Effect of Pr doping on the properties of $Bi_{0.5-x}Pr_xCa_{0.5}MnO_3$ ($0.0 \leq x \leq 0.50$) manganites

4.1. Introduction

The half doped manganites have always attracted more interest due to the interesting physics they offer. In these systems the Mn-site is equally occupied by Mn^{3+} ($3d^4: t_{2g}^3 e_g^1$), and Mn^{4+} ($3d^3: t_{2g}^3 e_g^0$) ions. The bulk $Pr_{0.5}Ca_{0.5}MnO_3$ system shows a sharp charge ordered (CO) peak at 250 K and a CE-type antiferromagnetic (AFM) transition at 170 K and reentrant spin glass (RSG) state below 40 K due to the competition between ferromagnetic (FM) and AFM interactions [16, 80]. The half doped $Bi_{0.5}Ca_{0.5}MnO_3$ manganite exhibits C-type AFM structure below ~120 K. Although both are CO systems, they exhibit quite different magnetic properties as a function of temperature. In the present work, we have carried out a detailed study of the effect of Pr-doping at Bi-site on the physical properties of $Bi_{0.5-x}Pr_xCa_{0.5}MnO_3$ (x = 0.0, 0.05, 0.10, 0.15, 0.20, 0.30, 0.40 and 0.50) manganites. The variation in structure and physical properties with Pr-doping is discussed in view of changes in $6s^2$ lone pair character of Bi^{3+}ions and disorder in the system.

4.2. Sample preparation

The stoichiometric amounts of pure $Bi(NO_3)_3.6H_2O$, $Pr(NO3)_3.6H_2O$, $Ca(NO_3)_2.4H_2O$ and $MnCl_2.4H_2O$ were dissolved in distilled water to obtain the clear solution. Citric acid was added with constant stirring and the ratio of metal

cation to citric acid was fixed to 1:2. The pH of the solution was adjusted to ~ 6-7 by adding ammonia solution. Ethylene-glycol was added to this to get a viscous solution. The solution was slowly evaporated to get a gel by keeping the temperature at ~ 60-70 ^{o}C with constant stirring for several hours (hrs). The gel was decomposed at 250 ^{o}C. Then the resultant powder was sintered at 900 ^{o}C in the furnace for 10 hrs. Then, at the end, the powder was pressed into pellets and again sintered for 10 hrs.

4.3. Results and discussion

4.3.1. Structure and morphology studies

Fig. 4.1 depicts the Rietveld refinement of x-ray diffraction (XRD) data of $Bi_{0.5-x}Pr_xCa_{0.5}MnO_3$ ($0.0 \leq x \leq 0.50$) manganite samples. Using refinement, XRD data is well described by the orthorhombic structure with *Pnma* space group. From the Rietveld refinement the estimated values of various structural parameters, namely atomic positions (x, y and z), the average Mn-O bond length ($<d_{Mn-O}>$), the average bond Mn-O-Mn angle (<Mn-O-Mn>) and the goodness of fit (S) are listed in table 4.1. The average ionic size of the A-site cations ($<r_A>$), variance of the A-site cation size distribution (σ^2) [using equation (1.2)] and tolerance factor (t) [using equation (1.1)] of various samples are also obtained (table 4.1). Using the structure parameters, the crystal structure of $Bi_{0.20}Pr_{0.30}Ca_{0.50}MnO_3$, representative of the whole series, is generated as shown in Fig. 4.2. Fig. 4.3 shows the variation in the lattice parameters (a, b and c) and the unit cell volume (V) (inset of Fig. 4.3) as a function of x (Pr content), estimated from the refinement of XRD data. The large splitting among the lattice parameters of the undoped (x = 0.0) sample is a typical feature of CO phase with strong Jahn-Teller (J-T) distortion [170]. The lattice parameters of the samples with $0.0 \leq x \leq 0.20$ obey the rule $b/\sqrt{2} \leq c \leq a$, which is characteristic of O´-type

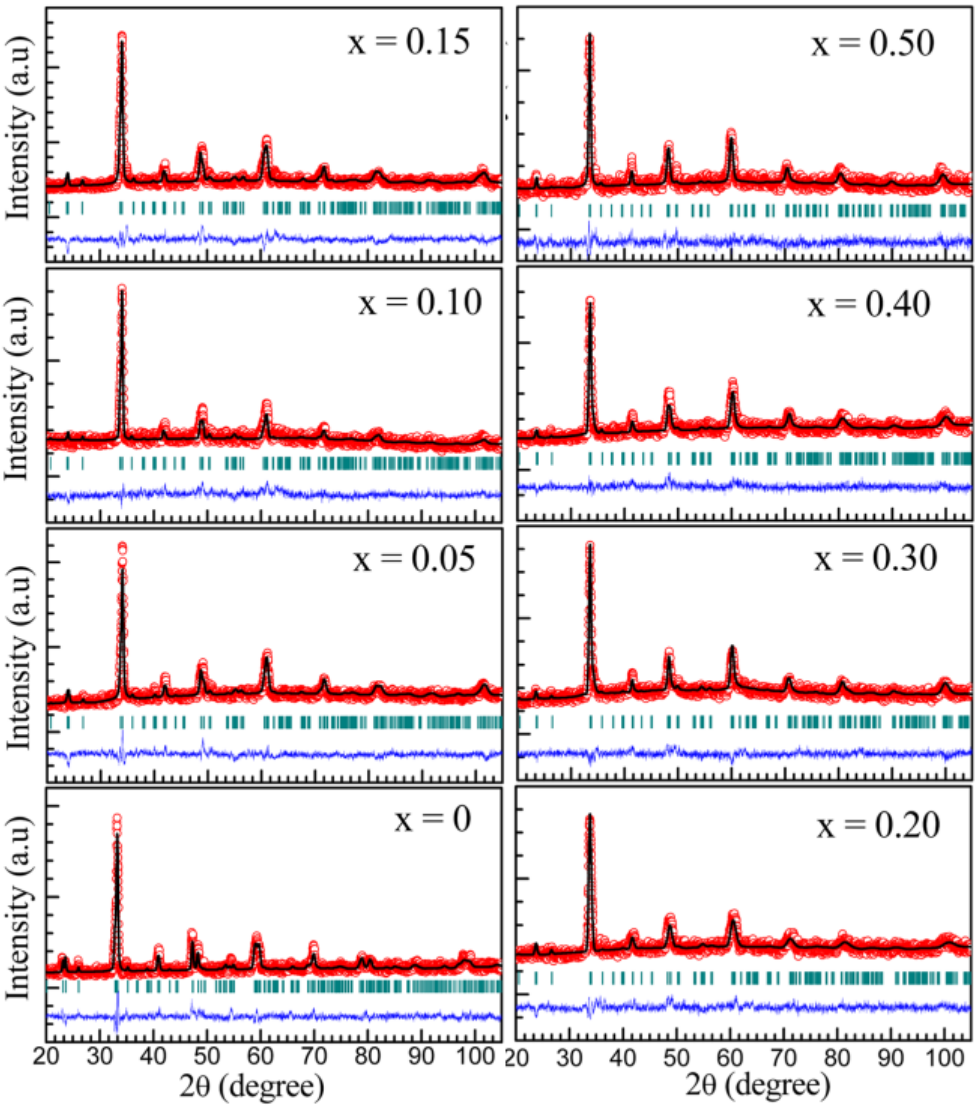

Fig. 4.1. Rietveld refinement (solid black lines) of the XRD data of $Bi_{0.5-x}Pr_xCa_{0.5}MnO_3$ samples (open red circles) along with diffraction planes (green lines) and difference between the experimental and fitting data (blue lines).

distorted perovskite structure, whereas the lattice parameters of the samples with $0.30 \leq x \leq 0.50$ obey the rule $b/\sqrt{2} \leq a \leq c$, which is characteristic of O´´-type distorted perovskite structure of manganites. The combination of octahedral tilting and a cooperative J-T distortion produce O´-type of distortion [168]. With the

Table 4.1. List of the structural parameters [atomic positions (x, y and z), *S*, $<d_{Mn-O}>$ and <Mn-O-Mn>] estimated from the refinement of the XRD data of $Bi_{0.5-x}Pr_xCa_{0.5}MnO_3$ samples. The calculated values of $<r_A>$, σ^2 and *t* are also listed in table. The average GS (GS) values, estimated from FESEM images, are also listed in table.

Sample (*x*)	**0.0**	**0.05**	**0.10**	**0.15**	**0.20**	**0.30**	**0.40**	**0.50**
Bi/Pr/Ca								
x	0.039	0.030	0.036	0.021	0.024	0.026	0.024	0.021
y	0.250	0.250	0.250	0.250	0.250	0.250	0.250	0.250
z	0.989	0.983	0.989	0.982	0.995	0.990	0.994	0.999
Mn								
x	0.500	0.500	0.500	0.500	0.500	0.500	0.500	0.500
y	0.500	0.500	0.500	0.500	0.500	0.500	0.500	0.500
z	0	0	0	0	0	0	0	0
O (1)								
x	0.491	0.510	0.498	0.491	0.531	0.544	0.514	0.526
y	0.250	0.250	0.250	0.250	0.250	0.250	0.250	0.250
z	0.052	0.048	0.068	0.065	0.042	0.058	0.053	0.073
O (2)								
x	0.228	0.172	0.265	0.203	0.234	0.307	0.313	0.316
y	0.534	0.521	0.544	0.523	0.540	0.472	0.476	0.446
z	0.214	0.274	0.260	0.267	0.275	0.227	0.283	0.227
S	2.46	1.69	1.75	1.86	1.79	1.22	1.16	1.36
$<d_{Mn-O}>$ (Å)	1.935	1.939	1.9058	1.883	1.893	1.905	1.917	1.940
<Mn-O-Mn>(°)	161.34	156.40	158.865	158.82	159.69	160.81	158.79	154.09
$<r_A>$ (Å)	1.2100	1.1754	1.1759	1.1763	1.1768	1.1777	1.1786	1.1795
σ^2 (x10^{-4}) (Å^2)	9.000	0.243	0.232	0.218	0.199	0.150	0.084	0.002
t	0.9276	0.9154	0.9156	0.9157	0.9159	0.9162	0.9165	0.9169
GS (nm)	405	249	213	190	200	238	141	157

increase in Pr content from $x = 0.0$ to 0.05, a large decrease in unit cell volume is observed. For samples with $0.05 < x \leq 0.50$, the unit cell volume increases steadily with the increase in Pr content. The effective ionic size of Bi^{3+} is 1.170 or 1.24 Å depending on whether the $6s^2$ lone pair character is constrained or dominant, respectively [213, 214]. In the present system the higher cell volume of the undoped sample can be due to the strengthened dominant $6s^2$ lone pair

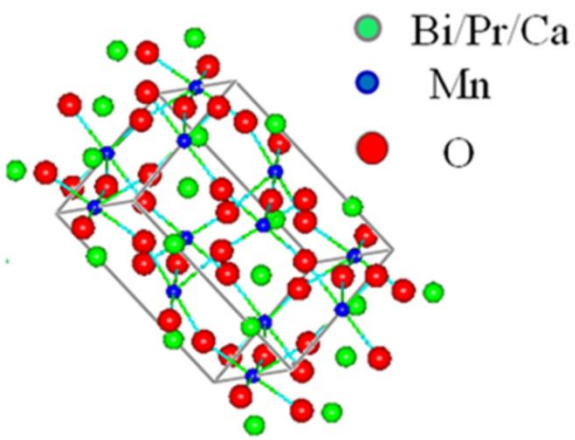

Fig. 4.2. Crystal structure of $Bi_{0.20}Pr_{0.30}Ca_{0.50}MnO_3$ sample.

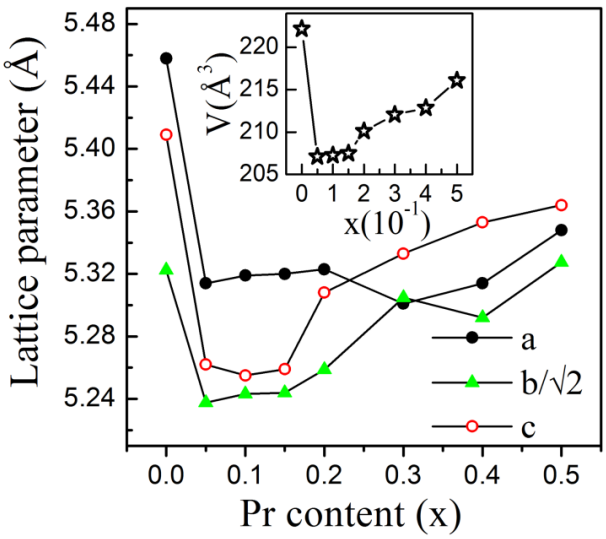

Fig. 4.3. Lattice parameter (*a*, *b* and *c*) vs *x* (Pr content) of $Bi_{0.5-x}Pr_xCa_{0.5}MnO_3$ samples. Inset shows the variation of unit cell volume (*V*) as a function of *x*.

character of Bi^{3+} ions. The sharp drop in the cell volume of the sample with x = 0.05 indicates that the constrained effect of the $6s^2$ lone pair becomes strong due to Pr-doping. The constrained effect of lone pair maintains the ionic size of Bi^{3+} ion at 1.170 Å, which is smaller than that of the Pr^{3+} ion (1.179 Å). As a result,

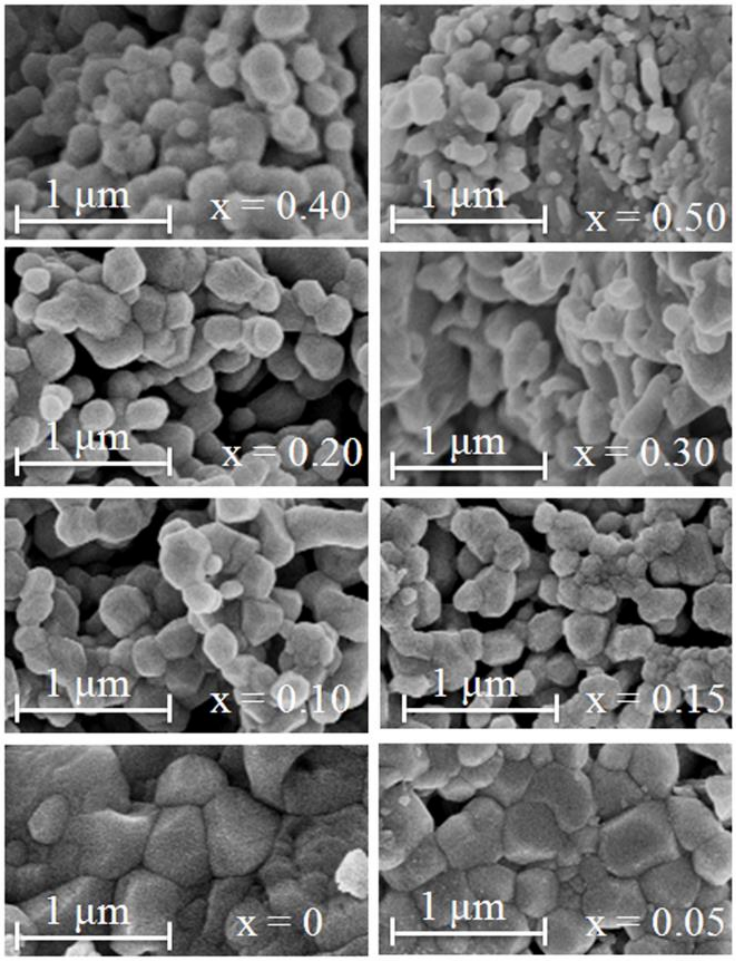

Fig. 4.4. Microstructure of $Bi_{0.5-x}Pr_xCa_{0.5}MnO_3$ samples.

the cell volume increases for samples with $x > 0.05$. A similar trend is reported in La, Pr-doped Bi-manganites [17, 213]. Similarly the value of $<r_A>$ and t decreases from $x = 0.0$ to 0.05, and for $x > 0.05$ increases with increase in x, whereas the value of σ^2 decreases with increase in the value of x. The average Mn-O-Mn bond angle values of the samples in the composition range $0.05 < x < 0.40$ show a slight increasing trend with the increase in the value of $<r_A>$. However, though the value of $<r_A>$ is increased with further increase in x, decrement in the value of the average Mn-O-Mn bond angle is observed.

The field emission scanning electron microscopy (FESEM) micrographs for various samples are shown in Fig. 4.4. As the Pr content increases, the average grain size (GS) of the samples (table 4.1) decreases and the grains become more regular shaped with well-defined boundaries. The energy dispersive x-ray spectroscopy (EDX) results confirm the purity of the samples.

4.3.2. Electron spin resonance studies

The electron spin resonance (ESR) spectra for all the samples, at some selected temperatures, are shown in Fig. 4.5. The spectra consist of a resonance line which could be fitted to Lorentzian line shape [equation (3.1)] in the entire measured temperature range. The Lorentzian line shape fitting curves to the ESR

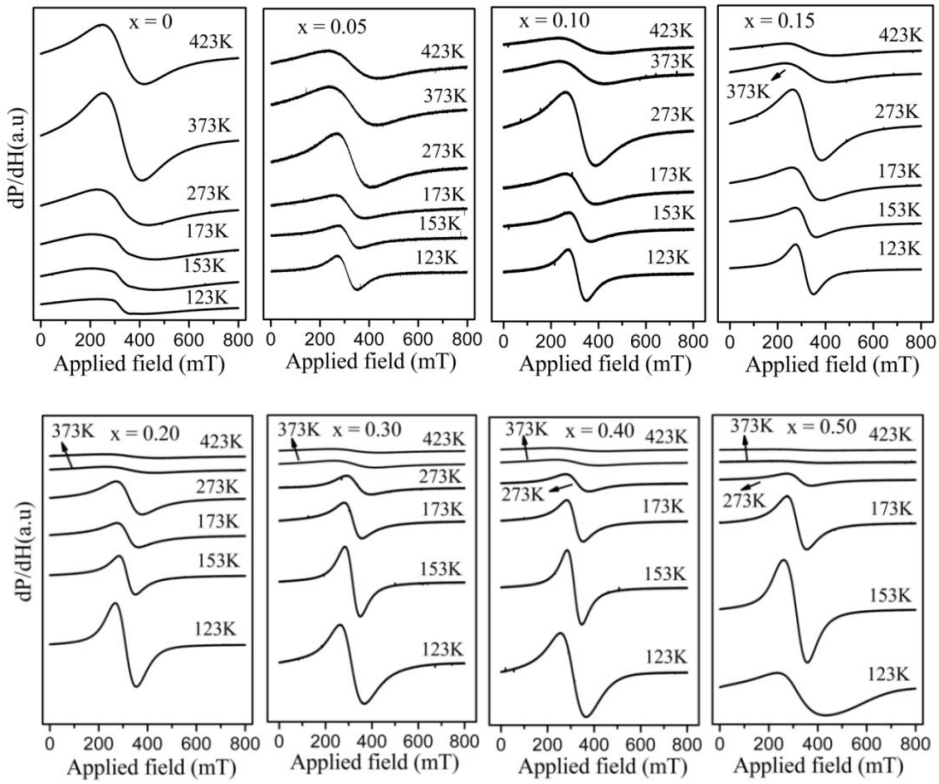

Fig. 4.5. ESR spectra of $Bi_{0.5-x}Pr_xCa_{0.5}MnO_3$ samples measured at various temperatures.

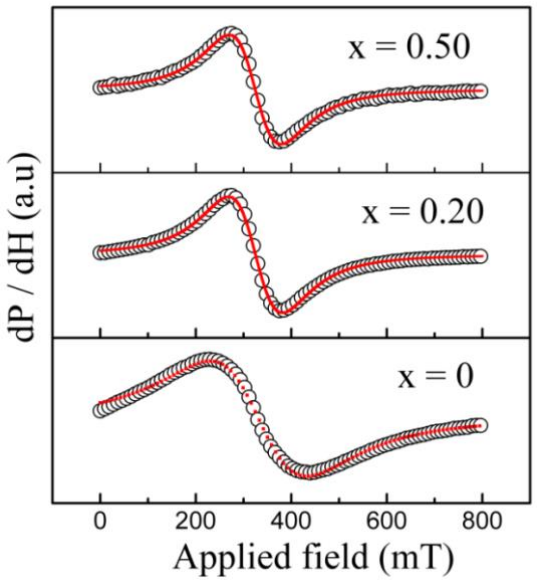

Fig. 4.6. Lorentzian fit (solid red line) to the ESR spectra (open circles) of $Bi_{0.5-x}Pr_xCa_{0.5}MnO_3$ samples measured at 273 K.

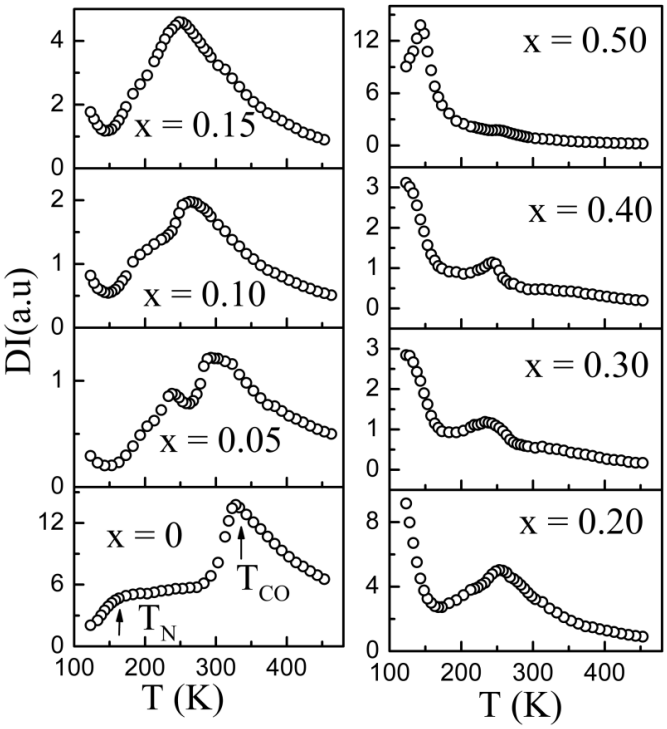

Fig. 4.7. *DI* vs *T* plots of $Bi_{0.5-x}Pr_xCa_{0.5}MnO_3$ samples

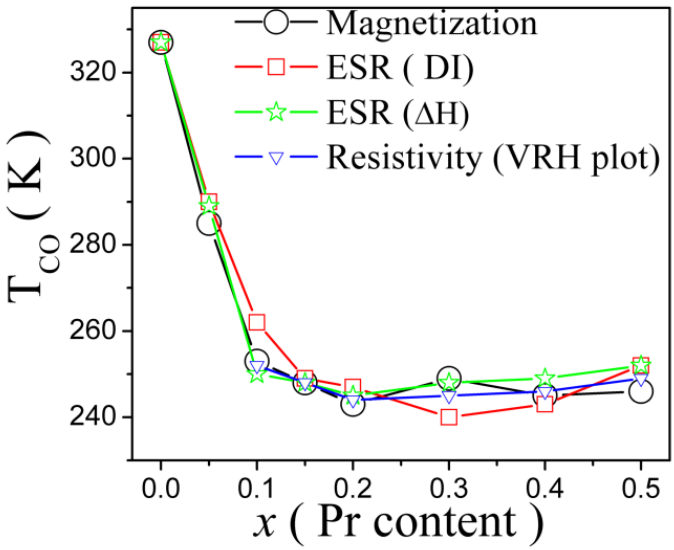

Fig. 4.8. T_{CO} vs x of $Bi_{0.5-x}Pr_xCa_{0.5}MnO_3$ samples.

spectra of x = 0.0, 0.20 and 0.50 samples, measured at 273 K, are shown in Fig. 4.6. The normalized double integrated intensity (*DI*) as a function of temperature for all the samples is shown in Fig. 4.7. For all the samples, as the temperature decreases from high-temperature (453 K), *DI* increases and reaches its maximum value at charge ordering temperature (T_{CO}) [7, 9, 104, 215, 216]. T_{CO} decreases (Fig. 4.8) as x increases from 0.0 to 0.20 and becomes independent of doping content with further increase in x. The peak observed at T_{CO} become broader with the increase in Pr content. For samples with $x \geq 0.20$, the decreasing behavior of *DI* on either side of T_{CO} is not as sharp as that observed for samples with $x \leq 0.15$. For sample with x = 0.0, *DI* becomes constant in the temperature range 280-180 K with the decrease in temperature due to orbital ordering [7, 104]. A sharp decrease in *DI* can be due to long-range AFM ordering. This temperature is taken as Neel temperature (T_N) [7, 104, 215, 216]. For x = 0.0 sample, the estimated value of T_N is around 150 K and it increases with Pr-doping. The shift in T_N with Pr-doping could be due to the enhancement of FM cluster size embedded in the long-range

AFM matrix. For x = 0.05 sample the appearance of another shoulder peak at ~230 K may be due to the chemical phase separation in the sample [215]. The *DI* reaches the minimum value at ~150 K for samples with $0.05 \leq x \leq 0.15$. The observed minima in *DI* shifts towards higher temperature with increase in x and disappears for the sample with x = 0.50. Below this minimum, the increasing trend in *DI* becomes sharp with the increase in Pr content. For x = 0.50 sample *DI* increases with the decrease in temperature and reaches a maximum value at ~140 K followed by decreasing trend with further decrease in temperature. The upward and downward trend in the behavior of *DI* as a function of temperature indicates the coexistence of FM and AFM correlations, respectively.

The 1/*DI* vs *T* plots for various samples are shown in Fig. 4.9. The linear fit in the temperature range $T > T_{CO}$ for undoped sample is as per Curie-Weiss law.

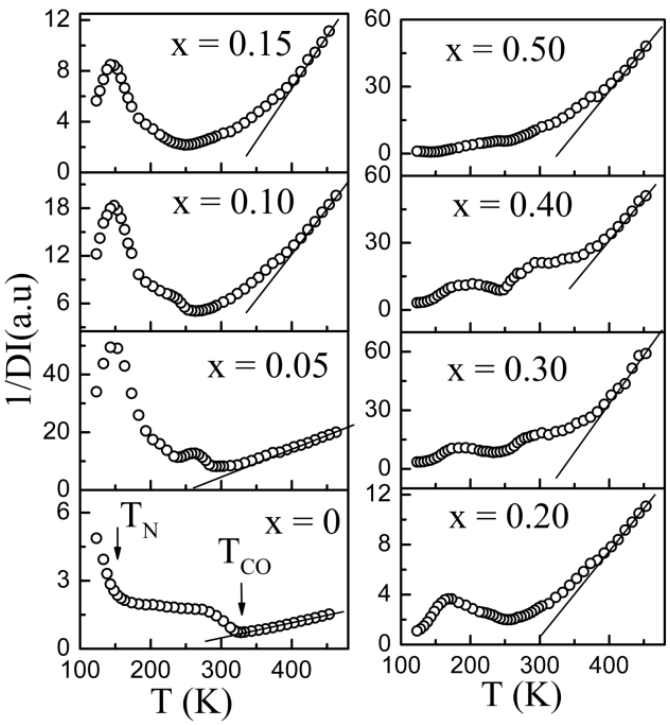

Fig. 4.9. 1/ *DI* vs *T* plots of $Bi_{0.5-x}Pr_xCa_{0.5}MnO_3$ samples.

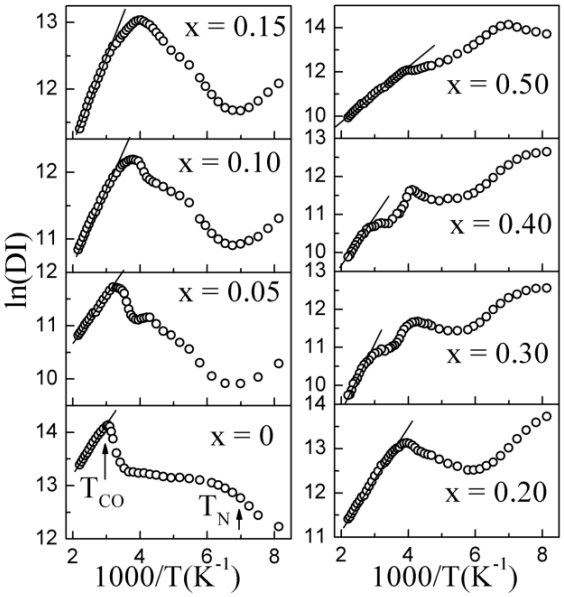

Fig. 4.10. ln*DI* vs 1000/*T* plots of $Bi_{0.5-x}Pr_xCa_{0.5}MnO_3$ samples.

Above T_{CO}, nonlinear variation of 1/*DI* as a function of temperature is observed for doped samples (except for $x = 0.05$). This non-linearity increases with increase in Pr content. However, 1/*DI* vs *T* plots show linear trend above 400 K as shown in Fig. 4.9. The nonlinear behavior is ascribed to the enhancement of FM interactions in the paramagnetic (PM) matrix. The ESR data confirms that above T_{CO}, the PM state is dominant and this state can be treated as PM matrix. In this matrix FM correlations exist which strengthen with the decrease in temperature. A similar trend in ESR data on other manganites has been explained in view of Griffiths theory [7, 81, 104, 215, 216]. According to this model there is a probability of finding FM clusters above the critical temperature (T_C or T_{CO}). Below the critical temperature the size of FM clusters decreases with the decrease in temperature and coexists with AFM clusters.

For all the samples ln*DI* vs 1000/*T* plots and their linear fits according to the equation (3.6) [187] in the temperature range $T > T_{CO}$ are drawn, shown in Fig. 4.10. Above T_{CO}, with increase in Pr content the range of linearity in ln*DI* as a

function of temperature and the slope of the curves (except for x = 0.05) increases, which indicates the strengthening of short-range FM cluster formation [177].

The variation in peak to peak linewidth (ΔH) of ESR signal as a function of temperature is shown in Fig. 4.11. ΔH decreases with the decrease in temperature from high-temperature (453 K) and reaches a minimum value at T_{CO}. The increase in ΔH just below T_{CO} is due to the residual effect of AFM clusters which gave rise to CO state [7, 104, 215, 216]. For x = 0.0 sample below T_N, ΔH decreases sharply. This may be due to the contributions of FM correlations spread in the long-range ordered AFM matrix. At ~200 K, ΔH decreases sharply and reaches a minimum at ~130 , 150 and 160 K for samples with $0.05 \leq x \leq 0.15$, $0.20 \leq x \leq 0.40$ and x = 0.50, respectively. These minima indicate the existence of FM

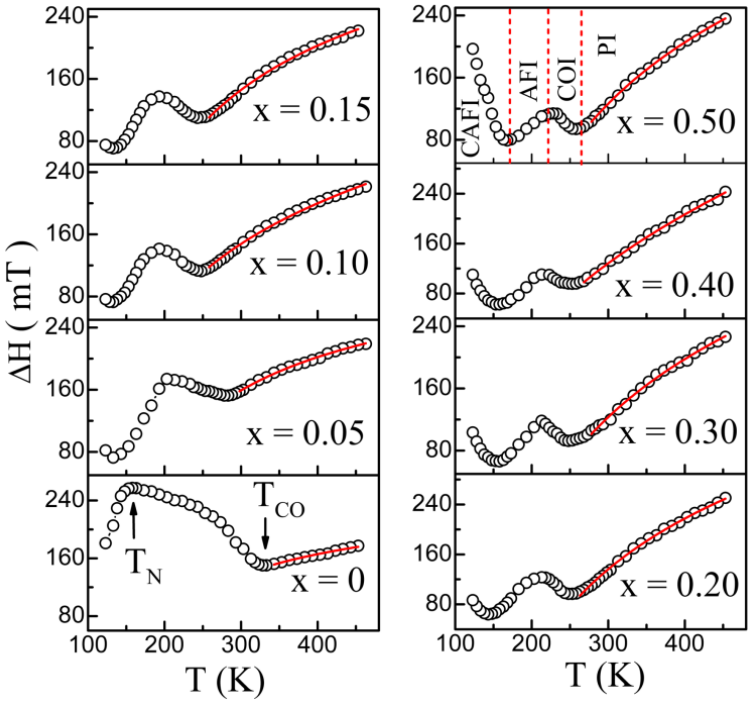

Fig. 4.11. ΔH vs T plots of $Bi_{0.5-x}Pr_xCa_{0.5}MnO_3$ samples. The PI, COI, AFI and CAFI indicate the paramagnetic insulator, charge-ordered insulator, antiferromagnetic insulator and canted antiferromagnetic insulator, respectively. The solid red line is as per theoretical model [173, 176].

Table 4.2. List of the various parameters (θ_C, $\Delta H(\infty)$ and B) of $Bi_{0.5-x}Pr_xCa_{0.5}MnO_3$ samples, estimated from ESR (ΔH vs T) data.

Sample (x)	**θ_C (K)**	**$\Delta H(\infty)$ (G)**	**B (GK^{-1})**
0.0	134	2515	0
0.05	145	2995	0.51
0.10	159	2679	1.64
0.15	178	3383	0.67
0.20	191	2572	3.93
0.30	195	2692	2.92
0.40	189	2159	4.41
0.50	190	2209	4.24

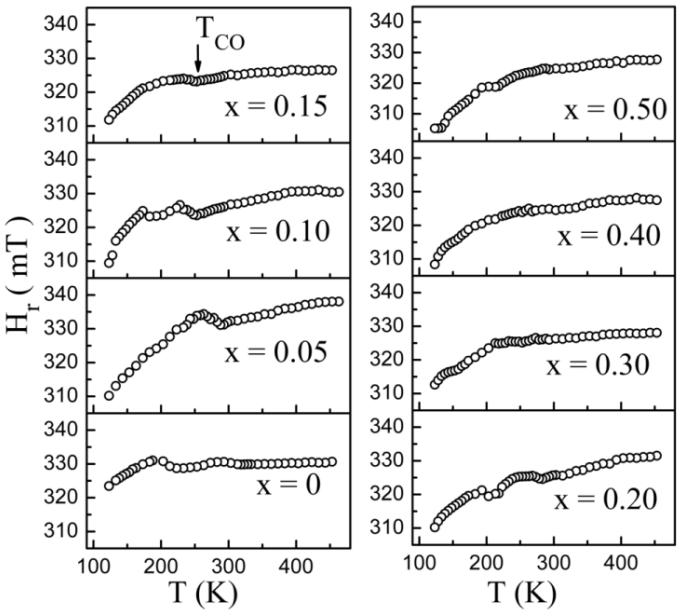

Fig. 4.12. H_r vs T plots of $Bi_{0.5-x}Pr_xCa_{0.5}MnO_3$ samples.

magnetic clusters embedded in the AFM matrix [7, 104, 215, 216]. Below this minimum the increase in ΔH with temperature is due to the evolution of canted-AFM (C-AFM) interactions [13]. The ESR data shows that one of the magnetic states, i.e., PM, FM, AFM or C-AFM, is dominant in a particular temperature range depending on the composition of the sample.

Using the equation (3.7) [173, 176], ΔH vs T fits in the temperature range $T > T_{CO}$ are drawn, shown in Fig. 4.11 and the estimated values of various parameters [Curie-Weiss temperature (θ_C), high-temperature asymptote (ΔH (∞)) and the strength of interactions between the e_g electrons (B)] are listed in table 4.2. The increase (overall) in the values of B with doping is an indicative of the strengthening of electron spin-lattice interactions [217]. This may be due to short-range FM clusters evolving with the decrease in temperature [215].

Fig. 4.12 shows the temperature dependences resonance field (H_r) for the samples. For all the samples as the temperature decreases from high temperature, the H_r value is approximately same down to ~200 K. At T_{CO} though, H_r shows small kink is followed by a decreasing trend due to spin-spin interactions and short-range FM correlations evolving with the decrease in temperature. J. P. Joshi et al. [191] have suggested that the variations in H_r (or g-factor) below T_{CO} could be due to the strengthening of orbital ordering and increasing crystal field effects.

4.3.3. Magnetization studies

4.3.3.1. Temperature dependent magnetization

Fig. 4.13 shows magnetization (M) as a function of temperature plots measured under a static magnetic field (H) of 500 Oe in zero-field cooled (ZFC) and field cooled (FC) conditions. As the temperature decreases from high-temperature, both ZFC magnetization (M_{ZFC}) and FC magnetization (M_{FC}) curves show a peak at T_{CO}. The CO peak becomes broad with the increase in Pr content. The variation in T_{CO} as a function of composition is in good agreement with the values obtained from the ESR data (Fig. 4.8). The T_{CO} observed for x = 0.50 sample (shown in the inset of Fig. 4.13) is close to the earlier reported value but it is not as prominent as observed by other groups [16, 80]. The decrease in M below T_{CO} with the decrease in temperature is an indicative of the decrease in FM cluster size. This supports the ESR results. The broadening of charge ordering

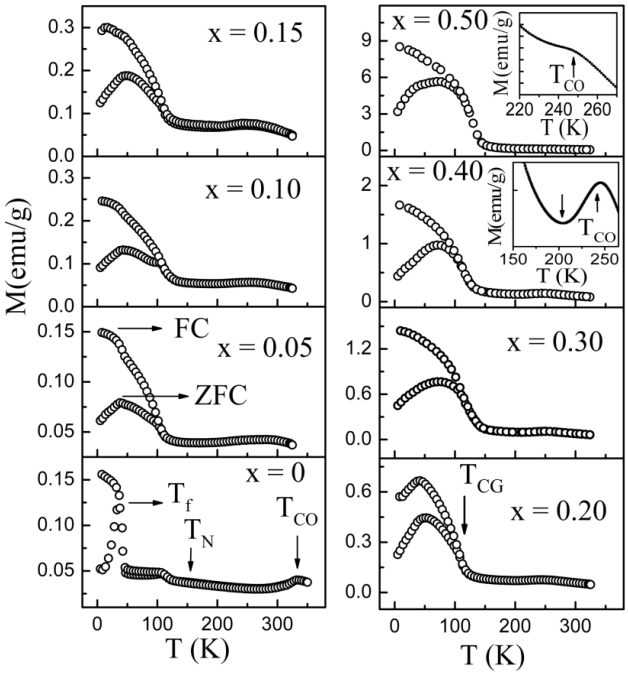

Fig. 4.13. *M* vs *T* plots of $Bi_{0.5-x}Pr_xCa_{0.5}MnO_3$ samples measured in a static magnetic field of 500 Oe.

transition for Pr-doped samples may be due to the delocalization of charge carriers because of the decrease in grain size [218]. For doped samples small increase in *M* below 200 K (inset of Fig. 4.13 for $x = 0.40$ sample) could be due to increasing FM- double exchange (DE) interactions as temperature decreases. A sharp rise in *M* observed below 45 K for $x = 0.0$ and below 115 K for $x \geq 0.05$ samples is an indicative of FM-cluster glass (CG) formation [219]. Below this temperature, M_{ZFC} shows a peak at a temperature known as spin freezing temperature (T_f) [16], while M_{FC} (except for $x = 0.20$) increases continuously with the decrease in temperature. This is characteristic of spin glass (SG) behavior which appears because of competition between FM and AFM correlations [220]. Monte Carlo simulation techniques reveal that this behavior can be attributed to RSG phenomena [221]. Below T_f, the decrease in M_{ZFC} presumably due to the

disturbance of the aligned moments in the sample by thermal fluctuations as well as the randomly oriented frozen FM clusters [216]. At this temperature, the spin of Mn ions changes from long-range FM order to the short-range FM order in the SG state [80].

In the $Bi_{1-x}Ca_xMnO_3$ system, as it is already discussed in the chapter 3, the appearance of SG state has been ascribed to the competition between FM interactions in $BiMnO_3$-type clusters and AFM coupling within clusters where Mn^{3+} orbitals are frozen in random orientations [87]. For x = 0.20 sample, the observed decrease in M_{FC} at 40 K is similar to what has been reported for $Pr_{0.5}Ca_{0.5}MnO_3$ [80]. This is RSG behavior which occurs due to the existence of frustrated spins at the expense of long-range ordering [222].

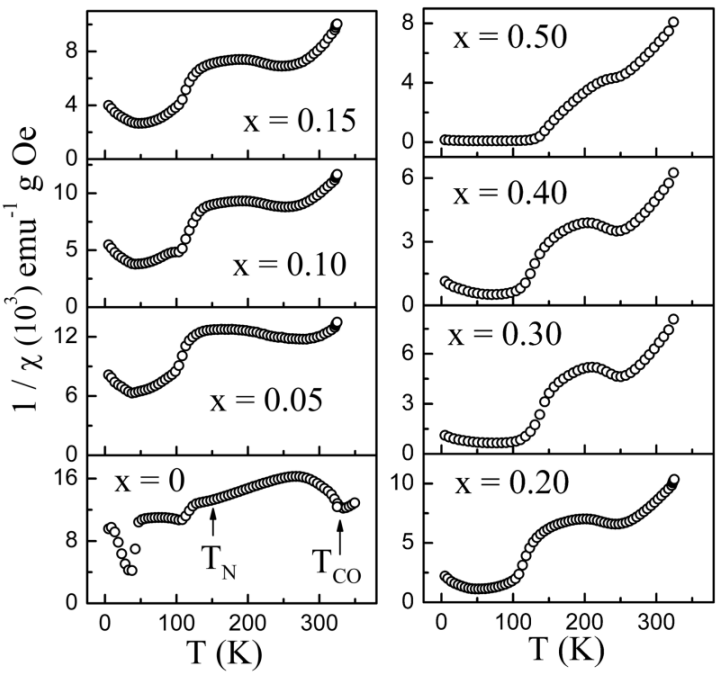

Fig. 4.14. $1/\chi$ vs T plots for M_{ZFC} (measured in a static magnetic field of 500 Oe) of $Bi_{0.5-x}Pr_xCa_{0.5}MnO_3$ samples.

The inverse susceptibility ($1/\chi$) vs T plots obtained from M_{ZFC} data are shown in Fig. 4.14. The nonlinear behavior in these plots above T_{CO} supports the conclusions drawn from $1/DI$ vs T plots of ESR data. For Pr-doped samples, below T_{CO}, the range of temperature in which increasing trend in $1/\chi$ is observed becomes narrow with the increase in Pr content and it disappears for x = 0.50 sample. This could be due to the enhancement of FM moment in the AFM matrix.

4.3.3.2. Magnetic field dependent magnetization at 5 K

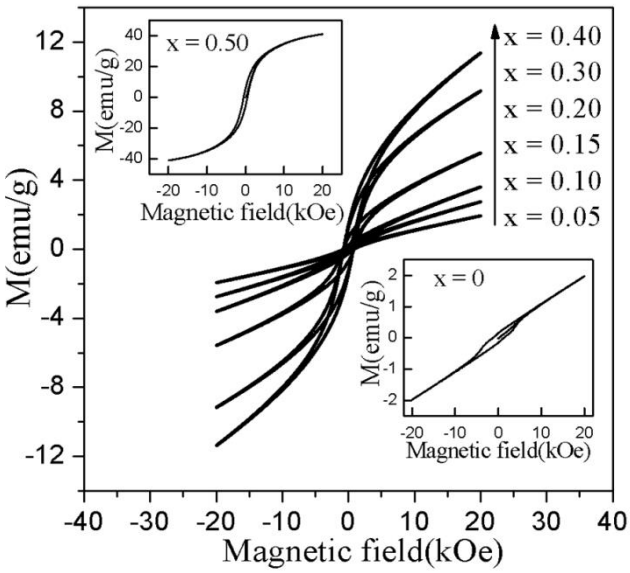

Fig. 4.15. M vs magnetic field (H) plots of $Bi_{0.5-x}Pr_xCa_{0.5}MnO_3$ samples measured at 5 K.

Fig. 4.15 shows M-H plots for various samples, measured by applying a maximum magnetic field of 20 kOe, at 5 K. All the samples show hysteresis, indicating the formation of FM clusters. From this the estimated values of saturation magnetization (M_{sat}) (at 5 K, 20 kOe) are around 0.005, 0.009, 0.019, 0.025, 0.071, 0.146, 0.172 and 0.992 μ_B/f.u for x = 0.0, 0.05, 0.10, 0.15, 0.20, 0.30, 0.40 and 0.50, respectively.

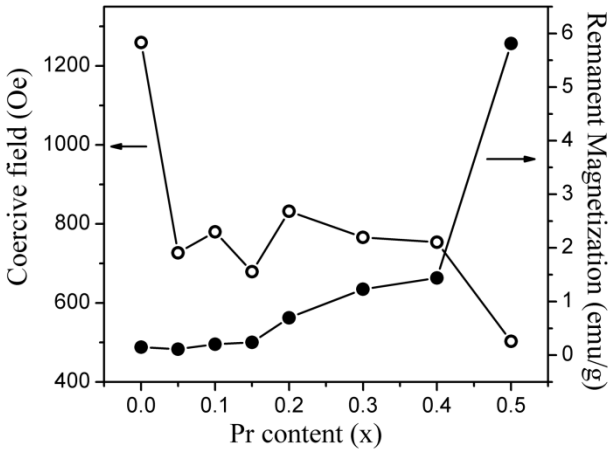

Fig. 4.16. Coercive field and remanent magnetization vs x plots of $Bi_{0.5-x}Pr_xCa_{0.5}MnO_3$ samples measured at 5 K.

Fig. 4.16 shows the variation of coercive field and remanent magnetization as a function of temperature, measured from *M*-*H* plots (at 5 K), of all the samples. With the increase in Pr content, remanent magnetization increases. The undoped sample has the high value of coercive field whereas sample with $x = 0.50$ has the minimum value. For samples with $0.05 \leq x \leq 0.40$, coercive field shows weak dependence on Pr content. With the increase in Pr content the volume fraction of FM clusters increases, resulting in the enhancement of *M* value. The high *M* value for $x = 0.50$ sample and a weak CO peak may be due to the suppression of chemical inhomogeneities in the sample as compared to the earlier reports [175].

4.3.3.3. Critical phenomena and phase transitions

The Curie temperature (T_C) values of all the samples are calculated using the dip observed in the d*M*/d*T* vs *T* plots (not shown) and listed in table 4.3. It is observed that the value of T_C increases with increase in Pr content. For all the samples isotherms are measured near the T_C by applying a maximum field of 40 kOe and show in Fig. 4.17. The critical behavior at the critical point is investigated using Arrott plot (M^2 vs H/M) analysis. Fig. 4.18 shows Arrott plot

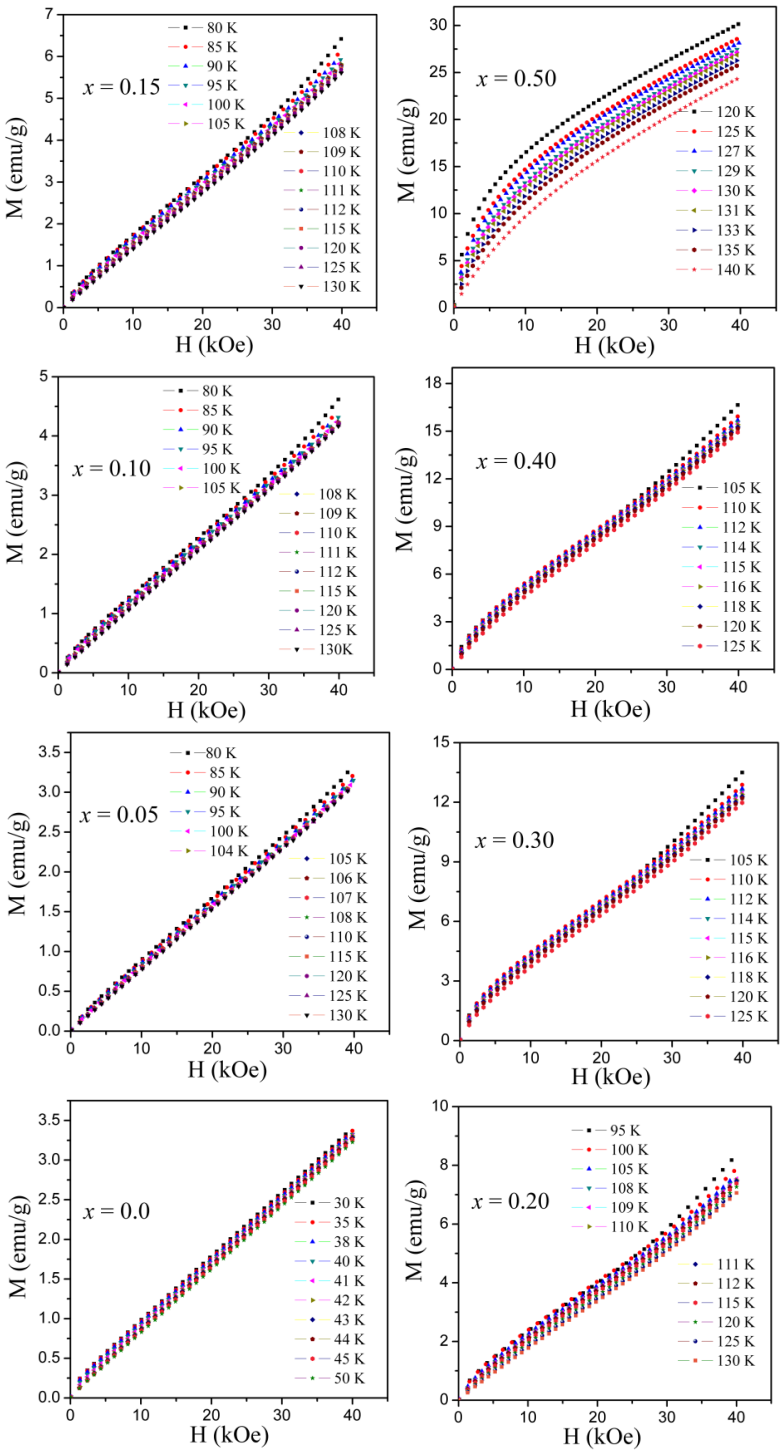

Fig. 4.17. Isotherms: *M-H* plots of $Bi_{0.5-x}Pr_xCa_{0.5}MnO_3$ samples.

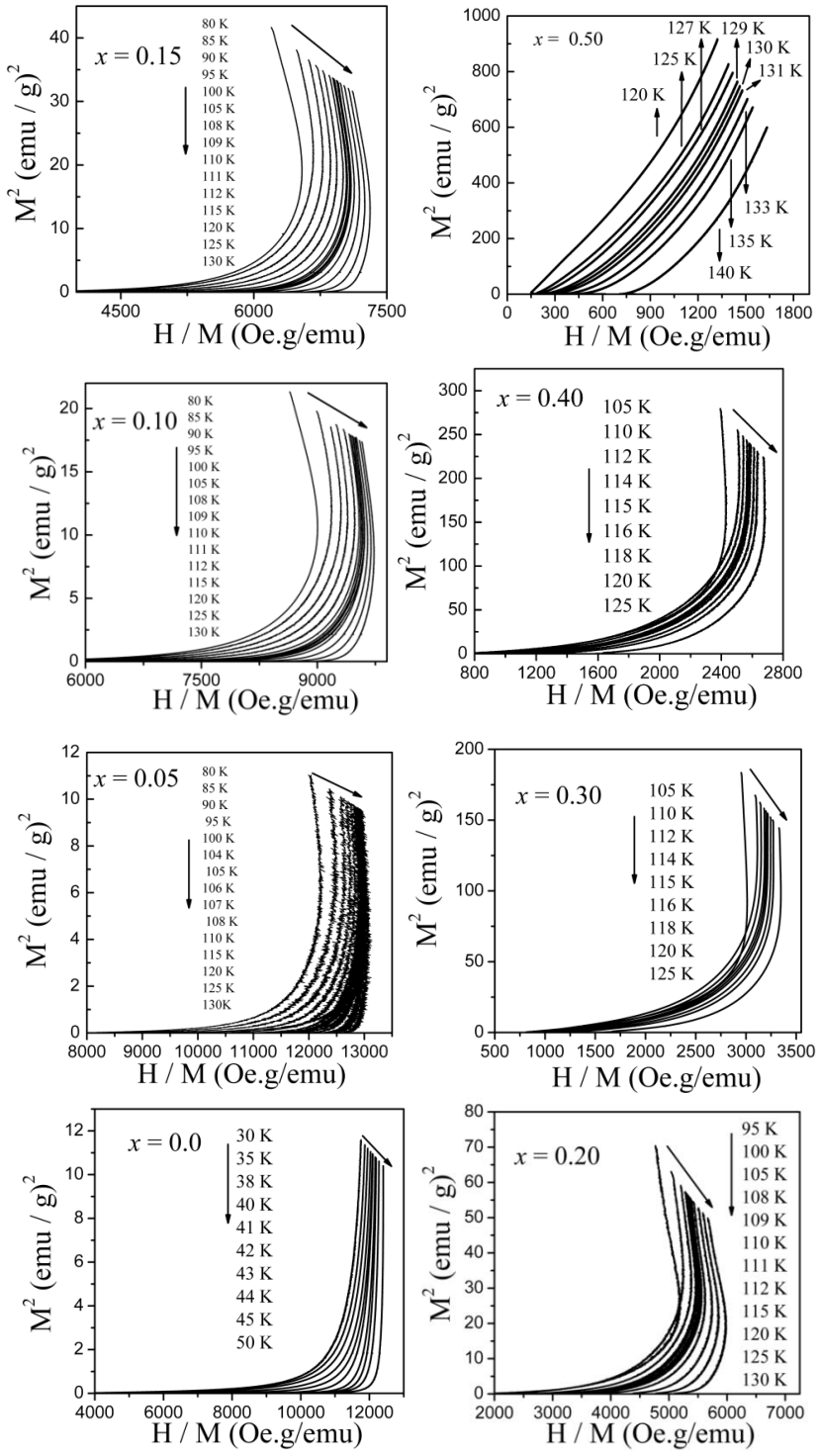

Fig. 4.18. Arrott plot isotherms of M^2 vs H/M of $Bi_{0.5-x}Pr_xCa_{0.5}MnO_3$ samples.

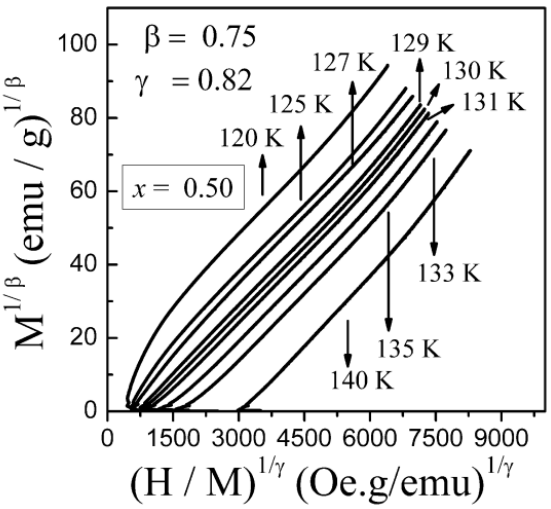

Fig. 4.19. Modified-Arrott plot isotherms of $M^{1/\beta}$ vs $(H/M)^{1/\gamma}$ of $Bi_{0.5-x}Pr_xCa_{0.5}MnO_3$.

Table 4.3. List of the estimated parameters (T_C and $|\Delta S_m|$) from the magnetization data of $Bi_{0.5-x}Pr_xCa_{0.5}MnO_3$.

Sample (*x*)	**T_C (K)**	**$\lvert\Delta S_m\rvert$(J. kg^{-1}. K^{-1}) at T_C**			
		1T	**2T**	**3T**	**4T**
0.0	41	0.021	0.036	0.048	0.070
0.05	106	0.006	0.013	0.029	0.079
0.10	109	0.006	0.012	0.017	0.161
0.15	109	0.011	0.021	0.038	0.057
0.20	109	0.026	0.049	0.105	0.129
0.30	115	0.053	0.097	0.169	0.206
0.40	115	0.072	0.130	0.197	0.257
0.50	129	0.473	0.874	1.069	1.220

isotherms with the critical exponents, β = 0.5 and γ = 1.0 [mean-field theory (MFT) predictions]. The isotherms of M^2 versus H/M plots of the samples with x = 0.0-0.40 have negative slope, whereas the isotherms of M^2 versus H/M plots of the sample with x = 0.50 have positive slope. The negative and positive slopes of the isotherms of these plots indicate the first-order and second-order PM-FM transition, respectively, near the critical point [223]. However, the isotherms of M^2 versus H/M plot of the sample with x = 0.50 are not linear which indicates the absence of long-range FM order and spreading of magnetic transition due to the

competition arising from FM and AFM interactions. To find critical exponents accurately, we have used the critical exponents proposed in MFT as initial values and then performed iteration method using modified-Arrott plot method [224]. Using $\beta = 0.78$ and $\gamma = 0.82$, the plotted modified Arrott plot of the sample with $x = 0.50$ is shown in Fig. 4.19. The curves of this plot comparatively more linear than the other set of critical exponent values chosen in the iteration method. However, the estimated critical exponents do not fall into any universality class. The detailed work on critical analysis is given in chapter 5.

4.3.3.4. Magnetocaloric effect

The magnetic entropy change which is associated with magnetocaloric effect (MCE) is calculated from the isotherms (*M*-*H*) of the samples. Using Maxwell thermodynamics equations magnetic entropy change can be written as

$$\Delta S_m(T,H) = \int_0^{H_{\max}} \left(\frac{\partial M}{\partial T}\right)_H dH \tag{4.1}$$

Since we have measured isotherms at discrete temperatures, the magnetic entropy change is calculated using the following expression

$$\left|\Delta S_m\right| = \sum_i \frac{M_i - M_{i+1}}{T_{i+1} - T_i} \Delta H \tag{4.2}$$

where M_i and M_{i+1} are magnetization values measured in an applied field of H at temperatures T_i and T_{i+1}, respectively [107]. Using equation (4.2) the estimated values of $|\Delta S_m|$ are plotted as a function of temperature, as shown in Fig. 4. 20 and for all the samples the values of $|\Delta S_m|$, estimated at T_C, are listed in table 4.3. The

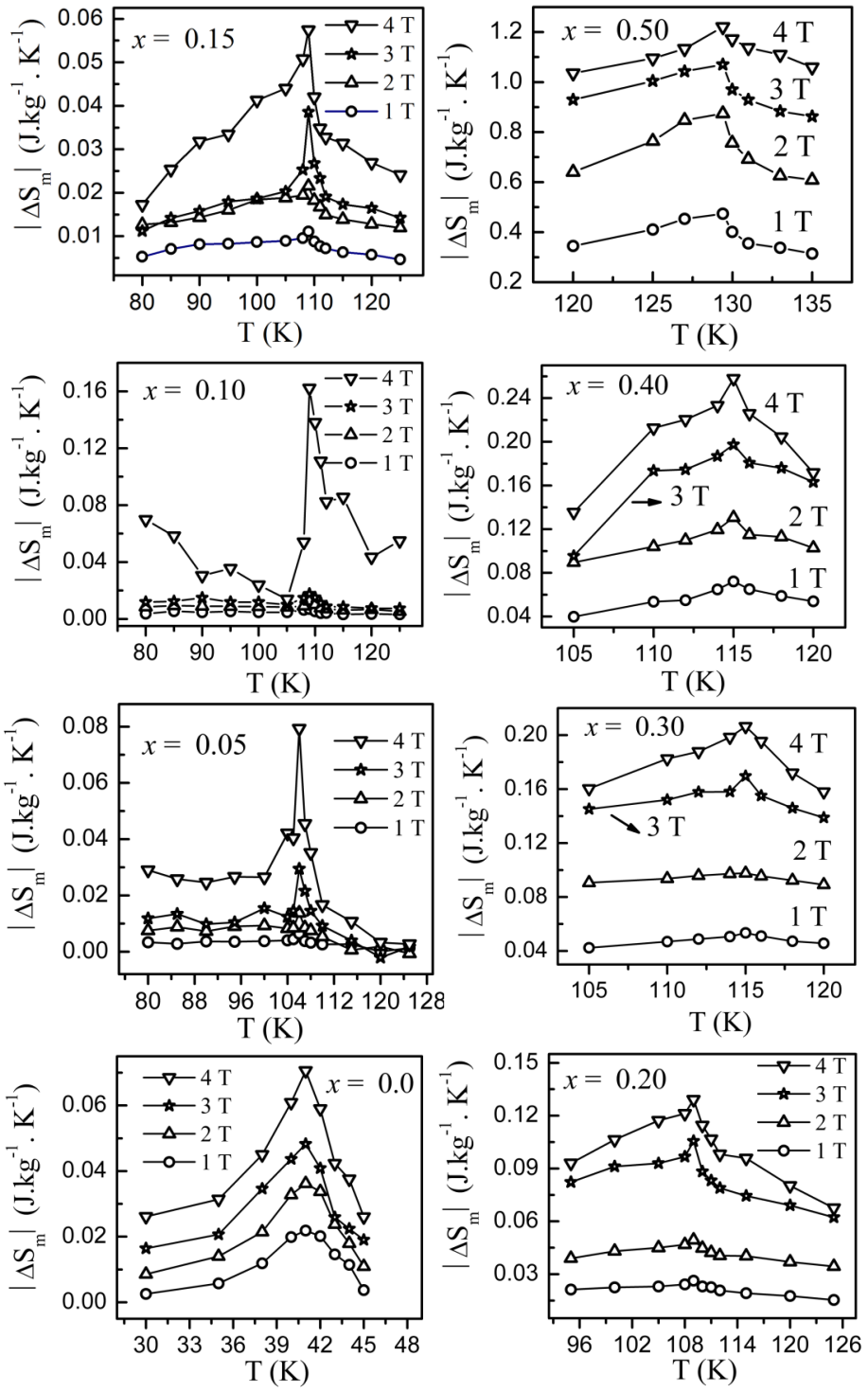

Fig. 4.20. Temperature dependence of the entropy change ($|\Delta S_m|$) of $Bi_{0.5-x}Pr_xCa_{0.5}MnO_3$.

sample with x = 0.50 shows a maximum magnetic entropy change ($|\Delta S_m|$ = 1.22 J.kg^{-1}.K^{-1}) at T_C in the applied field of 40 kOe. For this sample the estimated T_C and $|\Delta S_m|$ are found to be greater than the earlier reports [16, 225]. Since, T_C and $|\Delta S_m|$ increased with Pr-doping, these materials can be used in magnetic refrigeration technology [225, 226].

4.3.4. Transport studies

Fig. 4.21 shows resistivity (ρ) vs T plots for various samples. As the temperature decreases the exponential increase in ρ indicates the activated electronic transport nature of conduction in the samples [7, 19]. The ρ values are in the range ~ 0.50-15 Ω cm at room temperature and it reaches to the order of 10^6 Ω cm at ~70 K. This type of semiconducting behavior is observed in other manganites also [7, 19] and has been ascribed to charge localization.

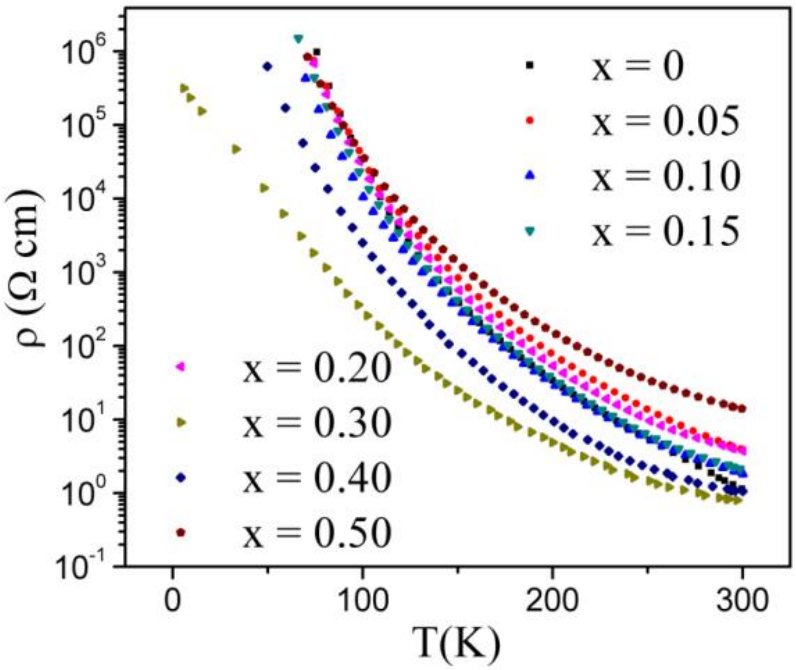

Fig. 4.21. ρ vs T plots of $Bi_{0.5-x}Pr_xCa_{0.5}MnO_3$ samples.

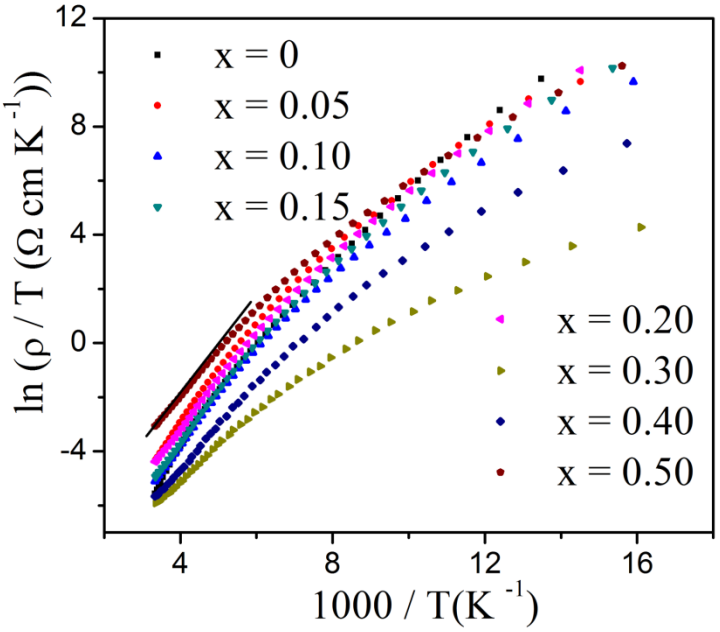

Fig. 4.22. ln(ρ/T) vs 1000/T plots of $Bi_{0.5-x}Pr_xCa_{0.5}MnO_3$ samples.

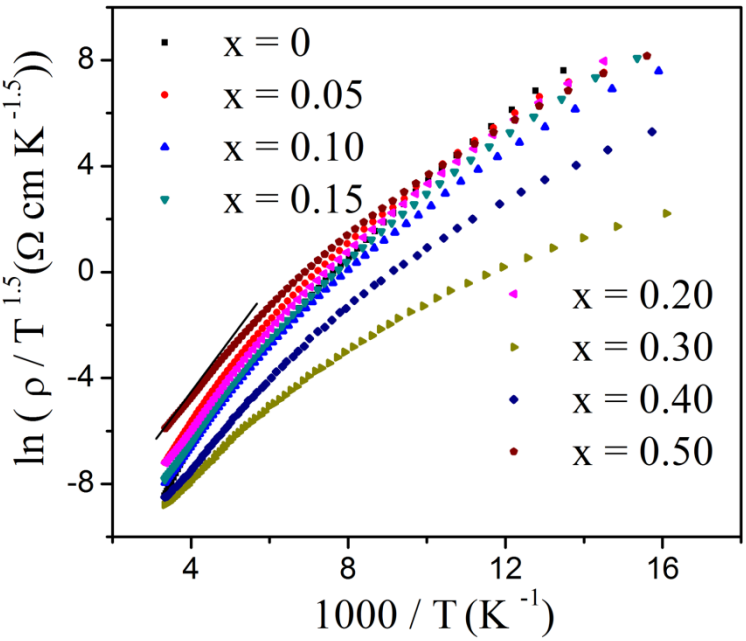

Fig. 4.23. ln($\rho/T^{1.5}$) vs 1000/T plots of $Bi_{0.5-x}Pr_xCa_{0.5}MnO_3$ samples.

According to equation (3.11), $\ln(\rho/T)$ vs $1000/T$ and $\ln(\rho/T^{1.5})$ vs $1000/T$ plots should follow linear trend. However, Fig. 4.22 and Fig. 4.23 show continuous curvature in these plots below $T < T_{CO}$, indicating that these equations are not useful to analyze the present data. However, the data in the temperature range $T > T_{CO}$ follows linear behavior indicating the validity of small polaron hopping (SPH) model. Using this model in the temperature range $T > T_{CO}$ the estimated values of activation energy (E_p) are in the range of 0.10-0.20 eV which are reasonable [7].

Fig. 4.24 shows $\ln(\rho)$ vs $1/T^{1/4}$ plots for various samples in the temperature range 70-300 K. All the samples, except the undoped sample, show linear temperature dependence behavior below T_{CO}. The data for doped samples show small deviation from linear fit at T_{CO}. Whereas the undoped sample shows two linear fits, one in the temperature range $T_{CO} > T > T_N$ and the other one below T_N. This behavior is similar to the results that have already been reported on the undoped Bi-manganite in our earlier work [7]. Using a value of $N(E_F)$ ~3 x 10^{18} $cm^{-3}eV^{-1}$, various model parameters have been estimated and are listed in

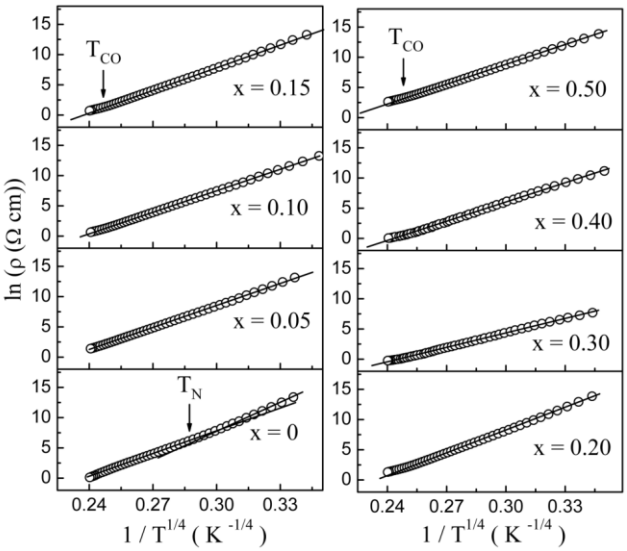

Fig. 4.24. $\ln\rho$ vs $1/T^{1/4}$ plots of $Bi_{0.5-x}Pr_xCa_{0.5}MnO_3$ samples.

Table 4.4. List of the various parameters (T_0, ρ_0, ξ, R and W) of $Bi_{0.5-x}Pr_xCa_{0.5}MnO_3$ estimated from VRH model.

Sample (x)	T_0 (x10^8 K)	ρ_0 (x10^{-13} Ω cm)	ξ (Å)	R (nm)	W (ev)
0.0	0.83	0.94	6.51	5.62	0.149
0.05	0.73	6.95	6.82	5.69	0.144
0.10	0.66	5.88	7.04	5.73	0.140
0.15	0.83	1.03	6.52	5.62	0.149
0.20	0.82	1.63	6.54	5.63	0.148
0.30	0.13	3053	11.97	6.55	0.094
0.40	0.46	30	7.94	5.91	0.128
0.50	0.48	324	7.83	5.89	0.130

table 4.4. For x = 0.0 sample below T_N the estimated values of characteristic temperature (T_0), characteristic resistivity (ρ_0), correlation length (ξ), hopping distance (R) and hopping energy (W) are 1.76 (x10^8 K), 0.00044(x10^{-13} Ω cm), 5.08 Å, 5.28 nm and 0.18 eV, respectively. The localization length of present series of samples is greater than the Mn-Mn distance (~5 Å); the hopping distance is several times to that of Mn- Mn distance [7, 227]. The present results are in good agreement with theoretically predicted values, indicating the validity of Mott's variable range hopping (VRH) model.

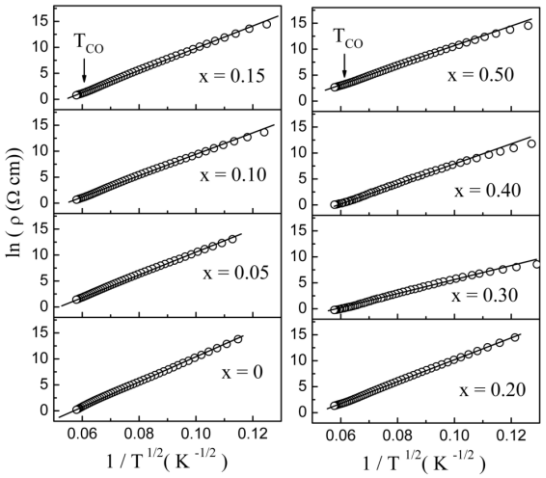

Fig. 4.25. lnρ vs $1/T^{1/2}$ plots of $Bi_{0.5-x}Pr_xCa_{0.5}MnO_3$ samples.

Table 4.5. List of the various parameters (T_0, ρ_0 and ξ) of $Bi_{0.5-x}Pr_xCa_{0.5}MnO_3$ estimated from ES-VRH model.

Sample (x)	T_0 (x10^4 K)	ρ_0(x10^{-5} Ω cm)	ξ (Å)
0.0	5.39	0.24	5.30
0.05	4.43	2.59	6.48
0.10	3.95	2.69	7.28
0.15	4.45	1.28	6.45
0.20	4.35	2.30	6.60
0.30	1.90	30.62	15.1
0.40	3.39	2.47	8.47
0.50	3.24	55.30	8.87

ln(ρ) vs $1/T^{1/2}$ plots are depicted in Fig. 4.25 within the temperature range 70-300 K. All the samples show linear behavior below T_{CO}. We have estimated the various parameters (table 4.5), taking K~500 [228]. The ρ_0 values of the present system are much lower than the theoretical values predicted by Mott [211], indicating that the present system does not follow the Efros and Shklovskii-VRH (ES-VRH) model.

The ρ vs T plots and plots drawn according to adiabatic and non-adiabatic model do not show the T_{CO}. But in the plots of VRH and ES-VRH model the change in slope of the curves indicates the signature of charge ordering. The values of T_{CO} estimated from ρ data are in good agreement with the values that are estimated from the ESR and magnetization data (shown in Fig 4.8). ρ does not vary significantly in the composition range $0.0 \leq x \leq 0.20$. The x = 0.30 sample shows lower resistivity. For samples with $0.30 < x \leq 0.50$ the resistivity increases. The small grain size of the samples increases the grain boundary scattering which gives rise to the increase in resistivity for x = 0.40 and 0.50 [229, 230]. The lower value of ρ of the sample with x = 0.30 and increase in the value of ρ with the increase in x can also be due to change in the value of bond angles. Due to the increase in the value of the average Mn-O-Mn bond angle of the sample with

x = 0.30, bandwidth increases which results in the enhancement of e_g electron mobility. As a result, the value of ρ decreases and it is consistent with the reports [28]. It has been reported that in La-doped BCMO system adiabatic small polaron conduction mechanism is responsible for the transport behavior above charge ordering transition and below this Mott's VRH mechanism [231]. The data of the present set of samples also follow small polaron conduction mechanism above T_{CO} and the Mott's VRH mechanism below this temperature. The percolation model has been extensively used in mixed valence Mn oxides [6, 10, 60, 68] to understand the phase separation phenomena. According to this model, in all samples, FM clusters exist above T_{CO}. As the temperature reaches T_{CO}, AFM interactions grow at the expense of FM interactions. With the further decrease in temperature AFM domains grow progressively and FM cluster size decreases simultaneously, as a result of which large increase in resistivity is observed [7, 19].

4.3.5. Discussion

The observed variations in T_{CO}, enhancement in M, T_C and evolution of different magnetic correlations with Pr-doping can be explained as follows. The high T_{CO} of the undoped sample, as explained in earlier works by several groups [100, 213, 214, 232-234], is due to the strong electron-lattice coupling induced by J-T distortion and long-range Coulomb interaction. With increasing Pr content the effect of $6s^2$ lone pair of Bi^{3+} ions and the hybridization of Bi^{3+} and O^{2-} ions decreases, resulting in the decrease of T_{CO}. For $x \geq 0.20$, Pr^{3+}probably stabilizes the effect of the $6s^2$ lone pair of Bi^{3+} ions, and hence, the CO state becomes same as that of Pr-manganite.

With increasing Pr content the disorder is also likely to decrease because of similar ionic radii of Pr^{3+} and Ca^{2+} ions which are confirmed by the decrease in the value of σ^2 with increase in the value of Pr content. The formation of FM or

FM-CG state and shift of this transition towards higher temperature is ascribed to decrease in disorder. However, for all the samples the value of $t > 0.915$, which suggests the existence of disordered CG state [80]. The drastic change in CG transition temperature from ~ 45 to 115 K can be due to the sharp decrease in the value of σ^2 shown in table 4.1 [28, 232]. In the present system, there is a strong possibility that the GS effects are present. For $x = 0.0$ and 0.05 samples doping does not affect M but it shifts the FM transition towards higher temperature. This may be due to the decrease in GS drastically. Reduction in GS increases the surface to volume ratio resulting in the appearance of FM clusters. Furthermore, because of the canted nature of the system, some of the FM clusters near the surface find a percolation path, in spite of the canted AFM host matrix, leading to the occurrence of FM transition at higher temperature [16]. The decrease in disorder, increase in the surface to volume ratio due to the decrease in GS and the unscreened Coulomb attraction introduced at the surface results in an increase of charge density in the system [235]. The enhanced itinerant e_g electron density changes the collinear AFM configuration and hence weakens the AFM superexchange (SE) interaction, thereby improving the DE interaction, leading to the enhancement of M, T_C and damping of the CO state. The sample with $x = 0.50$ has average GS of 157 nm and T_{CO} at 246 K with broad transition, which is lower than the value for bulk sample but in excellent agreement with the results reported on the same sample with GS of 150 nm [16]. The observed features are attributed to the small GS of the sample. The decrease in GS enhances surface area and distributes charge inhomogeneously leading to phase separation at nanoscales [235]. On the other hand, the tunneling of carriers between two Mn ions belonging to different adjacent connecting nanocrystal grains also induces FM-DE correlations [16, 175, 215, 236]. The increase in unit cell volume with Pr doping, in the composition range $0.05 \leq x \leq 0.50$, is due to the increase in average ionic size caused by the substitution of larger Pr^{3+} ion for smaller Bi^{3+} ion at A-

site. As a result the average Mn-O-Mn bond angle increases (except for x = 0.40 and 0.50) and the length of Mn-O bond decreases, leading to broadening of bandwidth and the increase in mobility of e_g electrons [18]. This results in the strengthening of FM-DE coupling leading to increasing in magnetization. However, a slight oscillation in Mn-O-Mn bond angles as well as in the Mn-O bond lengths may be due to local distortion which arises from oxygen displacement [28].

4.4. Conclusions

In conclusion, we report the temperature dependent electron spin resonance (ESR), magnetization (M) and transport studies on $Bi_{0.5-x}Pr_xCa_{0.5}MnO_3$ ($0.0 \leq x \leq 0.50$) manganites synthesized by sol-gel method. The charge ordering temperature (T_{CO}) decreases from 327 K to 250 K with increase in Pr content from 0.0 to 0.15. The T_{CO} value remains ~250 K as x increases from 0.20 to 0.50. The estimated value of Curie temperature (T_C) increases with increasing in Pr content. The samples with $0.0 \leq x \leq 0.40$ show first-order and the sample with x = 0.50 shows second-order paramagnetic (PM)-ferromagnetic (FM) phase transition near the critical point. The estimated critical exponents β = 0.75 and γ = 0.82 of x = 0.50 sample, do not fall into any universality class. The sample with x = 0.50 shows a maximum magnetic entropy change ($|\Delta S_m|$= (1.22 $J.kg^{-1}.K^{-1}$) at T_C in the applied magnetic field of 40 kOe, which is associated with the magnetocaloric effect (MCE). Resistivity (ρ) data analyses reveal the semiconducting nature of the samples and also samples follow the Mott's variable range hopping (VRH) model below the charge ordering temperature (T_{CO}). The changes in magnetic and transport properties are associated with the changes in structural properties of the samples. The decrease in T_{CO}, increase in M, T_C and $|\Delta S_m|$ with Pr-doping in the present system are ascribed to the decrease in effect of $6s^2$ lone pair character of

Bi^{3+} ions, decrease in disorder due to the similar ionic radii of Pr^{3+} and Ca^{2+} ions and also due to the variation in surface/volume ratio of grains.

Chapter 5

Effect of Bi and Sm doping on the properties of $La_{0.37}D_{0.30}Ca_{0.33}MnO_3$ (D = Bi, Sm) and $La_{0.37}Bi_{0.15}Sm_{0.15}Ca_{0.33}MnO_3$

5.1. Introduction

In $La_{1-x}Ca_xMnO_3$ (LCMO) system the sample with x = 0.33 shows relatively large magnetization (M) and Curie temperature (T_C) [106]. It exhibits first-order paramagnetic (PM)-ferromagnetic (FM) phase transition near the critical point. A significant research work on the effect of Bi doping at La-site in $La_{0.67-x}Bi_xCa_{0.33}MnO_3$ has been reported. However, this study is limited to lower concentrations ($x \leq 0.20$) only [105-110]. Due to $6s^2$ lone pair electrons of Bi^{3+} ions, a much-complicated behavior is expected when a high content of Bi is substituted at La-site in $La_{0.67}Ca_{0.33}MnO_3$. The effective ionic size of Sm^{3+} is much smaller than that of La^{3+}; as a result a large disorder is expected due to the size mismatch of A-site cations. In this chapter the doping-induced changes in the structure, magnetic and transport properties of Bi and Sm (rich in concentration) doped (at La-site) $La_{0.67}Ca_{0.33}MnO_3$ are discussed.

5.2. Sample preparation

The stoichiometric amounts of pure La_2O_3, Bi_2O_3/Sm_2O_3, $CaCO_3$ and MnO_2 were converted into nitrates then dissolved in distilled water to obtain the clear solution. Citric acid was added with constant stirring and the ratio of metal cation to citric acid was fixed at 1:2. The pH of the solution was adjusted to ~ 6-7 by adding ammonia solution. Ethylene-glycol was added to this to get a viscous

solution. The solution was slowly evaporated to get a gel by keeping the temperature at ~ 60-70 ^{o}C with constant stirring for several hours (hrs). When the solution was cooled to room temperature a pink gel was formed. This gel was decomposed at 250 ^{o}C. Then the resulting powder was annealed in a furnace at 900 ^{o}C for 25 hrs. In the final stage, powder was pressed into pellets, which were annealed at 900 ^{o}C for 25 hrs.

5.3. Results and discussion

5.3.1. Structure and morphology studies

The Rietveld refinement of the x-ray diffraction (XRD) data for

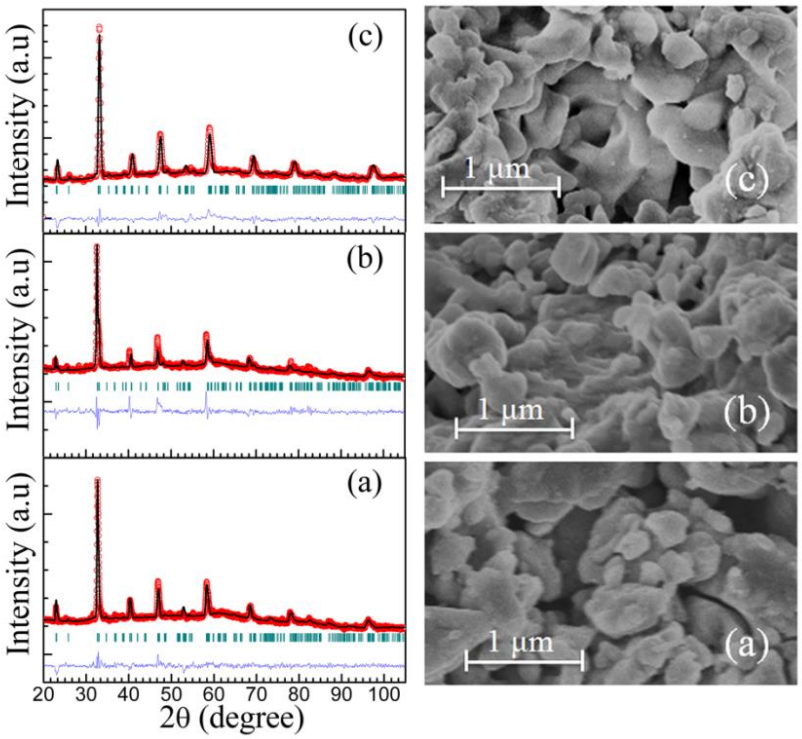

Fig. 5.1. Rietveld refinement (solid black lines) of the XRD data (open red circles (left panel) along with diffraction planes (green lines) and the difference between experimental and fitting data (blue lines) and FESEM images (right panel) of (a) $La_{0.37}Bi_{0.30}Ca_{0.33}MnO_3$, (b) $La_{0.37}Bi_{0.15}Sm_{0.15}Ca_{0.33}MnO_3$ and (c) $La_{0.37}Sm_{0.30}Ca_{0.33}MnO_3$ samples.

Table 5.1.List of the structural parameters [atomic positions(x, y and z), lattice parameters (*a*, *b* and *c*), *V*, *S*, $<d_{Mn-O}>$ and <Mn-O-Mn>] estimated from the refinement of the XRD data of all the samples. The calculated values of $<r_A>$, σ^2 and *t* and are also listed in the table.

Sample	**B30**	**B15S15**	**S30**
La/Bi/Sm/Ca			
x	0.020	0.025	0.024
y	0.250	0.250	0.250
z	0.992	0.999	0.987
Mn			
x	0.500	0.500	0.5000
y	0.500	0.500	0.5000
z	0.000	0.000	0.000
O(1)			
x	0.499	0.538	0.497
y	0.250	0.250	0.250
z	0.053	0.072	0.057
O(2)			
x	0.208	0.286	0.200
y	0.517	0.559	0.523
z	0.322	0.310	0.265
***a* (Å)**	5.479	5.464	5.375
***b* (Å)**	7.756	7.552	7.691
***c* (Å)**	5.421	5.477	5.433
***V*(Å^3)**	230	226	224
S	2.62	2.89	2.40
$<d_{Mn-O}>$ (Å)	1.944	1.994	1.931
<Mn-O-Mn> (^{o})	163.84	149.66	161.82
$<r_A>$ (Å)	1.264	1.222	1.180
σ^2 (Å^2)	0.005	0.017	0.026
t	0.946	0.932	0.917

$La_{0.37}Bi_{0.30}Ca_{0.33}MnO_3$ (B30), $La_{0.37}Bi_{0.15}Sm_{0.15}Ca_{0.33}MnO_3$ (B15S15) and $La_{0.37}Sm_{0.30}Ca_{0.33}MnO_3$ (S30) samples is shown in the left panel of Fig. 5.1. Refinement confirms the single phase orthorhombic structure with *Pnma* space group of the samples. From the refinement the estimated values of structural parameters, namely atomic positions (x, y and z), lattice parameters (*a*, *b* and *c*),

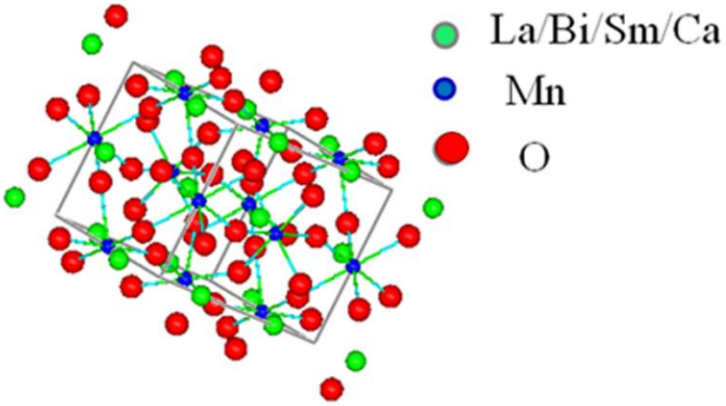

Fig. 5.2. Crystal structure of $La_{0.37}Bi_{0.15}Sm_{0.15}Ca_{0.33}MnO_3$.

unit cell volume (V), the goodness of fit (S), the average Mn-O bond length ($<d_{Mn-O}>$), the average Mn-O-Mn bond angle (<Mn-O-Mn>) are listed in table 5.1. The estimated values of average ionic size of A-site cations ($<r_A>$), the variance of A-site cation size (σ^2) and tolerance factor (t) of the samples are also listed in table 5.1. The decrease in the unit cell volume for these samples compared to $La_{0.67}Ca_{0.33}MnO_3$ (~231 $Å^3$) could be due to the smaller ionic radii of Bi^{3+} (1.24 Å) and Sm^{3+} (0.96 Å) than that of La^{3+}(1.36 Å) [108, 111, 120]. The field emission scanning electron microscopy (FESEM) microstructure of the samples is shown in the right panel of Fig. 5.1, indicating an agglomeration in the samples. This may be due to annealing, which helps the grains to coalesce. Energy dispersive x-ray spectroscopy (EDX) results confirm the purity of the samples. Using structural parameters, the crystal structure of $La_{0.37}Bi_{0.15}Sm_{0.15}Ca_{0.33}MnO_3$ sample, representative of all the samples, is generated and shown in Fig. 5.2.

5.3.2. Electron spin resonance studies

Fig. 5.3 depicts the electron spin resonance (ESR) spectra of B30 sample at a few selected temperatures. Above 223 K, the ESR spectra of B30 sample show a

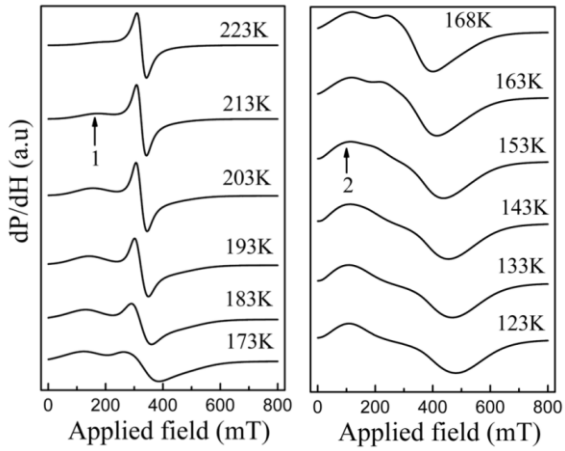

Fig. 5.3. ESR spectra of $La_{0.37}Bi_{0.30}Ca_{0.33}MnO_3$ sample measured at various temperatures.

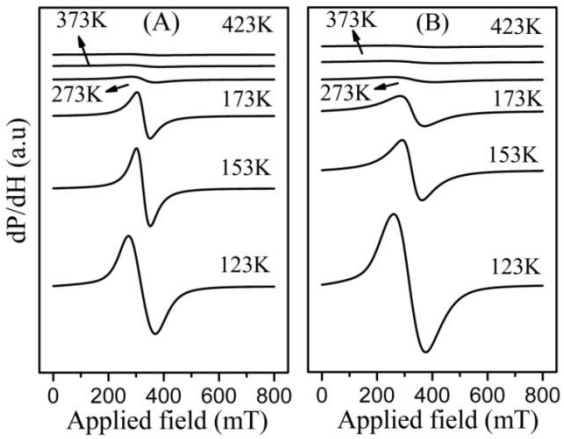

Fig. 5.4. ESR spectra of (A) $La_{0.37}Bi_{0.15}Sm_{0.15}Ca_{0.33}MnO_3$ and (B) $La_{0.37}Sm_{0.30}Ca_{0.33}MnO_3$ samples measured at various temperatures.

single resonance line at ~326 mT, which is the characteristic of PM interactions. Below this, FM correlations evolve in the PM matrix, which is confirmed from the observed hump (shown with '↑1') in the low-field region. This can be assigned to low-moment state. With further decrease in temperature, FM correlations grow at the expense of PM interactions, resulting in a complete PM-FM transition below a particular temperature (~153 K). This is confirmed by the shift of the hump towards further low-field region (shown with '↑2'). This can be

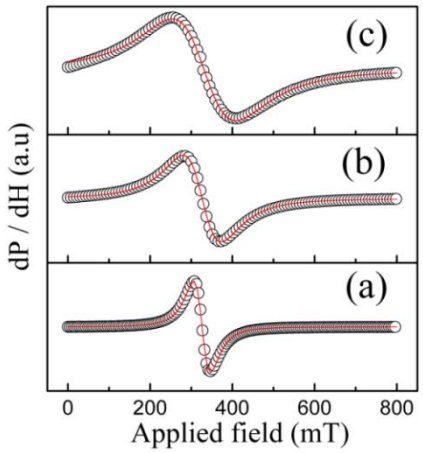

Fig. 5.5. Lorentzian fit (solid red line) to the ESR spectra (open circles) of (a) $La_{0.37}Bi_{0.30}Ca_{0.33}MnO_3$, (b) $La_{0.37}Bi_{0.15}Sm_{0.15}Ca_{0.33}MnO_3$ and (c) $La_{0.37}Sm_{0.30}Ca_{0.33}MnO_3$ samples measured at 273 K.

assigned to high-moment state. Similar results have been reported earlier [237, 238]. In the temperature range, 153 K < T < 223 K, the coexistence of FM and PM signals suggests phase separation in the vicinity of T_C. Neutron scattering results supports this phase separation phenomenon [70, 239]. For B15S15 (Fig. 5.4 (A)) and S30 (Fig. 5.4 (B)) samples, only PM feature is observed up to 123 K, below this we could not do measurements because of instrument limitation. Fig. 5.5 shows Lorentzian [equation (3.1)] fit to the ESR spectra of the samples measured at 273 K.

Fig. 5.6 (A) depicts the peak to peak linewidth (ΔH) of ESR signal as a function of temperature. ΔH decreases with decreasing temperature from 453 K, reaches a minimum at ~ 230, 170 and 150 K for B30, B15S15 and S30 samples, respectively. This behavior can be ascribed to a critical slowing down due to the FM ordering [240]. For all the samples, ΔH increases with the further decrease in temperature. Previous reports suggested that the minimum value of ΔH and the increasing behavior of ΔH below the minimum are sample dependent and these features may be associated with magnetic inhomogeneity of the sample arising

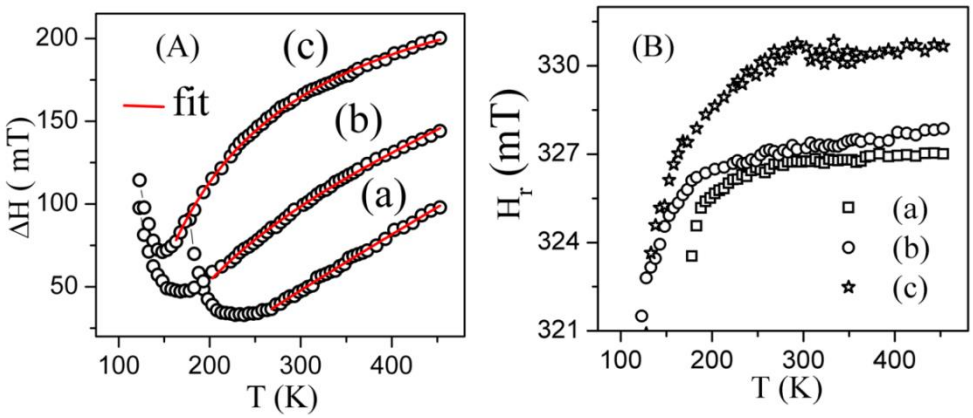

Fig. 5.6 (A) ΔH vs T and (B) H_r vs T plots of (a) $La_{0.37}Bi_{0.30}Ca_{0.33}MnO_3$, (b) $La_{0.37}Bi_{0.15}Sm_{0.15}Ca_{0.33}MnO_3$ and (c) $La_{0.37}Sm_{0.30}Ca_{0.33}MnO_3$ .Solid red lines are the fits according to equation (3.7)[173, 176].

Table 5.2. List of the various parameters (θ_C, $\Delta H(\infty)$, B and μeff) estimated from ESR and magnetization data of all the samples.

Sample	**ESR (ΔH vs T)**			**Magnetization ($1/\chi$ vs T)**	
	θ_C **(K)**	$\Delta H(\infty)$ **(G)**	B **(GK^{-1})**	θ_C **(K)**	μeff**(μ_B)**
B30	188	455	2.78	186	5.64
B15S15	126	1069	2.11	124	6.09
S30	115	2673	0	114	5.88

from local variations in chemical composition or oxygen stoichiometry [172, 241, 242] or demagnetization fields arising from pores between the grains of samples [243]. These inhomogeneities are inherent and may exist in large size [244].

In most of the manganites, it is observed that the temperature dependence of ΔH is very similar to the temperature dependence of electrical conductivity [196, 245]. The data is further analyzed in the PM region using Huber et al. [173] and Auslender et al. [176] models given in chapter 3. ΔH vs T fits using equation (3.7) are shown with solid red lines in Fig. 5.6 (A). From the fitting, the estimated values of Curie-Weiss temperature (θ_C), high-temperature asymptote ($\Delta H(\infty)$) and B which describes the strength of interaction between the e_g electrons and

impurities with spin reversal, are listed in table 5.2. From these values it is concluded that the observed ΔH behavior of S30 sample can only be due to pure ion-ion spin relaxation, whereas in B30 and B15S15 samples this behavior is due to both ion-ion spin relaxation and carrier spin-lattice interactions. For understanding the spin dynamics and magnetic properties, Harder et al. [246] have used a technique called electrical detection of ferromagnetic resonance. Resonance field (H_r) as a function of temperature is shown in Fig. 5.6 (B). H_r is constant in the PM region and decreases with decrease in temperature in the FM region. However, in temperature range from 133-123 K, H_r increases again for B30 samples (not shown). The complex temperature dependences of H_r observed in this compound could be a sign of rearrangement of spin orientation and domain structure near high-moment state onset temperature [108, 241, 242].

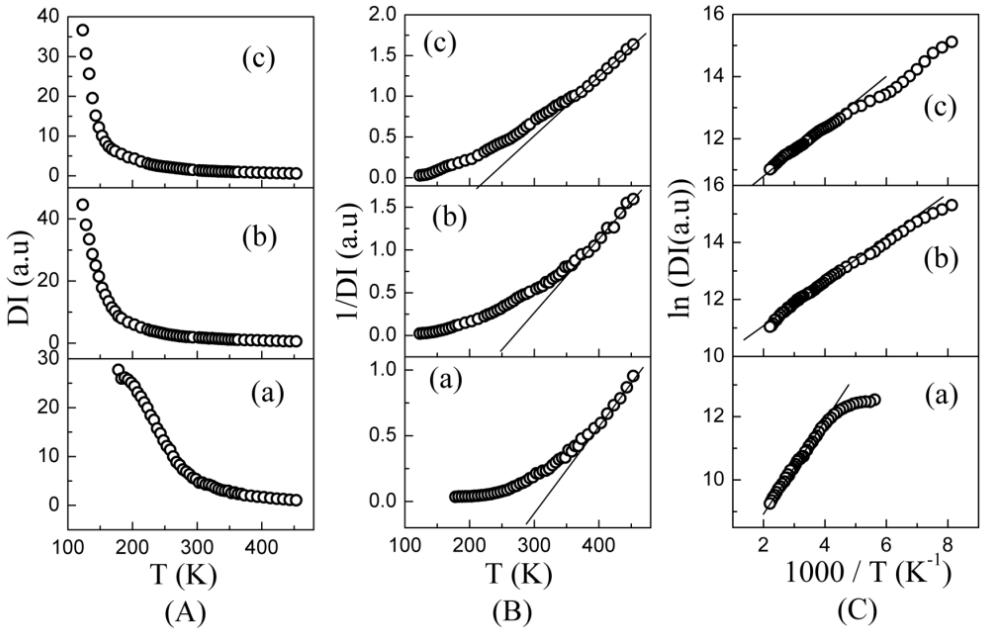

Fig. 5.7 (A) *DI* vs *T*, (B) 1/*DI* vs *T* and (C) ln*DI* vs 1000/*T* plots of (a) $La_{0.37}Bi_{0.30}Ca_{0.33}MnO_3$, (b) $La_{0.37}Bi_{0.15}Sm_{0.15}Ca_{0.33}MnO_3$ and (c) $La_{0.37}Sm_{0.30}Ca_{0.33}MnO_3$ samples.

The normalized double integrated intensity (*DI*) as a function of temperature is shown in Fig. 5.7(A). For all the samples, *DI* increases slowly with the decrease in temperature. With further decrease in temperature, *DI* increases rapidly around 270, 150 and 150 K for B30, B15S15 and S30 samples, respectively. Fig. 5.7(B) shows 1/*DI* vs *T* plots for all the samples. The 1/*DI* plots show linear behavior above 400, 370 and 350 K for B30, B15S15 and S30 samples, respectively. Below this temperature nonlinear behavior in 1/*DI* with further decrease in temperature is observed, which may be due to the formation of FM clusters in the PM matrix [7, 81]. The increasing trend of nonlinearity on approaching T_C might be due to the evolving spin-lattice interactions. This is in good agreement with the predicted adiabatic polaron hopping model [247]. The exponential decay of 1/*DI* reflects the formation of polarons when critical point is approached. These polarons can be centered by the Mn^{3+} and Mn^{4+} ions and mediated by the double exchange (DE) activated hopping of the electrons via the O^{2-} ion. Fig. 5.7(C) depicts the ln*DI* vs1000/*T* plots for all the samples. The ln*DI* show linear behavior in the PM region, then it deviates from the linear behavior with decrease in temperature, which indicates the evolution of FM correlations.

5.3.3. Magnetization studies

5.3.3.1. Temperature dependent magnetization

Fig. 5.8 (A) depicts *M* vs *T* plots, both in zero-field (ZFC) and field (FC) modes in an applied static magnetic field (*H*) of 500 Oe. PM-FM transition temperature, i.e., T_C, is assigned to the minimum in the plot of d*M*/d*T* vs *T* (for S30 sample). For B15S15and S30 samples, the estimated value of T_C is ~100 K. B30 sample shows two magnetic transitions at ~166 and 208 K, which can be assigned to the magnetic transition of the high-moment state (T_C(H)) and low-moment state (T_C(L)), respectively. Whereas ESR studies show T_C(H) and T_C(L) at 153 K and 223 K, respectively. Being an atomic probe, the ESR technique is

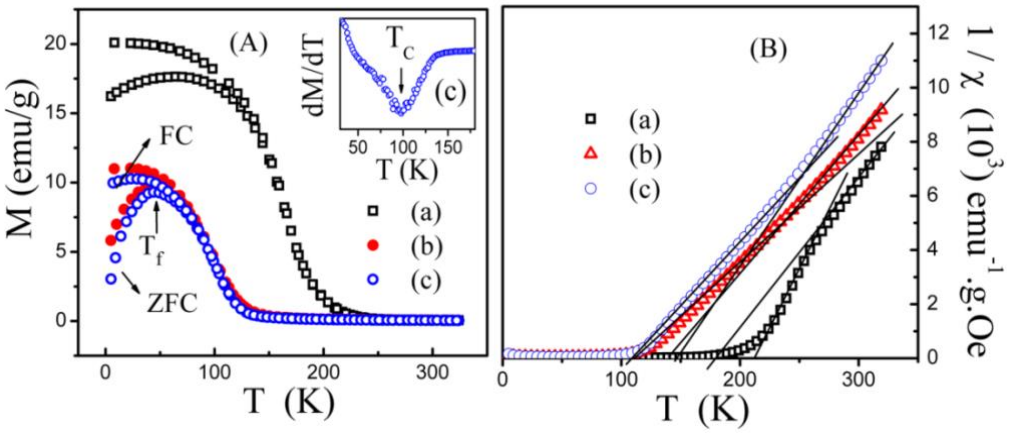

Fig. 5.8 (A) M vs T (in a static magnetic field of 500 Oe) and (B) $1/\chi$ vs T (for M_{ZFC}) plots of (a) $La_{0.37}Bi_{0.30}Ca_{0.33}MnO_3$, (b) $La_{0.37}Bi_{0.15}Sm_{0.15}Ca_{0.33}MnO_3$ and (c) $La_{0.37}Sm_{0.30}Ca_{0.33}MnO_3$. Inset of (A) shows d$M$/d$T$ vs T plot of $La_{0.37}Sm_{0.30}Ca_{0.33}MnO_3$ sample.

able to detect the evolution of FM phase at 223 K and the existence of PM phase down to 153 K. The observed single resonance line in ESR spectra indicates that the magnetic interaction is weak between Mn^{3+} and Mn^{4+} above T_C. Below T_C magnetic interactions become strong between Mn^{3+} and Mn^{4+} and these interactions are either FM or canted (C)-(FM/antiferromagnetic (AFM)) depending on the distance and angle of Mn-O-Mn bond and Mn^{4+}/Mn^{3+} ratio. By the application of magnetic field C-(FM/AFM) can transform into FM-type, leading to the appearance of two resonances in the ESR spectra [105]. The behavior of two magnetic transitions has been observed in other manganites also [10, 248, 249]. The sharp rise in M at 180, 120 and 120 K, a peak called spin freezing temperature (T_f) in ZFC magnetization (M_{ZFC}) at 65, 43 and 43 K are observed for B30, B15S15 and S30 samples, respectively. This behavior is attributed to the evolution of spin or cluster glass state, reported in other manganites also [219]. Increase in M_{ZFC} with increasing temperature (from 5 K) is ascribed to the competition between the demagnetization and magnetic-domain orientation process [250]. The deviation of FC magnetization (M_{FC}) from M_{ZFC}

depends on the magnetic homogeneity of the FM material and the strength of the applied field. A large bifurcation of B15S15 and S30 samples indicate the strong competition between FM and AFM phases. This in turn develops the magnetic frustration in the sample [251-253]. In general the response of the spin to the external magnetic field depends on the competition between magneto crystalline anisotropy energy and the applied field strength. At low-temperatures, the value of M_{ZFC} depends on the anisotropy energy. If the strength of the applied field is low compared to anisotropy internal field within the sample, only few spins orient in the direction of the magnetic field, resulting in decrease in M_{ZFC} of the samples [200, 254].

Fig. 5.8 (B) depicts inverse susceptibility ($1/\chi$) as a function of temperature for M_{ZFC} vs T data. The linear fits are according to Curie-Weiss law. The two linear fits for B30 indicate that the evolution of FM interaction is getting stronger and hence the slope alone changes with the decrease in temperature. The estimated values of θ_C are listed in table 5.2. The θ_C values are in good agreement with the values obtained from ESR data analysis. For all the samples the estimated values of effective magnetic moment (μ_{eff}) (table 5.2) are greater than the theoretical value ($4.55\mu_B$). This, as mentioned earlier chapter, could be due to the presence of magnetic polarons [216].

5.3.3.2. Magnetic field dependent magnetization

Fig. 5.9 depicts the *M-H* data at various temperatures. The solid red lines are fitting curves according to the approach to saturation model given by the equation

$$M(T,H) = M(0,H)[1-(a/H)-(b/H^2)] + \chi_{hf} H \qquad (5.1)$$

where a, b and χ_{hf} are constants. The a/H term describes the defects/imperfections, b/H^2contribution due to magnetocrystalline anisotropy. The $\chi_{hf}H$ term corresponds

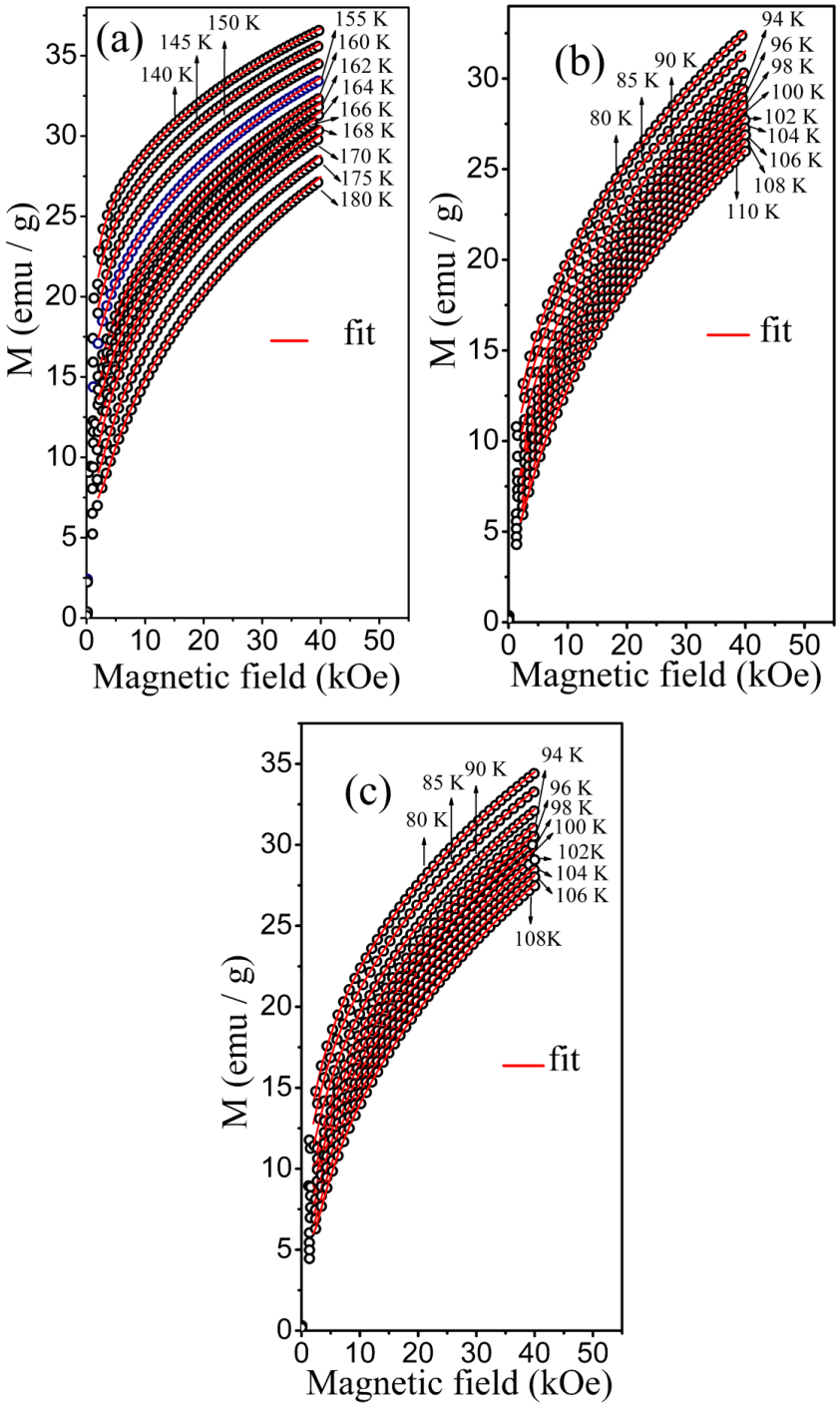

Fig. 5.9. Isotherms (*M-H* plots) of (a) $La_{0.37}Bi_{0.30}Ca_{0.33}MnO_3$, (b) $La_{0.37}Bi_{0.15}Sm_{0.15}Ca_{0.33}MnO_3$ and (c)$La_{0.37}Sm_{0.30}Ca_{0.33}MnO_3$ samples.

to a paramagnetic-like behavior. However, so far there is no clear explanation about this term [255]. The lack of saturation in *M-H* data for samples up to the applied magnetic field of 40 kOe clearly indicates the existence of magnetic inhomogeneity or short-range FM order.

5.3.3.3. Critical phenomena and phase transitions

In order to study the critical behavior near the T_C, where a magnetic system undergo a second-order phase transition from PM (above T_C) to FM (below T_C) state is characterized by a set of critical exponents and amplitudes, we have used various techniques such as modified-Arrott plots, Kouvel-Fisher method and critical isotherm analysis. The mathematical definitions of the critical exponents from magnetization measurements are given as per the following relations [256, 257]:

$$M_s(T) = M_0|\varepsilon|^{\beta} \qquad \varepsilon < 0, T < T_C \tag{5.2}$$

$$\chi_0^{-1}(T) = (h_0 / M_0)\varepsilon^{\gamma} \qquad \varepsilon > 0, T > T_C \tag{5.3}$$

$$M = DH^{1/\delta} \qquad \varepsilon = 0, T = T_C \tag{5.4}$$

where M_0, h_0 and D are the critical amplitudes and $\varepsilon = (T\text{-}T_C/T_C)$ is the reduced temperature. The critical exponents are determined from Arrott plot [224] and Kouvel-Fisher method [258].

Four models are generalized for obtaining the values of critical exponents: mean-field model (β = 0.5 and γ = 1); 3D-Heisenberg model (β = 0.365 and γ = 1.386); 3D-Ising model (β = 0.325 and γ = 1.241) and tricritical mean-field model (β = 0.25 and γ = 1). The critical exponents are not defined for first-order PM-FM phase transition since the magnetic field can shift the transition, leading to a field dependent phase boundary at critical point [259, 260].

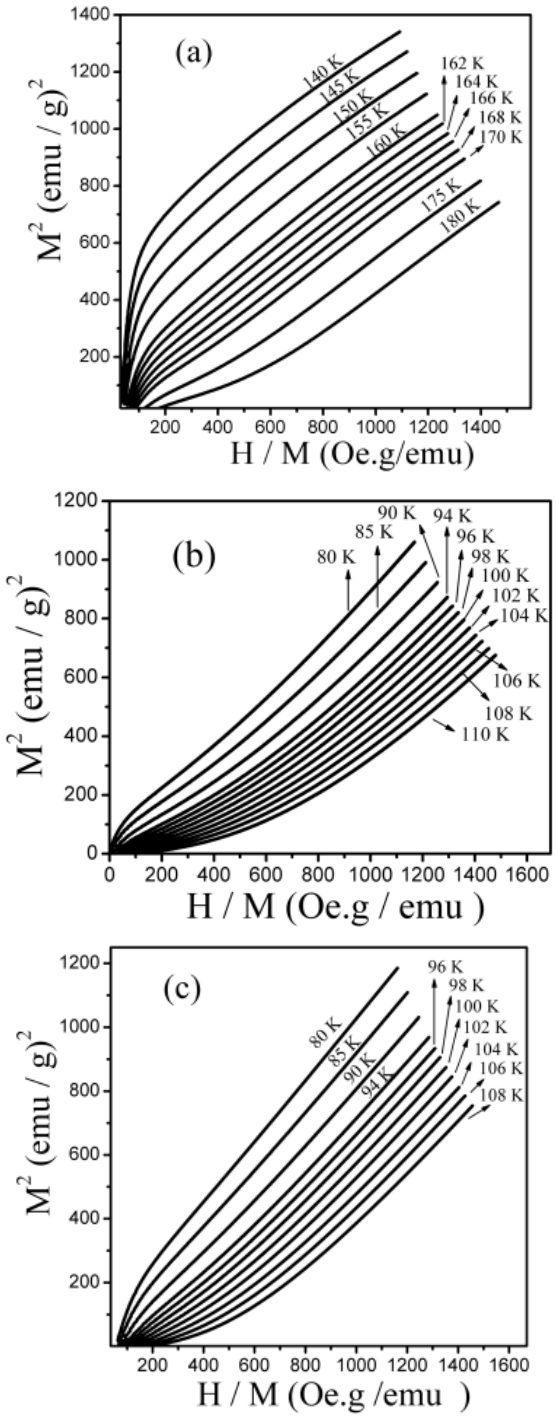

Fig. 5.10. Arrott plots isotherms of M^2 vs H/M of (a) $La_{0.37}Bi_{0.30}Ca_{0.33}MnO_3$, (b) $La_{0.37}Bi_{0.15}Sm_{0.15}Ca_{0.33}MnO_3$ and (c) $La_{0.37}Sm_{0.30}Ca_{0.33}MnO_3$ samples.

According to the mean-field theory (MFT) which is proposed for a system exhibiting the second-order PM-FM phase transition and long-range FM interactions, the Gibbs free energy (G) can be written in terms of the order parameter M near the critical temperature region, given in the following equation [260]

$$G(T,M) = G_0 + (1/2)A(T)M^2 + (1/4)B(T)M^2 - MH \tag{5.5}$$

where the coefficients A and B are temperature dependent parameters.
At equilibrium,

$$\partial G / \partial M = 0 \tag{5.6}$$

Then the obtained magnetic equation of state can be written as,

$$H / M = A + BM^2 \tag{5.7}$$

The slope of this equation determines the nature of magnetic transition as explained by Banerjee [223]. Banerjee criterion states that if the isotherms of M^2 vs H/M have positive slope then PM-FM transition of the system is of second-order type and if isotherms have negative slope then PM-FM transition of the system is of the first-order type. If a FM system was obeying the MFT in the vicinity of T_C, then the M^2 vs H/M curves should be parallel straight lines and the curve at T_C passes through the origin. However, the curves of M^2 vs H/M plots of the present samples, shown in Fig. 5.10, do not show the linear behavior, indicating the absence of long-range FM order. However, the positive slope indicates that the transition from PM-FM is of the second-order type [223]. Banerjee condition has been extensively used in several manganites to identify the order of phase transition [257, 260, 261].

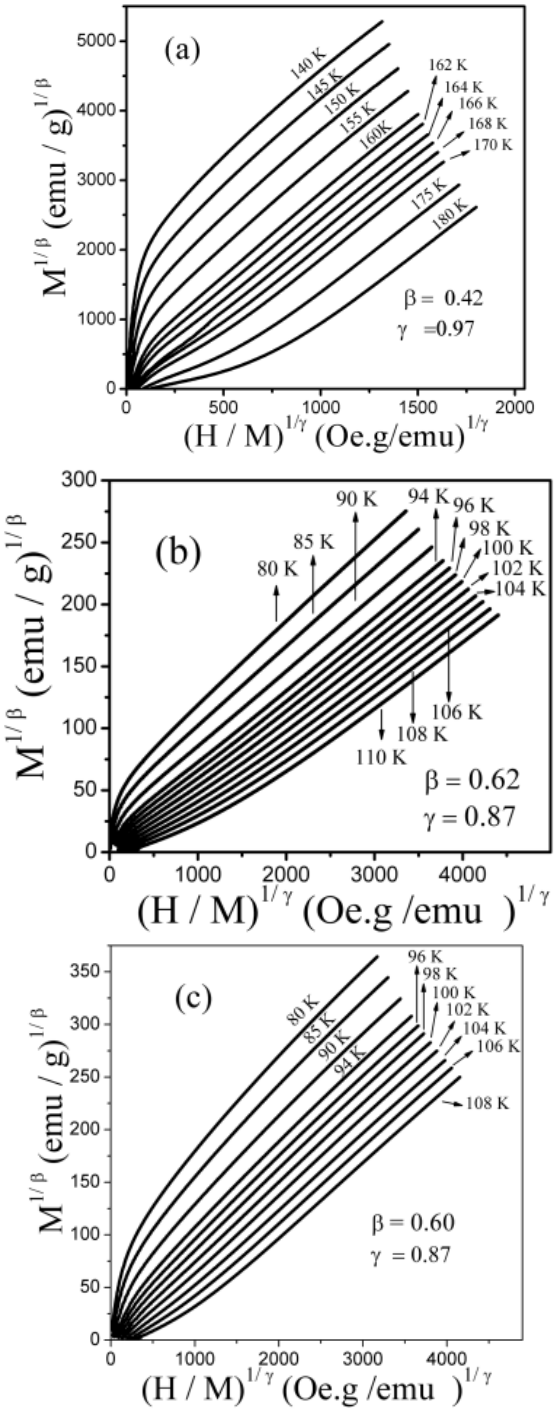

Fig. 5.11. Modified-Arrott plot isotherms of $M^{1/\beta}$ vs $(H/M)^{1/\gamma}$ of (a) $La_{0.37}Bi_{0.30}Ca_{0.33}MnO_3$, (b) $La_{0.37}Bi_{0.15}Sm_{0.15}Ca_{0.33}MnO_3$ and (c) $La_{0.37}Sm_{0.30}Ca_{0.33}MnO_3$ samples.

In order to find the appropriate critical exponents we have used the modified-Arrott plot method known as Arrott-Noakes equation of state [224] given by the equation

$$(H/M)^{1/\gamma} = a(T - T_C)/T + bM^{1/\beta} \tag{5.8}$$

where a and b are considered to be constants. In this, we have used mean-field values as initial values and then followed iteration method to find out the proper values of β and γ. From this the estimated values of β, γ and T_C for B30, B15S15 and S30 samples are listed in table 5.3. Fig. 5.11 is generated using the critical exponents obtained from the equation (5.8).

Fig. 5.12 illustrates the temperature dependent spontaneous magnetization, M_s (intercepts on $M^{1/\beta}$axis, below T_C), and the inverse initial susceptibility, χ_0^{-1} (intercepts on $(H/M)^{1/\gamma}$ axis, above T_C), plots. The best fit values obtained for theses samples and are listed in table 5.3.

Table 5.3. List of the values of β, γ, δ and T_C estimated from various plots.

Sample	**B30**				**B15S15**				**S30**			
Parameters	β	γ	δ	T_C (K)	β	γ	δ	T_C (K)	β	γ	δ	T_C (K)
Modified-Arrot	0.42	0.97	3.30	166	0.62	0.87	2.40	100	0.60	0.87	2.40	100
M_s vs T	0.43	-	3.25	165.6	0.60	-	2.45	98.37	0.59	-	2.49	99.96
χ_0^{-1}vs T	-	0.97		165.9	-	0.87		98.34	-	0.88		99.97
Kouvel-Fisher	0.43	-	3.30	165.6	0.62	-	2.35	98.30	0.61	-	2.42	100.10
	-	0.99		166.9	-	0.84		98.30	-	0.87	-	99.95
Eq. 5.4	-	-	3.27	-	-	-	2.26	-	-	-	2.56	-

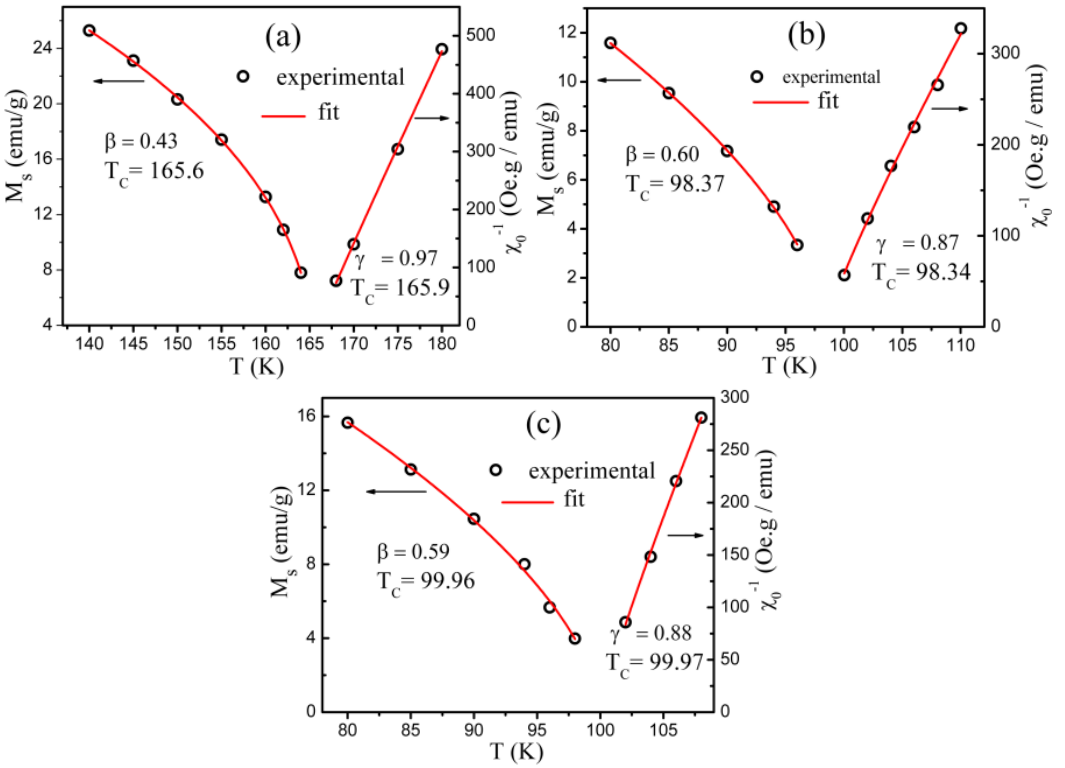

Fig. 5.12. Temperature dependence of spontaneous magnetization (M_s)[left, open circles]and the inverse initial susceptibility (χ_0^{-1})[right, open circles) of (a) $La_{0.37}Bi_{0.30}Ca_{0.33}MnO_3$, (b) $La_{0.37}Bi_{0.15}Sm_{0.15}Ca_{0.33}MnO_3$ and (c) $La_{0.37}Sm_{0.30}Ca_{0.33}MnO_3$ samples.

In order to find the critical exponents and T_C more accurately, we have used Kouvel-Fisher method [258, 262]. According to this, the equations are written as given below

$$M_S(T)/dM_S(T)/dT = (T - T_C)/\beta \tag{5.9}$$

$$\chi_0^{-1}(T)/d\chi_0^{-1}(T)/dT = (T - T_C)/\gamma \tag{5.10}$$

The exponent values for β and γ (table 5.3) are obtained from the fits based on these equations to the experimental data for M_s and χ_0^{-1}, depicted in Fig. 5.13. We have also calculated the value of δ both from Widom scaling relation [256],

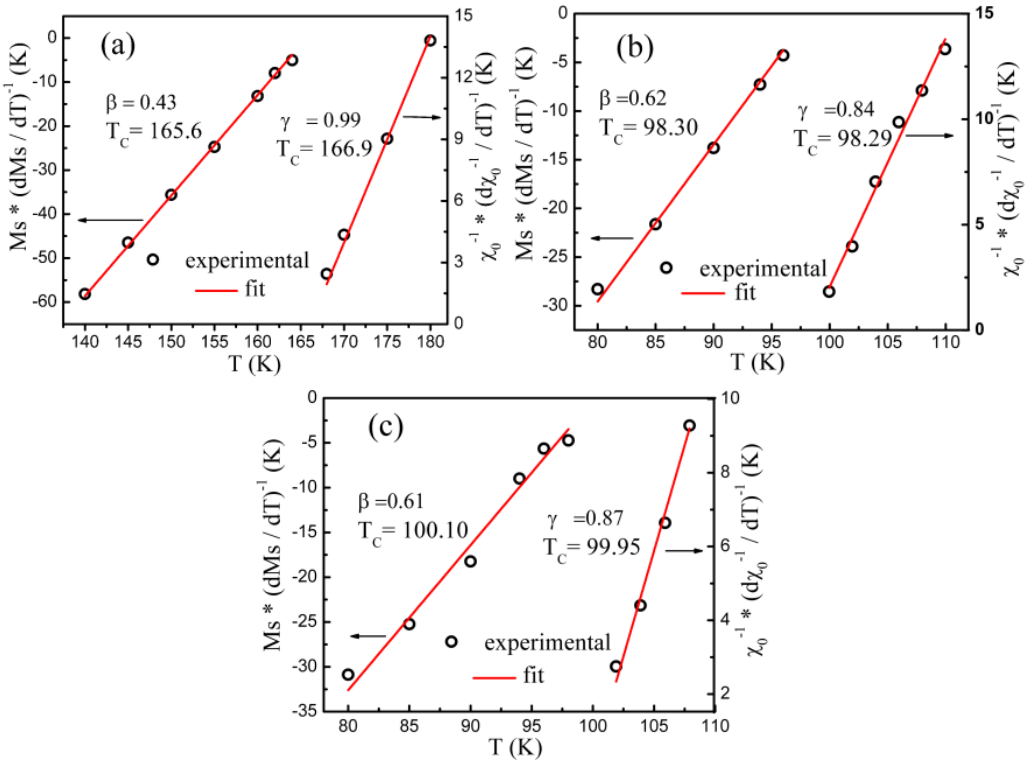

Fig. 5.13 Kouvel-Fisher plots for the spontaneous magnetization (M_s)[left, open circles] and the inverse initial susceptibility (χ_0^{-1}) [right, open circles] of (a) $La_{0.37}Bi_{0.30}Ca_{0.33}MnO_3$, (b) $La_{0.37}Bi_{0.15}Sm_{0.15}Ca_{0.33}MnO_3$ and (c) $La_{0.37}Sm_{0.30}Ca_{0.33}MnO_3$ samples.

$$\delta = 1 + \gamma / \beta \qquad (5.11)$$

and equation (5.4), listed in table 5.3.

Using scaling equation,

$$M(H, \varepsilon) = \varepsilon^{\beta} f_{\pm}(H / \varepsilon^{\beta+\gamma}) \qquad (5.12)$$

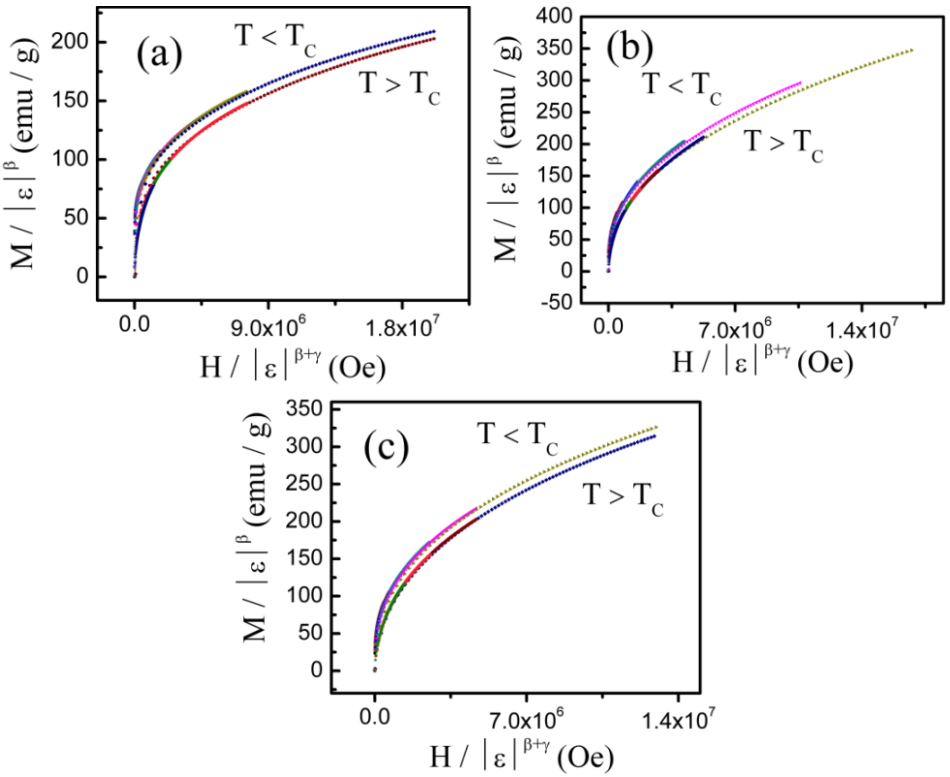

Fig. 5.14: Scaling ($M/|\varepsilon|^{\beta}$ vs $H/|\varepsilon|^{\beta+\gamma}$) plots below and above T_C using the critical exponents determined from Kouvel-Fisher method of (a) $La_{0.37}Bi_{0.30}Ca_{0.33}MnO_3$, (b) $La_{0.37}Bi_{0.15}Sm_{0.15}Ca_{0.33}MnO_3$ and (c) $La_{0.37}Sm_{0.30}Ca_{0.33}MnO_3$ samples.

where f_+ (f_-) for $T > T_C$ ($T < T_C$) are regular functions [256], we have plotted $M(H,\varepsilon)|\varepsilon|^{-\beta} vs\, H|\varepsilon|^{-(\beta+\gamma)}$ plots, shown in Fig. 5.14. These plots are fallen on two curves, one above T_C and the other below T_C and are in good agreement with the scaling theory. This indicates that the calculated critical exponents are reliable.

5.3.4. Transport studies

Fig. 5.15(A) shows the resistivity (ρ) vs T plots for the samples. All the samples show semiconducting behavior with decreasing temperature. At low doping levels ($x \leq 0.20$) metal-insulator behavior has been reported. However,

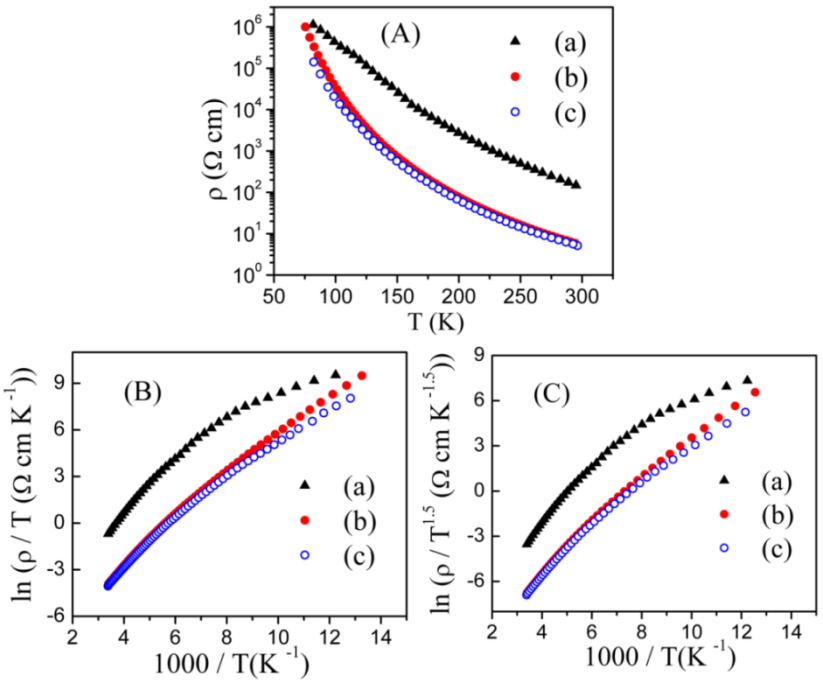

Fig. 5.15(A) ρ vs T, (B) $\ln(\rho/T)$ vs $1000/T$ and (C) $\ln(\rho/T^{1.5})$ vs $1000/T$ plots of (a) $La_{0.37}Bi_{0.30}Ca_{0.33}MnO_3$, (b) $La_{0.37}Bi_{0.15}Sm_{0.15}Ca_{0.33}MnO_3$ and (c) $La_{0.37}Sm_{0.30}Ca_{0.33}MnO_3$ samples.

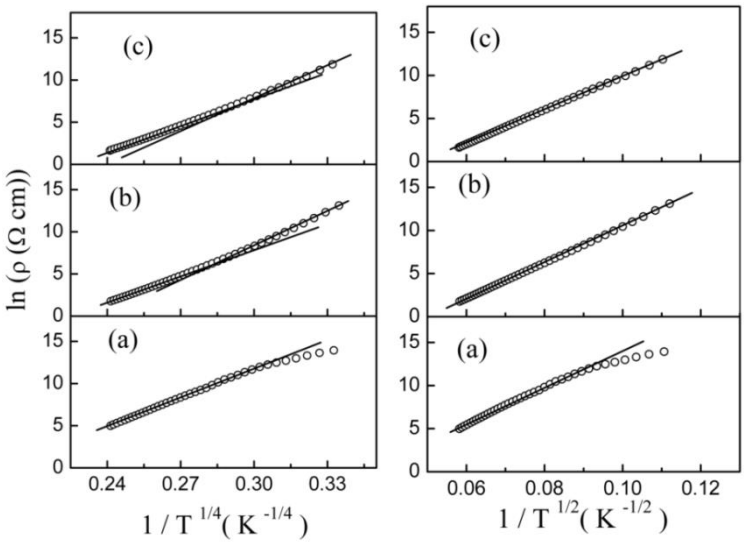

Fig. 5.16. $\ln\rho$ vs $1/T^{1/4}$ (left panel) and $\ln\rho$ vs $1/T^{1/2}$(right panel) plots of (a) $La_{0.37}Bi_{0.30}Ca_{0.33}MnO_3$, (b) $La_{0.37}Bi_{0.15}Sm_{0.15}Ca_{0.33}MnO_3$ and (c) $La_{0.37}Sm_{0.30}Ca_{0.33}MnO_3$ samples.

Table 5.4. List of the various parameters (T_0 and ρ_0) estimated from VRH model.

Sample	T_0 (10^8 K)		ρ_0 (10^{-13} Ω cm)	
	300 > T > 140	T < 140	300 > T > 140	T < 140
B30	0.593	-	1207	-
B15Sm15	0.47	1.24	192	0.0312
Sm30	0.42	0.66	385	9.40

Table 5.5. List of the various parameters (ξ, R and W) estimated from VRH model.

Sample	ξ (Å)		R (nm)		W (eV)	
	300 > T >140	T < 140	300> T >140	T <140	300 > T > 140	T < 140
B30	7.31	-	5.79	-	0.137	-
B15Sm15	7.87	5.72	5.89	5.44	0.129	0.164
Sm30	8.20	7.04	5.95	5.73	0.125	0.140

Table 5.6 List of the various parameters (T_0, ρ_0 and ξ) estimated from ES-VRH model.

Sample	T_0 (10^4 K)	ρ_0 (10^{-5}Ωcm)	ξ (Å)
B30	4.48	79.59	6.41
B15Sm15	4.43	2.63	6.49
Sm30	3.77	7.04	7.62

in present samples, in which doping levels are high (x = 0.30), such kind of behavior is not observed. Fig. 3.15(B) and Fig. 3.15(C) plots drawn using equation (3.11) and the continuous curvature in these plots indicate that the small polaron hopping (SPH) model is not suitable to analyze the data [19].

Using the variable range hopping (VRH) model (left panel of Fig. 5.16) the calculated values of various parameters such as characteristic temperature (T_0), characteristic resistivity (ρ_0), correlation length (ξ), hopping distance (R) and hopping energy (W) are listed in tables 5.4 and 5.5. Using Efros and Shklovskii-VRH (ES-VRH) model (right panel of Fig. 5.16) the estimated values of the various parameters are also listed in table 5.6. The values estimated from VRH model and theoretically predicted [211] values are in good agreement with each other.

5.3.5. Origin of disorder

The properties of the present samples differ from $La_{0.67}Ca_{0.33}MnO_3$. M and T_C are decreased when La is replaced by Bi and/or Sm. Below ~65 K for B30 and ~43 K for B15S15 and S30 samples, the drop in M_{ZFC} indicates the evolution of competing AFM and FM phases. As a result, the system will exhibit spin-cluster glass behavior. The sharp drop in M_{ZFC} for B15S15 and S30 is presumably due to the increased competition between AFM and FM interactions with Sm doping. This can be due to randomly distributed magnetic potential and Coulomb potential of Sm which prevents Mn-O-Mn bonds from forming the homogeneous long-range order and leads the formation of the cluster and spin-cluster glass state [263, 264]. In previous reports, it has been pointed out that $La_{0.67}Ca_{0.33}MnO_3$ manganite exhibits first-order transition. The present doped samples, however, exhibit second-order transition. The estimated critical exponents are close to values predicted by MFT. The decrease in M, T_C and evolution of spin or cluster glass and the nature of phase transition, i.e., second-order phase transition (compared to first-order transition in $La_{0.67}Ca_{0.33}MnO_3$), are ascribed to the disorder in the samples due to the lattice distortion caused by the size mismatch of the A-site cations by Bi^{3+} and Sm^{3+} ion doping at La-site [108, 265]. A well-known fact is that the T_C is directly proportional to the total exchange integral ($J_{ex,\ total}$). The $J_{ex,\ total}$ which is the sum of exchange integral due to DE($J_{ex,DE}$) and SE($J_{ex,SE}$) interaction [266] decreases and hence, T_C also decreases when La^{3+} is replaced by smaller Sm^{3+} ion. The Sm^{3+} doping may lead to distortion in Mn-O-Mn network and weakening of FM-DE exchange interactions, as a result $J_{ex,\ SE}$ increases. Hence, $J_{ex,\ total}$ decreases, this results in the decrease of T_C [263, 267]. In the case of Bi-doped sample apart from the difference of ionic radius between La^{3+} and Bi^{3+}, it is necessary to consider the effect of $6s^2$ lone pair electrons of Bi^{3+} ion on the properties of Bi-doped samples [110]. Because of covalent nature, the Bi-O bond is shorter than La-O bond. Due to the electronegativity of Bi, the

hybridization between 6s of Bi^{3+} orbitals and 2p of O^{2-} may enhance and produce a local distortion. The smaller angle of Mn-O-Mn for Bi-doped sample compared to undoped sample is evidence for the enhancement in hybridization and local distortion. As we know that the local distortion can hinder the movement of e_g electrons from Mn to Mn. This in turn causes the localization of electrons around Bi^{3+} ions and weakens the FM-DE interactions, as a result, the decrease in T_C and M are observed [107]. The localization state act as pinning center to small polaron hopping, probably this could be the reason for higher resistivity of Bi-doped sample [110].

It has been reported [107] that low level of Bi doping in $La_{0.62}Bi_{0.05}Ca_{0.33}MnO_3$ shows first order phase transition from FM to PM. In the present study, the high level of Bi doping in $La_{0.37}Bi_{0.30}Ca_{0.33}MnO_3$ shows second-order phase transition from FM to PM. This difference is because of additional disorder induced by the high level of Bi doping. It has been reported that the $La_{0.7-x}Sm_xCa_{0.3}MnO_3$ with $x \geq 0.05$ show second order FM-PM transition [120]. It is reported that single crystal of $La_{0.7}Sr_{0.3}MnO_3$ (LSMO) shows second-order phase transition from FM-PM with critical exponents for $\beta = 0.37\pm0.04$, $\gamma = 1.22\pm0.03$ and $\delta = 4.25\pm0.2$, which are close to the values predicted for conventional Heisenberg ferromagnet [268]. Whereas $La_{1-x}Ca_xMnO_3$ manganite undergoes first-order FM-PM transition in the composition range $0.30 \leq x \leq 0.40$ [259, 269, 270]. This difference between the nature of FM-PM transition of the two systems is presumably due to the increased average A-site ionic radius of LSMO [Sr^{2+} (1.32Å)] compared to LCMO [Ca^{2+} (1.12 Å)]. However, the present doped samples show second-order transition at the critical point, although the average A-site ionic radius is reduced when Bi/Sm is substituted at La-site. The present results suggest that it is not the A-site ionic radius alone which decides the nature of FM-PM transition. The disorder introduced in the system by the dopant ion is also important in deciding the nature of FM-PM transition [271]. The structural

analysis of the samples reveals that the $<r_A>$ decreases due to the substitution of smaller ionic radii (Bi^{3+} and Sm^{3+}) ions in place of higher ionic radii (La^{3+}) ions at the A-site which causes the value of t to decrease, leading to the decrease in Mn-O-Mn bond angle and the increase of Mn-O bond length. This in turn reduces the bandwidth which results in the decrease of the mobility of e_g electrons [18, 26]. The decrease in bandwidth and the mobility of e_g electrons weakens the FM-DE coupling and hence M and T_C decrease rapidly [263, 265]. Similar results are reported in Nd-doped La-manganites [257].

5.4. Conclusions

In conclusion, $La_{0.37}D_{0.30}Ca_{0.33}MnO_3$ (D = Bi, Sm) and $La_{0.37}Bi_{0.15}Sm_{0.15}Ca_{0.33}MnO_3$ manganite samples are synthesized by sol-gel method. The structural studies on these samples confirm the orthorhombic nature with *Pnma* space group. The critical behavior was investigated through various techniques such as modified-Arrot plots, Kouvel-Fisher method and critical isotherm analysis. The samples show second-order phase transition near the critical point. Resistivity data follow the semiconducting behavior. The decrease in magnetization (M), Curie temperature (T_C), evolution of spin or cluster glass behavior and the nature of second-order phase transition compared to first-order transition in $La_{0.67}Ca_{0.33}MnO_3$ are ascribed to the disorder caused by the size mismatch of the A-site cations with Bi and Sm doping at La-site.

This page is intentionally left blank

Chapter 6

Effect of nonmagnetic ion doping on the properties of $Bi_{0.7}Ca_{0.3}Mn_{0.95}Y_{0.05}O_3$(Y = Mg, Al and Sn)

6.1. Introduction

Doping of Mn in manganites by magnetic or nonmagnetic ion directly affects various physical properties such as magnetic and transport since B-site substitution has the direct impact on the Mn-O network and e_g electron density. In this chapter, we report the effect of nonmagnetic ion doping at the Mn-site on the properties of $Bi_{0.7}Ca_{0.3}Mn_{0.95}Y_{0.05}O_3$(Y = Mg, Al and Sn) system. The results are analyzed in view of disorder induced by the substitution of nonmagnetic ions at the Mn-site.

6.2. Sample preparation

The stoichiometric amounts of pure $Bi(NO_3)_3.5H_2O$, $Ca(NO_3)_2.4H_2O$, $MnCl_2.4H_2O$ and $Mg(NO_3)_2.6H_2O$/$Al(NO_3)_3.5H_2O$/ $SnCl_2.4H_2O$ were dissolved in distilled water to obtain clear solution. Citric acid was added with constant stirring and the ratio of metal cation to citric acid is kept at 1:2. The pH of the solution was adjusted to ~6-7 by adding ammonia solution. Ethylene-glycol was added to this to a get viscous solution. The solution was slowly evaporated to get a gel by keeping the temperature at ~60-70 ^oC with constant stirring for several hours (hrs). Then the prepared gel was decomposed at 250 ^oC. Then the powder was sintered in a furnace at 900 ^oC for 4 hrs. Then the sintered powder was mixed in an agate mortar. Then in the final step the powder was pressed into pellets and

again sintered at 900 ^{o}C for 4 hrs. The synthesized samples, $Bi_{0.7}Ca_{0.3}MnO_3$, $Bi_{0.7}Ca_{0.3}Mn_{0.95}Mg_{0.05}O_3$, $Bi_{0.7}Ca_{0.3}Mn_{0.95}Al_{0.05}O_3$ and $Bi_{0.7}Ca_{0.3}Mn_{0.95}Sn_{0.05}O_3$ are named as Mn100, Mn95Mg5, Mn95Al5 and Mn95Sn5, respectively.

6.3. Results and discussion

6.3.1. Structure and morphology studies

Ionic radii of Mg^{2+}, Al^{3+}, Sn^{2+}, Mn^{3+} and Mn^{4+} ions are 0.88, 0.53, 1.02, 0.64 and 0.53 Å, respectively. Due to the large difference between the ionic radii of A-site [Bi^{3+} (1.24 Å) and Ca^{2+} (1.12 Å)] cations and dopants, occupation of A-site may not be possible [272] so that we believe that all the dopants replace the Mn-site. The Rietveld refinement of the room temperature x-ray diffraction (XRD) pattern of the samples is shown in Fig. 6.1. For all the samples except Al doped sample, two impurity peaks (marked with *) at a diffraction angle ~29^{o} and 30^{o}

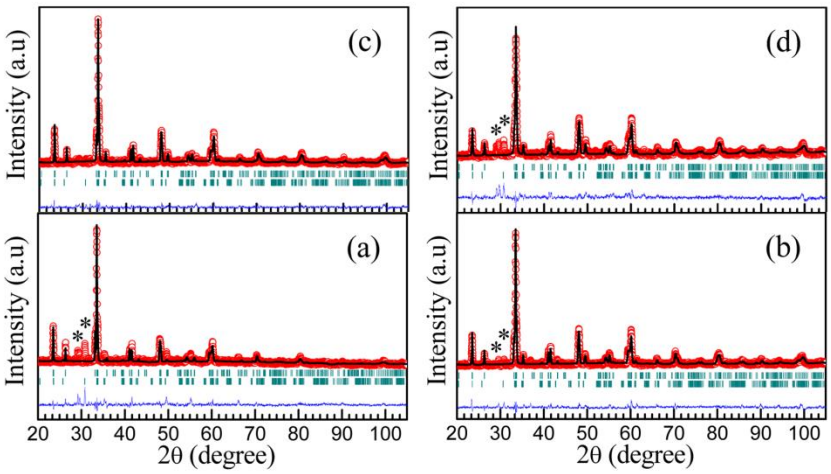

Fig. 6.1 Rietveld refinement (solid black lines) of the XRD data (open red circles) along with diffraction planes (green lines) and difference between the experimental and fitting data (blue lines) of (a) $Bi_{0.7}Ca_{0.3}MnO_3$, (b) $Bi_{0.7}Ca_{0.3}Mn_{0.95}Mg_{0.05}O_3$, (c) $Bi_{0.7}Ca_{0.3}Mn_{0.95}Al_{0.05}O_3$ and (d) $Bi_{0.7}Ca_{0.3}Mn_{0.95}Sn_{0.05}O_3$ samples.

Table 6.1. List of the structural parameters (orthorhombic percentage, (atomic positions(x, y and z), lattice parameters (*a*, *b* and *c*), *V*, *S* <d_{Mn-O}> and <Mn-O-Mn> estimated from the refinement of the XRD data of all the samples.

Sample	**Mn100**	**Mn95Mg5**	**Mn95Al5**	**Mn95Sn5**
Orthorhombic (%)	75.20	79.52	89.21	70.34
Bi/Ca				
x	0.035	0.046	0.044	0.049
y	0.250	0.250	0.250	0.250
z	0.998	0.995	0.992	0.998
Mn/Mg/Al/Sn				
x	0.500	0.500	0.500	0.500
y	0.500	0.500	0.500	0.500
z	0	0	0	0
O(1)				
x	0.413	0.488	0.498	0.521
y	0.2500	0.250	0.250	0.250
z	0.011	0.083	0.045	0.088
O(2)				
x	0.219	0.273	0.229	0.207
y	0.509	0.484	0.521	0.505
z	0.199	0.273	0.191	0.219
***a* (Å)**	5.329	5.408	5.402	5.406
***b* (Å)**	7.400	7.549	7.542	7.549
***c* (Å)**	5.378	5.312	5.308	5.314
***V* (Å^3)**	212	216	216	216
S	2.28	2.54	2.46	2.51
<d_{Mn-O}> (Å)	1.927	1.918	1.916	1.926
<Mn-O-Mn> (^{o})	156.82	160.26	162.55	157.29

are observed. It has been reported that the undoped sample exists in the monoclinic structure with *C* 2/*c* space group [115]. However, we could not get a proper refinement with this structure. Then, orthorhombic parameters with *Pnma* space group are used for refining the structure of the samples. Though orthorhombic structure gave relatively best fit, a few reflections which were fitted using with monoclinic structure are missing. From this, it is concluded that the

Table 6.2. List of the structural parameters (monoclinic percentage, atomic positions(x, y and z) lattice parameters (*a*, *b*, *c* and *β*) and *V* estimated from the refinement of the XRD data of all the samples.

Sample	**Mn100**	**Mn95Mg5**	**Mn95Al5**	**Mn95Sn5**
Monoclinic (%)	24.80	20.48	10.71	29.66
Bi/Ca				
x	0.135	0.130	0.131	0.130
y	0.242	0.239	0.237	0.243
z	0.132	0.136	0.130	0.130
Mn(1)/Mg(1) /Al(1)/Sn(1)				
x	0.000	0.000	0.000	0.000
y	0.337	0.292	0.300	0.338
z	0.750	0.750	0.750	0.750
Mn(2)/Mg(2) /Al(2)/Sn(2)				
x	0.250	0.250	0.250	0.250
y	0.250	0.250	0.250	0.250
z	0.500	0.500	0.500	0.500
O (1)				
x	0.083	0.090	0.091	0.090
y	0.180	0.189	0.190	0.190
z	0.564	0.585	0.576	0.576
O (2)				
x	0.152	0.153	0.182	0.154
y	0.565	0.520	0.529	0.566
z	0.370	0.317	0.335	0.327
O (3)				
x	0.336	0.404	0.292	0.346
y	0.545	0.484	0.480	0.526
z	0.154	0.151	0.158	0.158
***a* (Å)**	9.240	9.315	9.302	9.305
***b* (Å)**	5.304	5.322	5.328	5.304
***c* (Å)**	9.287	9.267	9.255	9.279
***B* (degree)**	109.54	109.16	109.02	109.10
***V* (Å^3)**	455	459	458	457

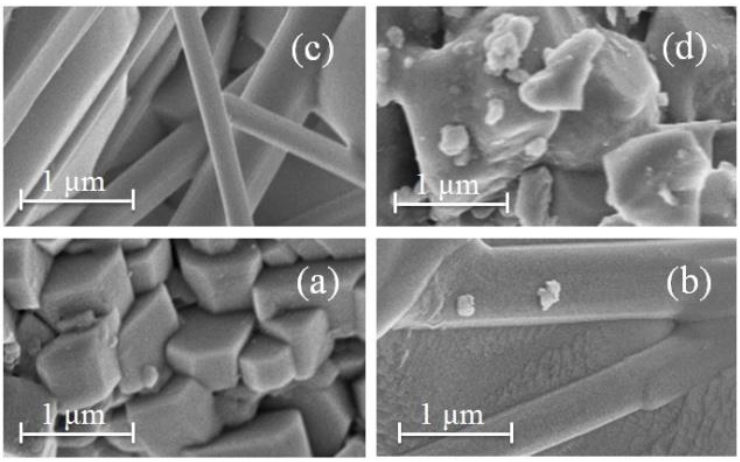

Fig. 6.2. FESEM micrographs of (a) $Bi_{0.7}Ca_{0.3}MnO_3$, (b) $Bi_{0.7}Ca_{0.3}Mn_{0.95}Mg_{0.05}O_3$, (c) $Bi_{0.7}Ca_{0.3}Mn_{0.95}Al_{0.05}O_3$ and (d) $Bi_{0.7}Ca_{0.3}Mn_{0.95}Sn_{0.05}O_3$ samples.

existence of the reflections of both the structures. In order to achieve the best fit, both phases are simultaneously used for refining the structure. However, the refinement confirms that the percentages of both the phases vary from sample to sample. The estimated percentage of each phase, atomic positions (x, y and z), lattice parameters (*a*, *b* and *c*), unit cell volume (*V*) and the goodness of fit (*S*) are listed in tables 6.1 and 6.2. For the orthorhombic phase the average Mn-O bond length ($<d_{Mn\text{-}O}>$) and the average Mn-O-Mn bond angle (<Mn-O-Mn>) values are estimated and also listed in table 6.1. The present series of samples have more than 70 % of orthorhombic phase which contradicts the literature [115]. The change in the crystal structure compared to the literature may be due to the increased homogeneity of the samples or sintering conditions which in turn may affect oxygen valency [273]. All the samples have same structure irrespective of the type of doping [144]. A slight increment in the value of unit cell volume is observed with doping which is ascribed to the higher ionic radii of dopants [272, 274]. In order to explore the effect of impurity on structural parameters, refinement has also been performed by excluding impurity part of the diffraction

angle. However, no changes are observed in the corresponding structural parameters of the samples. The field emission scanning electron microscopy (FESEM) micrographs of the samples are shown in Fig. 6.2, indicating the change in the microstructure with doping. The grains of the undoped sample have cuboid structure. The grains of Mg and Al doped samples have similar kind of microstructure to each other. The energy dispersive x-ray (EDX) spectroscopy results confirm the purity of the samples.

6.3.2. Electron spin resonance studies

The electron spin resonance (ESR) spectra, at some selected temperatures are shown in Fig. 6.3. It is observed that for all the samples, at a given temperature the ESR spectra have similar trend, indicating that the doping does not have much impact on the spectra. Since all the spectra are symmetric, Lorentzian line shape equation [equation (3.1)] is used to fit the spectra and shown in Fig. 6.4 for all the samples measured at 273 K. The normalized double integrated intensity (*DI*) of

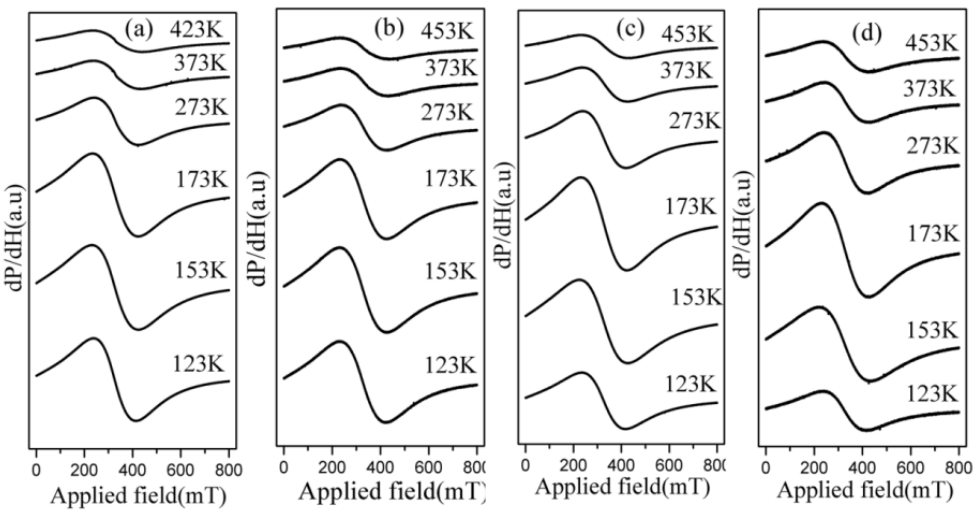

Fig. 6.3. ESR spectra of (a) $Bi_{0.7}Ca_{0.3}MnO_3$, (b) $Bi_{0.7}Ca_{0.3}Mn_{0.95}Mg_{0.05}O_3$, (c) $Bi_{0.7}Ca_{0.3}Mn_{0.95}Al_{0.05}O_3$ and (d) $Bi_{0.7}Ca_{0.3}Mn_{0.95}Sn_{0.05}O_3$ samples measured at various temperatures.

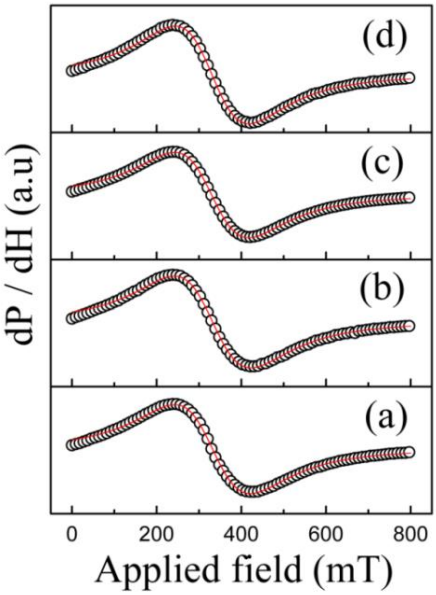

Fig. 6.4. Lorentzian fit (solid red line) to the ESR spectra (open circles) of (a) $Bi_{0.7}Ca_{0.3}MnO_3$, (b) $Bi_{0.7}Ca_{0.3}Mn_{0.95}Mg_{0.05}O_3$, (c) $Bi_{0.7}Ca_{0.3}Mn_{0.95}Al_{0.05}O_3$ and (d) $Bi_{0.7}Ca_{0.3}Mn_{0.95}Sn_{0.05}O_3$ samples measured at 273 K.

ESR signal as a function of temperature is shown in Fig. 6.5(A) for various samples. As the temperature decreases from 453 K, *DI* increases and reaches its maximum at ~160 K. Below Neel temperature (T_N), a rapid decrease in *DI* is observed for all the samples. Although, *DI* shows a small peak at charge ordering temperature (T_{CO}), it is not as prominent as observed for $Bi_{1-x}Ca_xMnO_3$ ($0.40 \leq x \leq 0.60$) [7, 104, 215, 216]. For all the samples, the inverse of *DI* as a function of temperature is shown in Fig. 6.5(B).The x-axis intercepts of these plots are indicative of the kind of magnetic interactions dominating the ESR signals. The positive intercept on the x-axis in the temperature range $T > T_{CO}$ indicates the existence of ferromagnetic (FM)-double exchange (DE) correlations. Fig. 6.5(C) shows the ln*DI* vs 100/*T* plots of the samples. The data follow linear behavior above T_{CO}. No prominent changes in the slope of the samples are observed which indicate that doping does not affect the behavior of the samples.

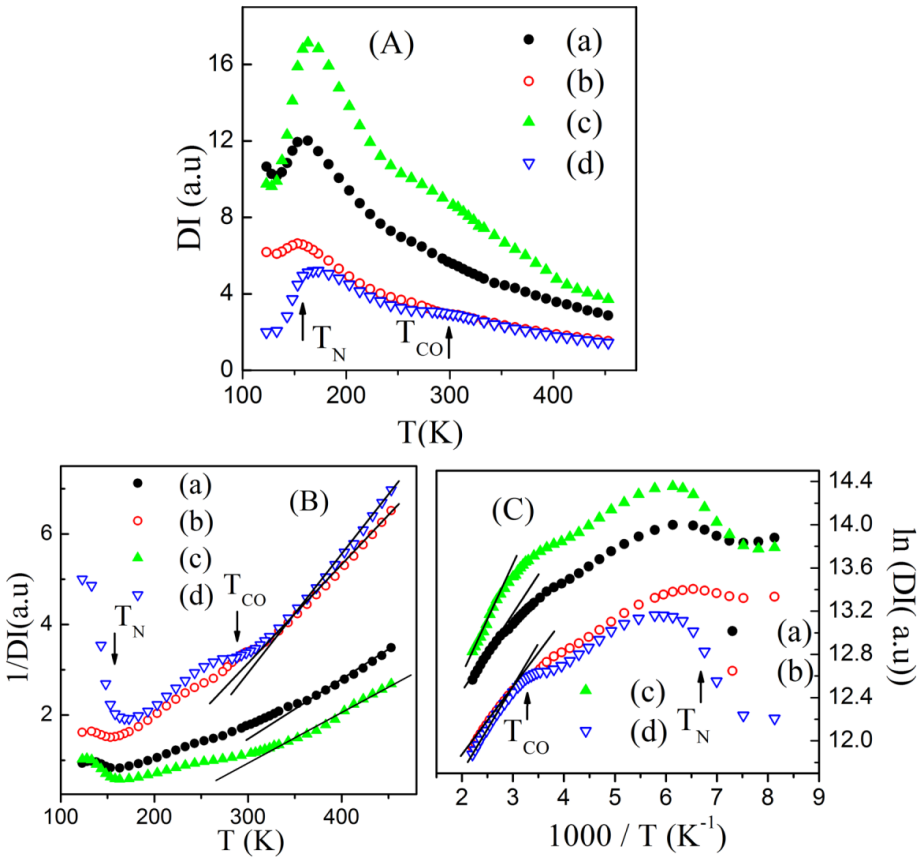

Fig. 6.5 (A) *DI* vs *T*, (B) 1/*DI* vs *T* and (C) ln*DI* vs 1000/*T* plots of (a) $Bi_{0.7}Ca_{0.3}MnO_3$, (b) $Bi_{0.7}Ca_{0.3}Mn_{0.95}Mg_{0.05}O_3$, (c) $Bi_{0.7}Ca_{0.3}Mn_{0.95}Al_{0.05}O_3$ and (d) $Bi_{0.7}Ca_{0.3}Mn_{0.95}Sn_{0.05}O_3$ samples.

For all the samples temperature dependences of peak to peak linewidth (ΔH) is shown in Fig. 6.6(A). As the temperature decreases from 453 K, ΔH decreases reaches its minimum at T_{CO} and then increases. The estimated values of T_{CO} and T_N from ΔH plots are listed in table 6.3. For all the samples, resonance field (H_r) as a function of temperature is shown in Fig. 6.6(B). H_r decreases with decreasing temperature from 453 K. The estimated value of Lande *g*-factor (*g*) in the high-temperature region is ~1.98 which is the strong evidence for their paramagnetic (PM) nature. The small dip in the H_r as function temperature is observed, which corresponds to the $T_{CO.}$ The sharp decrease in the H_r below ~160 K is an indicative

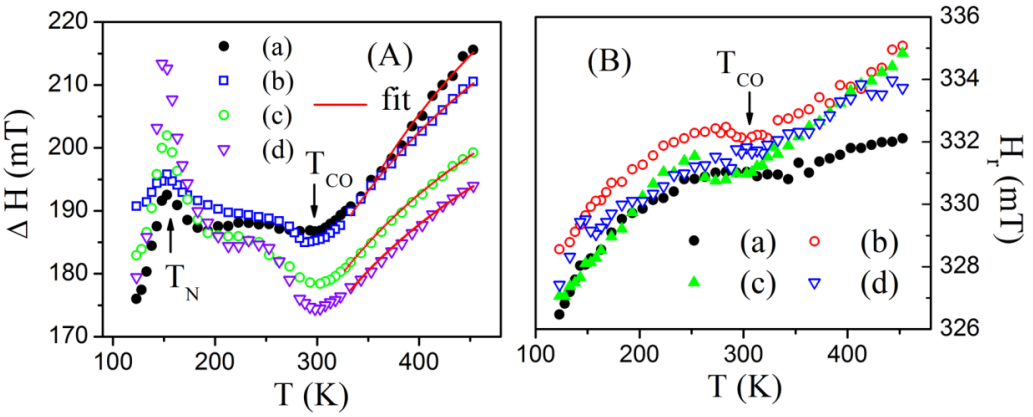

Fig. 6.6 (A) ΔH vs T and (B) H_r vs T plots of (a) $Bi_{0.7}Ca_{0.3}MnO_3$, (b) $Bi_{0.7}Ca_{0.3}Mn_{0.95}Mg_{0.05}O_3$, (c) $Bi_{0.7}Ca_{0.3}Mn_{0.95}Al_{0.05}O_3$ and (d) $Bi_{0.7}Ca_{0.3}Mn_{0.95}Sn_{0.05}O_3$ samples. Solid red lines in Fig. 6.6 (A) are according to theoretical model [173, 176].

Table 6.3. List of the various parameters (T_N, T_{CO}, $\Delta H(\infty)$ and B) estimated from ESR (ΔH vs T) data of all the samples.

Sample	T_N (K)	T_{CO} (K)	$\Delta H(\infty)$ (G)	B (GK^{-1})
Mn100	153	300	2967	0
Mn95Mg5	153	291	2661	0.031
Mn95Al5	153	300	2448	0.03
Mn95Sn5	148	295	2370	0.035

of the existence of FM clusters in the low-temperature region [7, 104].

In order to understand the spin dynamics of the system, ΔH data is analyzed using equation (3.7) [173, 176] and the fitting parameters, high-temperature asymptote ($\Delta H(\infty)$) and the strength of interactions between the e_g electrons (B) of these plots are listed in table 6.3. For all the samples the estimated values of Curie-Weiss temperature (θ_C) are around 95 K. The undoped sample has zero B value whereas all the doped samples have its value around ~ 0.03. This indicates that the observed ΔH behavior of the undoped samples can only be due to pure ion-ion spin relaxation. However decrease in the value of $\Delta H(\infty)$ and non-zero

value of *B* for doped samples is an indication of weakening of the strength of spin-spin relaxation and evolution of spin-lattice interactions, respectively.

6.3.3. Magnetization studies

6.3.3.1. Temperature dependent magnetization

Fig. 6.7 shows the temperature dependences of magnetization (*M*) for all the samples both in zero-field cooled (ZFC) and field cooled (FC) modes in a static magnetic field (*H*) of 500 Oe. For all the samples, as the temperature decreases from 325 K, *M* increases slowly. For undoped and Sn-doped samples *M* reaches a peak at T_N, as shown in the inset of Fig. 6.7, below this *M* decreases slightly then it increases with further decrease in temperature. Whereas for Al and Mg-doped samples no T_N is observed and *M* continuously increases with decrease in temperature. Below ~50 K, *M* increases sharply in both ZFC and FC modes. Below this, *M* in ZFC mode reaches a peak at spin freezing temperature (T_f),

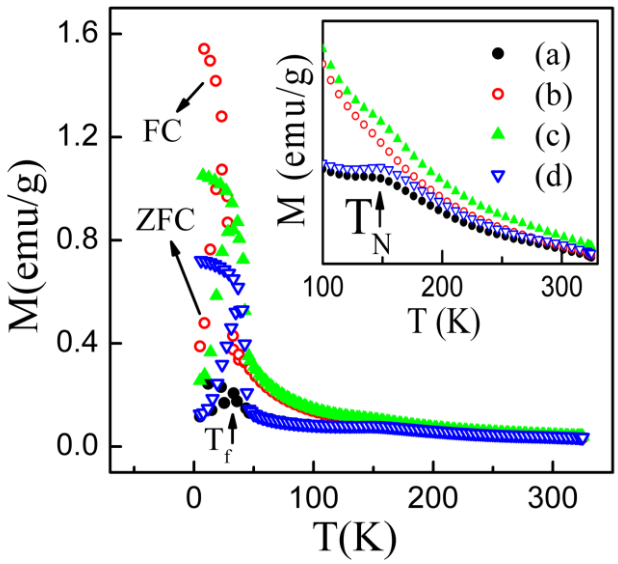

Fig. 6.7 *M* vs *T* plots of (a) $Bi_{0.7}Ca_{0.3}MnO_3$, (b) $Bi_{0.7}Ca_{0.3}Mn_{0.95}Mg_{0.05}O_3$, (c) $Bi_{0.7}Ca_{0.3}Mn_{0.95}Al_{0.05}O_3$ and (d) $Bi_{0.7}Ca_{0.3}Mn_{0.95}Sn_{0.05}O_3$ samples measured in a static magnetic field of 500 Oe. Inset shows *M* vs *T* expansion in the temperature range 100 K < *T* < 325 K.

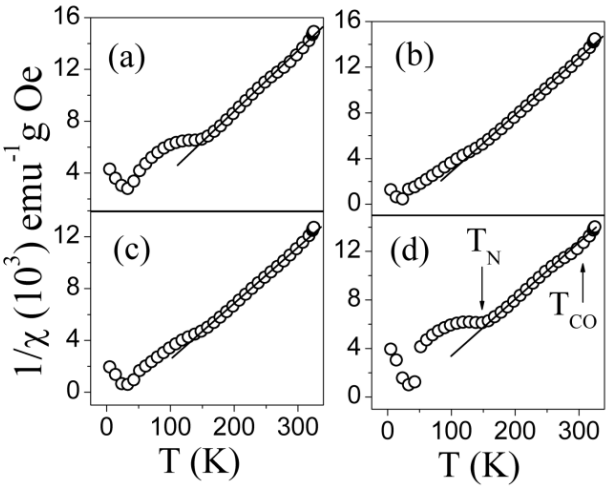

Fig. 6.8. $1/\chi$ vs T plots (for M_{ZFC} data) of (a) $Bi_{0.7}Ca_{0.3}MnO_3$, (b) $Bi_{0.7}Ca_{0.3}Mn_{0.95}Mg_{0.05}O_3$, (c) $Bi_{0.7}Ca_{0.3}Mn_{0.95}Al_{0.05}O_3$ and (d) $Bi_{0.7}Ca_{0.3}Mn_{0.95}Sn_{0.05}O_3$ samples.

Table 6.4. List of the various parameters (T_N, T_{CO}, θ_C and μ_{eff}) of all the samples estimated from magnetization data.

Sample	T_N (K)	T_{CO} (K)	θ_C (K)	μ_{eff} (μ_B)
Mn100	150	298	20	6.52
Mn95Mg5	-	-	46	6.47
Mn95Al5	148	-	45	6.83
Mn95Sn5	150	294	33	6.55

whereas M in FC mode continuously increases with decrease in temperature. This behavior is attributed to spin glass (SG) behavior.

In order to extract further information about the magnetic interaction we have plotted the ZFC magnetization (M_{ZFC}) data as per Curie-Weiss law, is shown in Fig. 6.8. From this fit the estimated values of θ_C and effective magnetic moment (μ_{eff}) [$T < T_{CO}$] are listed in table 6.4. From the estimated values of θ_C, it is concluded that substitution of Mn by Mg, Al and Sn enhances the FM correlations than that of undoped material. The estimated values of T_{CO} and T_N are listed in table 6.4.

6.3.3.2. Magnetic field dependent magnetization

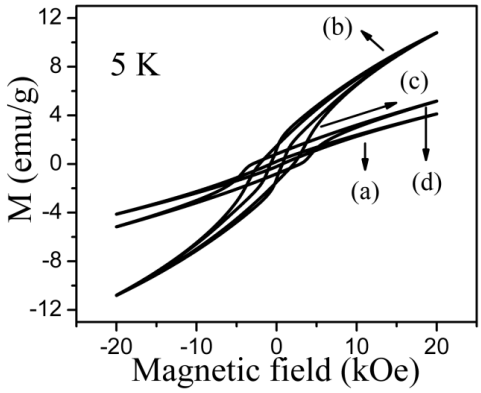

Fig. 6.9. *M* vs magnetic field (*H*) plots, measured at 5 K, of (a) $Bi_{0.7}Ca_{0.3}MnO_3$, (b) $Bi_{0.7}Ca_{0.3}Mn_{0.95}Mg_{0.05}O_3$, (c) $Bi_{0.7}Ca_{0.3}Mn_{0.95}Al_{0.05}O_3$ and (d) $Bi_{0.7}Ca_{0.3}Mn_{0.95}Sn_{0.05}O_3$ samples.

For all the samples magnetic field dependences of magnetization plots are shown in Fig. 6.9. All the samples display hysteresis at 5 K, indicating the FM cluster formation. From this the estimated values of saturation magnetization (M_{sat}) (at 5 K, 20 kOe) are around 0.023, 0.117, 0.0925 and 0.0382 μ_B/f.u for unoped, Mg, Al and Sn doped samples, respectively.

6.3.4. Transport studies

Fig. 6.10 (A) shows the resistivity (ρ) as a function of temperature plots for the samples. All the samples show semiconducting behavior with decreasing temperature. Fig. 6.10 (B) and Fig.6.10 (C) plots were drawn using equation (3.11), and the continuous curvature of these plots indicate that the small polaron hopping (SPH) model is not suitable to analyze the data. Using the variable range hopping (VRH) model (left panel of Fig.6.11) the calculated values of various parameters such as characteristic temperature (T_0), characteristic resistivity (ρ_0), correlation length (ξ), hopping distance (R) and hopping energy (W) are listed in

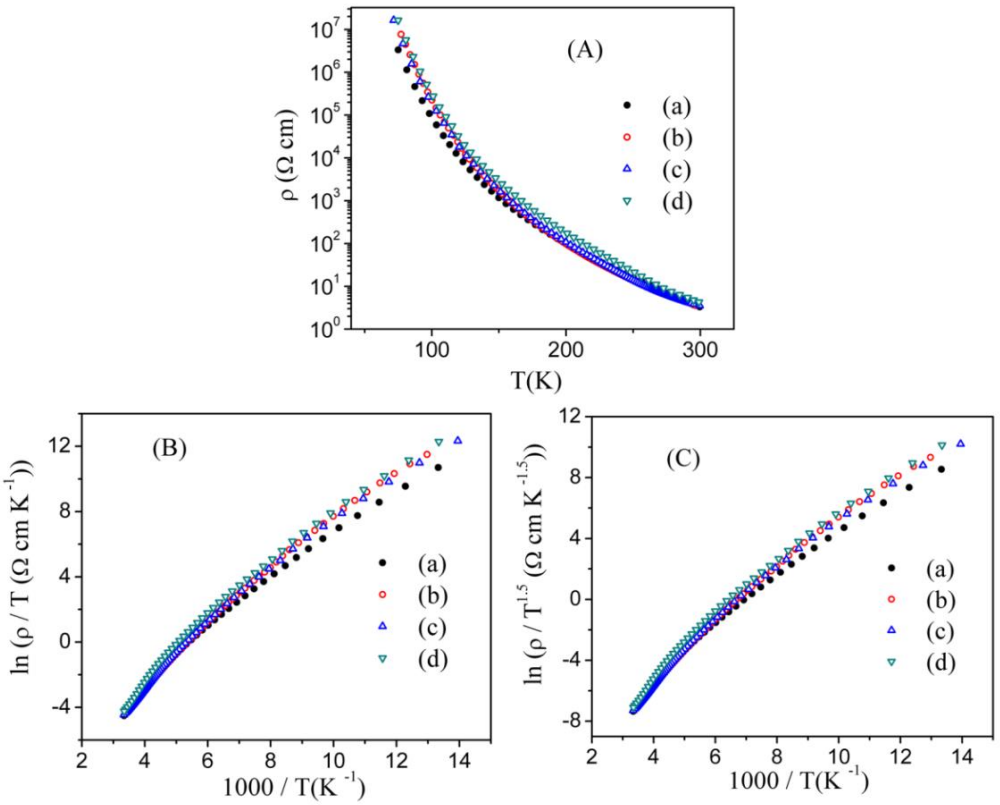

Fig. 6.10 (A) ρ vs T, (B) ln(ρ/T) vs 1000/T and (C) ln($\rho/T^{1.5}$) vs 1000/T plots of (a) $Bi_{0.7}Ca_{0.3}MnO_3$, (b) $Bi_{0.7}Ca_{0.3}Mn_{0.95}Mg_{0.05}O_3$, (c) $Bi_{0.7}Ca_{0.3}Mn_{0.95}Al_{0.05}O_3$ and (d) $Bi_{0.7}Ca_{0.3}Mn_{0.95}Sn_{0.05}O_3$ samples.

Table 6.5. List of the various parameters (T_0 and ρ_0) of all the samples estimated from VRH model.

Sample	**T_0 (10^8 K)**		**ρ_0 (10^{-13} Ω cm)**	
	$T_{CO} > T > T_N$	$T < T_N$	$T_{CO} > T > T_N$	$T < T_N$
Mn100	0.842	1.71	2.70	0.0019
Mn95Mg5	1.27	2.70	0.0739	1.51366E-05
Mn95Al5	1.30	2.25	0.0611	0.000123732
Mn95Sn5	1.26	2.46	0.142	7.14585E-05

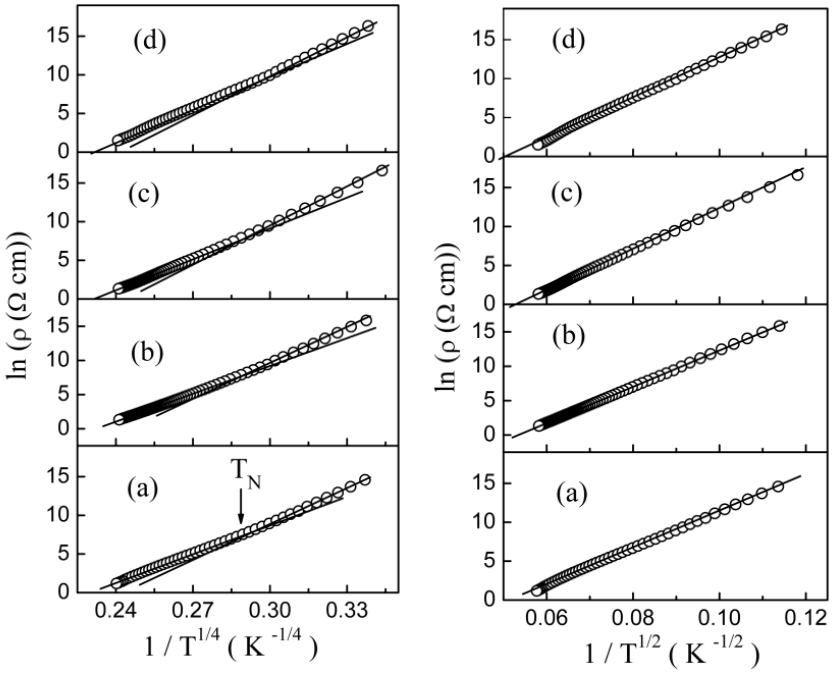

Fig. 6.11. lnρ vs $1/T^{1/4}$ (left panel) and lnρ vs $1/T^{1/2}$ (right panel) plots of (a) $Bi_{0.7}Ca_{0.3}MnO_3$, (b) $Bi_{0.7}Ca_{0.3}Mn_{0.95}Mg_{0.05}O_3$, (c) $Bi_{0.7}Ca_{0.3}Mn_{0.95}Al_{0.05}O_3$ and (d) $Bi_{0.7}Ca_{0.3}Mn_{0.95}Sn_{0.05}O_3$ samples.

Table 6.6. List of the various parameters (ξ, R and W) of all the samples estimated from VRH model.

Sample	ξ (Å)		R (nm)		W(ev)	
	$T_{CO} > T > T_N$	$T < T_N$	$T_{CO} > T > T_N$	$T < T_N$	$T_{CO} > T > T_N$	$T < T_N$
Mn100	6.50	5.13	5.62	5.30	0.149	0.178
Mn95Mg5	5.67	4.41	5.43	5.10	0.165	0.199
Mn95Al5	5.62	4.69	5.42	5.18	0.166	0.190
Mn95Sn5	5.69	4.54	5.43	5.14	0.165	0.195

Table 6.7. List of the various parameters (T_0, ρ_0 and ξ) of all the samples estimated from ES-VRH model.

Sample	T_0 (10^4 K)	ρ_0 (10^{-6} Ω cm)	ξ (Å)
Mn100	5.41	6.80	5.30
Mn95Mg5	6.9	0.75	4.10
Mn95Al5	6.46	1.67	4.45
Mn95Sn5	6.54	2.37	4.39

tables 6.5 and 6.6. Using Efros and Shklovskii-VRH (ES-VRH) model (right panel of Fig. 6.11) the estimated values of various parameters are also listed in table 6.7. The value of various parameters estimated from VRH model is in good agreement with the values predicted theoretically [211].

6.3.5. Discussion

In the present system doping has not much impact on the properties except that a significant enhancement in *M* at low-temperatures. It has been reported that the doping of magnetic ion enhances the magnetic properties, whereas nonmagnetic ion doping suppresses the magnetic properties [121-139]. A few theoretical [140, 141] and experimental [130, 138, 142] reports supports the present results, i.e., enhancement of magnetization due to small amount of nonmagnetic ion doping. This may be due to the development of disorder in the samples at low-temperatures. Disorder modifies the effective Mn^{3+}/Mn^{4+} ratio which results in the enhancement of magnetic properties. A significant change in the properties of the present doped systems is expected when nonmagnetic ion is substituted for Mn. However, no such changes were observed. This might be due to that the nonmagnetic ion doping percentage is not sufficient; as a result, physical properties are not affected.

6.4. Conclusions

In conclusion, $Bi_{0.7}Ca_{0.3}MnO_3$ and $Bi_{0.7}Ca_{0.3}Mn_{0.95}Y_{0.05}O_3$(Y = Mg, Al and Sn) samples are synthesized by sol-gel method. The studies on $Bi_{0.7}Ca_{0.3}MnO_3$ and $Bi_{0.7}Ca_{0.3}Mn_{0.95}Y_{0.05}O_3$(Y = Mg, Al and Sn) reveal that nonmagnetic ion doping does not affect the transition temperatures (T_{CO} and T_N) and the crystal structure. Substitution of Mn with nonmagnetic ions enhances *M*. This may be due to the defects created at lattice site, due to which disorder is induced in all

doped samples, which in turn affects the Mn^{3+}/Mn^{4+} ratio, leading to the enhancement of magnetization. Semiconducting behavior is observed in undoped and doped samples.

Chapter 7

Effect of grain size on the properties of $Bi_{0.5}Ca_{0.5}MnO_3$ manganite nanoparticles

7.1. Introduction

Manganites exhibit different properties when the size of the grain is reduced to nanoscale compared to their bulk counterpart, particularly in the low-temperature region. Apart from the external field and pressure, the environment at the surface of the system is also responsible for the properties of the materials. The surface to volume ratio of nano-grains plays an important role on the properties of the nanomaterial. In bulk $Bi_{0.5}Ca_{0.5}MnO_3$ manganite antiferromagnetic (AFM) correlations exist below ~325 K [7, 216]. When the grain size (GS) of this material is reduced to nanoscale, the uncompensated surface spins may destroy the collinear AFM configuration, which in turn may lead to the suppression of charge ordered (CO) state and enhance the ferromagnetic (FM) behavior. In view of this, we have undertaken a detailed study of the effect of GS on the properties of $Bi_{0.5}Ca_{0.5}MnO_3$ manganite.

7.2. Sample preparation

The stoichiometric amounts of pure $Bi(NO_3)_3.6H_2O$, $Ca(NO_3)_2.4H_2O$ and $MnCl_2.4H_2O$ were dissolved in distilled water to obtain a clear solution. Citric acid was added with constant stirring in the ratio of metal cation to citric acid as 1:2. The pH of the solution was adjusted to ~6-7 by adding ammonia solution. Ethylene-glycol was added to get a viscous solution. The solution was slowly evaporated to get a gel by keeping the temperature at ~60-70 ^oC with constant

stirring for several hours (hrs). The gel was decomposed at 250 ^{o}C. The resulting powder was separated into three parts and annealed at 500, 800 and 1000 ^{o}C to obtain the samples with different grain sizes.

7.3. Results and discussion

7.3.1. Structure and morphology studies

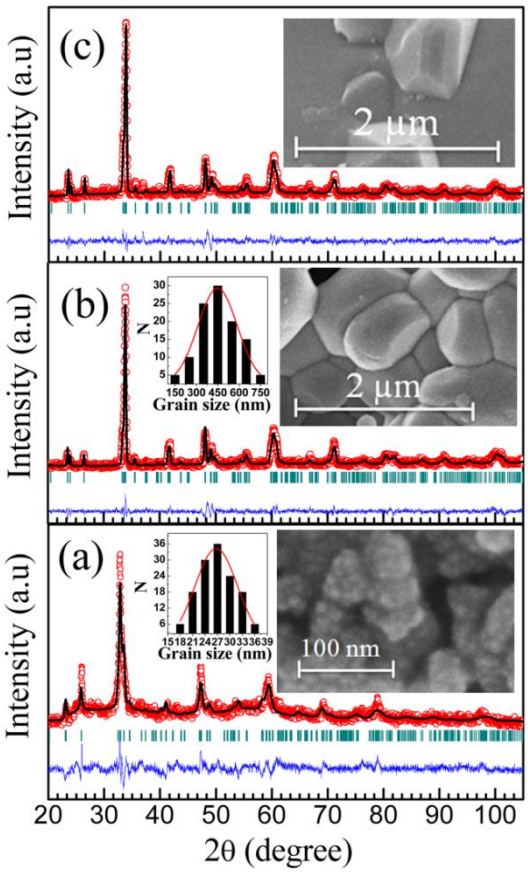

Fig. 7.1. Rietvled refinement (solid black lines) of XRD plots of $Bi_{0.5}Ca_{0.5}MnO_3$ sample (open red circles) annealed at (a) 500, (b) 800 and (c) 1000 ^{o}C along with diffraction planes (green lines) and difference between experimental and fitting data (blue lines). Inset shows the FESEM images of the samples. It also shows the grain size distribution of the samples annealed at (a) 500 and (b) 800 ^{o}C.

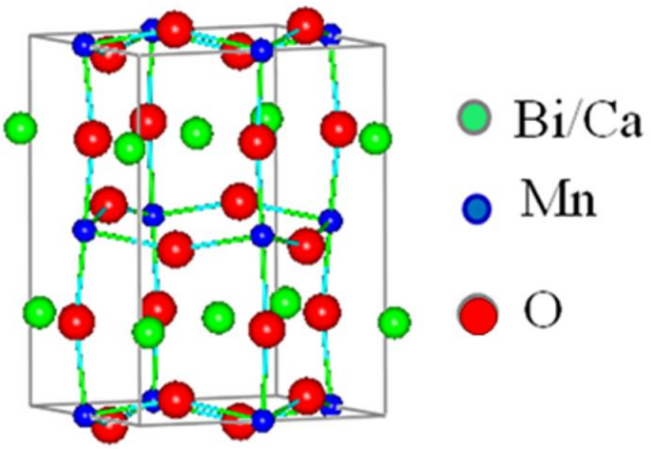

Fig. 7.2 Crystal structure of $Bi_{0.5}Ca_{0.5}MnO_3$ sample annealed at 800 ^oC.

Fig. 7.1 depicts the Rietveld refinement of x-ray diffraction (XRD) pattern for $Bi_{0.5}Ca_{0.5}MnO_3$ sample annealed at 500, 800 and 1000 ^oC. Rietveld refinement confirms the single phase orthorhombic nature of all the samples with *Pnma* space group. From the refinement, the estimated values of various structural parameters such as atomic positions (x, y and z), lattice parameters (*a*, *b* and *c*), unit cell volume (*V*), goodness of fit (*S*), average Mn-O bond length ($<d_{Mn-O}>$) and average Mn-O-Mn bond angle (<Mn-O-Mn>) are listed in table 7.1. Inset of Fig. 7.1 shows the field emission scanning electron microscopy (FESEM) micrographs and also GS distribution of the samples annealed at different temperatures. The estimated average GS are 27, 450 and 1080 nm for the samples annealed at 500, 800 and 1000 ^oC, respectively. The agglomeration in the sample with GS 1080 nm may be due to high annealing temperature, giving the grains enough time to coalesce. The energy dispersive x-ray spectroscopy (EDX) results on various samples at different regions confirm the purity of the samples. The decrease in unit cell volume with increase in average GS is observed. It has been reported that the unit cell volume increases with increasing GS [275], whereas others reported

Table 7.1. List of the atomic positions(x, y and z), lattice parameters (*a*, *b* and *c*), *V*, *S*, <d_{Mn-O}> and <Mn-O-Mn> values estimated from the refinement of the XRD data of $Bi_{0.5}Ca_{0.5}MnO_3$ sample annealed at different temperatures. Average GS values, estimated from FESEM images are also listed in the table.

Annealing temperature	**500 °C**	**800 °C**	**1000 °C**
Bi/Ca			
x	0.051	0.040	0.041
y	0.250	0.250	0.250
z	0.999	0.992	0.996
Mn			
x	0.500	0.500	0.500
y	0.500	0.500	0.500
z	0	0	0
O(1)			
x	0.498	0.491	0.482
y	0.250	0.250	0.250
z	0.086	0.059	0.054
O(2)			
x	0.246	0.225	0.358
y	0.530	0.547	0.469
z	0.340	0.213	0.278
***a* (Å)**	5.513	5.372	5.377
***b* (Å)**	7.719	7.414	7.416
***c* (Å)**	5.345	5.322	5.330
***V* (Å^3)**	227	211	212
S	2.54	1.62	1.82
<d_{Mn-O}> (Å)	1.933	1.918	1.944
<Mn-O-Mn> (°)	154.16	157.64	153.60
GS (nm)	27	450	1080

that the unit cell volume decreases with increasing GS [276]. The variations in the unit cell volume as a function of GS may be due to the different preparation techniques. Using the structure parameters, the crystal structure of $Bi_{0.5}Ca_{0.5}MnO_3$ sample annealed at 800 °C, representative of whole series, is generated as shown in Fig. 7.2.

7.3.2. Electron spin resonance studies

Fig. 7.3 shows the electron spin resonance (ESR) spectra at some selective temperatures for the samples with different GS. Fig. 7.4 shows the ESR spectra

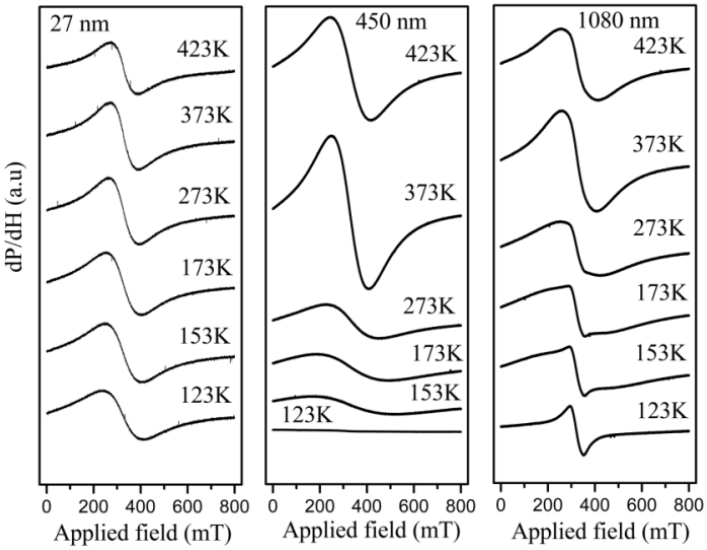

Fig. 7.3. ESR spectra of $Bi_{0.5}Ca_{0.5}MnO_3$ sample with different average grain sizes measured at various temperatures.

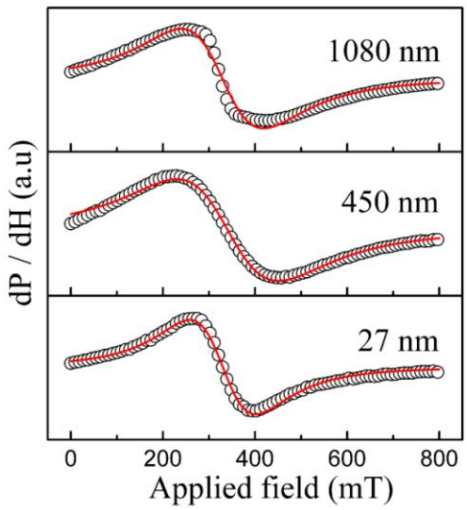

Fig. 7.4. Lorentzian fit (solid red line) to the ESR spectra (open circles) of $Bi_{0.5}Ca_{0.5}MnO_3$ sample with different average grain sizes measured at 273 K.

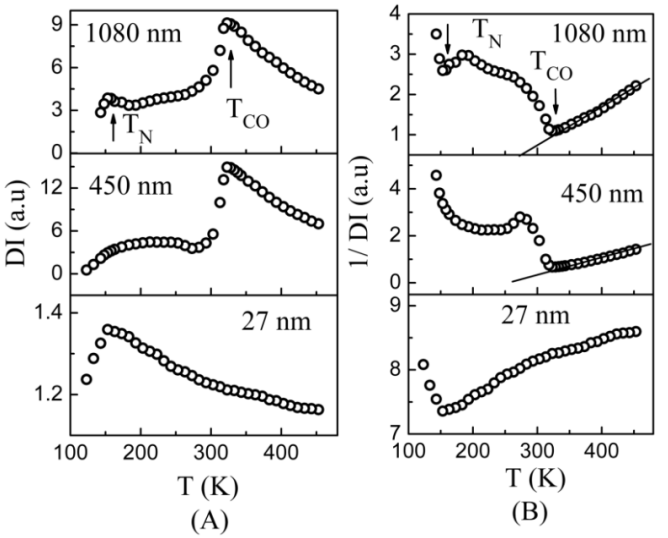

Fig. 7.5 (A) *DI* vs *T* and (B) 1 /*DI* vs *T* (B) plots of $Bi_{0.5}Ca_{0.5}MnO_3$ sample with different average grain sizes.

(open circles) as well as its fit (solid red line) using Lorentzian equation (equation (3.1)) for the samples measured at 273 K. Fig. 7.5 (A) shows the normalized double integrated intensity (*DI*) of the ESR signal as a function of the temperature. For all the samples, *DI* increases as the temperature decreases from 453 K. All the samples, except the sample with GS 27 nm, show a peak at ~327 K, which can be assigned to charge ordering temperature (T_{CO}). Below $T_{CO,}$ *DI* decreases sharply and shows a weak temperature independent behavior due to orbital ordering, in the temperature range 250-180 K. The sharp decrease in *DI* at ~150 K is due to long-range AFM ordering. This is assigned as Neel temperature (T_N). The T_{CO} and T_N values are close to that of the bulk samples as reported earlier [7, 216]. For the sample with GS 27 nm, *DI* increases with decreasing temperature and reaches its maximum value at ~150 K, and then it decreases with further decrease in temperature similar to the samples with GS 450 and 1080 nm. No peak corresponds to the CO state is observed.

The 1/*DI* vs *T* plots are shown in Fig. 7.5 (B). Linear fits to the data in the

temperature range $T > T_{CO}$ is as per Curie-Weiss law. The positive intercepts on the x-axis of samples with GS 450 and 1080 nm indicate the existence of dominating FM-double exchange (DE) interactions which can be attributed to thermally activated Mn^{3+}-Mn^{4+} hopping of small polaron. As the temperature reaches T_{CO}, the straight line deviates from the linearity, indicating the evolution of AFM ordering in the sample, giving rise to the CO state. In the temperature range $T_{CO} > T > T_N$, evolving domains of FM and AFM correlations coexist, because the Mn spins do not completely undergo orbital ordering. The sample with GS 27 nm shows nonlinear dependence of 1/*DI* with the decrease in temperature. It is pointed out by E. Rozenberg et al. [15] that the nonlinear behaviors of 1/*DI* vs *T* plot follows Neel paramagnetic (PM) susceptibility behavior.

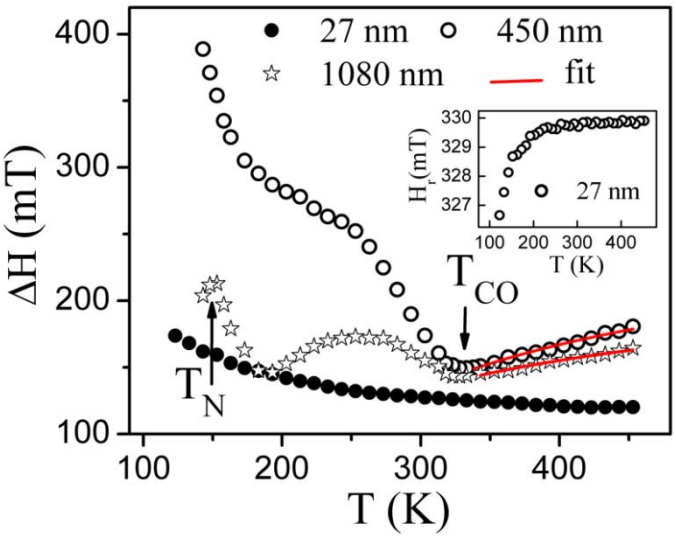

Fig. 7.6. Δ*H* vs *T* plots of $Bi_{0.5}Ca_{0.5}MnO_3$ sample with different average grain sizes. Solid red line is according to theoretical model. Inset shows H_r vs *T* plot for sample with GS 27 nm sample.

Fig. 7.6 shows the variation of linewidth (Δ*H*) of ESR signal with temperature. On decreasing temperature from 453 K, Δ*H* decreases, reaches a

Table 7.2. List of the parameters (θ_C, ΔH and B) estimated from ESR and magnetization data of $Bi_{0.5}Ca_{0.5}MnO_3$ sample with different average GS.

Average GS (nm)	ΔH vs T			$1/\chi$ vs T
	θ_C (K)($T > T_{CO}$)	$\Delta H(\infty)$(G)	B (GK^{-1})	θ_C (K) ($T < T_{CO}$)
27	-	-	-	-189
450	148	2652	0	-219
1080	117	2196	0	-251

minimum at T_{CO} (~327 K) for samples with GS 450 and 1080 nm. Below T_{CO}, ΔH increases with decreasing temperature. The 1080 nm sample show mixed behavior below T_{CO}. Below T_N, ΔH decreases sharply. This maybe because of the contribution of FM correlations spread in the long-range AFM ordered matrix [171, 216]. For the sample with GS 27 nm, ΔH increases gradually with decreasing temperature. The magnitude of ΔH of the sample with GS 27 nm is low compared to the other samples in the measured temperature range (123-453 K), which indicate the existence of FM correlations. For the sample with GS 450 nm, below T_{CO} the sharp rise in ΔH and disappearance of ESR signal at 123 K (Fig. 7.3) compared to the other samples indicate the evolution of dominant AFM correlations. The line broadening of these samples can be due to the random orientation of the anisotropy energy axes from grain to grain and the demagnetizing fields arising from nonmagnetic inclusions as well as pores between grains [243].

To understand the spin dynamics of the present system we have used the Huber et al. [173] and Auslender et al. [176] model which has been already used in our earlier works [277]. For samples with GS 450 and 1080 nm, ΔH vs T fits (solid red lines) in the temperature range $T > T_{CO}$ are drawn using equation (3.7) and shown in the Fig. 7.6. From this fit, the estimated values of Curie-Weiss temperature (θ_C), high-temperature asymptote ($\Delta H(\infty)$) and the strength of interactions between the e_g electrons (B) are listed in table 7.2. The lower value of

$\Delta H(\infty)$ for the sample with GS 1080 nm indicate the weak spin-spin relaxation in this sample compared to the sample with GS 450 nm [217]. Resonance field (H_r) as a function of temperature (inset of Fig. 7.6 for 27 nm sample) shows approximately constant behavior in the temperature range 453 K > T > 200 K and it is in the PM region, whereas below ~ 200 K, H_r decreases for all samples, indicating the evolution of FM spin correlations.

7.3.3. Magnetization studies

7.3.3.1. Temperature dependent magnetization

Fig. 7.7 (A) shows the temperature dependences of magnetization (M) for all the samples measured in both zero-field cooled (ZFC) and field cooled (FC) conditions in the applied field of 500 Oe. For the samples with GS 450 and 1080 nm, as the temperature decreases from 350 K, M in both ZFC and FC modes

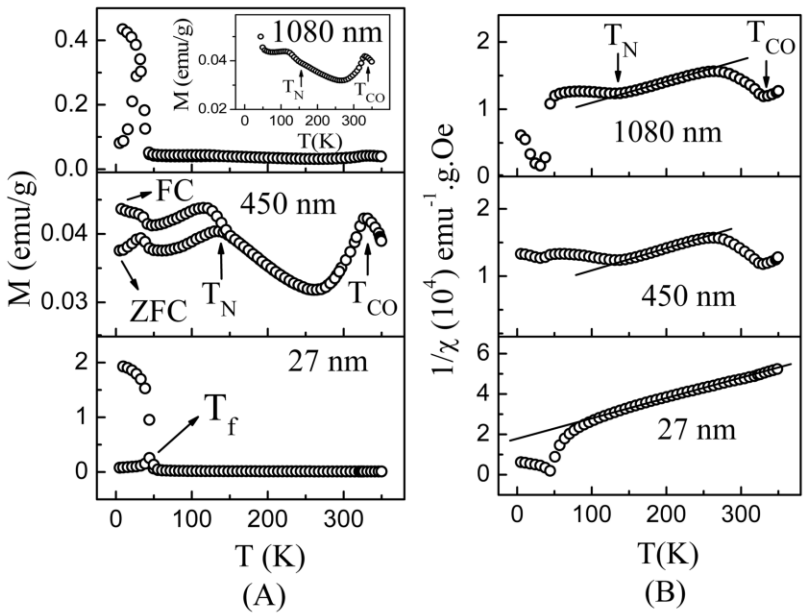

Fig. 7.7 (A) M vs T [measured in an applied static magnetic field of 500 Oe] and (B) $1/\chi$ vs T [for M_{ZFC} data] plots of $Bi_{0.5}Ca_{0.5}MnO_3$ sample with different average grain sizes.

increases reaching a peak value at T_{CO} (~327 K). At high-temperatures, FM correlations exist due to the hopping of e_g electrons between Mn^{3+} and Mn^{4+} ions. As the temperature decreases to T_{CO}, charge ordered state freezes out the hopping of the e_g electrons [278], resulting in slight decrease in M below T_{CO}, then it increases and shows maxima at T_N in ZFC mode whereas M increases continuously in FC mode. The decrease in M below T_{CO} is an indicative of the formation of AFM correlations. M raises sharply below ~40 K for the samples with GS 450 and 1080 nm and ~50 K for the sample with GS 27 nm, which indicate the FM-cluster glass (CG) formation. Below this M in ZFC mode shows a peak at spin freezing temperature (T_f) [16, 219] while M in FC mode continuously increases with decreasing temperature. The magnitude of M in the high-temperature range is approximately same for all the samples whereas it shows a mixed behavior in the low-temperature region. There are two possibilities which are responsible for the change in the magnitude of M. One is the change in the GS and the other one change in the ratio of Mn^{3+}/Mn^{4+} which depends on oxygen stoichiometry [279]. The T_{CO} and T_N of the sample with GS 27 nm are suppressed. The increase in the value of M below ~50 K and the suppression of T_{CO} and T_N for the sample with GS 27 nm can be explained according to core-shell model proposed by Bhowmik et al. [280]. As the GS decreases surface to volume ratio increases, which leads to the deviation of the shell spins from the collinear AFM arrangement of the core spins. This in turn develops the uncompensated surface spins. These uncompensated surface spins are responsible for the increase in the surface chemical disorder. The surface chemical disorder and the enhancement of inter-particle interactions within agglomerated nano-sample results in well-defined core-shell structure [281] and the relaxation of superexchange (SE) on the surface layer allows formation of FM shell [282]. The increase in the surface to volume ratio also introduces the unscreened Coulomb attraction at the surface, which results in an increase of the charge density in the system [235]. The

enhanced itinerant e_g electron density changes the collinear AFM configuration and hence weakens the AFM-SE interaction, thereby improving the DE interaction, leading to the enhancement of M and suppression of long-range charge ordered state.

According to an empirical equation [52] given as

$$T_{CO}(D) = T_{CO}^{b}\left(1 - \frac{D_0}{D}\right)^{\gamma} \tag{7.1}$$

where T_{CO}^{b} is the charge ordered transition of bulk sample. D_0 is the critical particle /grain size for the disappearance of the charge ordered state. γ is a fitting parameter. If the particle size is below a critical diameter, surface energy will become comparable with the CO energy, leading to the disappearance of the CO state. In the low-temperature range, all the spins freeze in random direction in the absence of magnetic field in ZFC mode. As the temperature increases the randomly oriented FM clusters melt and get oriented by an external magnetic field leading to increasing in magnetization. As the temperature reaches a particular value of ~ 30-40 K, thermal fluctuations dominate, resulting in the decrease in magnetization due to disturbed moments [283].

In order to get further information about the magnetic interaction, we have plotted the ZFC magnetization (M_{ZFC}) data as per Curie-Weiss law and shown in Fig. 7.7(B). The estimated values of θ_C ($T < T_{CO}$) are listed in table 7.2. Below T_{CO} the negative value of θ_C and increasing trend in ΔH of all samples indicate the existence AFM correlations. However, the decrease in the negative value of θ_C for the sample with GS 27 nm can be ascribed to the short-range AFM correlations rather long-range order.

7.3.3.2. Magnetic field dependent magnetization

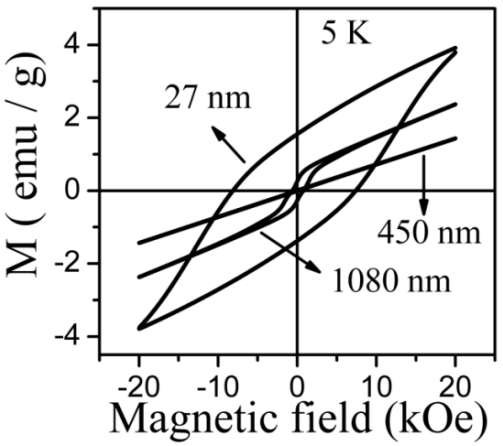

Fig. 7.8. *M* vs Magnetic field (*H*) plots, measured at 5 K, of $Bi_{0.5}Ca_{0.5}MnO_3$ sample with different average grain sizes.

Fig. 7. 8 depicts the magnetic field dependent magnetization measured at 5 K by applying a maximum magnetic field of 20 kOe. The large hysteresis of the sample with GS 27 nm supports the results obtained from *M* vs *T* plots. The large coercivity of the sample with 27 nm is a general behavior observed for many FM materials when the size is reduced to the nano scale.

7.3.4. Transport studies

Resistivity (ρ) as a function of temperature of the samples with GS 450 and 1080 nm is shown in Fig. 7.9 (A).The behavior of ρ is similar to what we have reported in Chapter 3 and 4 for the same composition. Since the value of ρ becomes high below ~200 K, we could not measure the resistivity of the sample with GS 27 nm. This behavior is ascribed to grain boundary scattering when GS is reduced [229, 230]. Fig.7.9 (B) and Fig. 7.9(C) plots drawn using equation (3.11) and the continuous curvature of these plots indicate that the small polaron hopping (SPH) model is not suitable to analyze the data [7]. Using the variable

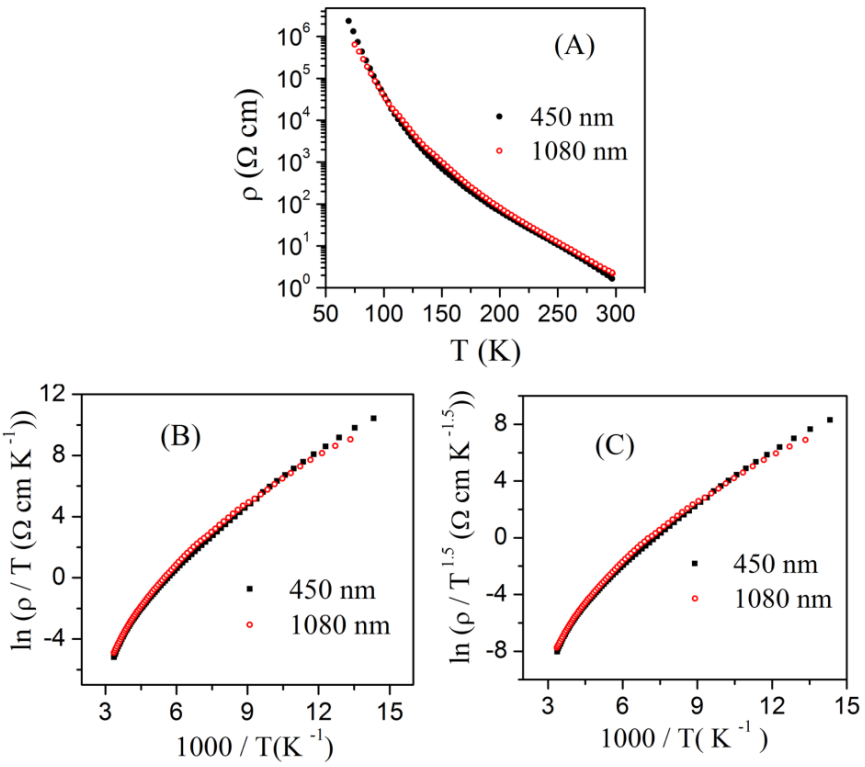

Fig. 7.9 (A) ρ vs T, (B) ln(ρ/T) vs 1000/T and (C) ln($\rho/T^{1.5}$) vs 1000/T plots of $Bi_{0.5}Ca_{0.5}MnO_3$ sample with different average grain sizes.

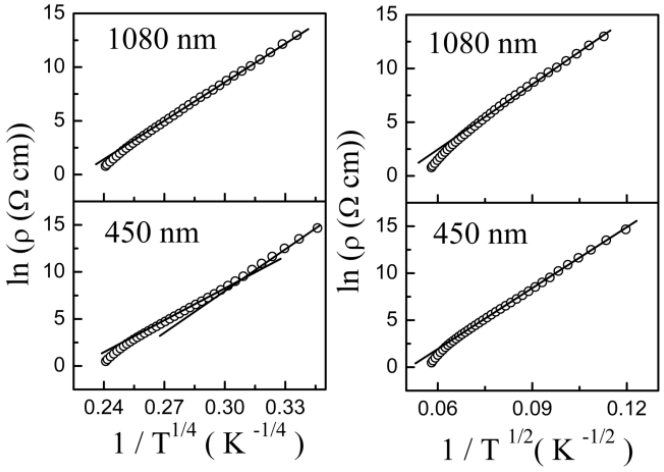

Fig. 7.10. ln(ρ) vs $1/T^{1/4}$ (left panel) and ln(ρ) vs $1/T^{1/2}$ (right panel) plots of $Bi_{0.5}Ca_{0.5}MnO_3$ sample with different average grain sizes.

Table 7.3 List of the various parameters (T_0, ρ_0, ξ, R and W) estimated from VRH model in the temperature range $T_{CO} > T > T_N$ of $Bi_{0.5}Ca_{0.5}MnO_3$ sample with different average GS.

Average GS (nm)	T_0 (10^8 K)	ρ_0 (10^{-13} Ω cm)	ξ (Å)	R (nm)	W(ev)
450	0.689	13.882	6.98	5.72	0.141
1080	0.755	5.73	6.74	5.67	0.145

range hopping (VRH) model (left panel of Fig. 7.10) the calculated values of various parameters are listed in table 7.3. Below T_N, for sample with GS 450 nm the value of characteristic temperature (T_0), characteristic resistivity (ρ_0), correlation length (ξ), hopping distance (R) and hopping energy (W) is found to be 1.38 x10^8 K , 0.01x 10^{-13}Ω cm, 5.51 Å, 5.39 nm and 0.16 eV, respectively. Using Efros and Shklovskii-VRH (ES-VRH) model (right panel of Fig. 7.10) the estimated values T_0, ρ_0 and ξ are found to be 4.82 x10^4 K, 1.11x 10^{-5}Ω cm and 5.96 Å, respectively for 450 nm sample. Similarly for 1080 nm sample the estimated values T_0, ρ_0 and ξ are found to be 3.89 x10^4 K, 10.57x 10^{-5}Ω cm and 7.39 Å, respectively. These values of ρ_0 do not match with Mott's predicted values. The values estimated from VRH model and Mott's predicted [211] values are in good agreement with each other.

7.3.5. Discussion

Magnetization studies of $Nd_{0.5}Ca_{0.5}MnO_3$ nanoparticles [53] show the suppression of charge ordering down to the particle size of 40 nm, whereas the temperature dependence of ΔH and Lande g-factor show the typical charge ordering even in the 40 nm sample. Similarly in the present study ESR results show the existence of the AFM ordering for the sample with GS 27 nm. Das et al. [284] used density-functional theory and mean-field theories to understand the effect of GS reduction on the properties of half doped $La_{0.5}Ca_{0.5}MnO_3$ manganite and pointed out that the lattice structure changes with reduction in GS. These

structural changes are responsible for the weakening of charge and orbital order. But the slight decrease in GS can be due to oxygen non-stoichiometry too, which causes the systematic deviation from the real composition [285]. This could be reason for the random variations in bond angle and bond distance as a function of GS. There are some systems which show complex behavior when GS is reduced to nanometric scale [52]. In some materials GS reduction causes the increase in disorder resulting in the reduction of magnetization as compared to the bulk sample [279]. On the other hand some materials show the enhancement in the magnetization as the GS is reduced to nanometric size [16]. In the study of $Bi_{0.2}Ca_{0.8}MnO_3$ nanoparticles the observed variation in the charge ordered state and the appearance of the spin glass state were interpreted in terms of martensitic strain and surface effects [286]. In the present system also the effects of martensitic strain cannot be ruled out. E. Rozenberg et al. [175] have proposed a model to understand the effect of chemical/magnetic disorder, associated with size of the particles, on the coexistence of different magnetic/electronic phases. However, the complexity, i.e., the evolution of different properties with reducing GS is still in the debate.

7.4. Conclusions

In conclusion, the studies on the $Bi_{0.5}Ca_{0.5}MnO_3$ manganite samples with different grain size (GS) (27, 450 nm and 1080 nm) show that for sample with GS 27 nm the long-range charge ordering and antiferromagnetic (AFM) ordering transitions are suppressed. However the electron spin resonance (ESR) and magnetization results reveal that even for the sample with GS 27 nm the AFM correlations still exist in the form of short-range order. The evolving different magnetic correlations with the decrease in grain size are ascribed to increase in surface to volume ratio of grains.

This page is intentionally left blank

Summary and conclusions

In the present work, the doping as well as size induced changes in structural, magnetic and transport properties of Bi and rare earth manganites are reported.

Structural analysis indicates that the series of samples, i.e., $Bi_{1-x}Ca_xMnO_3$ ($0.40 \leq x \leq 0.90$), $Bi_{0.5-x}Pr_xCa_{0.5}MnO_3$ ($0.0 \leq x \leq 0.50$), $La_{0.37}D_{0.30}Ca_{0.33}MnO_3$ (D = Bi, Sm), $La_{0.37}Bi_{0.15}Sm_{0.15}Ca_{0.33}MnO_3$ and $Bi_{0.5}Ca_{0.5}MnO_3$ manganite with different average grain sizes (27, 450 and 1080 nm) possess orthorhombic structure with *Pnma* space group. Whereas for $Bi_{0.7}Ca_{0.3}MnO_3$ and $Bi_{0.7}Ca_{0.3}Mn_{0.95}Y_{0.05}O_3$ (Y = Mg, Al and Sn) samples, although majority of the x-ray diffraction (XRD) peaks correspond to orthorhombic phase but some XRD peaks corresponding to monoclinic phase have also been observed. The energy dispersive x-ray spectroscopy (EDX) results confirm composition of the samples very close to the starting composition.

The structural studies of $Bi_{1-x}Ca_xMnO_3$ ($0.40 \leq x \leq 0.90$) reveal that the average ionic radii of A-site cations ($<r_A>$), tolerance factor (t), and the unit cell volume (V) decreases with increase in Ca content. This is ascribed to the lower ionic radii of Ca^{2+} (1.12 Å) than that of Bi^{3+} (1.24 Å) ion. The estimated values of average grain size (GS) from field emission scanning electron microscopy (FESEM) data are in the range 200-650 nm. The value of average GS decreases with increasing Ca content.

The electron spin resonance (ESR) data analysis was done using normalized double integrated intensity (*DI*) as a function of temperature for samples with $0.40 \leq x \leq 0.80$. As the temperature decreases from high-temperature (453K), *DI* increases and reaches its maximum value at a temperature which is assigned as charge ordering temperature (T_{CO}). Below $T_{CO,}$ *DI* decreases, evidencing the existence of antiferromagnetic (AFM) correlations, and reaches a minimum value

and then it increases with further decrease in temperature for $0.65 \leq x \leq 0.80$. For samples with $x = 0.85$ and 0.90 no T_{CO} is observed and for these samples, on cooling from high-temperature, *DI* increases gradually. For samples with $0.40 \leq x \leq 0.80$ sharp decrease in *DI* below 126-150 K is ascribed to onset of long-range AFM ordering and this temperature taken as Neel temperature (T_N).

For samples with $x \geq 0.65$ peak to peak linewidth (ΔH) of the ESR signal shows prominent minima at ~150 K. For all the samples, the ESR signal persists only for a few degrees below 150 K and then it disappears evidencing the onset of long-range AFM state. ΔH increases linearly with the increase in temperature in the temperature range $T > T_{CO}$. As T_{CO} decreases with increase in *x*, ΔH shows saturation effect with increase in temperature.

For samples with $0.40 \leq x \leq 0.80$, magnetization (*M*) as a function of temperature, measured under a static magnetic field (*H*) of 500 Oe, shows similar trend, i.e., as the temperature decreases from 350 K, both zero-field cooled (ZFC) and field cooled (FC) curves show a peak at T_{CO}. On further decrease in temperature, *M* decreases slightly. A broad maximum at ~150 K, representing long - range AFM order (T_N), is observed for samples with $x \leq 0.50$.

The $Bi_{1-x}Ca_xMnO_3$ phase diagram is constructed from the estimated values of T_{CO} and T_N from the ESR and magnetization data. For samples $0.30 \leq x \leq 0.80$ (T_{CO} and T_N values of the sample with $x = 0.30$ are taken from chapter 6) the magnetic phase in the temperature range $T > T_{CO}$ is dominated by ferromagnetic (FM)-double exchange (DE) interactions. The paramagnetic (PM)-FM transition at ~150 K co-exists with PM to canted-antiferromagnetic (C-AFM) transition at ~120 K for samples with $0.50 \leq x \leq 0.80$. Whereas, only PM to C-AFM transition is observed for the samples with $x = 0.85$ and 0.90.

From the resistivity (ρ) studies of $Bi_{1-x}Ca_xMnO_3$ ($0.40 \leq x \leq 0.90$) samples, it is observed that ρ increases with increasing Ca content from $x = 0.40$ to 0.50 and then decreases in the composition range $0.50 < x \leq 0.75$, again increasing for *x* up

to 0.90. The samples with $x \leq 0.60$ have higher values of ρ compared to that of the other samples. This, presumably, is due to the distortion arising from the A-site disorder as well as due to $6s^2$ lone pair electrons of Bi^{3+} ions. For samples with $0.50 < x \leq 0.75$, the average Mn-O-Mn bond angle increases with increasing Ca content and the sample with $x = 0.75$ shows the lowest ρ value (in the 100 K< T < 300 K range) for which the average Mn-O-Mn bond angle has the highest value. This could be due to decrease in disorder for which the strength of the $6s^2$ lone pair electrons of Bi^{3+} ions is weakened with increasing Ca content. In M vs T plots, the shift in FM-cluster glass (CG) state towards higher temperature from ~50 K for samples with $x \leq 0.60$ to 115 K for samples with $x \geq 0.65$ is also associated to the decrease in disorder. For all the samples, a sharp increase in ρ in the temperature range ~120-150 K is observed, which is characteristic of the AFM nature.

The structural studies of $Bi_{0.5-x}Pr_xCa_{0.5}MnO_3$ ($0.0 \leq x \leq 0.50$)(BPCMO) show that with increase in Pr content from $x = 0.0$ to 0.05, the unit cell volume decreases drastically. For samples with $0.05 \leq x \leq 0.50$, the unit cell volume is found to increase steadily with increase in Pr content. The higher cell volume of undoped sample can be due to the strengthened dominant lone pair character of Bi^{3+} ion. The sharp drop in the cell volume for the sample with $x = 0.05$ indicates that the constrained effect of the $6s^2$ lone pair becomes strong due to Pr-doping. The constrained effect of the lone pair maintains the ionic size of the Bi^{3+} ion at 1.170 Å, which is smaller than that of the Pr^{3+} ion (1.179 Å). As a result the cell volume increases for samples with $x > 0.05$. From the microstructure the estimated average GS are found to be 405, 249, 213, 190, 200, 238, 141 and 157 nm for $x = 0.0$, 0.05, 0.10, 0.15, 0.20, 0.30, 0.40 and 0.50, respectively.

The value of T_{CO} as a function of Pr content, estimated from ESR data, matches quite well with that estimated from magnetization and resistivity data

analysis. T_{CO} decreases as x increases from 0.0 (T_{CO} = 327 K) to 0.20 (T_{CO} = 249 K) and becomes independent of doping content with further increase in x.

From the magnetization studies of BPCMO, it is observed that the undoped sample shows CG behavior below 45 K and for doped samples it is below 115 K. For $0.0 \leq x \leq 0.20$ samples, Curie-Weiss temperature (θ_C) increases with Pr-doping. The estimated value of Curie temperature (T_C) is increases with increasing in Pr content. The samples with x = 0.0-0.40 show first-order and the sample with x = 0.50 shows second-order phase transition near the critical point. The estimated critical exponents for sample with x = 0.50 are found to be β = 0.75 and γ = 0.82, do not fall into any universality class. The sample with x = 0.50 shows a maximum magnetic entropy change ($|\Delta S_m|$ = 1.22 $J.kg^{-1}.K^{-1}$) at T_C in the applied magnetic field of 40 kOe, which is associated with the magnetocaloric effect (MCE). Since T_C and $|\Delta S_m|$ increased with Pr-doping, these materials can be used in magnetic refrigeration technology. For all the samples *M-H* plots measured under the application of a maximum field of 20 kOe at 5 K show hysteresis, indicating the formation of FM clusters.

For all the samples, ρ increases exponentially with decreasing temperature. The value of ρ does not vary significantly in the composition range $0.0 \leq x \leq 0.20$. The x = 0.30 sample shows lower resistivity. For samples with $0.30 < x \leq 0.5$ the resistivity increases. The small grain size in the samples increases the grain boundary scattering, which gives rise to the increase in resistivity for x = 0.40 and 0.50 samples. In all the samples, FM clusters exist above T_{CO}. As the temperature reaches T_{CO}, AFM interactions grow at the expense of FM interactions. With the further decrease in temperature AFM domains grow progressively and the FM cluster size decreases simultaneously, as a result of which large increase in the resistivity is observed.

The high T_{CO} of the undoped sample is due to strong electron-lattice coupling induced by Jahn-Teller (J-T) distortion and long-range Coulomb interaction. With

increasing Pr content the effect of $6s^2$ lone pair of Bi^{3+} ions and the hybridization of Bi^{3+} and O^{2-} ions decreases, resulting in decrease of T_{CO}. For $x \geq 0.20$, Pr^{3+}probably stabilizes the effect of $6s^2$ lone pair of Bi^{3+} ions and hence, the charge ordered state becomes same as that of Pr-manganite.

With increasing Pr content the disorder is also likely to decrease because of similar ionic radii of Pr^{3+} and Ca^{2+} ions, which are confirmed from the decrease in the value of the variance of the A-site cation size distribution (σ^2) with increase in the Pr content. The formation of FM or FM-CG state and shift of this transition towards higher temperature is ascribed to decrease in disorder. In the present system there is a strong possibility that grain size effects are present. For $x = 0.0$ and 0.05 samples doping does not affect *M*, but it shifts the FM transition towards higher temperature. This may be due to the decrease in grain size. Reduction in grain size increases the surface to volume ratio, resulting in appearance of FM clusters. In the composition range $0.05 \leq x \leq 0.50$, an increment in the value of $<r_A>$ is observed with the increase in Pr content. As a result, the average Mn-O-Mn bond angle increases and the length of Mn-O bond decrease, leading to widening of bandwidth and the increase in mobility of e_g electrons. This results in strengthening of FM-DE coupling, leading to increasing in magnetization and T_C.

From the structural studies of $La_{0.37}Bi_{0.30}Ca_{0.33}MnO_3$ (B30), $La_{0.37}Bi_{0.15}Sm_{0.15}Ca_{0.33}MnO_3$ (B15S15) and $La_{0.37}Sm_{0.30}Ca_{0.33}MnO_3$ (S30) samples, it is confirmed that these samples have lower unit cell volume compared to $La_{0.67}Ca_{0.33}MnO_3$ (~231 $Å^3$), which could be due to the smaller ionic radii of Bi^{3+} (1.24 Å) and Sm^{3+} (0 .96 Å) than that of La^{3+} (1.36 Å).

M as well as T_C decreases when La is replaced by Bi and/or Sm. Below ~ 60 K for B30 and ~40 K for B15S15 and S30, the drop in ZFC magnetization (M_{ZFC}) indicates the evolution of competing AFM and FM phases. As a result the system exhibits spin-cluster glass behavior. The sharp drop in M_{ZFC} for B15S15 and S30 is presumably due to the increased competition between AFM and FM

interactions with Sm doping. This can be due to the randomly distributed magnetic potential and Coulomb potential of Sm, which prevents Mn-O-Mn bonds from forming homogeneous long-range order, leading to the formation of cluster and spin-cluster glass state. The samples show second-order phase transition near the critical point. The estimated critical exponents are close to the values predicted in mean field theory (MFT). The scaling plots fallen on two curves, one above T_C and the other below T_C, and are in agreement with the scaling theory. This indicates that the calculated critical exponents are reliable. The decrease in the M, T_C and evolution of spin or cluster glass and the nature of second-order phase transition (compared to first-order transition in $La_{0.67}Ca_{0.33}MnO_3$) are ascribed to the disorder in the samples due to the lattice distortion caused by the size mismatch of the A-site cations by Bi^{3+} and Sm^{3+} ion doping at La-site.

The studies on $Bi_{0.7}Ca_{0.3}MnO_3$ and $Bi_{0.7}Ca_{0.3}Mn_{0.95}Y_{0.05}O_3$(Y = Mg, Al and Sn) reveal that nonmagnetic ion doping does not affect the transition temperatures (T_{CO} and T_N) and the crystal structure. Substitution of Mn with nonmagnetic ions enhances M. This may be due to the defects created at lattice site, due to which disorder is induced in all doped samples, which in turn affects the Mn^{3+}/Mn^{4+} ratio, leading to the enhancement of M.

The studies on the $Bi_{0.5}Ca_{0.5}MnO_3$ manganite samples with different GS (27, 450 nm and 1080 nm) show that for sample with GS 27 nm the long-range charge ordering and AFM ordering transitions are suppressed. However, the ESR and magnetization results reveal that even for the sample with GS 27 nm the AFM correlations still exist in the form of short-range order. The evolving different magnetic correlations with the decrease in GS are ascribed to increase in surface to volume ratio of grains.

All the samples follow the semiconducting behavior. The ρ of the samples follow Mott's variable range hopping (VRH) model in the temperature range $T < T_{CO}$.

In conclusion, doping (A/B-site) as well as change in grain size induces changes in structural, magnetic and transport properties of the samples. The changes in magnetic and transport properties of the samples are associated with the changes in structural parameters. ESR and magnetization studies reveal that the phase separation is an intrinsic phenomenon in these manganite compounds.

This page is intentionally left blank

References

[1] Y. Tokura (ed), *Colossal Magnetoresistive Oxides*, (London: Gordon and Breach), 2000.

[2] R. Mahendiran, S. K. Tiwary, A. K. Raychaudhuri, T. V. Ramakrishnan, R. Mahesh, N. Rangavittal and C. N. R. Rao, *Phys. Rev. B* **53** (1996) 3348.

[3] L. Liang, L. Li, H. Wu and X. Zhu, *Nanoscale Research Letters* **9** (2014) 325.

[4] M. Fiebig, Th. Lottermoser, D. Frohlich, A. V. Goltsev and R. V. Pisarev, *Nature* **419** (2002) 818.

[5] Th. Lottermoser, Th. Lonkai, U. Amann, D. Hohlwein, J. Ihringer and M. Fiebig, *Nature* **430** (2004) 541.

[6] M. Mayr, A. Moreo, J. A. Vergés, J. Arispe, A. Feiguin and E. Dagotto, *Phys. Rev. Lett.* **86** (2001) 135.

[7] J. Kurian and R. Singh, *J. Phys. D: Appl. Phys*. **41** (2008) 215006.

[8] H. Woo, T. A. Tyson, M. Croft, S.W. Cheong and J. C. Woicik, *Phys. Rev. B* **63** (2001) 134412.

[9] W. Bao, J. D. Axe, C. H. Chen and S.W. Cheong, *Phys. Rev. Lett*. **78** (1997) 543.

[10] M. Uehara, S. Mori, C. H. Chen and S-W. Cheong, *Nature (London)* **399** (1999) 560.

[11] C. Cui and T. A. Tyson. *Phys. Rev. B* **70** (2004) 094409.

[12] X. Wang, Q. Cui, Y. Pan, W. Gao, J. Zhang and G. Zou, *J. Alloys. Compd*. **321** (2001) 72.

[13] Y. Tomioka, A. Asamitsu, H. Kuwahara, Y. Moritomo and Y. Tokura, *Phys. Rev. B* **53** (1995) R1689.

[14] C. P. Yang , S. S. Chen, D. H. Guo, H. Wang, G. H. Rao, V. Morchshakov and K. Barner, *J. Alloys. Compd*. **467** (2009) 54.

[15] E. Rozenberg, A. I. Shames and M. Auslender, *Nanosci. and Nanotechnolo. Lett*. **3** (2011) 531.

[16] T. Zhang and M. Dressel, *Phys. Rev. B* **80** (2009) 014435.

[17] R. R. Zhang, G. L. Kuang, L. H. Yin and Y. P. Sun, *J. Appl. Phys*. **108** (2010) 103903.

[18] J. Yang, W. H. Song, Y. Q. Ma, R. L. Zhang, B. C. Zhao, Z. G. Sheng, G. H. Zheng, J. M. Dai and Y. P. Sun, *Phys. Rev. B* **70** (2004) 144421.

[19] J. Kurian and R. Singh, *J. Alloys. Compd.* **509** (2011) 5127.

[20] S. Hcini, M. Boudard, S. Zemni and M. Oumezzine, *Ceramics International* **40** (2014)16041.

[21] Y. Li, Q. Cheng and D. Qi, *Ceramics International* **39** (2013) 1345.

[22] J. C. C. Freitas, R. A. Victor, M. T. D. Orlando, A. Y. Takeuchi, I. S. Oliveira and T. J. Bonagamba, *J. Phys.: Condens. Matter* **20** (2008) 095214.

[23] Z. Cheng and J. Lin, *Cryst. Eng. Comm*. **12** (2010) 2646.

[24] G. H. Jonker and J. H. Van Santen, *Physica* **16** (1950) 337.

[25] V. M. Goldschmidt, 1958, *Geochemistry*(Oxford University).

[26] H. Y. Hwang, S-W. Cheong, P. G. Radaelli, M. Marezio and B. Batlogg, *Phys. Rev.Lett*.**75** (1995) 914.

[27] J. P. Zhoua, J. T. McDevitt, J. S. Zhou, H. Q. Yin, J. B. Goodenough, Y. Gim and Q. X. Jia, *Appl. Phys. Lett*. **75** (1999) 1146.

[28] K. F. Wang, Y. Wang, L. F. Wang, S. Dong, D. Li, Z. D. Zhang, H. Yu, Q. C. Li and J-M. Liu, *Phys. Rev. B* **73** (2006) 134411.

[29] J. Kurian, *Electron spin resonance and resistivity studies of Bi manganites*, University of Hyderabad, 2009.

[30] H. Jahn and E. Teller, *Proceedings of the Royal Society A* **161** (1937) 220.

[31] O. Gaier, *A study of exchange interaction, magnetic anisotropies, and ion beam induced effects in thin films of Co_2-based Heusler compounds*, 2009.

[32] A. Mukherjee, *The field induced melting of charge order in manganites*,

2009.

[33] C. Zener, *Phys. Rev*. **81** (1950) 440.

[34] C. Zener, *Phys. Rev*. **82** (1951) 403.

[35] C. Zener, *Phys. Rev*. **83** (1951) 229.

[36] P. W. Anderson and H. Hasegawa, *Phys. Rev*. **100** (1955) 675.

[37] P. G. de Gennes, *Phys. Rev*. **118**, (1960) 141.

[38] J. B. Goodenough, *Phys. Rev*. **100** (1955) 564.

[39] J. B. Goodenough, *Phys. Rev*. **55** (1955) 3015.

[40] J. Kanamori, *J. Phys. Chem. Solids* **10** (1959) 87.

[41] H. A. Kramers, *Physica* **1** (1934) 182.

[42] P. W. Anderson, *Phys. Rev*. **79** (1950) 350.

[43] E. J. W. Verwey, *Nature* **144** ((1939) 327.

[44] M. S. Senn, J. P. Wright and J. P. Attfield. *Nature* **481** (2011)7380.

[45] M. Coey, *Nature* **430** (2004)155.

[46] A. Daoud-Aladine, J. Rodriguez-Carvajal, L. Pinsard-Gaudart, M. T. Fernandez-Diaz and A. Revcolevschi, *Phys. Rev. Lett.* **89** (2002) 097205.

[47] G. Zheng and C. H. Patterson, *Phys. Rev. B* **67** (2003) 220404.

[48] J. B. Goodenough, *Localized to Itinerant Electronic Transition in Perovskite Oxides*, (Springer-Verlag Berlin Heidelberg New York, 2001.

[49] C. N. R. Rao, A. Arulraj, A. K. Cheetam and B. Raveau, *J. Phys.Condens. Matter* **12** (2000) R83.

[50] H. Kuwahara, Y. Tomioka, A. Asamitsu, Y. Moritomo and Y. Tokura, *Science* **270** (1995) 961.

[51] Y. Moritomo, H. Kuwahara, Y. Tomioka and Y. Tokura, *Phys. Rev. B* **55** (1997)7549.

[52] T. Zhang, T. F. Zhou, T. Qian and X. G. Li, *Phys. Rev. B* **76** (2007) 174415.

[53] S. Zhou, Y. Guo, J. Zhao, L. He, C. Wang and L. Shi, *J. Phys. Chem. C* **115** (2011) 11500.

[54] S. S. Rao and S. V. Bhat, *J. Nanosci. Nanotechnol*. **7** (2007) 2025.

[55] Z. Jirak, *Phys. Rev. B* **46** (1992) 8725.

[56] M. W. Lofaso and P. M. Woodward, *Acta. Cryst. B* **60** (2004) 10.

[57] University of Oslo Theoretical activity in solid state chemistry and material science, folk.uio.no/ravi/activity/ordering/spinordering.html.

[58] E. Dagotto, *Nanoscale Phase Separation and Colossal Magnetoresistance*, Springer Series in Solid State Physics136 (Springer-Verlag, Berlin, Heidelberg), 2003.

[59] E. Dagotto, *Science* **309** (2005) 257.

[60] A. Moreo, M. Mayr, A. Feiguin, S. Yunoki and E. Dagotto, *Phys. Rev. Lett*. **84** (2000) 5568.

[61] E. L. Nagaev, *Colossal magnetoresistence and phase separation in magnetic semiconductors* (Imperial college press, London, 2002).

[62] E. L. Nagaev, *JETP Lett*. **6** (1967) 18.

[63] E. L. Nagaev, *JETP Lett*. **66** (1972) 394.

[64] E. O. Wollan and W. C. Koehler, *Phys. Rev*. **100** (1955)545.

[65] J. H. Van Santen and G. H. Jonker, *Physica* **16** (1950) 599.

[66] S. Mori, C. H. Chen and S. W. Cheong, *Nature* **392** (1998) 473.

[67] C. Renner, G. Aeppli, B. G. Kim, Y. A. Soh and S. W. Cheong, *Nature* **416** (2002) 518.

[68] A. Moreo, S. Yunoki and E. Dagotto, *Science* **283** (1999) 2034.

[69] A. P. Ramirez, *J. Phys.: Condens. Matter* **9** (1997) 8171.

[70] J. M. De Teresa, M. R. Ibarra, P. A. Algarabel, C. Ritter, C. Marquina, J. Blasco, J. Garcia, A . del Moral and Z. Arnold, *Nature* (London) **386** (1997) 256.

[71] H. L. Ju and H. Sohn, *J. Magn. Magn. Matter*. **167** (1997) 200.

[72] I. Felner, M. I. Tsindlekht, G. Gorodetsky and R. Rosenberg, *J. Supercond.* **13**, (2000) 659.

[73] V. Chechersky, Amar Nath, I. Isaac, Jurgen P. Franck, Kartik Ghosh, Honglyoul Ju, and Richard L. Greene, *Phys. Rev. B* **59** (1999) 497.

[74] M. M. Savosta, A. S. Karnachev, S. Krupicka, J. Hejtmanek, Z. Jirak, M. Marysko and P. Novak, *Phys. Rev. B* **62** (2000) 545.

[75] C. N. R. Rao, Asish K. Kundu, Md. Motin Seikh and L. Sudheendra, *Dalton Trans*. (2004) 3003.

[76] V. B. Shenoy and C. N. R. Rao, Phil. *Trans. R. Soc. A* **366** (2008) 63.

[77] A. Maignan, C. Martin, S. Hebert and V. Hardy, *J. Mater. Chem*. **17** (2007) 5023.

[78] A. Llobet, C. Frontera, J. L. Garcıa-Munoz, C. Ritter and M. A. G. Arnada, *Chem. Mater*. **12** (2000) 3648.

[79] W. J. Lu, Y. P. Sun, B. C. Zhao, X. B. Zhu and W. H. Song, *Phys. Rev. B* **73** (2006) 214409.

[80] G. X. Cao, J. C. Zhang, S. P. Wang, J. Yu, C. Jing, S. X. Cao and X. C. Shen, *J. Magn. Magn. Mater*. **301** (2006) 147.

[81] R. B. Griffiths, *Phys. Rev. Lett*. **23** (1969) 17.

[82] T. Sarkar, B. Ghosh, A. K. Raychaudhuri and T. Chatterji, *Phys. Rev. B* **77** (2008) 235112.

[83] Z. Jirak, E. Hadova, O. Kaman, K. Knizek, M. Marysko, E. Pollert, M. Dlouha and S. Vratislav, *Phys. Rev. B* **81** (2010) 024403.

[84] X. H. Huang, J. F. Ding, G. Q. Zhang, Y. Hou, Y. P. Yao and X. G. Li, *Phys. Rev. B* **78** (2008) 224408.

[85] V. Markovich, I. Fita, A. Wisniewski, G. Jung, D. Mogilyansky, R. Puzniak, L. Titelman and G. Gorodetsky, *Phys. Rev. B* **81** (2010) 134440.

[86] V. A. Bokov, N. A. Grigoryan and M. F. Bryzhina, *Phys. Status Solidi.* **20** (1967) 745.

[87] I. O. Troyanchuk, O. S. Mantytskaya and A. N. Chobot, *Physics of the Solid State* **44** (2002) 2266.

[88] J. L. Garcıa-Munoz, M. A. G. Aranda, A. Llobet, C. Frontera, M. J. Martınez-Lope, C. Ritter, M. Respaud and J. M. Broto, *J. Alloys. Compds*. **323-324** (2001) 408.

[89] H. Chiba, M. Kikuchi, K. Kusaba, Y. Muraoka and Y. Syono, *Solid State Communications* **99** (1996) 499.

[90] Y. Qin, T. A. Tyson, K. Pranzasand and H. Eckerlebe, *J. Phys.: Condens. Matter* **20** (2008) 195209.

[91] H. Taguchi, *Phys. Status Solidi A* **88** (1985) K79.

[92] S. Yoon, M. Rübhausen, S. L. Cooper, K. H. Kim and S-W. Cheong, *Phys. Rev. Lett.***85** (2000) 3297.

[93] M. Rubhausen, S. Yoon, S. L. Cooper, K. H. Kim and S-W. Cheong, *Phys. Rev. B* 62 (2000) R4782.

[94] J. L. Garcıa-Munoz, C. Frontera, P. Beran, N. Bellido, J. S. Lord, C. Ritter and I. Margiolaki, *J. Phys.: Condens. Matter* **19** (2007) 406212.

[95] K. Shimizu, Y. Qin and T. A. Tyson, *Phys. Rev. B* **73** (2006) 174420.

[96] M. Giot, A. Pautrat, G. Andre, D. Saurel, M. Hervieu and J. Rodriguez-Carvajal, *Phys. Rev. B* **77** (2008) 134445.

[97] Y. Su, C-H. Du, P. D. Hatton, S. P. Collins and S-W. Cheong, *Phys. Rev. B* **59** (1999) 11687.

[98] I. I. Smolyaninov, V. N. Smolyaninova, C. C. Davis, B-G. Kim, S-W. Cheong and R. L. Greene, *Phys. Rev. Lett*. **87** (2001) 127204.

[99] S. B. Wilkins, P. D. Spencer, P.D. Hatton, D. Mannix, S.D. Brown, T. dAlmeida and S-W. Cheong, *Physica B* **318** (2002) 295.

[100] A. Kirste, M. Goiran, M. Respaud, J. Vanaken, J. M. Broto, H. Rakoto, M. von Ortenberg, C. Frontera and J. L. Garcıa-Munoz, *Phys. Rev. B* **67** (2003) 134413.

[101] J. L. García-Muñoz and C. Frontera, *J. Appl. Phys*. **103** (2008) 07F718.

[102] Y. Murakami, D. Shindo, H. Chiba, M. Kikuchi and Y. Syono, *Phys. Rev. B* **55** (1197) 15043.

[103] H. L. Liu, S. L. Cooper and S-W. Cheong, *Phys. Rev. Lett*. **81** (1998) 4684.

[104] J. Kurian and R. Singh, *J. Appl. Phys.***103 (**2008) 07F707.

[105] M. C. Walsh, M. Foldeaki, A. Giguere, D. Bahadur, S. K. Mandal and R. A. Dunlap, *Physica B* **253** (1998) 103.

[106] J. R. Sun, J. Gao, Y. Fei, R. W. Li and B. G. Shen, *Phys. Rev. B* **67** (2003) 144414.

[107] H. Gencer, S. Atalay, H. I. Adiguzel and V. S. Kolat, *Physica B* **357** (2005) 326.

[108] S. Atalay, V. S. Kolat, H. Gencer and H. I. Adiguzel, *J. Magn. Magn. Mater*. **305** (2006) 452.

[109] Z. C. Xia, L. X. Xiao, C. H. Fang, G. Liu, B. Dong, D. W. Liu, L. Chen, L. Liu, S. Liu, D. Doyananda, C. Q. Tang and S. L. Yuan, *J. Magn. Magn. Mater*. **297** (2006) 1.

[110] Y. Wu, Z. Xia, G. Zhang and J. Vanacken, J. *Low Temp. Phys*. **174** (2014) 207.

[111] L. Righai, M. Amboage, J. Gutierrez, J. M. Barandiaran, L. F. Barquin and M. T. F. Diaz, Physica B **276-278** (2000) 718.

[112] J. M. Barandiaran, J. Gutierrez, J. R. Fernandez, M. Amboage and L. Righi, *Physica B* **343** (2004) 379.

[113] X. L. Jiang, J. Gao, S. K. Ren, Q. Y. Xu, H. Sang, F. M. Zhang and Y. W. Du, *J. Alloys. Compd.* **384** (2004) 261.

[114] D. Vijayan, J. Kurian and R. Singh, *AIP. Conf. Proc*. **1447**(2012) 1191.

[115] L. Righi, J. Gutierrez and J. M. Barandiaran, *J. Phys.: Condens. Matter* **11** (1999) 2831.

[116] R. Li, Z. Qu, J. Fang, X. Yu, L. Zhang and Y. Zhang, *Solid State Communications* **150** (2010) 389.

[117] X. Wang, Q. Cui, Y. Pan and G. Zou, *J. Alloys. Compd.* **354** (2003) 91.

[118] J. R. Sun, J. Gao and L. Kang, *Appl. Phys. Lett*. **81** (2002) 508.

[119] Y-S. Wang, N-M. Xia, H-K Zuo, Y-N. Shen and Z-C. Xia, *Chin. Phys. Lett*. **31** (2014) 047501.

[120] M. Anwar, F. Ahmed, S. R. Lee, R. Danish and B. Koo, *J. J. Appl. Phys*. **52** (2013) 10MC12.

[121] I. Dhiman, A. Das, A. K. Nigam and Urs Gasser, *J. Phys.: Condens. Matter* **23** (2011) 246006.

[122] R. R. Zhang, G. L. Kuang, X. Luo and Y. P. Sun, *J. Alloys. Compds*. **484** (2009) 36.

[123] M. S. Sahasrabudhe, S. I. Patil, S. K. Date, K. P. Adhi, S. D. Kulkarni, P. A. Joy and R. N. Bathe, *Solid State Communications* **137** (2006) 595.

[124] Sunil Nair and A. Banerjee, *Phys. Rev. Lett*. **93** (2004) 117204.

[125] D. Cao, F. Bridges, M. Anderson, A. P. Ramirez, M. Olapinski, M. A. Subramanian, C. H. Booth and G. H. Kwei, *Phys. Rev. B* **64** (2001) 184409.

[126] T. S. Orlova, J. Y. Laval, Ph. Monod, P. Bassoul, J. G. Noudem and E. V. Orlenko, *Phys. Rev. B* **79** (2009) 134407.

[127] J. Fan, L. Pi, W. Tong, S. Xu, J. Gao, C. Zha and Y. Zhang, *Phys. Rev. B* **68** (2003) 092407.

[128] S. M. Yusuf, *Phys. Rev. B* **66** (2002) 064414.

[129] C. Hao, B. Zhao, G. Kuang, and Y. Sun, *Phys. Status Solidi B* **248** (2011) 2921.

[130] V. Suresh Kumar and R. Mahendiran, *J. Appl. Phys*. **109** (2011) 023903.

[131] D. Vijayan, J. Kurian and R. Singh, *J. Appl. Phys*. **111** (2012) 07D716.

[132] D. Vijayan, J. Kurian and R. Singh, *IEEE Trans. Magn.* **47** (2011) 2701.

[133] B. L. Ahuja, S. Tiwari, A. Dashora, H. S. Mund, J. Sahariya, D. M. Phase, R. J. Choudhary, A. Banerjee, M. Itou and Y. Sakurai, *Appl. Phys. Lett*. **99** (2011) 062512.

[134] S. Tiwari, D. M. Phase, R. J. Choudhary, H. S. Mund and B. L. Ahuja, *J. Appl. Phys*. **109** (2011) 033911.

[135] I. O. Troyanchuk, M. V. Bushinsky, H. Szymczak, K. Barner and A. Maignan, *Eur. Phys. J. B* **28** (2002) 75.

[136] I. Dhiman, A. Das, A. K. Nigam and R. K. Kremer, *J. Magn. Magn. Mater*. **334** (2013) 21.

[137] A. Banerjee, K. Mukherjee, Kranti Kumar and P. Chaddah, *Phys. Rev. B* **74**, (2006) 224445.

[138] Sunil Nair and A Banerjee, *J. Phys.: Condens. Matter* **16** (2004) 8335.

[139] T. S. Orlova, J. Y. Laval, Ph. Monod, J. G. Noudem and A. A. Greshnov, *J. Magn. Magn. Mater*. **342**(2013) 120.

[140] X. Chen, S. Dong, K. Wang, J-M. Liu and E. Dagotto, *Phys. Rev. B* **79** (2009) 024410.

[141] K. Pradhan, A. Mukherjee and P. Majumdar, *Euro. Phys. Lett.* **84** (2008) 37007.

[142] S. Hebert, C. Martin, A. Maignan, R. Retoux, M. Hervieu, N. Nguyen and B. Raveau, *Phys. Rev. B* **65** (2002) 104420.

[143] T. Kimura, Y. Tomioka, R. Kumai, Y. Okimoto and Y. Tokura, *Phys. Rev. Lett*. **83** (1999) 3940.

[144] M. Tseggai, R. Mathieu, P. Nordblad, R. Tellgren, L. V. Bau, D. N. H. Nam, N. X. Phuc, N. V. Khiem, G. Andre and F. Bouree, *J. Solid State Chem*. **177** (2004) 966.

[145] K. Woo, H. J. Lee, J-P. Ahn and Y. S. Park, *Adv. Mater*.**15** (2003) 1761.

[146] Z. Miao, D. Xu, J. Ouyang, G. Guo, X. Zhao and Y. Tang, *Nano Lett.* **2** (2002) 717.

[147] F. Jia, L. Zhang, X. Shang and Y. Yang, *Adv. Mater*. **20** (2008) 1050.

[148] L. L. Hench and J. K. West, *Chem. Rev*. **90** (1990) 33.

[149] C. Vazquez-Vazquez, M. Carmen Blanco, M. Arturo Lopez-Quintela Rodolfo D. Sanchez, Jose Rivas and Saul B. Oseroff, *J. Mater. Chem*. **8** (1998) 991.

[150] W. H. R. Shaw and J. J. Bordeaux, *J. Am. Chem. Soc*. **77** (1955) 4729.

[151] J. P. Barbier and R. Hugel, *Inorg. Chim. Acta,* **10** (1974) 93.

[152] R. B. Penland, S. Mizushima, C. Curran and J. V. Quagliano, *J. Am. Chem. Soc*. **79** (1957) 1575.

[153] F. W. Miller, Jr.. and H. R. Dittmar, *J. Am. Chem. Soc*., **56** (1934) 848.

[154] T. Zhang, C. Jin, J. Zhang, X. Lu , T. Qian and X. Li, *Nanotechnology* **16** (2005) 2743.

[155] B. D. Cullity and S. R. Stock, *Elements of X-ray diffraction* Prentice Hall Inc, 2001.

[156] S. Saipriya, *Structural optical and magnetic studies on RF-sputtered SnO_2 thin films and SnO_2/(Mn, Co and Cu-Zn ferrite) multilayers)*, UOH, 2012.

[157] G. Will, *Powder Diffraction : The Rietveld Method and Two Stage Method* (2006) Springer, Germany

[158] H. M. Rietveld, *J. Appl. Crystallography*. **2** (1969) 65.

[159] R. A. Young, The Rietveld Method, Oxford IUCr/OUP (1995).

[160] G. Lawes, *Scanning Electron Microscopy and X-ray Microanalysis*, John Wiley & Sons, Inc, New York, 1987.

[161] H. Jaksch, J-P Vermeulen, *New developments in Gemini FESEM technology*.

[162] https://en.wikipedia.org/wiki/Characteristic X-ray.

[163] C. S. Sunandana, Bull. Mater. Sci. **21** (1998) 1

[164] P. H. Rieger, *Electron Spin Resonance: Analysis and Interpretation*, The Royal Society of Chemistry, 2007.

[165] http://www.pharmatutor.org/articles/instrumentation-electron-spin-resonance-spectroscopy.

[166] B. D. Cullity and C. D. Graham, *Introduction to magnetic materials*, A John Wiley & Sons, Inc. 2009 .

[167] M. Giot, P. Beran, O. Perez, S. Malo, M. Hervieu, B. Raveau, M. Nevriva, K. Knizek and P. Roussel, *Chem. Mater.* **18** (2006) 3225.

[168] J. A. Collado, C. Frontera, J. L. Garcıa-Munoz, C. Ritter, M. Brunelli and M. A. G. Aranda, *Chem. Mater.* **15** (2003) 167.

[169] A. Maignan, C. Martin, C. Autret, M. Hervieu, B. Raveau and J. Hejtmanek, *J. Mater. Chem.***12** (2002) 1806.

[170] D. Tzankov, D. Kovacheva, K. Krezhov, R. Puzniak, A.Wisniewski, E. Svab and M. Mikhov, *J. Phys.: Condens. Matter* **17** (2005) 4319.

[171] J. Kurian and R. Singh, *J. Appl. Phys*. **105** (2009) 07D718.

[172] M. T. Causa, M. Tovar, A. Caneiro, F. Prado, G. Ibanez, C. A. Ramos, A. Butera, B. Alascio, X. Obradors, S. Pinol, Y. Tokura and S. B. Oseroff, *Phys. Rev. B* **58** (1998) 3233.

[173] D. L. Huber, G. Alejandro, A. Caneiro, M. T. Causa, F. Prado, M. Tovar and S. B. Oseroff, *Phys. Rev. B* **60** (1999) 12155.

[174] A. Kumar, N. Ghosh, J. P. Joshi, H. L. Bhat and S. V. Bhat, *Solid State Communications* **123** (2002) 379.

[175] E. Rozenberg, A. I. Shames, M. Auslender, G. Jung, I. Felner, J. Sinha, S. Banerjee, D. Mogilyansky, E. Sominski, A. Gedanken, Ya. M. Mukovskii, and G. Gorodetsky, *Phys. Rev. B* **76** (2007) 214429.

[176] M. Auslender, A. I. Shames, E. Rozenberg, E. Sominski, A. Gedanken and Ya. M. Mukovskii, *J. Appl. Phys*. **107** (2010) 09D702.

[177] A. I. Shames, E. Rozenberg, G. Gorodetsky and Ya. M. Mukovskii, *Phys. Rev. B* **68**, (2003)174402.

[178] K. N. Anuradha, S. S. Rao and S. V. Bhat, *Appl. Magn. Reson*.**36** (2009) 347.

[179] P. J. Janhavi, A. R. Bhagwat, S. Sarangi, A. Sharma and S. V. Bhat, *Physica B* **349** (2004) 35.

[180] M. S. Seehra, *Rev. Sci. Instrum*. **39** (1968)1044.

[181] C. A. Ramos, M. T. Causa, M. Tovar, X. Obradors and S. Pinol, *J. Magn. Magn. Mater*. **177-181** (1998) 867.

[182] A. Shengelaya, G. M. Zhao, H. Keller and K. A. Muller, *Phys. Rev. Lett.* **77** (1996) 5296.

[183] C. Rettori, D. Rao, J. Singley, D. Kidwell, S. B. Oseroff, M. T. Causa, J. J. Neumeier, K. J. McClellan, S-W. Cheong and S. Schultz, *Phys. Rev. B* **55** (1997) 3083.

[184] J. B. Goodenough and J-S. Zhou, *Nature* (London) **386** (1997) 229.

[185] J-S. Zhou, J. B. Goodenough, A. Asamitsu and Y. Tokura, *Phys. Rev. Lett*. **79** (1997) 3234.

[186] P. Tong, B. Kim, D. Kwon, T. Qian, Sung-Ik Lee, S-W. Cheong and B. G. Kim, *Phys. Rev B* **77** (2008) 184432.

[187] S. B. Oseroff, M. Torikachvili, J. Singley, S. Ali, S. W. Cheong and S. Schultz, *Phys. Rev.* B **53** (1996)6521.

[188] O. Chauvet, T. Stoto and L. Zuppiroli, *Phys. Rev. B* **49** (1994)5876.

[189] M. T. Causa, E. Winkler, D. Tobıa and M. Tovar, *Physica B* **398** (2007) 464.

[190] V. Chechersky, Amar Nath, S. E. Lofland, S. Newlander, L. Cerquoni, Y. Mukovskii, A. A. Arsenov, G. Karabshev, D. A. Shulyatev and R. L. Greene, *Phys. Rev. B* **63** (2001)214401.

[191] P. J. Janhavi, R. Gupta, A. K. Sood, S. V. Bhat, A. R. Raju and C. N. R. Rao, *Phys. Rev. B* **65** (2001) 024410.

[192] M. Auslender, A. I. Shames, E. Rozenberg, G. Gorodetsky and Ya. M. Mukovskii, *IEEE Trans. Magn.* **43** (2007) 3049.

[193] M. Auslender, A. I. Shames, E. Rozenberg, I. Felner, D. Mogilyansky, A. Pestun, Ya. M. Mukovskii and G. Gorodetsky, *J. Appl. Phys*. **109** (2011) 07D705.

[194] M. S. Seehra, M. Ibrahim, V. S. Babu and G. Srinivasan, *J. Phys.: Condens. Matter* **8** (1996) 11283.

[195] M. S. Seehra and R. P. Gupta, *Phys. Rev. B* **9** (1974) 197.

[196] A. Shengelaya, Guo-meng Zhao, H. Keller, K. A. Muller and B. I. Kochelaev, *Phys. Rev. B* **61** (2000) 5888.

[197] D. L. Huber and M. S. Seehra, *J. Phys. Chem. Solids* **36** (1975) 723.

[198] C. D. Hu, *J. Phys.: Condens. Matter*.**16** (2004) 6293.

[199] W. Ning, F. Wang, X. Q. Zhang, Z-H. Cheng and Y. Sun, *J. Magn. Magn. Mater*. **321** (2009) 88.

[200] H. W. Tian, W. T. Zheng, Z. D. Zhao, T. Ding, S. S. Yu, B. Zheng, X. T. Li, F. L. Meng and Q. Jiang, *Chem. Phys. Lett*. **401** (2005) 585.

[201] A. Arulraj, R. Gundakaram, A. Biswas, N. Gayathri, A. K. Raychaudhuri and C. N. R. Rao, *J. Phys.: Condens. Mater*. **10** (1998) 4447.

[202] C. N. R. Rao, *J. Phys. Chem*. *B* **104** (2000) 5877.

[203] J. L. Garcıa-Munoz, C. Frontera, M. A. G. Aranda, A. Llobet and C. Ritter, *Phys. Rev. B* **63** (2001) 064415.

[204] C. Frontera, J. L. Garcıa-Munoz, C. Ritter, L. Manosa, X. G. Capdevila and A. Calleja, *Solid State Communications* **125** (2003) 277.

[205] Z. Zeng, Z. M. Greenblatt and M. Croft, *Phys. Rev. B* **59** (1999) 8784.

[206] I. V. Solovyev and K. Terakura, *Phys. Rev. B* **63** (2001) 174425.

[207] S. Chandra, A. Biswas, S. Datta, B. Ghosh, V. Siruguri, A. K. Raychaudhuri, M. H. Phanand and H. Srikanth, *J. Phys: Cond. Matter* **24** (2012) 366004.

[208] C. Ritter, M. R. Ibarra, J. M. De Teresa, P. A. Algarabel, C. Marquina, J. Blasco, J. Garcıa, S. Oseroff and S-W. Cheong, *Phys. Rev. B* **56** (1997) 8902.

[209] J. A. Souza, J. J. Neumeier, R. K. Bollinger, B. McGuire, C. A. M. dos Santos and H. Terashita, *Phys. Rev. B* **76** (2007) 024407.

[210] S.de Brion, F. Ciorcas, G. Chouteau, P. Lejay, P. Radaelli and C. Chaillout, *Phys. Rev. B* **59** (1999) 1304.

[211] N. F. Mott and E. A. Davis, *Electronic Processes in Non-Crystalline Materials* (Oxford: Clarendon), 1971.

[212] A. L. Efros and B. I. Shklovskii, *J. Phys. C: Solid State Phys.* **8** (1975) L49.

[213] Y. Kamlesh and G. D. Varma, *J. Supercond. Nov. Magn*. **25** (2012) 1097.

[214] D. Shannon, *Acta Crystallogr*. *A* **32** (1976) 751.

[215] A. Ramesh and R. Singh, *IEEE Trans. Magn*. **48** (2012) 4562.

[216] A. Ramesh and R. Singh, *Physica B* **448** (2014) 273.

[217] E. Rozenberg, M. Auslender, A. I. Shames, Ya. M. Mukovskii, E. Sominski, and A. Gedanken, *J. Appl. Phys*. **105** (2009) 07D707.

[218] L. Sudheendra, H. D. Chinh, A. R. Raju, A. K. Raychaudhuri and C. N. R. Rao, *Solid State Communications* **122** (2002) 53.

[219] X. H. Huang, J. F. Ding, Z. L. Jiang, Y. W. Yin, Q. X. Yu, and X. G. Li, *J. Appl. Phys*. **106** (2009) 083904.

[220] B. Martınez, X. Obradors, Ll. Balcells, A. Rouanet and C. Monty, *Phys. Rev. Lett*. **80** (1998) 181.

[221] S. Abiko, S. Niidera and F. Matsubara, *Phys. Rev. Lett*. **94** (2005) 227202.

[222] M. Viswanathan and P. S. Anil Kumar, *Phys. Rev. B* **80** (2009) 012410.

[223] S. K. Banerjee, *Phys. Lett*. **12** (1964) 16.

[224] A. Arrott and J. E. Noakes, *Phys. Rev. Lett*. **19** (1967) 786.

[225] S. Narayana Jammalamadaka, S. S. Rao, S. V. Bhat, J. Vanacken and V. V. Moshchalkov, *J. Appl. Phys*. **112** (2012) 083917.

[226] M. Aparnadevi, S. K. Barik and R. Mahendiran, *J. Magn. Magn. Mater.* **324** (2012)3351.

[227] M. Viret, L. Ranno and J. M. D. Coey, *Phys. Rev.* B **55** (1997) 8067.

[228] J. Burgy, A. Moreo and E. Dagotto, *Phys. Rev. Lett.* **92** (2004) 097202.

[229] J. A. Souza and R. F. Jardim, *J. Phys. D: Appl. Phys*. **42** (2009) 032006.

[230] D. G. Kuberkar, R. R. Doshi, P. S. Solanki, U. Khachar, M. Vagadia, A. Ravalia and V. Ganesan, *Applied Surface Science* **258** (2012) 9041.

[231] R. Li, Z. Qua and J. Fang, *Physica B* **406** (2011) 1312.

[232] K. Yadav, H. K. Singh and G. D. Varma, *Physica B* **407** (2012) 1244.

[233] R. R. Zhang, G. L. Kuang, X. Luo and Y. P. Sun, *J. Magn. Magn. Mater*. **321** (2009) 3933.

[234] N. A. Hill and K. M. Rabe, *Phys. Rev. B* **59** (1999) 8759.

[235] S. Dong, R. Yu, S. Yunoki, J. M. Liu and E. Dagotto, *Phys. Rev. B* **78** (2008) 064414.

[236] J. C. Slonczewski, *Phys. Rev. B* **39** (1989) 6995.

[237] S. Angappane, M. Pattabiraman, G. Rangarajan and K. Sethupathi, *J. Appl. Phys*. **97** (2005) 10H705.

[238] B. Padmanabhan, Ajay Sharma, S. S. Rao, S. Elizabeth, H. L. Bhat and S. V. Bhat, *Physica B* **398** (2007) 107.

[239] W. Ning, X-Q. Zhang, Z-H. Cheng and Y. Sun, *J. Magn. Magn. Mater*. **321** (2009) 1159.

[240] K. W. Joh, C. H. Lee, C. E. Lee and Y. H. Jeong, *Phys. Stat. Sol.(b)* **239** (2003) 452.

[241] A. I. Shames, E. Rozenberg, W. H. Mc Carroll, M. Greenblatt and G. Gorodetsky, *Phys. Rev. B* **64** (2001) 172401.

[242] N. O. Moreno, P. G. Pagliuso, C. Rettori, J. S. Gardner, J. L. Sarrao, J. D. Thompson, D. L. Huber, J. F. Mitchell, J. J. Martinez and S. B. Oseroff, *Phys. Rev. B* **63** (2001) 174413.

[243] F. Rivadulla, M. A. Lopez-Quintela, L. E. Hueso, J. Rivas, M. T. Causa, C. Ramos, R. D. Sanchez and M. Tovar, *Phys. Rev. B* **60** (1999) 11922.

[244] M. Fath, S. Freisem, A. A. Menovsky, Y. Tomioka, J. Aarts and J. A. Mydosh, Science **285** (1999) 1540.

[245] G. Zhao, H. Keller, R. L. Greene and K. A. Muller, *in Physics of Manganites*, edited by T. A. Kaplan and S. D. Mahanti (Plenum, New York), (1999) 221.

[246] M. Harder, Z. X. Cao, Y. S. Gui, X. L. Fan and C-M. Hu, *Phys. Rev. B* **84** (2011) 054423.

[247] D. Emin and T. Holstein, *Ann. Phys*. **53** (1969) 439.

[248] G. H. Rao, J. R. Sun, J. K. Liang and W. Y. Zhou, *Phys. Rev. B* **55** (1997) 3742.

[249] K. H. Kim, M. Uehara, C. Hess, P. A. Sharma and S-W. Cheong, *Phys. Rev. Lett*. **84** (2000) 2961.

[250] The-Long Phan, P. Zhang, T. D. Thanh, Q. T. Tran and S. C. Yu, *Solid State Communications* **191**(2014) 25.

[251] D. N. H. Nam, R. Mathieu, P. Nordblad, N.V. Khiem and N. X. Phuc, *Phys. Rev. B* **62** (2000) 1027.

[252] A. K. Pramanik and A. Banerjee, *Phys. Rev. B* **79** (2009) 214426.

[253] A. N. Ulyanov, H. D. Quang, N. E. Pismenova and S.C. Yu, *IEEE Trans. Magn*. **41** (2005) 2745.

[254] D. C. Kundaliya, R. Vij, R. G. Kulkarni, A. A. Tulapurkar, R. Pinto, S. K. Malik and W.B. Yelon, *J. Magn. Magn. Mater*. **264** (2003) 62.

[255] H. Zhang, D. Zeng and Z. Liu, *J. Magn. Magn. Mater*. **322** (2010) 2375.

[256] D. Ginting, D. Nanto, Y. D. Zhang, S. C. Yu and T-L. Phan, *J. Appl. Phys*. **113** (2013) 17E110.

[257] J. Fan, L. Ling, B. Hong, L. Zhang, L. Pi and Y. Zhang, *Phys. Rev. B* **81** (2010) 144426.

[258] J. S. Kouvel and M. E. Fisher, *Phys. Rev*. **136** (1964) A1626.

[259] D. Kim, B. Revaz, B. L. Zink, F. Hellman, J. J. Rhyne and J. F. Mitchell, *Phys. Lett*. **89** (2002) 227202.

[260] M. Oumezzine, O. Pena, S. Kallel and S. Zemni, *Solid State Sciences* **13** (2011) 1829.

[261] S. Roßler, U. K. Roßler, K. Nenkov, D. Eckert, S. M. Yusuf, K. Dorr and K-H. Muller, *Phys. Rev. B* **70** (2004) 104417.

[262] R. Thiyagarajan, S. EsakkiMuthu, S. K. Barik, R. Mahendiran and S. Arumugam, *J. Appl. Phys.* **113** (2013) 023904.

[263] G. Huanyin, L. Ning, Y. Guoqing and T. Wei, *J. Rare Earths* **24** (2006) 206.

[264] S. Qixiang, W. Guiying, Y. Guoqing, M. Qiang, W. Wenqi and P. Zhensheng, J. *Rare Earths* **6** (2008) 821.

[265] J. W. Lynn, R. W. Erwin, J. A. Borchers, Q. Huang, A. Santoro, J-L. Peng and Z. Y. Li, *Phys. Rev. Lett*. **76** (1996) 4046.

[266] K. Cherif, J. Dhahri, E. Dhahri, M. Oumezzine and H. Vincent, *J. Solid State Chem*.**163** (2002) 466.

[267] M. H. Ehsani, P. Kameli, F. S. Razavi, M. E. Ghazi and B. Aslibeiki, *J. Alloys. Compds*. **579** (2013) 406.

[268] K. Ghosh, C. J. Lobb, R. L. Greene, S. G. Karabashev, D. A. Shulyatev, A. A. Arsenov and Y. Mukovskii, *Phys. Rev. Lett*. **81** (1998) 4740.

[269] N. Panopoulos, D. Koumoulis, G. Diamantopoulos, M. Belesi, M. Fardis, M. Pissas and G. Papavassiliou, *Phys. Rev. B* **82** (2010) 235102.

[270] C. P. Adams, J. W. Lynn, V. N. Smolyaninova, A. Biswas, R. L. Greene, W. Ratcliff II, S-W. Cheong, Y. M. Mukovskii and D. A. Shulyatev, *Phys. Rev. B* **70** (2004) 134414.

[271] A. Ramesh and R. Singh, AIP advances **5** (2015) 087105.

[272] A. I. Tovstolytkin and T. I. Polek, O. I. Vyunov, S. A. Solopan, A. G. Belous, A. F. Lozenko and P. A. Trotsenko, *Low Temp. Phys*. **37** (2011)

107.

[273] A. A. Belik, K. Kodama, N. Igawa, S. Shamoto, K. Kosuda, and E. Takayama-Muromachi, *J. Am. Chem. Soc.* **132** (2010) 8137.

[274] J. Dhahri, A. Dhahri, M. Oumezzine and E. Dhahri, *J. Magn. Magn. Mater*. **320** (2008) 2613.

[275] L. Liu, S. L. Yuan, Z. M. Tian, X. Liu, J. H. He, P. Li, C. H. Wang, X. F. Zheng and S. Y. Yin, *J. Phys. D: Appl. Phys*. **42** (2009) 045003.

[276] S. S. Rao, S. Tripathi, D. Pandey and S. V. Bhat, *Phys. Rev. B* **74** (2006) 144416.

[277] A. Ramesh and R. Singh, *Ceramics International* **41** (2014) 4759.

[278] M. Pissas, I. Margiolaki, K. Prassides, and E. Suard, *Phys. Rev. B* 72 (2005) 064426.

[279] M. A. Lopez-Quintela, L.E. Hueso, J. Rivas and Rivadulla, *Nanotechnology* **14** (2003) 212.

[280] R. N. Bhowmik, R. Nagarajan and R.Ranganathan, *Phys. Rev. B* **69** (2009) 054430.

[281] E. Rozenberg, M. Auslender, A. I. Shames, G. Jung, I. Felner, M. I. Tsindlekht, D. Mogilyansky, E. Sominski, A. Gedanken, Ya. M. Mukovskii, and G. Gorodetsky, *J. Appl. Phys*. **110** (2011) 073919.

[282] S. Dong, F. Gao, Z. Q. Wang, J-M. LiuandZ. F. Ren, *Appl. Phys. Lett*. **90** (2007) 082508.

[283] L. Liu, J. J. Zheng, Z. C. Xia S. L. Yuana and Z. M. Tian, *Solid State Communications* **150** (2010) 2322.

[284] H. Das, G. Sangiovanni, A. Valli, K. Held and T. Saha-Dasgupta, *Phys. Rev. Lett*. **107** (2011) 197202.

[285] V. Markovich and G. Jung, *Phys. Rev. Lett*. **108** (2012) 129701.

[286] J. Fang, Q. Wang, Y. Zou, X. Yu, R. Li and Y. Zhang, *J. Appl. Phys*. **104** (2008) 123905.

List of publications:

Journals:

1) "Electron Spin Resonance Studies of $Bi_{1-x}Ca_xMnO_3$ ($x \geq 0.65$)", **Ramesh Ade** and R. Singh, IEEE Trans. Magn. **48** (2012) 4562.
2) "Electron spin resonance and magnetization studies of $Bi_{1-x}C_xMnO_3$", **Ramesh Ade** and R. Singh, Physica B **448** (2014) 273.
3) "Effect of Pr doping on the properties of $Bi_{0.5-x}Pr_xCa_{0.5}MnO_3$($0 \leq x \leq 0.50$) manganites", **Ramesh Ade** and R. Singh, Ceramics International **41**(2015) 4759.
4) "Low Temperature Magnetization Studies of $Bi_{1-x}Ca_xMnO_3$", **Ramesh Ade** and R. Singh, Indian Journal of cryogenics, **40** (2015) 213.
5) "Disorder-driven phase transition in $La_{0.37}D_{0.30}Ca_{0.33}MnO_3$ (D= Bi, Sm) manganites", **Ramesh Ade** and R. Singh, AIP advances, **5** (2015) 087105.
6) "Electron spin resonance and magnetization studies of Bi rich La-manganites", D. Vijayan**, Ramesh Ade**, Joji Kurian and R. Singh, IEEE Trans. Magn, **51** (2015) 1000804.
7) "Structural, Magnetic and Transport Properties of $Bi_{0.5-x}Pr_xCa_{0.5}MnO_3$ ($0.0 \leq x \leq 0.50$) Manganites" **Ramesh Ade** and R. Singh (under review).
8) "Effect of Grain Size on Charge and Spin Correlations in $Bi_{0.5}Ca_{0.5}MnO_3$ Manganite Nanoparticles" **Ramesh Ade** and R. Singh (under review).

Book Chapter:

"Electron Spin Resonance and Magnetization Studies of Bi-Manganites",
R. Singh and **Ramesh Ade**, InTech Open Access Publisher (in press).

Conference Proceedings:

1) "Electron Spin Resonance and Magnetization Studies of Sol-Gel Synthesized $Bi_{0.4}Ca_{0.6}MnO_3$",
Ramesh Ade, Joji Kurian, D. Vijayan and R. Singh, AIP. Conf. Proc. **1147** (2012) 1443.
2) "Effect of Grain Size on Charge and Magnetic Ordering in $Bi_{0.67}Ca_{0.33}MnO_3$"
Ramesh Ade and R. Singh, AIP. Conf. Proc. **1591** (2014) 1529.
3) "Disorder-driven phase transition in $La_{0.37}Bi_{0.15}Sm_{0.15}Ca_{0.33}MnO_3$",
Ramesh Ade and R. Singh, AIP. Conf. Proc. **1665** (2015) 030007(1).
4) "Structural and Magnetic Properties of Cr Doped TiO_2",
Christeena Sebastian, **Ramesh Ade**, Roona N, V.P. Anusree, A. Antony, R. Singh and Anu Thomas, The first national conference on advanced nano materials, ISBN 978-81-931227-0-9 (2015) 37.
5) "Study of Structural and Magnetic Properties of Fe-Doped TiO_2",
L. T. Jose, **Ramesh Ade**, P. V. Jithin, P. Aswathi, V. D. Sudheesh, A. Antony, R. Singh and J. Kurian, The first national conference on advanced nano materials, ISBN 978-81-931227-0-9 (2015) 44.
6) "Structural and Magnetic Studies of Ni Doped SnO_2",
Mintu Issac, **Ramesh Ade**, C.T. Libin, Anu Thomas, Deepu Joseph, R. Singh, Joji Kurian, The first national conference on advanced nano materials, ISBN 978-81-931227-0-9 (2015) 119.

Conference / Workshops attended

1) Frontiers in Physics, 28th and 29th October 2011, School of Physics, University of Hyderabad (Poster Presentation).
2) DAE-SSPS 2011, (19-23rd December 2011) SRM University, Kattankulathur, Tamilnadu (Poster presentation).
3) Frontiers in Physics, 27-29th September 2012, School of Physics, University of Hyderabad (Poster presentation).
4) 24th National Symposium on Cryogenics, 22 -24th January2013, Institute of Plasma Research, Ahmadabad, India (Poster presentation).
5) Frontiers in Physics 20-22nd September 2013, School of Physics, University of Hyderabad (Participated).
6) (Innovations in science technology for emerging knowledge society) A. P. Science Congress- 14-16 November, 2013 (Participated).
7) International Conference on Magnetic Materials and Applications (MagMA-2013, 5-7th December 2013, IIT Guwahati) (poster presentation).
8) DAE-SSPS 2013(17-21st December, 2013), Patiala, Punjab (poster presentation).
9) Frontiers in Physics, 17-18 October 2014, School of Physics, University of Hyderabad (Participated).
10) 25th National Symposium on Cryogenics, 08-10th December 2014, University of Hyderabad, Telangana (Poster presentation).
11) DAE-SSPS 2014(16-20th December, 2014), VIT Vellore, Tamilnadu (Poster presentation).

Structural, Magnetic and Transport Properties of Bismuth and Rare Earth Manganites

ORIGINALITY REPORT

22%	8%	20%	%
SIMILARITY INDEX	INTERNET SOURCES	PUBLICATIONS	STUDENT PAPERS

PRIMARY SOURCES

1	Joji Kurian. "Electron spin resonance and resistivity studies of charge-ordered $Bi_{1-x}Ca_xMnO_3$", Journal of Physics D Applied Physics, 11/07/2008 Publication	1%
2	etheses.saurashtrauniversity.edu Internet Source	1%
3	www.science.gov Internet Source	1%
4	T. Zhang. "Effect of particle size on the structure and magnetic properties of La[sub 0.6]Pb[sub 0.4]MnO[sub 3] nanoparticles", Journal of Applied Physics, 2006 Publication	<1%
5	Kurian, J.. "Electron spin resonance and resistivity studies of charge-ordered Bi"("1"-"x")Sr"xMnO"3", Journal of Alloys and Compounds, 20110421 Publication	<1%